An EPR Investigation of Stable and Transient Oxygen Centred Radicals over Polycrystalline TiO_2

Emma Carter

Department of Chemistry

Cardiff University

2007

ProQuest LLC
789 East Eisenhower Parkway
P.O. Box 1346
Ann Arbor, MI 48106-1346

To my family, with love, as always

Acknowledgements

My thanks must go to the following:

To Dr Damien Murphy, a supervisor and a friend, whose enthusiasm and encouragement during this project has been continuous, even during the days spent tackling "The Beast"!

To Dr Albert Carley, who guided me through the sometimes terrifying world of UHV technology.

To my colleagues in the EPR, electrochemistry and surface science labs, whose humour and friendship has made my past three years so enjoyable.

And finally, my love goes to my family. To my parents, who have supported me in every way possible through my life within and outside of my studies. And, of course, to my husband Geoff, who remained immensely patient through the early mornings and the late nights, and who has been (and always will be) my reason for going home at the end of each day.

Abstract

Electron Paramagnetic Resonance Spectroscopy (EPR) has been used to identify and characterise the nature of several oxygen centred radicals over the surface of polycrystalline TiO_2. The observed radicals exhibit varying stabilities over the different polymorphs of TiO_2 samples studied, namely mixed-phase P25, pure phase anatase and a pure rutile material.

Paramagnetic Ti^{3+} centres were formed by thermal treatment of TiO_2 under vacuum. Following the addition of oxygen, the superoxide anion (O_2^-) was formed and exhibited a distribution of sites on the surface. In particular, O_2^- preferentially stabilises at oxygen vacancies on the surface. However, the degree of site occupancy was found to be temperature dependent. Pronounced activity for vacancy stabilised anions under the influence of thermal, photochemical and chemical treatment was identified compared to non vacancy sites.

Co-adsorption of a series of aliphatic and aromatic ketones and oxygen over P25, followed by low temperature (77K) UV irradiation led to the formation of a series of unstable (transient) alkylperoxy and peroxyacyl radicals. The sequential reaction of acetone with surface adsorbed superoxide anions was also found to result in the formation of an $[acetone\text{-}O_2^-]_{(a)}$ surface complex which was unstable at temperatures above 250K. Thermally produced Ti^{3+} centres reacted with acetone to form an unstable organic intermediate. This species subsequently dissociated and underwent further reaction with oxygen to generate peroxy and peroxacyl radicals. The identities of these oxygen centred radicals were confirmed using isotopically enriched $^{17}O_2$.

Finally, results are presented on the work involved in the development of an Ultra-High Vacuum EPR spectrometer for investigation of paramagnetic species on single crystal oxide surfaces. Samples of $Cu(acac)_2$ supported on quartz and $TiO_2(110)$ were examined by EPR and XPS. The two techniques were combined to identify paramagnetic centres on the single crystals and to provide proof of concept in the operation of the spectrometer.

Contents

Chapter 3

Brief Introduction to the Theory and Applications of Electron Paramagnetic Resonance (EPR) Spectroscopy in Polycrystalline Systems

Chapter 4

Experimental Details

Chapter 5

Stabilisation of O_2^- Radicals at Oxygen Vacancy Defects on Polycrystalline TiO_2

Chapter 7

Development of a UHV-EPR Assembly for Studies of Single Crystal Oxide Surfaces

Chapter 1

Structure, Properties and Reactivity of Polycrystalline and Single Crystal TiO_2

1.1 Introduction

There are numerous applications where metal oxide surfaces play an important role, for example as thin film gas sensors, as varister devices and as coatings. The desire to investigate the surface properties on a fundamental level is driven by the expectation that a deeper understanding of these materials will lead to increases in device performance in many applications. The physical and chemical properties of metal oxides has been related to their various applications in an extensive review by Henrich and Cox.[1]

Over the years TiO_2 has become one of the most commonly studied metal oxide materials in surface science. The reason for its popularity lies in its ease of use in many experimental techniques which makes the process of identifying new phenomena on its surface much easier. Thus, TiO_2 is now recognised as the model system for characterizing the surface science of single-crystal metal oxides.

It is of interest to study further the reactions that occur on the polycrystalline varieties of TiO_2, as it is frequently the powdered form of the material that is utilised in industrial applications and this therefore provides a more realistic view of the processes that occur over the semiconductor catalyst. However, it is very difficult to obtain any site specific information from the polycrystalline samples; for this it is necessary to study single crystals. Therefore, during the course of the investigation in this thesis, several reactions will be performed on powdered samples of TiO_2 in order to gain information on reaction mechanisms and surface stability of radicals.

1.2 Manufacturing Process, Crystal Structure and Properties of TiO_2

There are two processes commonly used to produce TiO_2, known as the sulphate process and the chloride process. The sulphate process produces both anatase and rutile forms, while the chloride process yields only the rutile form.

In the sulphate process the raw material ilmenite ($FeTiO_3$) is reacted with concentrated sulphuric acid at 433K to yield a mixture of iron sulphate and soluble titanyl sulphate. The iron is removed by fractional distillation to leave the titanyl residue, which is further hydrolysed to form a precipitate of hydrous titanium dioxide.

After filtering and several washing cycles, the precipitate is calcined at 1300K to remove any sulphurous gases and remaining water. The whole process is described in equations (1.1-1.3) below:

$$FeTiO_3 + 2H_2SO_4 \rightarrow TiOSO_4 + FeSO_4 + 2H_2O \quad (1.1)$$

$$TiOSO_4 \rightarrow TiO_2nH_2O + H_2SO_4 \quad (1.2)$$

$$TiO_2nH_2O \rightarrow TiO_2 + nH_2O \quad (1.3)$$

The sulphate process is traditionally deemed to be less environmentally friendly than the chloride process, due to the production of acid by-products. However, developments in waste recycling methods have over recent years made the sulphate process almost as clean as the chloride process. Despite the higher costs of the sulphate process, it is the only method available for production of the anatase form of TiO_2.

Similar to the sulphate process, the chloride process uses the raw material ilmenite, which is placed into a chlorinator at a temperature of 923K. Crushed coke is added to the top of the chlorinator to accelerate the burning process and raise the temperature to 1273K. At this temperature, chlorine gas is fed through the reactor which reacts with the ilmenite to form titanium tetrachloride vapour. The $TiCl_4$ is then oxidized by burning in a plasma flame with oxygen to produce the final product, TiO_2. The process can be described by the following equations (1.4-1.5):

$$TiO_2 \text{ (impure)} + 2Cl_2 + C \rightarrow TiCl_4 + CO_2 \quad (1.4)$$

$$TiCl_4 + O_2 \rightarrow TiO_2 \text{ (pure)} + 2Cl_2 \quad (1.5)$$

TiO_2 is found in nature in three crystalline forms; rutile, anatase and brookite listed in order of decreasing natural abundance. The brookite form has no commercial value and therefore few studies are carried out on this polymorph. The unit cells of rutile and anatase are shown in Figure 1.1. In both crystal forms, the basic building block consists of a titanium atom surrounded by six oxygen atoms in a distorted octahedron. In the rutile structure the neighbouring octahedra share one corner along the <110> type directions and the axes of neighbouring octahedral pairs alternate by 90°. In anatase, the octahedra are connected with their edges.[2]

Rutile is the most stable of the three forms and, due to its high refractive index, it is favoured in pigment applications. Anatase, by comparison is a metastable phase

and transforms into the rutile form at temperatures above ~ 1000K in a process known as rutilisation.[3] The transition temperature is dependent on the sample history, crystallite size and the presence of impurities, and these variables can be used to synthesise samples with accurately known morphology. Anatase has a lower refractive index than rutile, but has a higher photocatalytic activity compared to rutile in several reactions such as O_2 photo-oxidation and is therefore the favoured form in certain applications such as solar cells.[4] There is growing evidence to suggest that samples of mixed-phase titania, such as the commercially available P25 Degussa which is approximately 80% anatase and 20% rutile, exhibit higher photoactivities than either of the individual phases,[5,6] and this will be discussed in detail in section 1.7 below. It is evident that photoactivity is highly dependent on both the chemical and physical properties of the sample. The physical and structural properties of the three forms are listed in Table 1.1. A more comprehensive list of the bulk properties of the three polymorphs can be found elsewhere.[2]

Table 1.1 Physical properties of the three TiO_2 polymorphs.

Property	**Rutile**	**Anatase**	**Brookite**
Structure	Tetragonal	Tetragonal	Orthorhombic
Density/ gcm^{-3}	4.23	3.9	4.0
Hardness (Mohs scale)	7-7.5	5.5-6	5.5-6
Refractive Index	2.71	2.55	-
Crystal Size/ nm	160 – 250	130 – 150	-
Unit Cell Dimensions/nm			
a	0.4584	0.3758	0.9166
b	1.4584	0.3758	0.5436
c	2.953	0.9514	0.5135
Unit Cell	D_{4h}	D_{4a}	D_{2h}
Bandgap / eV	3.02	3.23	3.14
Bond Lengths (Ti-O)/ nm	1.946 (×4)	1.937 (×4)	1.84 1.99
	1.984 (×2)	1.964 (×2)	1.94 2.00
			1.95 2.03
Ti site symmetry	D_{2h}	D_{2d}	C_1

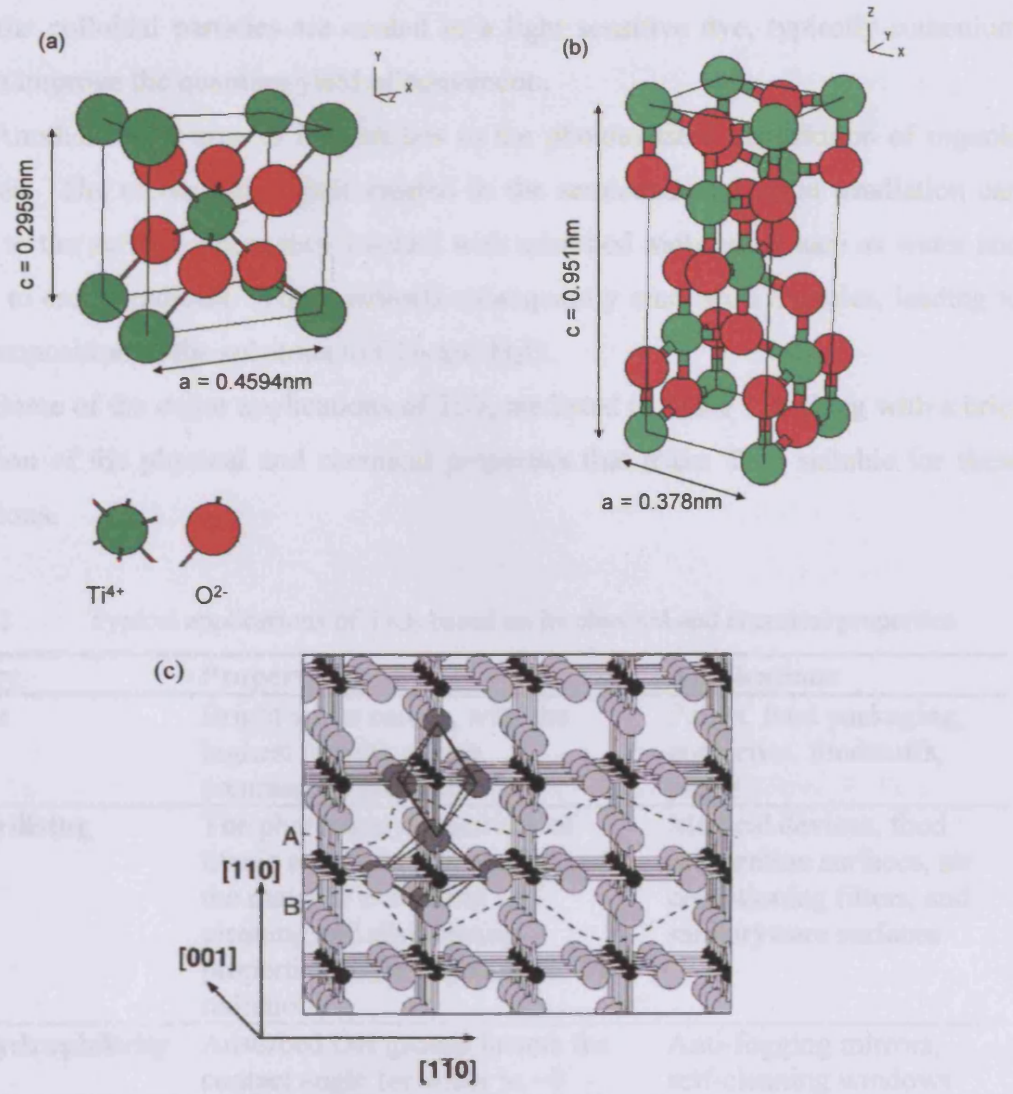

Figure 1.1 Crystal structures of the (a) anatase and (b) rutile forms of TiO_2. In (c) open channels along the [001] direction of the rutile lattice are visible.

1.3 Applications of TiO_2

The most common applications of TiO_2 include photocatalysis, white pigments in paints and cosmetics, as optical coatings and in ceramics. Its success as an opacifier results from the high refractive index of both the anatase and rutile forms (2.55 and 2.71 respectively) so that only a small amount of material is required to achieve a white opaque coating.

In recent years the photochemical properties of TiO_2 have become a major focus of research. This area of interest first came to light through the work of Fujishima and Honda[7] on the photolysis of water over TiO_2 electrodes without an external bias. Since that time, TiO_2 has been used in the conversion of sunlight into electricity in dye-sensitized nanocrystalline solar cells (DSNCs), the first of which was made by O'Regan and Grätzel.[4] Due to the wide bandgap of TiO_2, it is inefficient at solar conversion,

and so the colloidal particles are coated in a light sensitive dye, typically ruthenium based, to improve the quantum yield of conversion.

Another major area of interest lies in the photoassisted degradation of organic molecules. The electron-hole pair created in the semiconductor upon irradiation can migrate to the surface where they interact with adsorbed molecules, such as water and oxygen, to create radicals. These radicals subsequently react with organics, leading to the decomposition of the substrate to CO_2 and H_2O.

Some of the major applications of TiO_2 are listed in Table 1.2, along with a brief description of the physical and chemical properties that make TiO_2 suitable for these applications.

Table 1.2 Typical applications of TiO_2 based on its physical and chemical properties.

Category	Property	Applications
Pigment	Bright white colour, with the highest opacity of any commercial product	Paints, food packaging, cosmetics, foodstuffs, paper
Self-sterilising	The photocatalytic activity of titania results in thin coatings of the material exhibiting self cleaning and disinfecting properties under exposure to UV radiation.	Medical devices, food preparation surfaces, air conditioning filters, and sanitaryware surfaces
Superhydrophilicity	Adsorbed OH groups lowers the contact angle for water to ~0	Anti-fogging mirrors, self-cleaning windows
Water and air purifier	Photocatalyst under ambient conditions	Detoxify drinking water, decontaminate industrial wastewater, purify air streams
Gas Sensors	Electrical resistivity changes in presence of adsorbed gases	Monitoring exhaust fumes,
Solar Cells	Adsorbed dye molecules extend UV absorption into solar spectrum	Dye-sensitized nanocrystalline solar cells

TiO_2 is also used extensively in the paint and pigment industries due to its high refractive index. Although both the anatase and rutile forms of TiO_2 have been used in the pigment industry in many applications, it is the rutile form which is preferred. Although its high value of opacity makes TiO_2 the ideal choice for the pigment industry, several of its properties are actually detrimental to its performance, such as the "TiO_2 durability" effect (i.e. the effect which TiO_2 has on the durability of the pigment). TiO_2 is a good absorber of UV radiation; most of this energy is dissipated into the film as

heat. Reactions can occur at the surface of the pigment with adsorbed oxygen and water to form hydroxyl and superoxide radicals; these radicals are free to migrate, reacting with resin molecules, ultimately leading to the destruction of the paint film.

The absorption of UV light by TiO_2 can however also have an advantageous affect on the durability of a pigment. UV light photons are so energetic that they are capable of breaking weak bonds within the resin molecules themselves. The presence of TiO_2 particles therefore helps to remove the UV component of incident radiation and shields the resin molecules to some extent from direct degradation. Other UV absorbers and photo-stabilisers, such as hindered nitroxyl radicals and amines, are also added to pigments as polymer additives to effectively absorb UV light without forming chemically reactive species.[8] The beneficial properties of TiO_2 far outweigh the detrimental effects, to the extent that in some resins the presence of TiO_2 particles can almost treble the lifetime of the resin.

Owing to the importance of photocatalysis in the applications of TiO_2 and to this study, a more detailed description of the process is given in the following section 1.3.1.

1.3.1 Photocatalysis

1.3.1a Charge Carrier Generation

Photoexcitation with light of energy greater than the bandgap energy of a semiconductor promotes an electron from the occupied valence band to the unoccupied (or partially occupied) conduction band. This creates an electronic vacancy, referred to as a hole, in the valence band. More details of this process are given later in Chapter 2 during the discussion of solid state theory.

The photocatalytic activity of TiO_2 can be attributed to the size of the bandgap. The anatase polymorph has a bandgap of 3.2eV and rutile 3.0eV which makes them sensitive to photocatalytic excitation of light with wavelength <388nm. The lifetime of the electron/hole pair is sufficiently long in a semiconductor, in the nanosecond regime,[9] for the photogenerated charge carriers to migrate to the surface and participate in interfacial electron transfer with surface adsorbed species. A surface adsorbed electron acceptor can be reduced by accepting an electron from the surface (pathway C in Figure 1.2) and a surface adsorbed electron donor can be oxidised by transfer of an electron to a surface photogenerated hole (pathway D). These processes result in an anion radical and a cation radical as described by the following:

$$e^- + A \rightarrow A^{\cdot -} \quad (1.6)$$

$$h^+ + D \rightarrow D^{\cdot +} \quad (1.7)$$

The rate of the charge transfer from photogenerated charge carriers to surface adsorbed species depends on the positions of the valence and conduction bands of the solid and the redox potentials of the adsorbate species. Alternatively, electron and hole recombination can occur at the surface (pathway A) or, most probably, in the bulk of the semiconductor (pathway B).

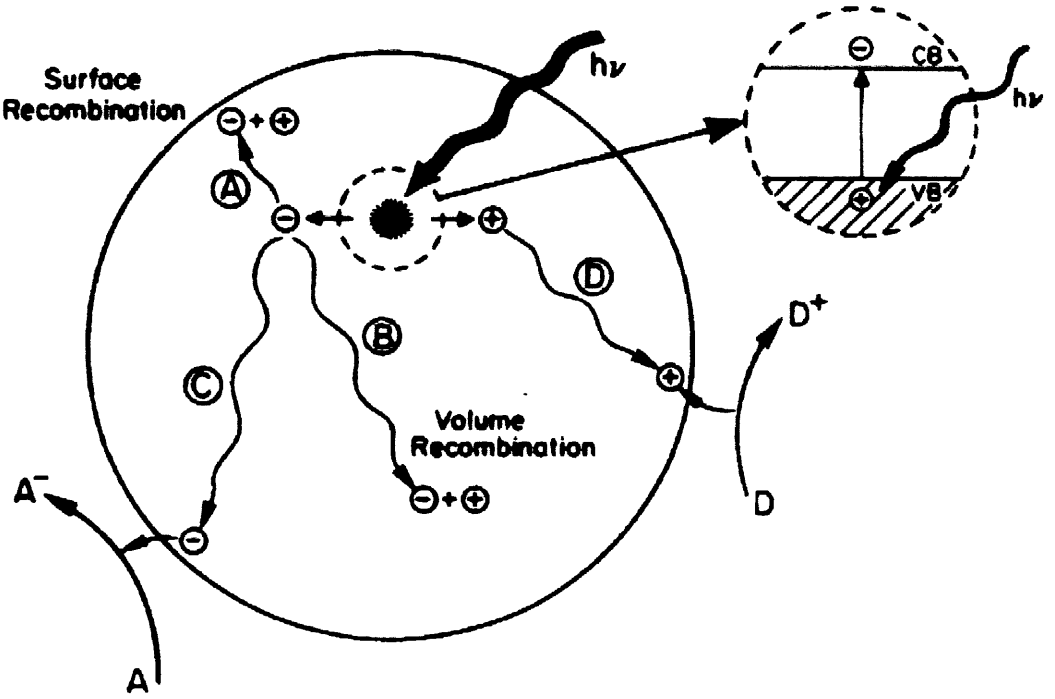

Figure 1.2 Schematic representation of photoexcitation in a semiconductor, followed by de-excitation events (including recombination and surface reaction).[10]

Photoinduced reduction can occur to any molecule possessing a reduction potential more positive than the conduction band edge. Similarly, photoinduced oxidation will occur for any molecule with an oxidation potential less positive than the semiconductor valence band edge since under these conditions interfacial electron transfer is thermodynamically allowed.[11]

In order for the photogenerated charge carriers to be photochemically productive they must remain spatially separated in the photoexcited solid until they are able to undergo further reactions with surface adsorbates. If the spatial separation of the charge carriers is insufficient, charge carrier recombination leads to dissipation of photon energy into heat. The study of charge carrier generation and recombination is therefore

essential for the development of efficient photocatalysts. In TiO_2 it is widely recognised that the conduction band electrons are trapped at local Ti^{4+} states within the TiO_2 lattice to form Ti^{3+} and the positive holes in the valence band are trapped at oxygen anion sites in the lattice. The overall process can be described as:

$$TiO_2 + hv \rightarrow e^-_{CB} + h^+_{VB} \quad (1.8)$$

$$e^-_{CB} + Ti^{4+} \rightarrow Ti^{3+} \quad (1.9)$$

$$h^+_{VB} + O^{2-} \rightarrow O^- \quad (1.10)$$

As the rate of carrier trapping is required to be faster than diffusion it is necessary that the charge trap is pre-associated with the photocatalyst surface before the onset of irradiation.[11]

1.3.1b Charge Carrier Separation

Electron and hole recombination at the surface or in the bulk of a semiconductor has an adverse effect on the photoefficiency. Several modifications can be made to the semiconductor to reduce the likelihood of recombination, such as metal doping and the use of charge traps. Over recent years the incorporation of metal dopants into the crystal lattice has attracted significant attention as it has been shown that even low levels of bulk dopants can have a major influence on the electronic properties of these materials.[12] The rutile structure of the semiconductor metal oxides TiO_2 and SnO_2 are particularly susceptible to the addition of metal dopants. A metal dopant can act as a mediator of charge transfer or as a recombination centre and the efficiency of the dopant depends on how well it performs either of these functions. In order to fully understand the increased activity of metal oxides with the addition of metal ion dopants, it is necessary to understand the structure of the dopants on an atomic scale.

Much work has been performed on vanadium doped SnO_2 and TiO_2, as exemplified by the work of Taverner *et al.*,[13] who utilised X-Ray Photoelectron Spectroscopy to determine the energy levels of the donor ions in the crystal lattice. It is predicted that the vanadium takes up substitutional sites in the lattice, resulting in a V^{4+} $3d^1$ paramagnetic ion. The EPR technique (describer later in Chapter 3) lends itself to the study of these systems to probe the electronic interactions and it is therefore surprising that there has been very little work reported in this area.[14]

Surface and bulk irregularities occur naturally in polycrystalline semiconductors such as TiO_2 and they differ in energy from the valence and conduction bands of the bulk solid. These states are able to act as charge traps, extending the lifetime of the charge carriers and thereby reducing the rate of recombination. Further discussion of surface irregularities and defects will be given in Chapter 5.

1.4 Activation of Adsorbed Species on Polycrystalline TiO_2

1.4.1 UV irradiation under an O_2 atmosphere

On production of charge carriers in TiO_2 (according to equation 1.8), the electrons and holes either become trapped, in shallow or deep traps, or they recombine. These processes have previously been studied by UV/Vis absorption spectroscopy to investigate the primary events immediately after band-gap excitation of the TiO_2.[15-17] These studies have mostly focussed on the relaxation process following excitation by a laser pulse source. However, as most photocatalysis is performed using continuous wave irradiation of lower light irradiances it is more useful to study the charge carriers under these conditions. For example, using diffuse reflectance IR spectroscopy to study TiO_2 samples after band-gap excitation using a high-pressure Xe lamp, Hoffmann *et al.*,[18] showed that the lifetimes of the photogenerated conduction band electrons are on a time-scale of minutes and are dependent upon the hydroxylation state of the sample surface.

Berger *et al.*,[19] used a combined EPR and IR study to investigate the charge trapping effects that occurred during photoexcitation of an anatase sample prepared by MOCVD (using a 350W high-pressure Hg lamp). After 20 minutes of UV exposure at 90K the EPR spectra of trapped holes, O^-, and trapped electrons, Ti^{3+}, could be resolved. The process of electron and hole trapping was followed using EPR spectroscopy by recording the intensity of the signal at fixed magnetic field values. The intensity of both signals increased monotonically within the first 100s. Thereafter the Ti^{3+} signal remained constant while the O^- signal continued to increase until it reached steady state after ~500s. As shown in Figure 1.3, the concentration of Ti^{3+} cations never exceeded 10% of the concentration of O^-, which implies that the majority of the photogenerated electrons remain in the conduction band of the TiO_2.

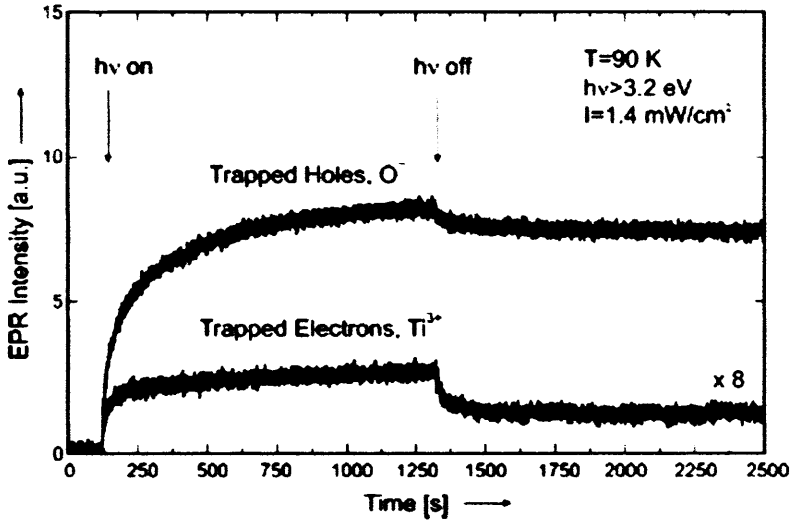

Figure 1.3 Concentration of O^- and Ti^{3+} centres as a function of UV exposure time.[19]

The temperature dependencies of the above processes were also identified through EPR spectroscopy. On UV excitation at 140K, no Ti^{3+} centres could be resolved, even on subsequent cooling of the sample to 90K. The O^- signal could still be resolved at 140K, although it was noticeably weaker in intensity. From these observations, Berger *et al.*,[19] concluded that there is an activation energy of ~ 0.01eV for the diffusion of photogenerated electrons trapped from shallow Ti^{3+} sites.

The lifetime of the photogenerated charge carriers can be extended by interaction with surface adsorbed species. In particular, several authors have reported that the adsorption of molecular oxygen results in the trapping of photogenerated electrons.[20,21] Berger *et al.*,[19] showed that on addition of oxygen to a pre-irradiated anatase sample (or irradiation in the presence of adsorbed oxygen) at 140K, no Ti^{3+} sites could be resolved but several oxygen centred radicals were found. The O^- signal due to trapped holes was still present, in addition to two different surface adsorbed superoxide (O_2^-) radicals. These radicals form as a result of interfacial transfer of electrons from localized paramagnetic states and the conduction band to molecular oxygen, as described by:

$$Ti^{3+} + O_2 \rightarrow Ti^{4+}.....O_2^- \quad (1.11)$$

$$Ti^{4+} + e^- + O_2 \rightarrow Ti^{4+}.....O_2^- \quad (1.12)$$

Upon irradiation of a thermally reduced anatase sample, no further increase in the Ti^{3+} concentration was seen, and only small traces of O^- trapped hole centres were resolved. It was further suggested that the absence of photoexcited trapped holes in thermally reduced TiO_2 is related to the deficiency of lattice oxygen trapping sites as a

result of the thermal treatment. This group also concluded that the surface concentration of superoxide anions is enhanced if UV irradiation is performed on the sample in the presence of oxygen compared to adsorption of oxygen to a pre-irradiated sample.[19]

Coronado *et al.*,[22] performed a detailed EPR and FTIR study on the characteristics of the species formed on UV irradiation of nanostructured TiO_2. UV irradiation of stoichiometric TiO_2 under static vacuum at 77K led to the evolution of Ti^{3+} centres, as predicted. After the cessation of the UV irradiation, the samples were subsequently exposed to molecular O_2 at 77K. On samples prepared by the hydrothermal method, a new signal with the g values of $g_1 = 2.024$, $g_2 = 2.009$ and $g_3 = 2.003$ replaced the Ti^{3+} signal with similar intensity, and this signal was later assigned to the superoxide radical.[22] The samples prepared by the thermal treatment showed a different set of signals following exposure to oxygen. The overall signal intensity increased compared to the UV irradiated sample, and the spectra were found to be composed of at least three different signals. The signal with the g parameters of $g_1 = 2.035$, $g_2 = 2.009$ and $g_3 = 2.003$ was assigned to $HO_2^{\bullet}$ radicals on the basis of theoretical calculations. A signal with the g parameters of $g_1 = 2.028$, $g_2 = 2.016$ and $g_3 = 2.002$ was also present on the UV irradiated sample, but was quenched upon addition of molecular oxygen; this was therefore attributed to surface O^- species (i.e. a surface trapped hole). Finally, the third signal identified on this sample had the g values of $g_1 = 2.011$, $g_2 = 2.007$ and $g_3 = 2.002$ and this was assigned to O_3^- radicals. These results are described by the following reactions:

Charge carrier

production:	$TiO_2 + hv$	$\rightarrow$	$TiO_2 (h^+ + e^-)$	(1.13)
e^- trap:	$Ti^{4+} + e^-$	$\rightarrow$	Ti^{3+}	(1.14)
h^+ trap:	$Ti^{4+}\text{-}O^{2-}\text{-}Ti^{4+}\text{-}OH^- + h^+$	$\rightarrow$	$Ti^{4+}\text{-}O^- - Ti^{4+}\text{-}OH^-$	(1.15)
	$Ti^{4+}\text{-}OH^- + h^+$	$\rightarrow$	$Ti^{4+}\text{-}OH^{\bullet}$	(1.16)
	$Ti^{4+}\text{-}O^{2-} + h^+$	$\rightarrow$	$Ti^{4+}\text{-}O^-$	(1.17)

In the presence of oxygen:

Ozonide:	$Ti^{4+}\text{-}O^- + O_2$	$\rightarrow$	$Ti^{4+}\text{-}O_3^-$	(1.18)
Superoxide:	$Ti^{3+} + O_2$	$\rightarrow$	$Ti^{4+}\text{-}O_2^-$	(1.19)

The authors[22] were able to identify a dependence on signal shape with sample treatment conditions. For instance, in the amorphous samples tested, the signal arising from Ti^{3+} cations appeared in the spectrum with a very broad shape, which was suggestive of a highly heterogeneous environment. In contrast, the highly crystalline hydrothermal samples resulted in much sharper Ti^{3+} signals which indicates a much more regular environment of axially distorted octrahedra. The increment of the surface-bulk ratio favoured the stabilization of photogenerated radicals, whereas the low crystallinity of the TiO_2 samples with small particle size could increase the e^-/h^+ recombination. These two opposing tendencies therefore resulted in a critical particle size for maximum photocatalytic efficiency.[22]

1.4.2 UV irradiation under an organic atmosphere

The photocatalytic oxidation of organic compounds is of considerable environmental interest for the degradation of waste materials in both aqueous and gaseous mediums. Volatile organic compounds (VOCs) are produced as by-products in many industrial activities, as shown in Figure 1.4. The remediation of these VOCs is particularly important as many are known to be health hazards. Semiconductor photocatalysis has been utilised in the treatment of wastewaters, most efficiently through flat-bed reactors where the photocatalyst is used continuously and regeneratively.

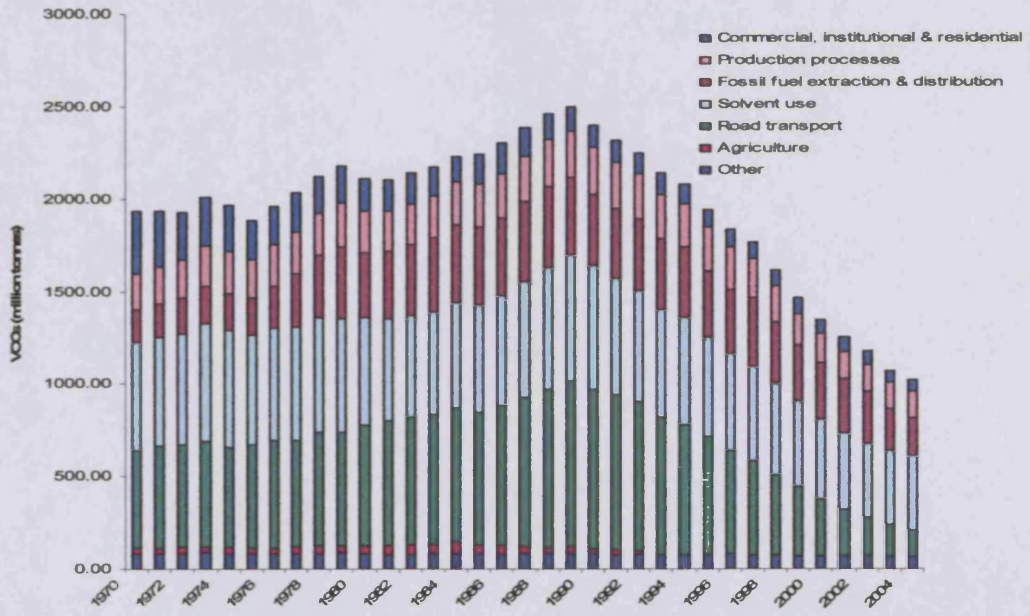

Figure 1.4 Aerial emissions of volatile organic compounds (VOCs) by sector in the UK, from 1970 to 2004.

As mentioned previously, the species formed as a result of UV irradiation of TiO_2 powders are significantly affected by the properties of the powders. Further evidence for this was provided by the studies performed by Nosaka *et al.*,[23,24] on the photocatalytic decomposition of acetic acid over platinized TiO_2 powder under deoxygenated conditions. A quartet with the hyperfine splitting of 0.349mT arising from the $^{\bullet}CH_3$ radical, and a triplet arising from $^{\bullet}CH_2COOH$ radicals were both observed when acetic acid solution underwent a photocatalytic reaction with Pt/TiO_2. This reaction is referred to as the photo-Kolbe reaction and the methyl radicals observed were formed *via*:

$$CH_3COOH + h^+ \rightarrow {}^{\bullet}CH_3 + CO_2 + H^+ \quad (1.20)$$

where the acetic acid traps a photogenerated hole from the valence band. Reaction of the acetic acid with surface OH groups leads to the formation of $^{\bullet}CH_3$ and $^{\bullet}CH_2COOH$ molecules competitively *via*:

$$^{\bullet}OH + CH_3COOH \rightarrow {}^{\bullet}CH_2COOH + H_2O \quad (1.21)$$

$$^{\bullet}OH + CH_3COOH \rightarrow {}^{\bullet}CH_3 + CO_2 + H_2O \quad (1.22)$$

The ratio of the two reaction products varied for the different forms of TiO_2 used throughout Nosaka's study.[23,24] Therefore it was concluded that the properties of TiO_2 must control the initial process in the photocatalytic oxidation. In this reaction, the authors[23,24] observed a decrease in the signal intensity of the above radicals in the presence of small amounts of oxygen, as the radicals underwent further oxidation. A previous study by Kaise *et al.*,[25] determined that the incorporation of a platinum group metal on the TiO_2 particles led to greater efficiency in the creation of radical intermediates, although there was an optimum loading amount of the metal [M/TiO_2 = $(0.5 - 1.5)\times10^{-3}$ in molar ratio].

Maira *et al.*,[26] made an attempt to link the surface properties of different TiO_2 catalysts with their relative activity towards photodegradation of toluene in the presence of oxygen. The EPR spectra of the TiO_2 catalysts (labelled P6, P11 and P16) after UV irradiation in the presence of oxygen only showed a progressive weakening of the signal due to subsurface O^- ions [Ti^{4+}-(O^-) -Ti^{4+}-OH^-] and a corresponding increase in the signal due to surface O^- ions [Ti^{4+}-(O^{2-})-Ti^{4+}-O^-] as the particle size increased. The P6 catalyst showed the best performance for the complete photooxidation of toluene to CO_2 and H_2O, whereas the remaining catalysts underwent partial oxidation to benzaldehyde. It was suggested that this was due to the increased separation of the photogenerated

electrons and holes that showed greater reaction at the surface of P6 compared to the charge carriers generated on the larger catalysts.[26] This increased separation was observed as an increase in the intensity of the superoxide radical at the surface, formed on capture of a photogenerated electron by an oxygen molecule. It was proposed that the different photoactivities of the different catalysts may result from the different structural sites (i.e. planar *vs* edge *vs* corner) present. For example, on the P6 catalyst there was a higher proportion of edge and corner sites that were able to trap the photogenerated charge carriers. This investigation proposed a correlation between the nature of surface sites and the relative photoactivity of the catalyst, but encouraged further work to be performed to investigate the role that the paramagnetic species discussed play in photocatalytic oxidation.[26]

Micic *et al.*,[27] performed an EPR investigation of the species formed on irradiation of aqueous TiO_2 colloids in the presence of methanol. A series of alkoxide TiO_2 colloids with chemisorbed methanol were prepared by hydrolyzing titanium isopropoxide in methanol in the presence of small amounts of OH^- ions. On irradiation of the alkoxide colloids with high intensity laser pulses, three EPR signals were recorded at 6K; a quartet (ratio 1:3:3:1) assigned to methyl radicals ($^{\bullet}CH_3$), a doublet assigned to formyl radicals ($^{\bullet}CHO$) and a weak signal due to methanol radicals [$^{\bullet}CH_2O(H)$].[27] The methyl radical was found to be unstable at temperatures above 60K, whereas the formyl and methanol radicals were stable at these temperatures. At lower intensity laser pulses (e.g. 2.5mJ/ pulse) only the methanol radical was observed. It was proposed that the observed radicals were possibly formed *via* the following reaction pathways:

$$Ti^{4+}\text{-}O\text{-}Ti^{4+}\text{-}OCH_3 + e^- \rightarrow Ti^{4+}\text{-}O\text{-}Ti^{4+}\text{-}O^- + {}^{\bullet}CH_3 \quad (1.23)$$

$$Ti^{4+}\text{-}O\text{-}Ti^{4+}\text{-}OCH_3 + h^+ \rightarrow Ti^{4+}\text{-}O\text{-}Ti^{4+}\text{-}O{}^{\bullet}CH_2 + H^+ \quad (1.24)$$

A second set of hydrous colloids, with surfaces completely saturated in bound hydroxide ions and water molecules, were also studied.[27] Hydroxide ions on the surface act as traps for photogenerated holes, resulting in an EPR signal with resonances at g = 2.014 and 2.007 assigned to the O^- radical. In the presence of methanol, UV irradiation of the aqueous colloids at low temperatures (2K) resulted in EPR signals due to the methanol radical and Ti^{3+} centres. Stepwise charge transfer was unlikely to occur at such low temperatures, therefore the charge transfer from the hole to methanol occurred *via*:

$$h^+ + CH_3OH \rightarrow {}^{\bullet}CH_2OH + TiO_2 + H^+ \quad (1.25)$$

Therefore, these results showed that the radical products formed on UV irradiation of aqueous TiO_2 colloids with methanol added to the solution ($^{\bullet}CH_2OH$) were different to those produced when methanol was chemisorbed on the TiO_2 particles ($^{\bullet}CH_3$, $^{\bullet}CH_2OH$ and $^{\bullet}CHO$). This suggests that only methanol molecules located within a few monolayers of the surface can accept photogenerated holes.[27]

Kim *et al.*,[28] used a batch photoreactor to elucidate the effect of water vapour and oxygen on the photodegradation of a series of organics including trichloroethylene (TCE), acetone and methanol over nanocrystalline TiO_2. The presence of hydroxyl groups or water molecules on the surface of the semiconductor act as a hole trap, and it was found that this enhanced the photodegradation rate of TCE and methanol up to concentrations of 1% volume.[28] However, the photodegradation of acetone was hindered by the presence of water vapour, as the water molecules competed with the acetone for adsorption sites on the surface. The presence of oxygen in the reactor led to an increase in the photodegradation rate of all the organics. The photogenerated electrons reacted with oxygen at the surface to form the superoxide radical (O_2^-) that subsequently reacted with adsorbed water to form hydroxyl radicals, which have previously been shown to increase photocatalytic degradation.[29]

Xu *et al.*,[30] performed an in-situ FTIR investigation of the photocatalytic oxidation of acetone over TiO_2 catalysts. They found that the adsorption of acetone onto TiO_2 powder was a relatively slow process and took a minimum of 30 minutes to reach equilibrium. The saturation coverage of acetone on the surface was determined to be 5 molecules/nm^2. On increasing the surface coverage of acetone, new peaks in the FTIR spectrum at 1666 cm^{-1} and 1595 cm^{-1} were resolved and assigned to mesityl oxide, the aldol condensation product of acetone. Some mesityl oxide degraded on the surface, forming a small amount of formate species which were weakly resolved in the FTIR spectra. At low O_2 pressures, the photocatalytic oxidation of acetone was shown to procede *via* mesityl oxide thermal fragmentation to formic acid, forming titanium formate and a surface OH group and then the final product CO_2.[31] The progress of acetone photooxidation was followed by integrating the areas of the FTIR peaks of the different species. The formation rate of CO_2 was almost constant until the acetone had been completely oxidized, as seen in Figure 1.5. Further, the authors[30] showed that the rate of photocatalytic oxidation of acetone increased as the partial pressure of oxygen present increased.

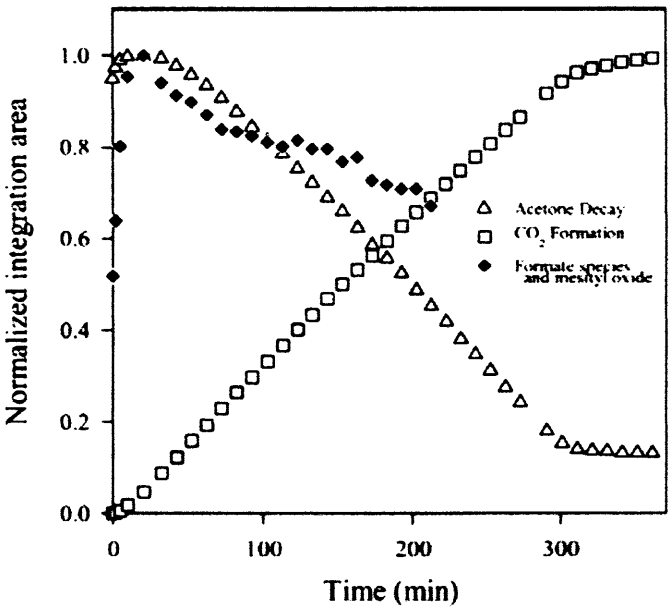

Figure 1.5 Kinetic curve for the photocatalytic oxidation of acetone over TiO_2 under continuous irradiation conditions.[31]

Gonzalez-Elipe and Che performed an EPR investigation of the photooxidation of ethylene over TiO_2 and identified a peroxy radical as an intermediate during photo-oxidation.[32] A small quantity of ethylene (5 – 10 Torr) was frozen over the surface of the TiO_2 before admitting oxygen (10^{-1} Torr) to the EPR cell at 77K. UV irradiation of this sample at 77K led to a paramagnetic species with the g values of g_1= 2.035, g_2 = 2.008 and g_3 = 2.001. From the observed hyperfine lines, using ethylene isotopically enriched in C_2D_4 or $^{13}C_2H_4$, it was found that the radical responsible for the above EPR signal contained both hydrogen and carbon. The radical was found to be unstable at temperatures above 260K. The identity of the radical was confirmed by the results obtained when the photooxidation was carried out in the presence of ^{17}O-enriched oxygen. Two sets of six hyperfine lines were resolved, centered on g_3, with splittings of $A_3(I)$ = 9.5mT and $A_3(II)$ = 3.5mT; no splittings could be resolved in either of the other two directions. Gonzalez-Elipe and Che attributed this signal to a peroxy radical, $ROO^{\bullet}$, with the largest hyperfine interaction corresponding to the terminal oxygen.[32]

It was proposed[32] that the mechanism did not involve O^-, O_2^-, O_3^- or O_3^{3-} radicals, but instead depended on the formation of $^{\bullet}OH$ surface groups by the capture of photogenerated holes, according to:

$$^{\bullet}OH + C_2H_4 \rightarrow HO\text{-}CH_2\text{-}CH_2^{\bullet} \quad (1.26)$$

$$HO\text{-}CH_2\text{-}CH_2^{\bullet} + O_2 \rightarrow HO\text{-}CH_2\text{-}CH_2\text{-}OO^{\bullet} \quad (1.27)$$

as analogous to equation (1.21) discussed earlier.

1.5 Structure of Single Crystalline TiO_2

Titanium dioxide is the most-investigated single crystalline system in the study of the surface science of metal oxides. As discussed, TiO_2 has a great many applications and the volume of research carried out on the single crystals is performed with the desire that a deeper understanding of processes on the fundamental level will aid in the improvement of device performance. In particular, on metal oxide surfaces geometric defects or non-stoichiometries directly affect the electronic structure and therefore there is a close relationship between structure and reactivity. Single crystal samples of TiO_2 are readily available from several suppliers and are well suited for study by conventional surface sensitive techniques including STM, XPS and UPS.

The rutile (110) face has received most of the attention, in conjunction with studies on the other stable faces of this polymorph (100) and (001). Single crystal studies on the anatase polymorph are lagging behind those of rutile, partly due to the thermodynamic instability of this phase, and its tendency to transform into rutile at high temperatures. However, studies on the anatase surface are particularly relevant as it is often considered to be the most photocatalytically active phase.

1.5.1 Surface Structure of Rutile (110)

Work by Ramamoorthy *et al.*,[33] on surface energy measurements concluded that the (110) surface has the lowest surface energy of rutile TiO_2. The results of their study can be seen in the Wulff construction in Figure 1.6. It is as a result of this that most work on TiO_2 has been performed on this surface. Because the concepts considered for this surface can also be applied to the other surfaces of a TiO_2 crystal, in addition to other metal oxides, it is useful to consider this surface in detail.

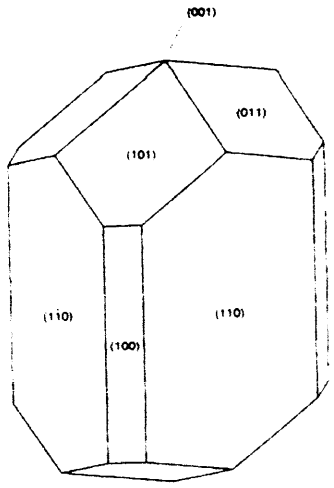

Figure 1.6 The equilibrium shape of a TiO_2 crystal using the Wulff construction based on the surface energies calculated in [33].

The rutile (110) surface has been studied extensively by several surface science techniques such as STM,[34 - 36] AFM[37] and XPS.[38] The (110) surface is quite flat, and has the lowest density of dangling bonds of all the surfaces of rutile TiO_2. The surface contains two types of Ti (5- and 6- fold) and O (2- and 3-fold) ions. The two-fold coordinated O atoms are in chains along the [001] direction ~2.36a.u above the plane of surface Ti atoms, and are referred to as bridging oxygens (position 5 in Figure 1.7). The distance between the chains of bridging oxygens in a (110)-(1×1) surface is about 12.21a.u. Each of the bridging oxygens is coordinated to a 6-fold Ti atom (position 1), which has the same coordination as Ti atoms in the bulk. Rows of 3-fold coordinated oxygen atoms (position 6) lie in the same plane as the Ti atoms, connecting the chains of 6- and 5-fold (position 2) coordinated Ti atoms.

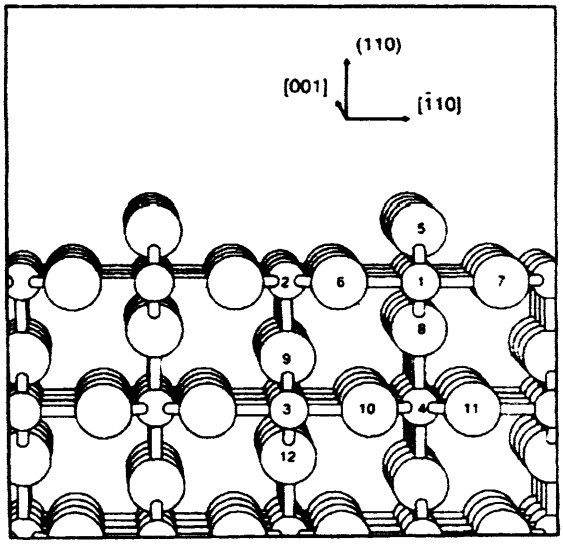

Figure 1.7 The structure of the unrelaxed stoichiometric TiO_2 (110) surface.[33]

In order to conserve energy, the surface must relax and as expected most of the relaxations occur perpendicular to the surface (i.e. in the (110) direction). The theoretical and experimental results for the displacements of the atoms as determined by several groups are summarised in [2]. Using the experimental results of Charlton *et al.*,[39] the displacements are shown in Figure 1.8, and were measured as follows: the bridging oxygen atoms relax downwards by 0.27Å, the 6-fold Ti atoms move upwards by 0.12Å, the 3-fold coordinated oxygen atoms move in the [110] direction by 0.05Å and towards the neighbouring 5-fold coordinated Ti atom by 0.16Å, and the 5-fold coordinated Ti atom itself relaxes downwards by 0.16Å.

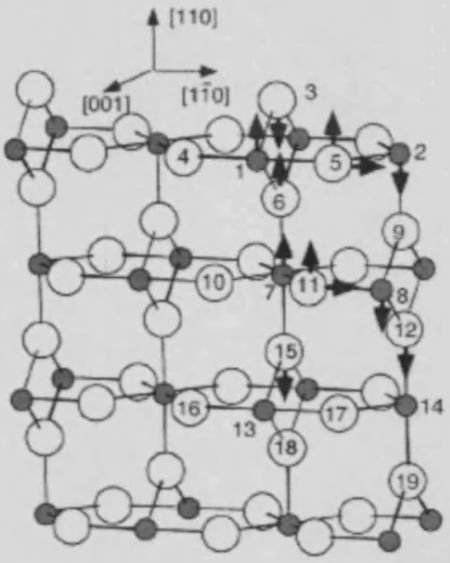

Figure 1.8 Model of the $TiO_2(1\times1)$ surface showing relaxations of the surface and sub-surface ions.[39]

The surface structure of TiO_2 can easily be resolved by studying with scanning tunneling microscopy (STM), although there has been much debate in the past as to whether the images are governed by geometric or electronic effects. Diebold *et al.*,[2] provided the first evidence to confirm that it is in fact electronic effects that dictate the image resolution. By observing the positions of single oxygen defects in bridging oxygen rows as bright features in dark rows it is concluded that bridging oxygen rows are imaged as dark rows and the in-plane Ti atoms are responsible for the bright rows. This conclusion has been confirmed by later adsorption studies carried out by several groups.

1.5.2 Surface Defects on Rutile

The nature of the surface and any defects on the surface strongly affect the reactions of TiO_2 powders and single crystal samples. The volume of studies performed on the $TiO_2(110)$ surface has led to a detailed understanding of the nature of these defects, and what surface preparations lead to their creation.

The oxygen vacancies created on the surface as a result of thermal annealing are of particular interest on both the powdered and single crystal samples. In STM images, defects on the $TiO_2(110)$ surface appear as bright spots on the dark rows often with a density of ~ 7% per surface unit cell. Defects induce changes in the electronic structure of the crystal and can therefore be studied by spectroscopic techniques such as X-Ray Photoelectron Spectroscopy and Ultraviolet Photoemission Spectroscopy. For example,

after TiO_2(110) surfaces have been annealed to high temperatures, UPS studies evidenced the growth of a surface state at 0.8eV below the Fermi level, which is removed on adsorption of oxygen.[40-42] This result suggests that there are oxygen vacancies on the vacuum annealed surface. The reaction of these surface defects with adsorbates provides chemical evidence for the nature of the defects. The chemisorption study of Lu *et al.*,[43] demonstrated the preferential extraction of O atoms from the adsorbate molecules (such as D_2O, $^{13}CH_2O$ and ^{15}NO) only on the vacuum annealed surface and not on the fully oxidized surface, confirming that the annealed surface is oxygen deficient.

Two types of surface oxygen defects can be created on the TiO_2(110) surface; removal of a bridging oxygen atom or removal of an in-plane oxygen atom. As the bridging oxygen atoms are coordinated to only two sublayer Ti cations whereas the in-plane oxygens are 3-fold coordinated, it is energetically more favourable to remove a bridging oxygen atom. The low on-set temperature (~500K) for the creation of the point defects on the surface also points to bridging oxygen vacancies as the more probable defect.

Vacancies can also be created by sputtering the surface with high energy rare gas ions, such as Ar^+. During the sputtering process, oxygen atoms are removed from the surface and subsurface regions leading to a change in symmetry from two-fold to four-fold.[44,45] Ar^+ sputtering is the technique used to induce reduction of the TiO_2(110) crystals studied in our EPR investigations, described in Chapter 7. One final method of creating defects on the surface is *via* UV irradiation. According to Shultz *et al.*,[46] there is no information available about the structure of the defects created during UV irradiation, but evidence regarding the reactivity of these sites will be provided in Chapters 5 and 6.

1.5.3 Bulk Defects

The Magneli phase diagram of TiO_2 is very rich, with many stable phases predicted, meaning that TiO_2 can be reduced easily. The bulk defects created during reduction of the crystal directly affect the surface properties and so the study of bulk defects is important to the understanding of the many surface reactions of TiO_2. The surface chemistry of metal oxides in relation to bulk defects can be understood by considering the nature of the bonding; many transition metal oxides have covalent

bonding with a high degree of ionic character, hence defects have a large effect on the local surface electronic structure which has a direct result on surface reactions.

There are several methods which can be used to reduce TiO_2 such as Ar^+ sputtering,[40,41] annealing to high temperatures in vacuum[40] and reduction with dry hydrogen at temperatures above 200°C.[47] The extent of the bulk reduction of single crystals of TiO_2 can to some extent be measured by the visible colour change of the crystal. An extensive study by Diebold[48] details the colour changes from a yellow transparent stoichiometric crystal to a dark blue/black heavily reduced crystal; the colour change is a result of the removal of oxygen atoms from the surface of the crystal, producing so-called colour centres. The reduction is a reversible process, so that the crystal can be re-oxidized back to its original stoichiometry by thermal annealing in air. These colour changes are shown in Figure 1.9.

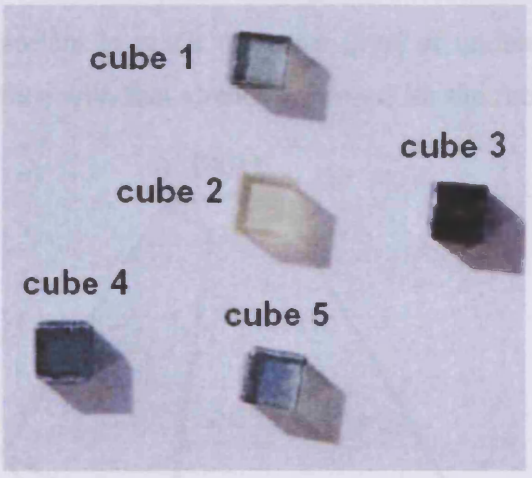

Figure 1.9 Colour changes in TiO_2(110) crystals after annealing as a result of bulk reduction.[48]

The nature of the defects in TiO_2 crystals vary depending on the extent of the oxygen deficiency, which is itself related to temperature, gas pressure and presence of impurities. At the present moment, the relationship between the type of defect and extent of oxygen deficiency is still not clearly established, although it has been shown that in the region from $TiO_{1.9996}$ to $TiO_{1.9999}$ the dominant defect is Ti interstitials.[49]

The creation of oxygen vacancies leads to reconstructions, which will be discussed in detail below. In order for reconstruction to take place, there must be a diffusion of atoms through the crystal and it is of interest to note that the diffusion mechanisms vary for the different defects. It is readily accepted that interstitial Ti atoms diffuse through the open channels in the <001> direction, i.e., the crystallographic c-

axis,[50] (see Figure 1.1). The case for oxygen diffusion however has still not been resolved. The simplest mechanism to be assumed for the diffusion of oxygen vacancies would be the movement of the neighbouring oxygen atom in the bridging row into the vacancy, which would lead to an oxygen vacancy one atom displaced from the original site; overall leading to diffusion along the [001] direction. However, STM work by Schaub *et al.*,[51] suggests that after exposure of the crystal to O_2, the vacancies diffuse perpendicular to the bridging oxygen rows in the $[1\bar{1}0]$ direction.

1.5.4 Surface Structure of Anatase

The behaviour of the two polymorphs of TiO_2, anatase and rutile, are very different for different applications. For example, anatase is more active for O_2 photo-oxidation than rutile, but its behaviour in gas-sensing devices is very different from that of rutile. As many powdered samples of TiO_2 are a mixture of anatase and rutile in varying ratios, it is important to reach the same level of understanding on the atomic scale on the anatase surface with that already achieved for the rutile polymorph.

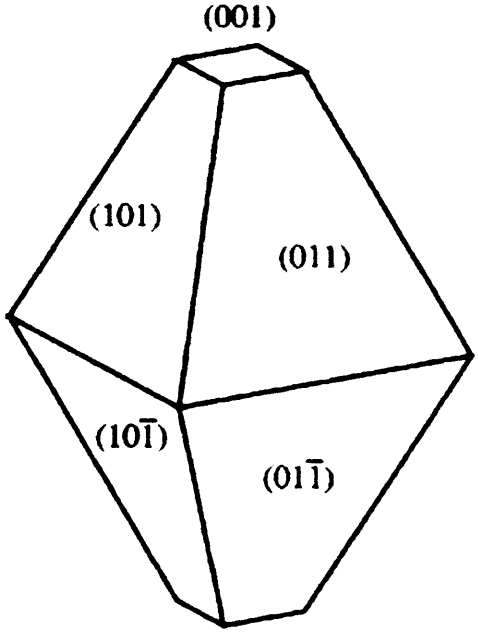

Figure 1.10 The equilibrium shape of the TiO_2 anatase crystal according to surface energy calculations.[52]

Several theoretical calculations have been performed in order to identify the relative stability of the different faces of the anatase crystal, resulting in the formation of the Wulff construction shown in Figure 1.10 of the equilibrium shape of the anatase crystal.

One of the main problems surrounding the study of anatase single crystal surfaces is that they are not readily available from commercial suppliers. Therefore, researchers are required to synthesize the anatase samples themselves. Ruzycki *et al.*,[53] used a naturally occurring mineral sample to study the (100) face of anatase. The clean anatase (100) surface initially exhibited a sharp (1×1) LEED pattern which was replaced by (1×n) periodicity as the surface became more ordered. The reconstruction of the surface is consistent with a (101) micro-faceted surface as observed by STM studies. The STM studies of Ruzycki[53] showed no evidence for the presence of surface oxygen vacancies on the (100) anatase surface, and they suggested that the absence of these highly reactive sites may be responsible for the different chemistry observed for their sample compared to the rutile polymorph.

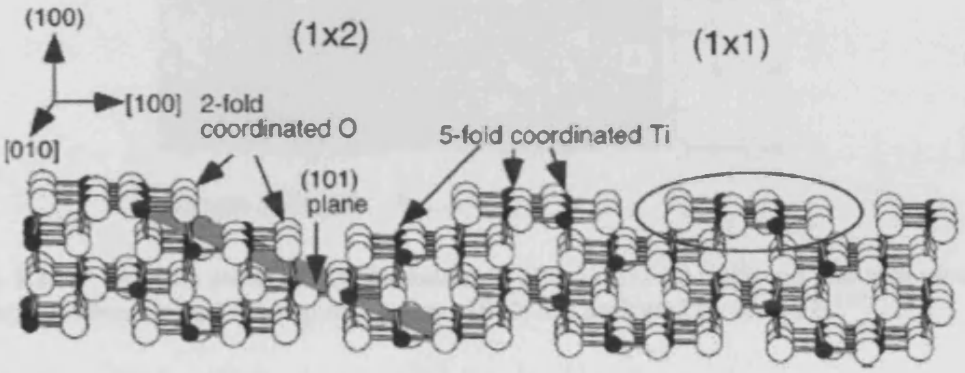

Figure 1.11 Model of the (1×2) reconstruction of the (100) anatase surface. The (1×1) termination on the right side can be transformed into a (1×2) reconstruction by removing the top unit indicated by the circle.[53]

A complementary STM study by Hebenstreit *et al.*,[54] investigated the nature of the (101) surface of anatase. The surface is seen to be autocompensated which exhibits a saw-tooth structure with two-fold coordinated oxygen ions at [010]-oriented ridges. The remaining oxygen ions are 3-fold coordinated as in the bulk. There are two types of surface Ti cations, that are 5-fold and 6-fold coordinated. In their study, Hebenstreit *et al.*,[54] used a natural anatase single crystal to act as a substrate for a 700Å thick epitaxial TiO_2 film grown *via* oxygen plasma assisted molecular-beam epitaxy. Reflection high-energy electron diffraction resolved a bulk-like (1×1) termination, with only Ti^{4+} cations present, as shown by XPS. A clear triangular terrace/step structure was observed with steps running in the [010], $[1\bar{1}1]$ and $[\bar{1}\bar{1}1]$ directions. Again, there was little evidence in the STM images for surface oxygen vacancies, which may be an indication that the (101) surface is stable against the loss of 2-fold coordinated oxygen

atoms. The 4-fold coordinated Ti cation sites on the saw-tooth edge were observed to be active centres for adsorption.

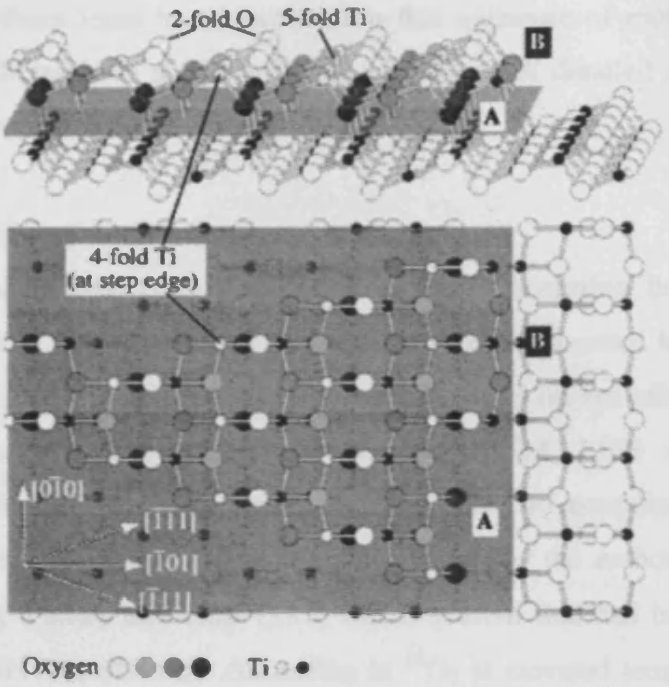

Figure 1.12 Atomic model of the anatase (101) (1×1) surface, with top and side view. The two possible terminations for step edges along [010] are indicated by A and B.[54]

Single crystal samples of anatase have also been synthesized by Sekiya *et al.*,[55] by a chemical vapour transport reaction method using NH_4Cl as a transport agent. Dehydrated TiO_2 powder was mixed in a 10:1 ratio with NH_4Cl and placed in a sealed, evacuated ampoule and subjected to thermal treatment at 750-800°C (source zone) and 650 – 700°C (growing zone) for a period of 2-3 weeks. Single crystals with a distorted octahedral shape, blue in colour and with optically flat surfaces were grown on the walls of the ampoule. One drawback of this synthesis is the inability to grow crystals with a preferred orientation, unlike the single crystals that can be grown as thin films on well-ordered substrates.

1.6 Activation of Adsorbates on Single Crystal TiO_2

A detailed knowledge of the different single crystal surfaces of TiO_2 is needed in order to understand the many reactions that occur on adsorption of molecules at the surface. The adsorption of atoms and molecules at the surface of TiO_2 and the subsequent reactions that occur (for example dissociation or further reaction to other products) forms the basis of most of the research performed on this metal-oxide

substrate. As discussed above, oxygen centred radicals have been widely studied on the polycrystalline forms of TiO_2 and the interaction of adsorbed oxygen with single crystal samples is also an important area of research. The presence of oxygen vacancies on reduced TiO_2 surfaces leads to an expectation that exposure of molecular oxygen to these surfaces will result in a filling of the vacancies. A detailed discussion of this phenomenon is given in 5.4.3.

1.6.1 Oxygen induced reconstructions

Many studies have been performed on the restructuring that occurs on the TiO_2(110) surface in the presence of molecular oxygen at elevated temperatures. For example, Li *et al.*,[56,57] performed a comprehensive study on the effect of oxidizing a TiO_2(110) surface at moderate temperatures using STM, LEIS and XPS. They investigated the dependence of the restructuring process on annealing time, annealing temperature and sample history. As the control surface, the authors[56] used a TiO_2 surface exhibiting a sharp and clear (1×1) LEED pattern that had been sputtered and annealed under UHV conditions. Annealing in $^{18}O_2$ at elevated temperatures led to a dramatic surface morphology change. After exposing the flat surface to $^{18}O_2$ at 520K, the morphology of the surface was dominated by rosette-like networks (~30Å wide). In between the rosette structures were small (1×1) islands (60×40Å). The LEED pattern was still (1×1) but the spots were now more diffuse and the background was enhanced compared to the UHV annealed surface.[56]

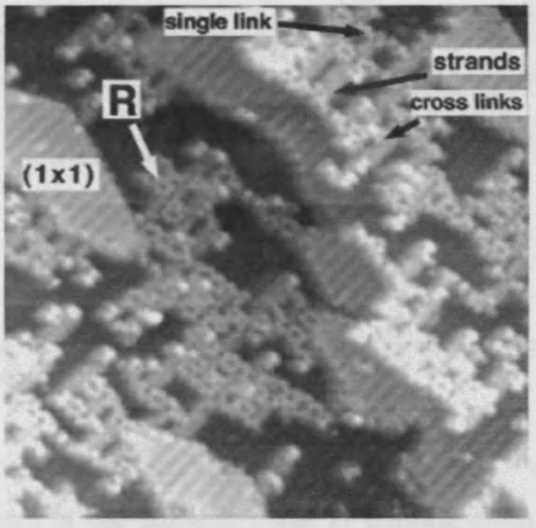

Figure 1.13 STM image (300×300Å) of a TiO_2(110) surface annealed in O_2 at 550K. Reoxidation of the reduced bulk causes formation of irregular networks of rosettes (R), (1×1) islands and strands.[56]

On increasing the annealing temperature to 550K, the surface was covered by larger (1×1) islands (80×60Å) with some rosette networks situated on top of these islands. The original (1×1) substrate was not detected by LEED at these annealing temperatures. The surface was much smoother after annealing at 660K due to the (1×1) islands connecting to each other to form (1×1) terraces. On increasing the annealing temperature further to 710K, the rosette networks were no longer visible, and [001]-oriented strands (~70Å long) were distributed uniformly on top of the (1×1) terraces.[56] Images of these different surface structures can be seen in Figure 1.13.

The authors[56] also determined that the rate of ^{18}O from the gas phase was also dependent on the history of the sample. For example, the surface structure seen on a sample that had undergone several sputter and anneal cycles before annealing in oxygen at 660K was more complicated than an as-received sample annealed under the same conditions. From SSIMS data it was reported that more heavily reduced samples incorporated ^{18}O at a much faster rate than more stoichiometric samples.

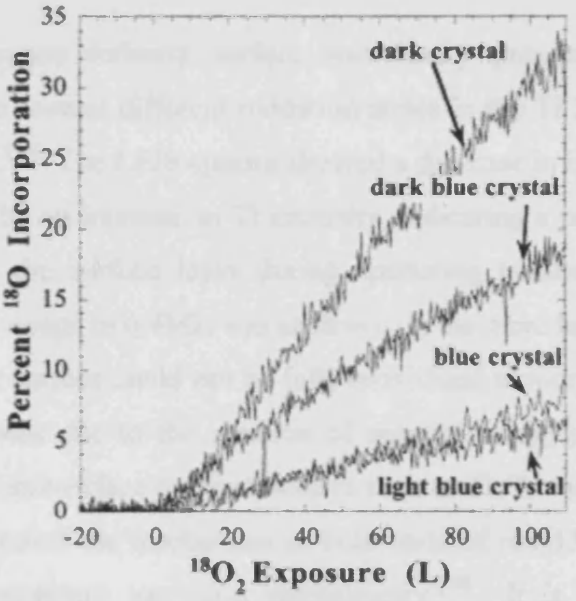

Figure 1.14 SSIMS of ^{18}O surface concentration during annealing at 830K for rutile crystals with different levels of bulk and surface reduction.[56]

The restructuring process determined by Li *et al.*,[56,57] was regarded as growth of additional TiO_2 layers at the surface, with Ti coming from the reduced bulk and oxygen from the gas phase. The Ti interstitials were driven out from the bulk in the vertical direction towards the surface. The lability of the subsurface interstitial Ti has

implications for reactions performed on the polycrystalline samples. The bulk of small rutile particles could act as sinks for excess Ti under reductive conditions, with the excess Ti returning to the surface under oxidizing conditions. The cycling of Ti between the bulk and the surface may affect the bulk electrical and photoabsorptive properties.

Pan *et al.*,[41] performed a LEIS study on adsorption of oxygen, water and hydrogen over TiO_2(110) surfaces with varying levels of surface defects. On the fully stoichiometric surface no ^{18}O was taken up from the gas phase, indicating that the surface was almost free of oxygen vacancies. A surface previously annealed to 1000K under UHV conditions was slightly oxygen deficient, as evidenced by the shoulder in the 2p photoemission line in the XPS spectrum. The surface oxygen vacancies were concentrated in the top surface layer and could be reoxidized by adsorption of oxygen from the gas phase at room temperature, as indicated by the return of the Ti 2p XPS photoemission spectrum to the original condition before UHV annealing. The adsorbate oxygen coverage on the UHV annealed surface was estimated to be saturated at 0.08ML.[41]

A highly oxygen deficient surface was finally prepared using 500eV Ar^+ sputtering, leading to several different oxidation states in the Ti 2p photoemission line in the XPS spectrum.[41] The LEIS spectra showed a decrease in intensity of the oxygen signal accompanied by an increase in Ti intensity, indicating a preferential removal of oxygen atoms from the surface layer during sputtering treatment. An increase in oxygen saturation coverage to 0.4ML was achieved on the more highly oxygen deficient surface, although the surface could not be fully reoxidized at room temperature. It was suggested that this was due to the creation of subsurface oxygen vacancies and the formation of reduced subsurface oxide structures such as Ti_2O_3 and TiO.[41]

Henderson studied the mechanism of bulk-assisted reoxidation of ion sputtered TiO_2 using static secondary ion mass spectrometry.[58] It is well known that ion sputtering the surface of the metal oxide leads to a preferential depletion of the surface oxygen until a steady state level of reduction has been established. The stoichiometry of the surface can be restored by the bulk through diffusion of either oxygen vacancies or Ti^{3+} interstitials on the surface into the bulk, as shown in Figure 1.15. It is generally accepted in most of the literature available that the diffusing species are oxygen atoms/ vacancies. Many of these studies use surface monitoring techniques such as XPS and AES to determine the surface ratio of O:Ti, and from this draw conclusions on the

mechanism involved in reoxidation. However, as pointed out by Henderson,[58] changes in the surface concentration ratios alone are not sufficient to infer diffusion mechanisms, as both possible mechanisms (diffusion of oxygen or diffusion of Ti) result in the same overall change in surface concentration ratio. The author[58] therefore performed a study utilising labelled $^{16}O/^{18}O$ and ^{46}Ti to monitor surface concentrations in order to differentiate between the oxygen and titanium diffusion processes.

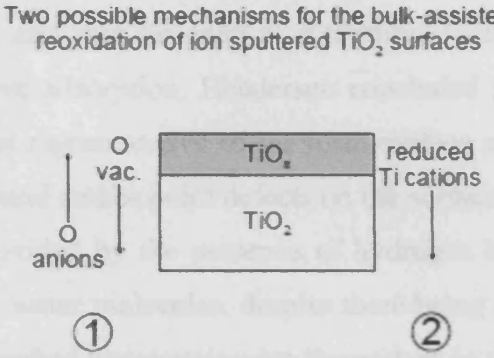

Figure 1.15 Schematic model showing two possible mechanisms for charge diffusion between the ion sputtered surface (TiO_x) and the bulk (TiO_2) during vacuum annealing.[59]

Henderson's results showed that the stoichiometry of the sputtered TiO_2 surface changed in two thermal regimes.[58] At temperatures <700K the surface remained reduced with only slight changes in the O:Ti ratio. From the labelling studies it was seen that both the ^{18}O and ^{46}Ti were mobile on the surface as the concentration of the labelled isotopes decreased on the surface. This change in concentration was attributed to a mixing of the O and Ti within the surface layer. At temperatures >700K the sputtered surface was rapidly reoxidized. There was no change in the ^{18}O:^{16}O ratio on the surface indicating that surface ^{18}O was not further diluted by diffusion of bulk ^{16}O to the surface. At the same time, the ^{46}Ti:^{48}Ti ratio changed indicating that the surface ^{46}Ti dissolved into the bulk of the oxide. From this data, it was concluded that the mechanism of bulk-assisted reoxidation of sputtered TiO_2 surfaces involves the subsurface diffusion of reduced Ti cations, and that both Ti and O mixing within the sputtered surface film proceeds the bulk-assisted surface reoxidation process.[58]

1.6.2 Water

The chemistry of water adsorption on TiO_2 surfaces is of fundamental importance due to the number of catalytic and photochemical applications involving aqueous-solid interactions over TiO_2 and since the discovery of the role of TiO_2 in the photodecomposition of water. Water can adsorb on the surface of TiO_2 *via* molecular or

dissociative pathways and the extent of each mode of adsorption was investigated by Henderson using HREELS and TPD on a TiO_2(110) surface.[60] The HREELS data collected by Henderson indicated that water adsorbs on the TiO_2(110) surface in a predominantly molecular state. However, in addition to this a weak loss feature resolved at 3690cm^{-1} implied that a small amount of dissociation (2×10^{13} molecules/cm^2) occurs on the surface at adsorption temperatures of 135K. The 3690cm^{-1} feature was assigned to the OH fragment of dissociated water residing at a five-coordinate Ti^{4+}site, and was assigned as a terminal hydroxyl. Due to the small percentage of dissociative adsorption, Henderson concluded that the sites responsible for dissociation were not representative of the ideal surface and proposed instead that these sites may be structural and/or point defects on the surface.[60] Further evidence for this assignment was provided by the presence of hydrogen bonding between the OH fragments and adsorbed water molecules, despite there being no evidence of hydrogen bonding between the adsorbed water molecules themselves in the monolayer.

Further investigation of the effect of the presence of defect sites on the TiO_2(110) surface on the adsorption of water was performed by Wang *et al.*[44] In their study it was observed that exposure of low vapour pressure water (<10^{-5}Torr, ~10^4L) had little effect on the intensity of Ti 3d defect sites in the XPS spectrum, which agreed with previous studies of Henrich[61] and Pan.[41] On increasing the pressure of the water vapour to 0.6 Torr (~10^8L coverage), the defect density was greatly reduced. In comparison to these figures, on the nearly defect-free surface the water coverage was ~0.02ML at 10^4L exposure at low vapour pressures, and ~0.07ML at 10^8L high vapour pressure exposure.[44]

Li *et al.*,[56] investigated the effects of water adsorption on the same reduced TiO_2(110) surfaces discussed above during oxygen adsorption. On the stoichiometric surface, LEIS measurements of the ^{18}O uptake (which is used to indicate the level of $H_2{}^{18}O$ adsorbed) saturated at a coverage of ~0.07ML. This coverage remained the same on the slightly oxygen deficient surface. However, on the highly oxygen deficient surface the ^{18}O uptake indicated an increase of surface coverage to 0.15ML. A small amount of reoxidation of the crystal was seen in the XPS spectra, but not to the same extent as the reoxidation following oxygen exposure.[56] The lower degree of surface coverage of oxygen following water exposure compared to oxygen exposure was attributed to a dissociation of the $H_2{}^{18}O$ into OH and H; some of the H radicals bond to

surface Ti sites forming Ti-H bonds and therefore reduce the number of sites available for further adsorption.

The debate concerning the dissociation of adsorbed water on TiO_2(110) surfaces still continues, with most experimental data suggesting that dissociation does not occur whereas theoretical calculations indicate that dissociation is energetically favoured on the perfect (110) surface. The DFT calculations performed by Norskov *et al.*,[62] support many of the experimental studies reported; water dissociation on the perfect surface is calculated to be an endothermic process, whereas it is an exothermic process on point defect sites.

1.7 Structure and Reactivity of Mixed Phase TiO_2

There is clear evidence showing that the photoactivity of mixed phase catalysts, such as Degussa P25, is higher than that of the pure polymorphs anatase and rutile. Of the two phases, despite its larger bandgap anatase is regarded as the more active phase as a result of lower rates of recombination of charge carriers and a greater adsorptive capacity at the surface. The original hypothesis proposed to explain the enhanced photoactivity of the mixed phase catalysts, shown diagrammatically in Figure 1.19(a), suggested that there is transfer of electrons from the anatase phase into lower energy trapping sites in the rutile phase, thus improving the efficiency of electron-hole separation and thereby yielding greater catalytic activity.[63]

Hurum *et al.*,[5,6] performed an EPR investigation of Degussa P25 in order to gain a deeper understanding of this phenomenon. They argued that the data supporting the hypothesis described above did not take into consideration the energy levels of the lattice or surface trapping sites of the two phases. As an example, it was stated that the anatase trapping site is 0.8eV below the anatase conduction band which places it below the energy of the rutile conduction band, therefore preventing the transfer of electrons from anatase to rutile.

In their investigation, Hurum *et al.*,[5,6] studied a series of colloidal suspensions of P25 prepared by a modified sonication/centrifugation method. The EPR results showed that as the size of the aggregates increased so too did the proportion of rutile within the aggregate and thus there was a corresponding increase in the population of the rutile lattice trapping sites. This suggested that there was less transfer of electrons from the rutile to the anatase phase. The transfer of electrons from rutile to anatase was confirmed by the EPR spectra recorded after UV irradiation of P25 in the presence of

methanol. The methanol acts as a hole scavenger, therefore the electron transfer processes could be studied in isolation from recombination processes. On cessation of the UV irradiation of the sample, the intensity of the anatase trapping sites was seen to increase at the same time as the rutile trapping site intensity decreased; therefore providing direct evidence of the transfer of rutile electrons to anatase. This process of electron transfer depends critically on the interface between the two phases in the TiO_2 sample and also on the size of the particles within each phase. In photoactive P25 the rutile particles are atypically small allowing intimate contact with the anatase phase, creating catalytic hot-spots at the phase interface.

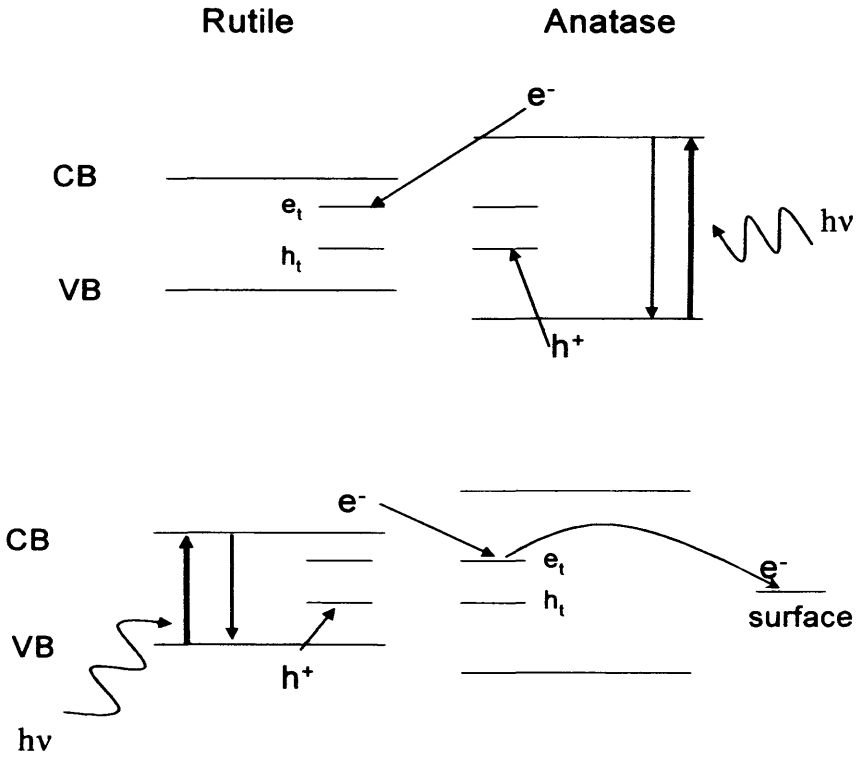

Figure 1.16 (a) Previously speculated model of P25 activity where charge separation occurs on the anatase polymorph and rutile acts as an electron sink. (b) Model proposed of a rutile antenna and subsequent charge separation.[5,6]

1.8 Conclusion

In this chapter, the crystal structure and properties of TiO_2 has been discussed and many important applications of the material have been described. Perhaps of greatest importance, and as will be discussed in greater detail throughout the rest of this thesis, is the photocatalytic properties of TiO_2 which depends critically on the type of TiO_2 used. Photoirradiation of the metal oxide with photons of energy greater than the

bandgap leads to the creation of electrons and holes that can participate in reactions with surface adsorbates. Furthermore, a major area of research focuses on the reaction of the photogenerated charge carriers with surface adsorbed oxygen, leading to several types of surface oxygen radicals. Oxygen is the most commonly used oxidising agent in photocatalytic reactions, which makes the study of the different oxygen radicals formed during photoirradiation particularly pertinent. As previously mentioned, TiO_2 is used extensively as a photocatalyst in the remediation of atmospheric pollution, therefore much emphasis is now placed on understanding the mechanisms involved in the photodegradation of organics in the presence of TiO_2.

In order to successfully design photocatalysts with high quantum yields, it is necessary to have a detailed understanding of the electron transfer processes that occur over the TiO_2 surface. Many of the results obtained on the polycrystalline samples suggest that there are sites on the surface which are more favourable towards adsorption and electron transfer. However, the specific location of these sites cannot be determined from studies of polycrystalline samples alone and instead it is necessary to focus attention on reactions over well-defined single crystal samples. It is the aim of this investigation to gain a deeper understanding of the nature of the oxygen radicals adsorbed over the different polymorphs of TiO_2 in powdered form, and then to supplement this with studies on the single crystal samples performed under Ultra-High Vacuum conditions (Chapter 7).

The spectroscopic method used throughout this investigation (Chapter 5 and 6) is Electron Paramagnetic Resonance (EPR) spectroscopy. This technique has the advantage that it can characterise many of the different oxygen radicals stabilised on the TiO_2 surface, which will be discussed in greater detail in later chapters. Further, the sensitivity and resolution of EPR spectroscopy permits the identification of different stabilisation sites on the surface. Additionally, through low temperature measurements, many intermediates in the photocatalytic reactions can be identified that may not readily be detected by other spectroscopic techniques at room temperature.

1.9 References

[1] V.E. Henrich, P.A. Cox, *The Surface Science of Metal Oxides*, **1996**, CUP, Cambridge.

[2] U. Diebold, *Surf. Sci. Rep.*, **2003,** *48*, 53.

[3] J.M.G Amores, V.S. Escribano, G. Busca, *J. Mater. Chem.*, **1995**, *5*, 1245.

[4] B. O'Regan, M. Grätzel, *Nature*, **1991**, *353*, 737.

[5] D.C. Hurum, A.G. Agrios, K.A. Gray, T. Rajh, M.C. Thurnauer, *J. Phys. Chem. B*, **2003**, *107*, 4545.

[6] D.C. Hurum, A.G. Agrios, S.E. Crist, K.A. Gray, T. Rajh, M.C. Thurnauer, *J. Elect. Spec. and Rel. Phen.*, **2006**, *150*, 155.

[7] A. Fujishima, K. Honda, *Nature*, **1972**, *238*, 37.

[8] G. Scott, *Pure & Appl. Chem.*, **1980**, *52*, 365.

[9] Y. Nosaka, M.A. Fox, *J. Phys. Chem.*, **1988**, *92*, 1893.

[10] A.L. Linsebigler, G. Lu, J. T. Yates, *Chem. Rev.*, **1995**, *95*, 735.

[11] M.A. Fox, M.T. Dulay, *Chem. Rev.*, **1993**, *93*, 341.

[12] E. Borgarello, J. Kiwi, M. Grätzel, E. Pelizzetti, M. Visca, *J. Am. Chem. Soc.*, **1982,** *104*, 2996.

[13] A.E. Taverner, C. Rayden, S. Warren, A. Gulino, P.A. Cox, R.G. Egdell, *Phys. Rev. B*, **1995**, *51*, 6833.

[14] D.M. Murphy, R. D. Farley, J. Marshall, D. J. Willock, *Chem. Phys. Lett.*, **2004**, *391*, 1.

[15] N. Serpone, D. Lawless, R. Khairutdinov, E. Pelizzetti, *J. Phys. Chem.*, **1995**, *99*, 16655.

[16] D.P. Colombo, R.M. Bowman, *J. Phys. Chem.*, **1995**, *99*, 11752.

[17] D.P. Colombo, R.M. Bowman, *J. Phys. Chem.*, **1996**, *100*, 18445.

[18] S.H. Szczepankiewicz, J.A. Moss, M.R. Hoffmann, *J. Phys. Chem. B*, **2002**, *106*, 2922.

[19] T. Berger, M. Sterrer, O. Diwald, E. Knözinger, D. Panayotov, T.L. Thompson, J.T. Yates Jr. *J. Phys. Chem. B*, **2005**, *109*, 6061.

[20] M. Anpo, M. Che, B. Fubini, E. Garrone, E. Giamello, M.C Paganini, *Top. Catal.*, **1999**, *8*, 189.

[21] K. Ishibashi, A. Fujishima, T. Watanabe, K. Hashimoto, *J. Phys. Chem. B*, **2000**, *104*, 4934.

[22] J.M. Coronado, A. J. Maira, J. C. Conesa, K. L.Yeung, V. Augugliaro, J. Soria, *Langmuir*, **2001**, *17*, 5368.

[23] Y. Nosaka, M. Kishimoto, J. Nishino, *J. Phys. Chem. B*, **1998**, *102*, 10279.

[24] Y. Nosaka, K. Koenuma, K. Ushida, A. Kira, *Langmuir*,**1996**, *12*, 736.

[25] M. Kaise, H. Nagai, K. Tokuhashi, S. Kondo, *Langmuir*, **1994**, *10*, 1345.

[26] A.J. Maira, K.L. Yeung, J. Soria, J.M. Coronado, C. Belver, C.Y. Lee, V. Augugliaro, *App. Catal B*, **2001**, *29*, 327.

[27] O.I. Micic, Y. Zhang, K.R. Cromack, A.D. Trifunac, M.C. Thurnauer, *J. Phys Chem*, **1993**, *97*, 13284.

[28] S.B. Kim, H.T. Hwang, S.C. Hong, *Chemosphere*, **2002**, *48*, 437.

[29] M. A. Fox, A. A. Abdel-Wahab, *J. Catal.*, **1990**, *126*, 693.

[30] W. Xu, D. Raftery, J.S. Francisco, *J. Phys. Chem. B*, **2003**, *107*, 4537.

[31] W. Xu, D. Raftery, *J. Catal.*, **2001**, *204*, 110.

[32] A.R. Gonzalez-Elipe, M. Che, *J. Chim. Phys*, **1982**, *79*, 355.

[33] M. Ramamoorthy, D. Vanderbilt, R.D. King-Smith, *Phys. Rev. B*, **1994**, *49*, 16721.

[34] A. Berko, F. Solymosi, *Langmuir*, **1996**, *12*, 1257.

[35] R.E. Tanner, M.R. Castell, G.A.D. Briggs, *Surf. Sci.*, **1998**, *412/413*, 672.

[36] R.A. Bennett, P. Stone, M. Bowker, *Faraday Disc.*, **1999**, *114*, 267.

[37] M. Ashino, T. Uchihashi, K. Yokoyama, Y. Sugawara, S. Morita, M. Ishikawa, *Phys. Rev. B*, **2000**, *61*,13955.

[38] D.R. Baer, P. Xiong-Skiba, A.N. Shultz, L.Q Wang, M.H. Englehard, *Surf. Sci. Spect.*, **1998**, *5*, 193.

[39] G. Charlton, P.B. Hoowes, C.L. Nicklin, P. Steadman, J.S.G. Taylor, C.A. Muryn, S.P. Harte, J. Mercer, R. McGrath, D. Norman, T.S. Turner, G. Thornton, *Phys. Rev. Lett.*, **1997**, *78*, 495.

[40] W. Göpel, G. Rocker, R. Feierabend, *Phys. Rev. B*, **1983**, *28*, 3427.

[41] J.M. Pan, B.L. Maschhoff, U. Diebold, T.E. Madey, *J. Vac. Sci and Tech.*, **1992**, *10*, 2470.

[42] R.L. Kurtz, R. Stockbauer, T.E Madey, E. Roman, J.L. de Segovia, *Surf. Sci.*, **1989**, *218*, 178.

[43] G. Lu, A. Linsebigler, J.T. Yates Jr., *J. Phys. Chem.*, **1994**, *98*, 11733.

[44] L.Q Wang, D.R. Baer, M.H. Englehard, A.N. Shultz, *Surf. Sci.*, **1995**, *344*, 237.

[45] H. Norenber, J.H. Harding, *Surf. Sci.*, **2001**, *473*, 151.

[46] A.N. Shultz, W. Jang, W.M.J Hetherington, D.R. Baer, L.Q Wang, M.H. Englehard, *Surf. Sci.*, **1995**, *339*, 114.

[47] H. Haerudin, S. Bertel, R. Kramer, *J. Chem. Soc. Faraday Trans.*, **1998**, *94,* 1481.

[48] U. Diebold, *Mat. Res. Soc. Symp. Proc.*, **2001**, *654*, AA5.1.1.

[49] E. Yagi, R.R. Hasiguti, M. Aono, *Phys. Rev. B*, **1996**, *54*, 7945.

[50] H.B. Huntington, G.A. Sullivan, *Phys. Rev. Lett.*, **1965**, *14*, 177.

[51] R. Schaub, E. Wahlström, A. Rønnau, E. Lægsgaard, I. Stensgaard, F. Besenbacher, *Science*, **2003**, *299*, 377.

[52] M. Lazzeri, A. Vittadini, A. Selloni, *Phys. Rev. B*, **2001**, *63*, 1554091.

[53] N. Ruzycki, G.S. Herman, L.A. Boatner, U. Diebold, *Surf. Sci.*, **2003**, *529*, L239.

[54] W. Hebenstreit, N. Ruzycki, G.S. Herman, Y. Gao, U. Diebold, *Phys. Rev. B*, **2000**, *62*, 16334.

[55] T. Sekiya, T. Yahisawa, N. Kamiya, D. DasMulmi, S. Kurita, Y. Murakami, T. Kodaira, *J. Phys. Soc. Jap.*, **2004**, *73*, 703.

[56] M. Li, W. Hebenstreit, L. Gross, U. Diebold, M. A. Henderson, D. R. Jennison, P. A. Schultz, M. P. Sears, *Surf. Sci.*, **1999**, *437*, 173.

[57] M. Li, W. Hebenstreit, U. Diebold, *Phys. Rev. B,* **2000**, *61*, 4926.

[58] M. A. Henderson, *Surf. Sci.*, **1995**, *343*, L1156.

[59] M. A. Henderson, *Surf. Sci.*, **1999**, *419*, 174.

[60] M. A. Henderson, *Surf. Sci.*, **1996**, *355*, 151.

[61] V.E. Henrich, G. Dresselhaus, H.J. Zieger, *Solid State. Comm.*, **1977**, *24*, 623.

[62] R. Schaub, P. Thostrup, N. Lopez. E. Lægsgaard, I. Stensgaard, J.K. Nørskov, F. Besenbacher, *Phys. Rev. Lett.*, **2001**, *87*, 2661041.

[63] R.I. Bickley, T. Gonzalez-Carreno, J.S. Lees, L. Palmisano, R.J.D. Tilley, *J. Solid State Chem.*, **1991**, *92*, 178.

Chapter 2

Introduction to Solid State Chemistry

2.1 Introduction

Many of the physical properties of solids can be attributed to the nature of the bonding found within them. In particular, the electronic conductivity, magnetic and optical properties of solids are determined by the behaviour of the electrons situated in the solid. A detailed understanding of the nature of the bonding between atoms in solids and of the interaction of electrons within a solid is therefore important. The electronic theory of valency provides the basis for the modern understanding of chemistry and hence motivates the further study of the electronic structure of solids. There are several theoretical approaches used to describe the bonding in solids, including the free electron theory and the molecular orbital theory. Although there are many advantages to the free electron theory in the discussion of metals, it does not adequately describe the situation for non-metals and semiconductors, both of which are important classes of compounds. Therefore, a detailed description of the molecular orbital approach will be given in this chapter with no further reference to the free electron theory.

Solid state chemistry is an important branch of chemistry that forms the background of understanding for many important devices. Semiconductor devices in particular are prevalent, being found in computers, medical diagnostic equipment and solar cells. The performance of the device is clearly dependent on the electronic properties. As TiO_2 is a component in many of these devices it is important to understand the electronic properties of this material further, and they will be discussed in the current chapter.

2.2 Band Theory

The band theory of solids is well supported by X-ray spectroscopic data. Band theory can itself be described using two different theoretical approaches, namely the chemical and physical approach. In the chemical approach, the concepts used in molecular orbital theory are applied to infinite three-dimensional structures. In the physical approach, the concepts first described in the free electron theory are extended to include quantum mechanics and Fermi-Dirac statistics. Both approaches will be discussed here.

2.2.1 The Chemical Approach

The chemical approach to band theory extends the concepts of molecular orbital theory to infinitely sized molecules. The orbitals in molecules are approximated by the linear combinations of atomic orbitals (LCAO) approach.[1] The H_2 molecule is the simplest one to consider, containing only two electrons with a linear combination of the 1s orbitals. The two possible combinations of the atomic orbitals, χ_A and χ_B, are given by:

$$\Phi_1 = \chi_A + \chi_B \tag{2.1a}$$

$$\Phi_2 = \chi_A - \chi_B \tag{2.1b}$$

and the orbitals are delocalised over both of the H atoms. The electron density for these orbitals is shown in Figure 2.1. It can be seen that the electron density is enhanced in the region between the nuclei for Φ_1, which leads to a favourable attractive potential. Therefore Φ_1 is a bonding molecular orbital with energy lower than either of the original atomic orbitals. The electron density is however decreased in the region between the nuclei for Φ_2, therefore this is an antibonding orbital with energy higher than the original atomic orbitals.

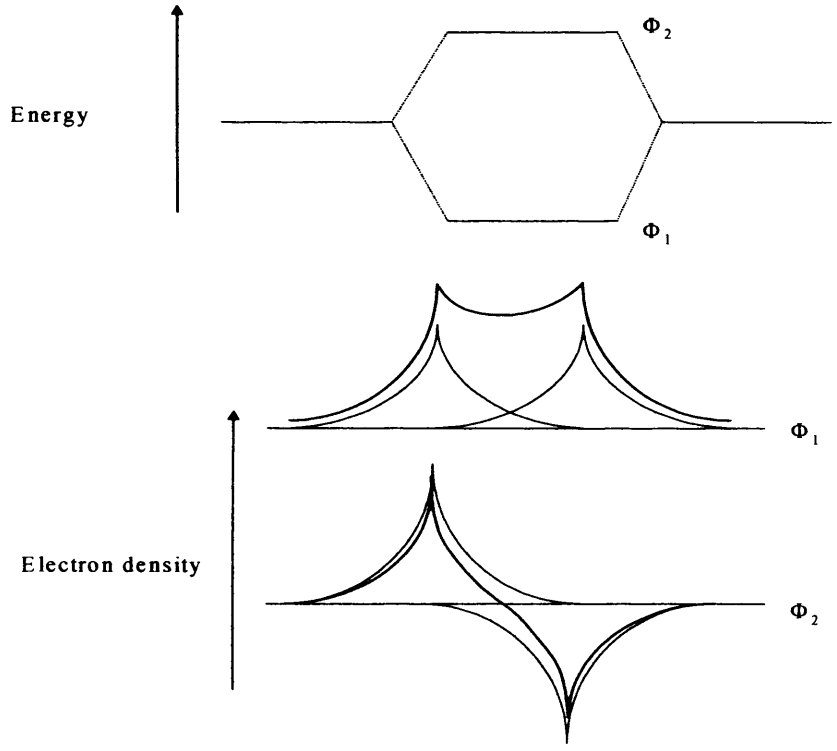

Figure 2.1 Bonding and antibonding molecular orbitals as described by the LCAO approach and their associated electron density distributions.

The bonding interaction between the two orbitals depends on the degree of overlap of the atomic orbitals. Effective combinations of atomic orbitals to give molecular orbitals requires that the atomic orbitals are similar in energy and are of the correct relative symmetry, i.e., σ type orbitals will not overlap with π type orbitals.

Molecular orbitals are extended over all constituent atoms in the molecule. The number of molecular orbitals is equal to the number of valence atomic orbitals on the atoms concerned. Hence, as the molecule becomes larger and more valence atomic orbitals are involved, the number of molecular orbitals increases and the energy between the levels decreases. In solids, the energy spacing between the molecular orbitals is so small that it is convenient to neglect it and to assume that the molecular orbitals form continuous bands of energy levels. The molecular orbitals are not distributed evenly over all energy levels which is a concept described by the density of states, N(E).[1] This can be defined as N(E)dE which is the number of allowed energy levels per unit volume of solid in the energy range E to (E+dE). As seen from Figure 2.2 there are regions of energies which are void of molecular orbitals termed the bandgap; the density of states within the bandgap of the solid is zero.

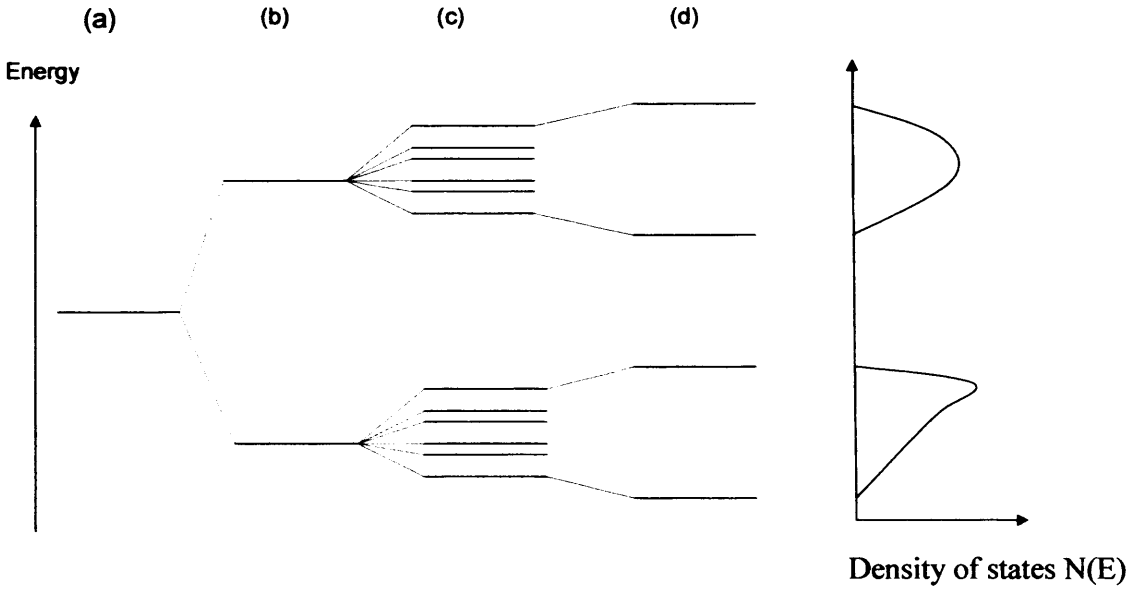

Figure 2.2 Orbital energies of (a) atom (b) small molecule (c) large molecule and (d) solid. The density of states [N(E)] corresponds to (d).

2.2.2 The Physical Approach

In the alternative physical approach of band theory the energy and wavelengths of the electrons are considered and extend upon the ideas first suggested in the free electron theory. In the free electron theory, the electrons are situated in quantized

energy levels that are filled from the lowest energy upwards with two electrons per level. A physical factor which is often referred to in the study of solids is the Fermi level, E_F, which represents the boundary between filled and empty levels and is a direct consequence of the Fermi-Dirac distribution. At absolute zero the Fermi level is the sharp cut off between occupied orbitals below the energy E_F and unoccupied orbitals above. In a metal the Fermi level corresponds to the energy of the upper-most filled orbital in the partly filled valence band.

2.2.2a Work Function

The work function, Φ, is defined as the energy necessary to remove an electron from the Fermi level in a material and place it in a vacuum an infinite distance away. The work function is important when considering thermionic emission, Schottky barrier formation and photoelectric emission. There are several techniques used to measure the value of the work function, but a note of caution must be added here. The different methods used to measure work functions often yield different answers, even when two techniques are used to study the same sample. For example, the Kelvin probe measurements give an average value of Φ of the whole surface, whereas the low energy cut-off in UPS measurements gives the minimum value for the surface.

Added to this, the work function is an extremely sensitive measurement of the state of a surface, with grain boundaries, defects and adsorbates all causing large changes in Φ. For these reasons, the absolute values are often not quoted in the research literature, focussing instead on the relative values and any changes to the value of Φ as a result of surface manipulation. An example of such variations in values is given in [2].

The free electron theory regards electrons as being situated in a well of constant potential, which can be analogous to the concept of a particle in a box used in quantum mechanics. However, this is an over-simplification and more refined theories consider the potential within a molecule to be periodic. The potential energy of the electrons is at a minimum in regions of positive charge exerted by cations within the molecule, and is at a maximum midway between adjacent nuclei. A consequence of this periodic potential is that an uninterrupted continuum of energy levels, as described by the density of states diagram in Figure 2.2, is not entirely accurate and instead only certain bands of energies are permitted.

The band lowest in energy and fully occupied by the valence electrons is termed the valence band. The next band is termed the conduction band which is empty or partially full of electrons. The upper and lower energy limits of these bands are denoted

E_V and E_C respectively, as indicated in Figure 2.3. The spacing between the valence and conduction bands, where there are no allowed energy levels, is termed the bandgap, and the value of this has a large effect on the chemistry of the semiconductor.

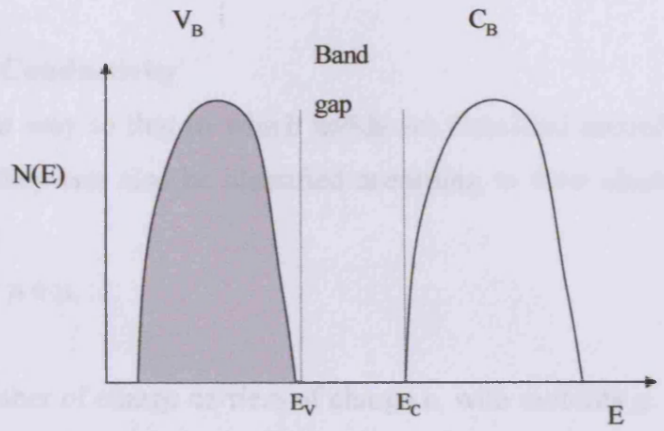

Figure 2.3 Band structure as described by the physical approach.

2.2.2b Fermi-Dirac Distribution Function

The population of an energy level at a given temperature can be calculated using the Fermi-Dirac[3] distribution function according to:

$$f(E) = \frac{1}{1+\exp[(E-E_F)/k_BT]} \qquad (2.2)$$

where E_F is the Fermi level, E is the energy of the level under consideration, k_B is the Boltzmann constant and T is the temperature. The distribution has the profile shown in Figure 2.4 for three different temperatures.

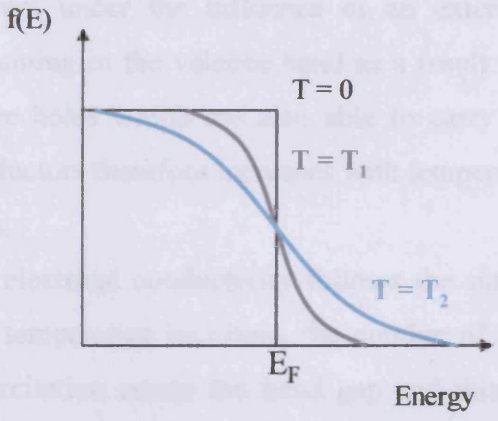

Figure 2.4 The Fermi-Dirac distribution function shown for three temperatures, T = 0 (absolute zero) and two higher temperatures where $T_2 > T_1 > T = 0$ K.

The number of electrons per energy level can be calculated by multiplying the density of states for the energy level by the probability of its occupation, described by the Fermi-Dirac distribution. This results in the equation:

$$n(E, T) = n(E)\, f(E, T) \tag{2.3}$$

2.3 Electrical Conductivity

In a similar way to that in which solids are classified according to the type of bonding present, they can also be classified according to their electrical conductivity, which is given by:

$$\sigma = n\, e\, \mu \tag{2.4}$$

where n is the number of charge carriers of charge e, with mobility μ. In metallic solids electrical conductivity is possible even at low temperatures. The valence band in a metal is only partially filled and there is no energy gap between the top filled orbital and the lowest energy unoccupied orbital. Therefore, electrons are easily promoted into the unoccupied level to result in an electric current due to the motion of the charged particles. The number of charge carriers in metals is large and it is therefore changes in the mobility of these charge carriers which results in variations in conductivity. At high temperatures the mobility of the charge carriers decreases slightly as a result of thermal vibrations, which leads to an overall decrease in the electrical conductivity of the metal.

Semiconductors are best described as non-metals that have electrical conductivity arising from thermal excitation of electrons across the bandgap. Electrons in the full valence band may gain enough thermal energy to be excited from the full valence band to the otherwise empty conduction band. The electrons themselves are then able to carry current under the influence of an external electric field. The unoccupied orbitals remaining in the valence band as a result of this excitation can be considered to be positive holes which are also able to carry current. The electrical conductivity of semiconductors therefore increases with temperature as n, the number of charge carriers, increases.

In insulators the electrical conductivity follows the same trend as that seen in semiconductors. As the temperature increases, the number of charge carriers increases as a result of thermal excitation across the band gap and this leads to an increase in electrical conductivity. Insulators and semiconductors are therefore differentiated from one another by the magnitude of the bandgap and resulting electrical conductivity. A typical semiconductor such as GaAs has a bandgap of 1.43eV[4] whereas an insulator

such as MgO has a bandgap of 7.8eV.[5] These trends of electrical conductivity with temperature are shown in Figure 2.5 and some typical values of bandgap with solid classifications are given in Figure 2.6.

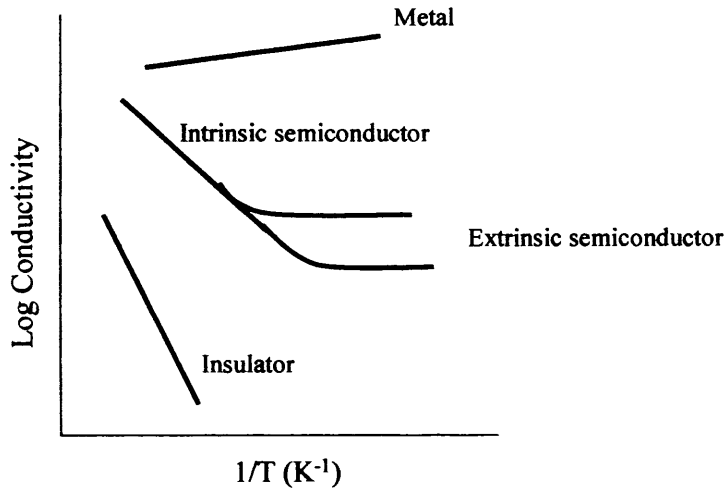

Figure 2.5 Conductivity of metals, semiconductors and insulators.[6]

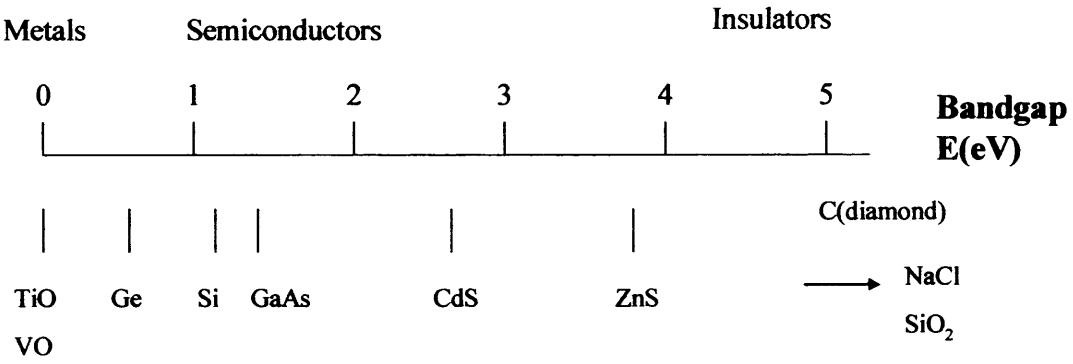

Figure 2.6 Relationship between the electronic properties and the magnitude of the bandgap, with typical examples.[6]

2.4 Semiconductors

In semiconductors E_F will be situated in the energy gap between the valence and conduction bands, although the exact location must be accurately derived. If a photon of energy greater than that of the bandgap is incident on the semiconductor, an electron is promoted from the valence band to the conduction band, leaving behind a positive "hole". The number of charge carriers in a semiconductor can be controlled by doping the semiconductor with charged impurities. The resulting semiconductor is therefore referred to as extrinsic. Semiconductors that have not been doped are referred to as intrinsic.

2.4.1 Intrinsic Semiconductors

At 0K in an intrinsic semiconductor the valence band is full of electrons and the conduction band is empty. Therefore, the Fermi level is mid-way between the two bands. At this temperature the semiconductor is non-conducting. At increased temperatures thermal energy can excite electrons across the bandgap into the conduction band giving rise to electrical conduction. The number of electrons in the conduction band will equal the number of holes in the valence band. The number of charge carriers in an intrinsic semiconductor can therefore be controlled by the temperature or the magnitude of the bandgap. For a given temperature, more electrons will be promoted into the conduction band for a solid with a smaller bandgap and so the solid with the smaller bandgap is the better conductor. The population of the conduction band is given by:

$$P \approx e^{-(E-E_F)/k_BT} \tag{2.5}$$

The exponential dependence of the number of electrons in the conduction band on the size of the bandgap means that small changes in the bandgap can result in large differences in the number of charge carriers.

2.4.2 Extrinsic Semiconductors

Extrinsic semiconductors are semiconductors that have been doped with impurities to control the number of charge carriers. The process of doping involves removing a known quantity of the original lattice element and replacing them with another element with more or less electrons than the original. The electronic conductivity of a semiconductor increases as a result of the presence of dopant atoms. The conductivity can be described by:

$$\sigma = n\,\mu_e\,e + p\,\mu_h\,e \tag{2.6}$$

where n and p are the concentrations of charge carriers, and μ_e and μ_h are their mobilities. The conductivity of a doped semiconductor increases with temperature as the number of electrons (holes) promoted into the conduction (valence) band increases, until a certain temperature is reached where all charge carriers have been promoted into their associated bands and there is no further increase in conductivity with temperature. This is referred to as the saturation region. As the temperature is increased above the saturation point there is an actual decrease in the conductivity of the semiconductor as

the relative mobilities of the charge carriers decrease as a result of thermal vibrations.

2.4.2a p-type semiconductors

In a p-type semiconductor, original lattice elements are removed and replaced with an element that has one fewer valence electron. One common example of a p-type semiconductor is silicon doped with gallium. Silicon is a group IV element and gallium is a group III element. Therefore, for every silicon atom that is replaced by a gallium atom the number of valence electrons in the valence band is reduced by one. The energy level associated with the Ga-Si bond does not form part of the valence band but instead forms a discrete 'acceptor' energy level just above the top of the valence band as illustrated in Figure 2.7. Thermal promotion of electrons from the valence band into the acceptor level is possible, resulting in mobile positive holes in the valence band and therefore electrical conductivity in the semiconductor. Materials such as this are referred to as p-type because the electrical conduction results from ***positive*** holes.

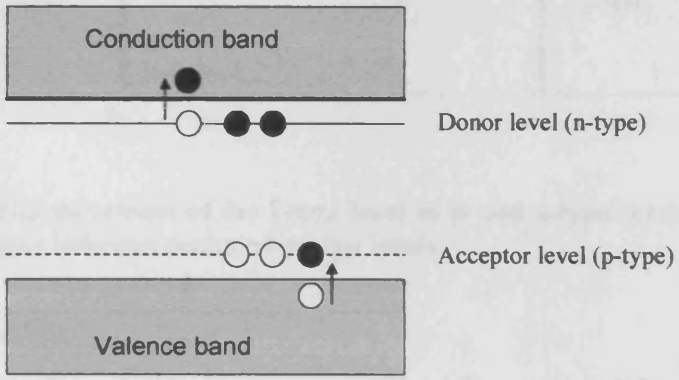

Figure 2.7 Schematic illustration of the donor and acceptor levels in extrinsic semiconductors.

2.4.2b n-type semiconductors

In n-type semiconductors, original lattice elements are removed and replaced with an element that has one extra valence electron. One common example of an n-type semiconductor is silicon doped with arsenic, which is a group V element. The additional electrons provided by the arsenic atoms lie in energy levels, referred to as donor levels, situated ~0.1eV from the bottom of the conduction band, as shown in Figure 2.7. Therefore the electrons are easily promoted into the conduction band and this promotion leads to an increase in charge carriers and thus electrical conductivity. Materials such as this are referred to as n-type because the electrical conductivity arises from ***negatively*** charged electrons.

Figure 2.8 illustrates the effect on the Fermi level of both n- and p-type semiconductors. As seen in the figure, E_F moves close to the conduction band in the former but moves towards the valence band in the latter.

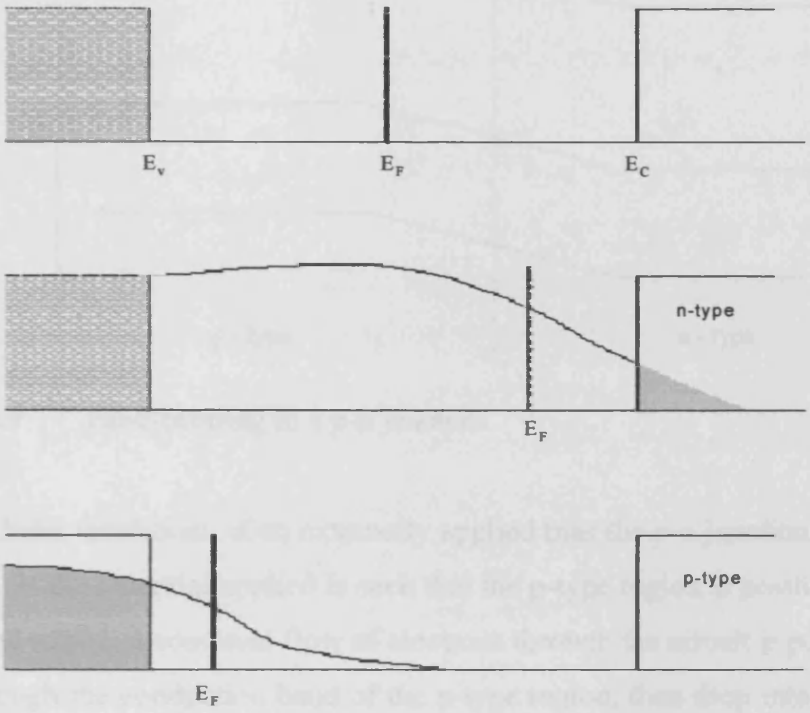

Figure 2.8 The movement of the Fermi level in p- and n-type semiconductors. The grey shading in the figure indicates occupied energy levels.

2.5 p-n junction

A p-n junction is the component utilised in many solid-state devices such as light emitting diodes (LEDs) and transistors.[7,8] The junction can be formed by depositing an n-type region onto a p-type region by methods such as chemical vapour deposition, or in the case of single crystals by simply doping different regions of the crystal with different types of dopant atoms. For a junction to be in equilibrium, the Fermi level must be at the same energy across the junction. In n-type materials, E_F lies approximately at the donor level and in p-type materials it lies at the acceptor level. Therefore, if the valence and conduction bands of the two regions are level the Fermi level will be at a different energy on each side. The attraction between the extra holes in the p-type region induces the flow of electrons from the n-type material into the p-type, forming a space-charge region where there are no carriers. The imbalance in concentration of the carriers on each side of the junction causes the bands to bend until the Fermi level is at a constant energy throughout the material.

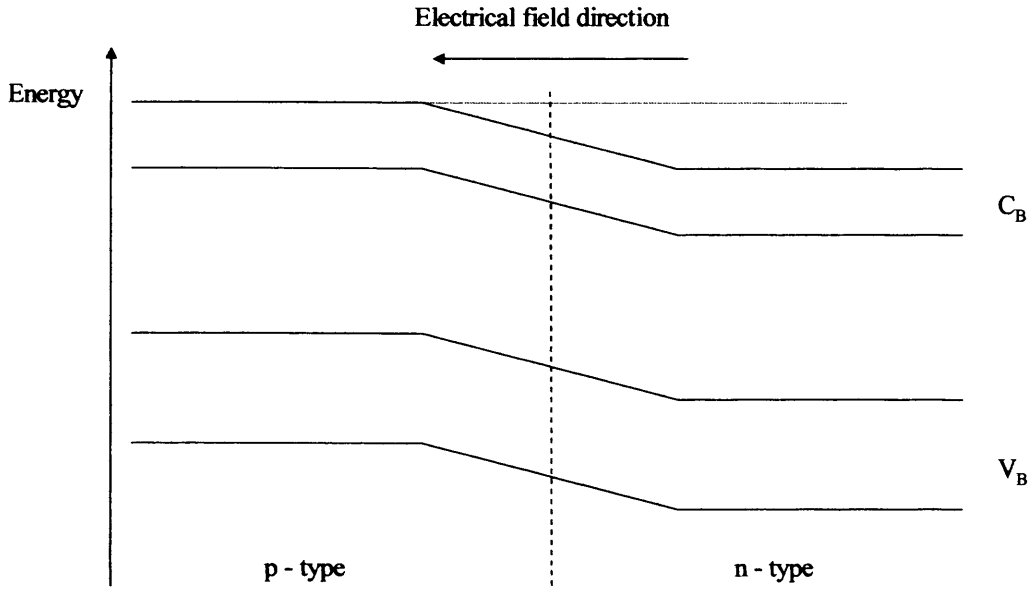

Figure 2.9 Band-bending in a p-n junction.

Under conditions of an externally applied bias the p-n junction is able to act as a rectifier. If the potential applied is such that the p-type region is positive with respect to the n-type region, a continual flow of electrons through the circuit is possible. Electrons flow through the conduction band of the n-type region, then drop into the valence band of the p-type region as they cross the p-n junction. Flow is continued through the p-type valence band by the motion of the positive holes and the electrons then leave the junction at the left-hand electrode. Flow is not possible in the reverse direction as the electrons do not have enough energy to surmount the barrier from left to right.

2.5.1 Band Bending

As explained before, the electronic structure of defects on surfaces is very different to perfect terraces. The different types of defects, such as point vacancies, adatoms and edges all differ from each other as seen by a difference in the Madelung potential experienced by each ion. In particular, the Madelung potential decreases rapidly with the ligand coordination of the surface site; for example a 5 coordinate site on MgO has a potential of 1.68155, a 4 coordinate site 1.56693 and a 3 coordinate site 0.87378.[9] These values are for an unrelaxed surface but, as mentioned above, the relaxation of the lattice accompanying defect formation greatly influences the electronic structure. In this case the relaxation leads to a further decrease in the potential of each defect to bring the Madelung constant closer to that of the bulk value.

The extent to which surface defects influence the overall electronic properties of

the lattice is dependent on the energies of the defect levels with respect to the band edges. The presence of defects at the surface in semiconductors leads to surface band bending, which is associated with differences in concentration of charge carriers at the surface. In an n-type semiconductor, such as TiO_2, a high concentration of surface O vacancies leads to an excess of electrons at the surface with respect to the bulk, termed an accumulation layer. Associated with this accumulation layer is a downward bending of the bands, as illustrated in Figure 2.9.

Alternatively, a depletion layer can form, possibly as a result of adsorbed oxygen species, e.g., O_2^- or O^-, which results in an upward bending of the bands, as shown in Figure 2.9. The band bending is caused in both cases by an unequal concentration of positive ionized impurity centres and negative electrons in the space-charge region. The concentration of charge carriers at the surfaces of metal oxides has an impact on the conductivity of the surface. This explains the use of TiO_2 as a gas sensor, as adsorption of gases influences surface conductivity.

2.6 Bonding in Transition Metal Compounds: TiO_2

The bonding in transition metal compounds is not accurately described by the ionic or covalent bonding present in other simpler compounds, but is best considered as a mixture between the two. The partially filled d bands of transition metals gives rise to an interesting and varied range of electronic behaviour, which can be understood by developing the ideas discussed in the previous sections.

The basic energy level diagram for a transition metal oxide has a valence band of O 2p character and a conduction band of metal character. The orbitals comprising the conduction band are d orbitals in contrast to the case of pre-transition elements where the conduction band is usually constructed from s or p orbitals. With reference to the molecular orbital approach, the valence band could be referred to as the bonding combination of oxygen and metal orbitals, and the conduction band as the antibonding combination. However, the use of "oxygen 2p" valence band and "metal d" is more useful as it gives a clearer indication of the atomic orbital constituents. In insulators the conduction band is empty, whereas for the early transition metals with a d^n configuration above d^0 the conduction band will be occupied. In TiO_2 for example, the Ti^{4+} cations have a d^0 configuration and this results in no electrical conduction. If the compound is reduced to form Ti^{3+} cations which have a d^1 configuration there is a partial occupancy of the conduction band and the compound exhibits electrical conduction. The two situations are illustrated in Figure 2.10 where the gap between the

occupied valence band and the unoccupied conduction band is termed the bandgap, and in the case of TiO_2 this gap is ~3eV.[10] This is a small bandgap, and is indicative of an appreciable covalent mixing between the oxygen and titanium atomic orbitals.

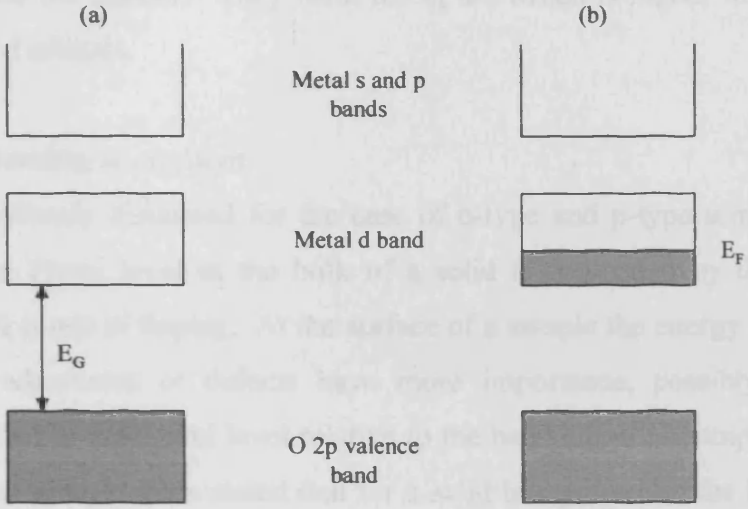

Figure 2.10 Energy bands of a transition metal oxide with a) an unoccupied d band and b) a partially filled d band.[10]

The d orbitals of a transition metal oxide are split in energy as a result of interaction of the metal orbitals with the surrounding ligand orbitals. Those d orbitals which point directly towards the ligands (forming σ combinations) have a larger degree of overlap than orbitals which point between the ligands (that form π combinations), and therefore form the major contribution to the ligand field splitting. The order of the d orbitals energy levels is dependent of the geometry of the ligands surrounding the transition metal atom; for TiO_2 the geometry around each Ti^{4+} cation is octahedral with the corresponding ligand field splitting shown in Figure 2.11.

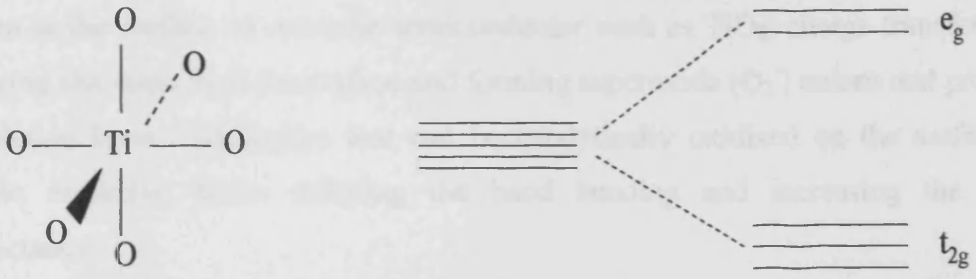

Figure 2.11 Octahedral geometry around the Ti^{4+} cation in TiO_2 and the corresponding ligand field splitting.

In octahedral geometry the metal d_{xy}, d_{xz} and d_{yz} orbital all point in between the ligands forming a degenerate set of orbitals of energy lower than the original d orbitals termed the t_{2g} set. The remaining d_{z^2} and $d_{x^2-y^2}$ orbitals are also degenerate and point directly towards the ligands. They form the e_g set which is higher in energy than the original metal d orbitals.

2.6.1 Band bending at surfaces

As previously discussed for the case of n-type and p-type semiconductors, the position of the Fermi level in the bulk of a solid is controlled by the energy levels introduced as a result of doping. At the surface of a sample the energy levels associated with surface adsorbates or defects have more importance, possibly resulting in a different position of the Fermi level relative to the band edges as compared to the bulk. However, it has already been stated that for a solid in equilibrium the Fermi level must be at the same energy throughout the solid. Therefore to achieve this equilibrium the band edges at the surface must bend.

For TiO_2, an n-type semiconductor, when there are surface states located in the bandgap there is transfer of electrons from the donor levels of the surface region in the surface states. This results in a depletion layer where there is an electrostatic field from the unbalanced positive charge of the ionized donors, causing the shift of the band energies. This is displayed in Figure 2.12.

The depletion layer formed as a result of diffusion of charge carriers through the solid gives rise to high surface resistance. The adsorption of molecules from the gas phase at the surface leads to occupancy of surface states and therefore alters the width of the depletion layer. This phenomenon is utilised in some solid-state sensors, where the presence of different gases alters the conductivity. For example, on adsorption of oxygen at the surface on a n-type semiconductor such as TiO_2, charge transfer occurs removing electrons from the surface and forming superoxide (O_2^-) anions and producing a depletion layer. Molecules that can be catalytically oxidized on the surface then liberate electrons, hence reducing the band bending and increasing the surface conductance.

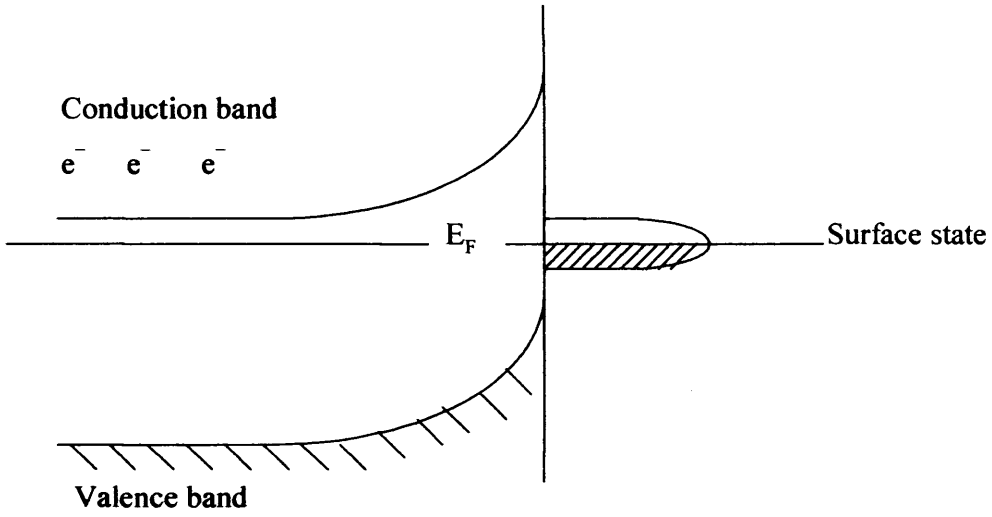

Figure 2.12 Band bending due to a surface state on a n-type semiconductor such as TiO_2.

2.6.2 Photoelectrochemistry

The band bending at the surface of semiconductors can be utilised in photoelectrochemistry, at the semiconductor-electrolyte interface. In an n-type semiconductor, electrons migrate into the bulk of the solid whilst holes migrate to the surface where they may participate in surface reactions, thereby acting as a photoanode. Similarly, electrons at the surface of a p-type semiconductor may act as a photocathode. In Figure 2.13 the two types of semiconductors form part of the same cell, separated by an electrolyte; opposite redox reactions will occur at the two electrodes resulting in a potential difference between them.

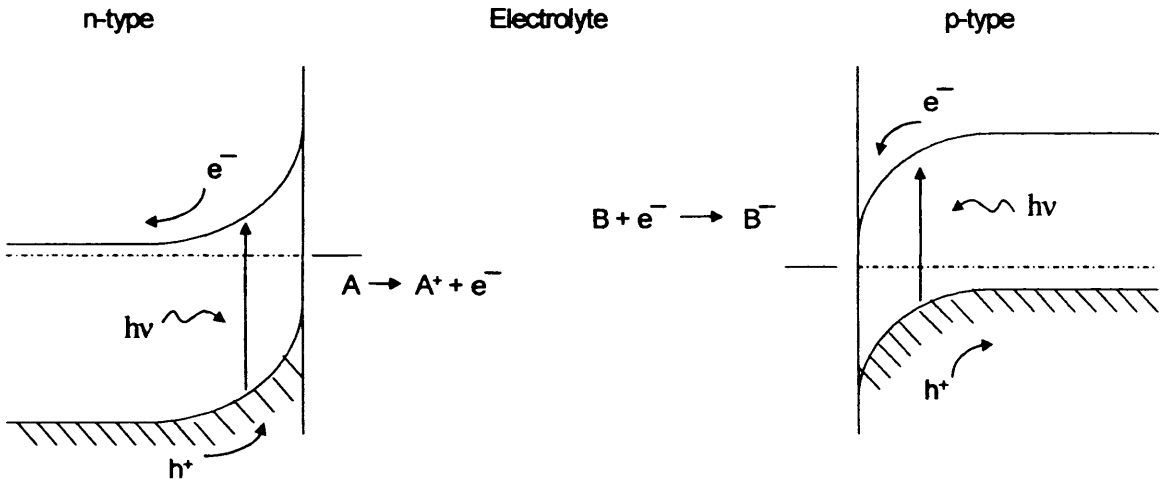

Figure 2.13 Semiconductor photoelectrodes separated by an electrolyte. Electrons and holes produced by light absorption are separated by band bending at the surface of the semiconductors.

The principle of photoelectrochemistry is used in solar cells to convert sunlight into useful electrical energy. The solar energy impinging on the earth's surface is approximately 3×10^{24} J every year, which is equivalent to 10^4 times the worldwide consumption of energy over the same time period. The desire to convert this energy source into useful forms is immediately apparent, and research into the development of solar energy utilisation has become a major area of interest. The first ever dye sensitized nanocrystalline solar cell (DSNC) was reported by Grätzel in Nature.[11] The solar cell utilises the semiconducting properties of TiO_2 to harvest solar energy and converts it into useful electrical power. The light absorption is performed by a monolayer of dye adsorbed to the semiconductor surface. After excitation of the dye by solar photons, an electron is transferred into the conduction band of the TiO_2 where subsequently, by virtue of the band bending occuring at the interface between the semiconductor and the SnO_2 glass substrate, the electron is extracted from the TiO_2 to flow around an external circuit. After passing through a load, the electron is returned to the cell *via* the counter electrode, where it is accepted by a redox electrolyte solution which fills the cell. Electron transfer then occurs between the reduced electrolyte and the dye to return the dye to its original form, effectively closing the circuit. The presence of the redox electrolyte ensures that the whole process is continuous and regenerative, resulting in solar cells that have a working life as long as the lifetime of the electrolyte solution. The whole process can be understood by considering Figure 2.14.

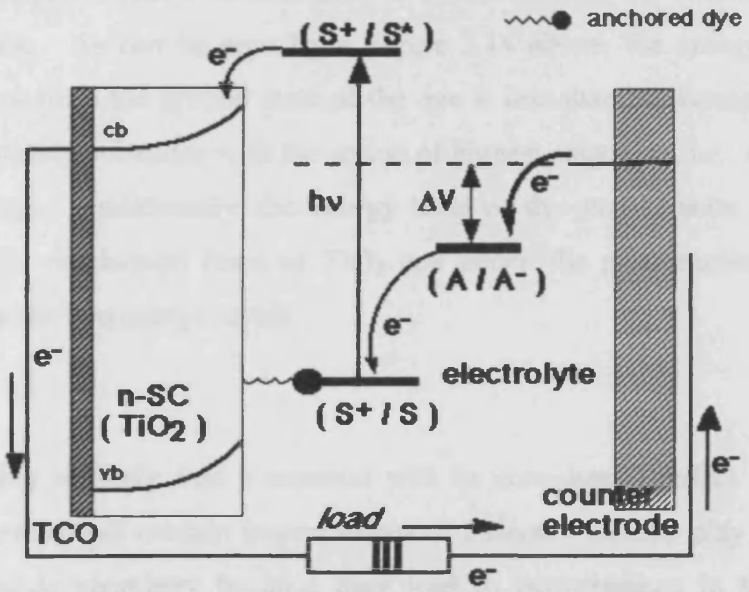

Figure 2.14 Principles of operation of a dye sensitized nanocrystalline solar cell (DSNC). (A/A^-) represents the redox couple, S represents the sensitizer (S* excited state, S^+ oxidised state).[11]

TiO_2 is selected as the choice of semiconductor in these solar cells because of its non-toxicity, plentiful abundance and low cost. Notably, however, the band gap of TiO_2 of approximately 3.0 eV is not ideal for the conversion of sunlight into electrical energy as the spectral output of energy from the sun is low in this region, as shown in Figure 2.15.

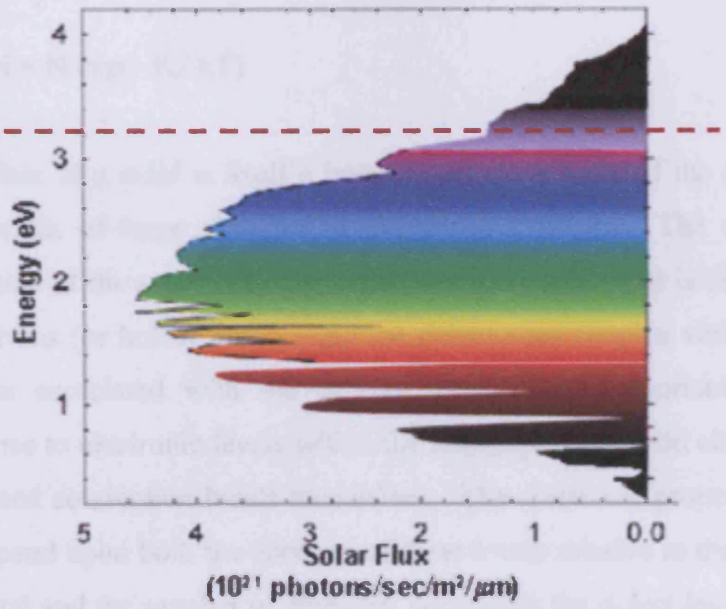

Figure 2.15 Solar spectrum, highlighting that the energy output from the Sun is low in the region of 3.0eV, the bandgap of TiO_2.

The dye is usually adsorbed onto the surface of the TiO_2 nanoparticles in order to reduce the bandgap required for excitation of an electron into the conduction band of the semiconductor. As can be seen from Figure 2.14 above, the energy required to excite an electron from the ground state of the dye is less than the bandgap energy of TiO_2, and importantly coincides with the region of highest solar flux, i.e., utilising more of the suns energy. Additionally, the energy level of the excited state of the dye is above that of the conduction band of TiO_2 and hence the photoexcited electron is "injected" across the two energy levels.

2.7 Defects

It is highly unlikely that a material will be completely perfect in its crystal structure, but instead will contain imperfections or defects. Defects play an important role in metal oxide chemistry because they lead to perturbations in the electronic structure of the solid, which may affect the electrical and mechanical properties of the system.[12] The presence of defects in a sample leads to an increase in the entropy of the

system, therefore it is dictated by thermodynamics that all crystals must contain a certain number of defects at non-zero temperatures and, in accordance with the Boltzmann distribution, the number of defects increases with temperature. For example, if the energy required to create a defect in a crystal containing N atoms is given by E_v, the equilibrium number of vacancies at a temperature T can be calculated from:

$$N = N \exp(- E_v / kT) \qquad (2.6)$$

The surface of a solid is itself a break in the periodicity of the structure and is therefore the origin of large changes in electronic structure. The changes to the electronic structure of the solid as a result of the presence of defects is dependent on the number of electrons (or holes) that occupy the defect sites coupled with the energy of the extra levels associated with the defects. Defects are important because they generally give rise to electronic levels within the bandgap of the solid close to the edges of the valence and conduction bands themselves. The electronic properties associated with defects depend upon both the energies of these levels relative to the band edges of the perfect crystal and the number of electrons occupying the defect levels. The energy required to excite the charge carriers into the corresponding band is low and therefore defects such as these often result in an increase in electrical conductivity. Unoccupied energy levels may also be introduced in the bandgap region by defects which may act as trapping centres for charge carriers.

There are two factors which significantly complicate the study of defects. Firstly, the presence of defects results in imbalances in charge over the whole of the solid and so other defects will be present to compensate for this. However, it is often the case that the nature of the defect responsible for compensating the defect under study is unknown. Secondly, consideration must be paid to the structural relaxations and rearrangements which accompany the formation of any defect.

2.7.1 Point defects; vacancies

The simplest type of defect in a crystal lattice is a vacancy, or Schottky defect, where an atom is missing from its site in the lattice. In the region around the defect there will be some atomic rearrangement or reconstruction to account for the vacancy, shown in Figure 2.16. To maintain charge balance in the solid, the defects occur in pairs; for example in a solid of stoichiometry MX there are an equal number of M^+ cation and X^- anion vacancies present.[13]

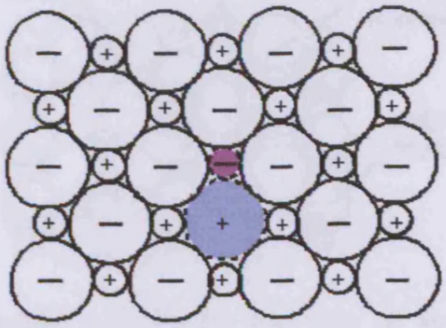

Figure 2.16 A lattice vacancy (Schottky defect).

Diffusion of atoms through the crystal lattice is facilitated by the presence of vacancies, and this will be further discussed in Chapter 5. Very little energy is required for an atom to move into an adjacent vacancy site, leaving its own site vacant, resulting in overall diffusion of atoms in one direction (or vacancies in the opposite direction).

In the case of MgO for example two important classes of defect are the anion (i.e. O^{2-}) vacancies found in the bulk and at surfaces, and the associated bulk and surface cation vacancies (F_s^{2+}).[14] The electrons and holes generated at these vacancies can be responsible for changing the oxidation state of the metal in the lattice, as in the case of TiO_2 where the electrons positioned at an oxygen vacancy reduce the Ti^{4+} metal ions to Ti^{3+}. The extent of defect formation can often be related to the ease of reduction or oxidation of the transition metal.

The loss of an oxygen anion from the surface of a crystal lattice results in a decrease in the coordination number of the neighboring cations. In the case of TiO_2(110) there are two possible sites for an oxygen vacancy, either a bridging oxygen ion or one from the main surface plane. On loss of a bridging oxygen, two 6-fold coordinated Ti^{4+} cations are reduced to 5-fold coordinated; in the latter case, two 5-fold coordinated cations become 4-fold. This reduction in coordination number is accompanied by an increase in chemical reactivity, as it is commonly viewed that low-coordination sites are more surface reactive than those of high coordination.

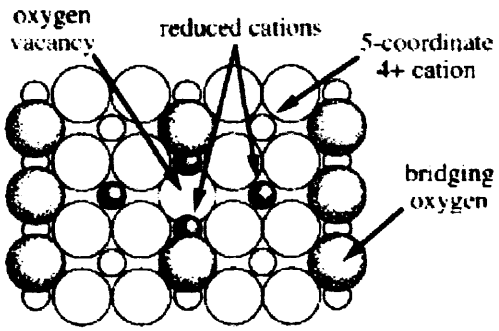

Figure 2.17 Schematic model showing the top view of an oxygen vacancy along the bridging oxygen row on $TiO_2(110)$.[15]

2.8 Conclusion

In the present chapter the importance of solid-state chemistry has been highlighted, with particular relevance to TiO_2. This area of chemistry focuses on the structure and properties of materials, and their related applications. In particular an understanding of the electronic structure of a solid, characterized by the number of free charge carriers, is important. As previously discussed, the three classes of materials (conductor, insulator and semiconductor) can be differentiated by their band structure and their electrical conductivity. In a conductor there are a large number of electrons located in the conduction band whereas in an insulator there are close to zero free charge carriers. In the third class of compounds, semiconductors, there is an intermediate number of charge carriers available and they cannot therefore be classified in either of the previous two categories. Semiconductors can further be classified into two groups, intrinsic and extrinsic. The conductivity of an intrinsic semiconductor is dependent on the size of the bandgap between the valence and conduction bands, and the temperature of the solid. Both of these variables control the number of free charge carriers available as described by the Boltzmann distribution discussed earlier. The electrical conductivity of an extrinsic semiconductor is controlled by the number of dopants added to the solid and the location of the acceptor or donor levels relative to the valence and conduction bands respectively.

2.9 References

[1] P. Atkins, J. de Paula, *Atkins' Physical Chemistry*, **2006**, *8th Edition*, OUP, Oxford.

[2] V.E. Henrich, P.A. Cox, *The Surface Science of Metal Oxides*, **1996**, *CUP*, Cambridge.

[3] J.R. Hook, H.E. Hall, *Solid State Physics*, **1991**, *2nd Edition*, Wiley, Sussex.

[4] S. Licht, O. Khaselev, P.A. Ramakrishnan, T. Soga, M. Umeno, *J. Phys. Chem. B*, **1998**, *102*, 2546.

[5] M.C. Gallagher, M.S. Fyfield, J.P. Cowin, S.A. Joyce, *Surf. Sci.*, **1995**, *339*, L909.

[6] A.R. West, *Basic Solid State Chemistry*, **1999**, Wiley, Sussex.

[7] X. Li, S.Q. Gu, E.E. Reuter, J.T. Verdeyen, S.G. Bishop, J.J. Coleman, *J. App. Phys.*, **1996**, *80*, 2687.

[8] G. Verzellesi, D. Bergamini, G-F. Dalla Betta, C. Piemonte, M. Boscardin, L. Bisisio, S. Bettarini, G. Batignani, *Semicon. Sci. and Tech.*, **2006**, *21*, 194.

[9] E. Giamello, P. Ugliengo, E. Garrone, *J. Chem. Soc. Faraday Trans. I*, **1989**, *85*, 1373.

[10] P.A. Cox, *The Electronic Structure and Chemistry of Solids*, **1987**, Oxford Science Publications.

[11] B.O' Regan, M. Grätzel, *Nature*, **1991**, *353*, 737.

[12] U. Diebold, *Surf. Sci. Rep.*, **2003**, *48*, 53.

[13] Shriver and Atkins, *Inorganic Chemistry*, **2006**, 4th Edition, *Oxford.*

[14] R.L. Nelson, A.J. Tench, B.J. Harmsworth, *Trans. Faraday Soc.*, **1967**, *63*, 1427.

[15] M.A. Henderson, W.S. Epling, C.L. Perkins, C.F.H. Peden, U. Diebold, *J. Phys. Chem. B*, **1999**, *103*, 5328.

Chapter 3

A Brief Introduction to the Theory and Applications of Electron Paramagnetic Resonance (EPR) Spectroscopy in Polycrystalline Systems

3.1 Introduction

Electron Paramagnetic Resonance (EPR) is a spectroscopic technique that detects chemical species possessing unpaired electrons. A great number of materials contain such paramagnetic entities and the technique has been successfully applied in disciplines as varied as chemistry, biology, medical science, physics and geology.[1-3] The technique is capable of obtaining detailed information on chemical kinetics and electron exchange, electrochemical processes and catalysis, crystalline structure and fundamental quantum theory.

The first observation of an EPR signal was recorded in 1945 by Zavoisky from a $CuCl_2.2H_2O$ sample.[4] The result was later interpreted by Frenkel[5] as showing paramagnetic resonance absorption and this gave rise to the technique of EPR. Following the end of World War II the availability of microwave components was high and this led to the rapid exploitation of the EPR technique. Equipment in the 9 GHz region had been extensively used in radar technology and was therefore readily available at low cost.

The technique itself is an extension of the famous Stern-Gerlach experiment of the 1920's which for the first time showed that an electron magnetic moment in an atom can take on only discrete orientations in a magnetic field.[6] The electron magnetic moment was subsequently linked to the concept of electron spin angular momentum and the energy levels resulting from interaction of the electron with the nucleus was later described by Breit and Rabi.[7]

A detailed account of the physics behind EPR can be found in the excellent book of Schweiger and Jeschke.[8] There are numerous textbooks on the subject of EPR that go into more detail on the practicalities of the technique, and also give a detailed account from different areas of chemistry; see for example Weil, Wertz and Bolton[9] or Mabbs and Collison,[10] among others.[11-14] There is also an excellent monograph by Lunsford on the application of EPR techniques to studies in heterogeneous catalysis.[15] The experiments discussed in this thesis have all been performed using continuous wave EPR (*cw*-EPR) spectroscopy at X-band (~9.5 GHz), hence the theory discussed in the

current chapter will only focus on this methodology. However, it is important to acknowledge that in recent years there has been extensive development in the areas of pulsed techniques and high-frequency EPR. High-frequency EPR provides several advantages over low-frequency techniques. For example, it offers increased resolution of g values, which is important in systems where spectral lines may not be resolved at lower fields. Additionally, high-frequency EPR has an increased absolute sensitivity making it particularly useful for studying systems where the number of paramagnetic species is inherently low. High-frequency EPR is used increasingly in structural biology, for example complex enzymes, in which the active sites often have large zero-field splitting which are not resolved at low frequency.

The prevalence of pulsed techniques has increased over recent years due to an increased availability in sufficiently fast electronics. The technique is now used in time-resolved EPR, as a tool for studying molecular motion and in EPR imaging. Echo-detected EPR is also particularly useful for measuring rates of reaction and determining relaxation times. Electron spin echo envelope modulation (ESEEM) allows the determination of small hyperfine coupling constants which are too small to be detected by *cw*-EPR, and this provides information on the number, identity and distance between weakly interacting nuclei within a system.

3.2 Basic Principles of EPR

An electron is a negatively charged particle which spins on its axis. This property of spin, which was first discovered by Stern and Gerlach in their famous experiment of 1921, forms the basis of EPR spectroscopy.[16] An oscillating charge will produce a magnetic moment, and interaction of these magnetic moments with an external magnetic field results in states of different energies. Transitions between these two states can be induced by absorption of a photon of the correct frequency, and it is these transitions which are detected by EPR.

The spin of an electron is quantified by the spin angular momentum |S|, which is related to the spin quantum number by:

$$|\mathbf{S}| = \sqrt{s(s+1)} \tag{3.1}$$

where s = spin quantum number.

Heisenberg's Uncertainty Principle states that one can only measure the magnitude of the angular momentum in one direction with certainty at any given

moment in time.[17] This direction is taken as standard to be the z direction, therefore the allowed orientations of the spin angular momentum along the z axis are given by:

$$\text{Allowed orientation} = M_s\hbar \tag{3.2}$$

where M_s is the spin angular momentum quantum number (allowed values given by $M_s = +s, s-1, s-2 \ldots -s$) and h = Planck's constant ($\hbar = h/2\pi$). For an unpaired electron s = ½, therefore $M_s = \pm 1/2$ and the allowed orientations of the spin angular momentum along the z axis are given by $\pm\hbar/2$.

The magnitude of the magnetic moment, μ, of the electron created by its spin is described by:

$$\mu = -\frac{geh}{4\pi m_e}\sqrt{s(s+1)} \tag{3.3}$$

where e = the charge on the electron (C), m_e = the mass of the electron (kg) and g = a proportionality constant.

Equation (3.3) above can be simplified to the following expression by replacing the combination of universal constants by another constant, the Bohr Magneton:

$$\mu_B = \frac{eh}{4\pi m_e} \tag{3.4a}$$

giving

$$\mu = -g\,\mu_B|S| \tag{3.4b}$$

The magnitude of the magnetic moment along the z-axis is then given by:

$$\mu_z = -g\mu_B M_S \tag{3.5}$$

As stated above, for a single unpaired electron the spin angular momentum quantum number can take on the value $M_s = \pm$½ and this results in two magnetic moments. In the absence of an external magnetic field the magnetic moments arising from the two values of spin angular momentum are degenerate i.e. they lie at the same energy. However, if an external field is applied to the system, the degeneracy is broken and the two states lie at different energy.

The energy of the interaction between the magnetic moment of the electron and the applied magnetic field is described by:

$$E = -\mu_z B \tag{3.6}$$

where E = energy of the interaction (J), μ_z = magnetic moment in the z direction (JT^{-1}), B = magnitude of the external magnetic field (T).

Substituting in the above expression for μ_z and the values of $M_s = \pm 1/2$ gives rise to the two Zeeman energy levels of energies $E = \pm \frac{1}{2} g \mu_B B$ separated by the Zeeman splitting:

$$\Delta E = g\mu_B B \tag{3.7}$$

which is directly proportional to the magnitude of the applied magnetic field.

As with other absorption spectroscopies, a transition between the two Zeeman levels can be induced by the absorption of a photon of the correct frequency, ν, given by:

$$E = h\nu \tag{3.8}$$

The transition of an electron from the lower to the upper Zeeman level is the basis of Electron Paramagnetic Resonance (see Figure 3.1). Although it is possible to perform the experiment by altering the frequency of the electromagnetic radiation in the presence of a constant magnetic field, experimentally it is easier if the frequency is held constant and the magnetic field is swept.

The position of a transition is reported in terms of its g-value, the proportionality constant of equation (3.7). By simple rearrangement, the g-value can be calculated from:

$$g = \frac{h\nu}{\mu_B B} \tag{3.9}$$

In quantum mechanics, the vector is replaced by the corresponding operator, giving the simplified form of the spin Hamiltonian:

$$\hat{\boldsymbol{H}} = g\mu_B \mathbf{S}.\mathbf{B} \tag{3.10}$$

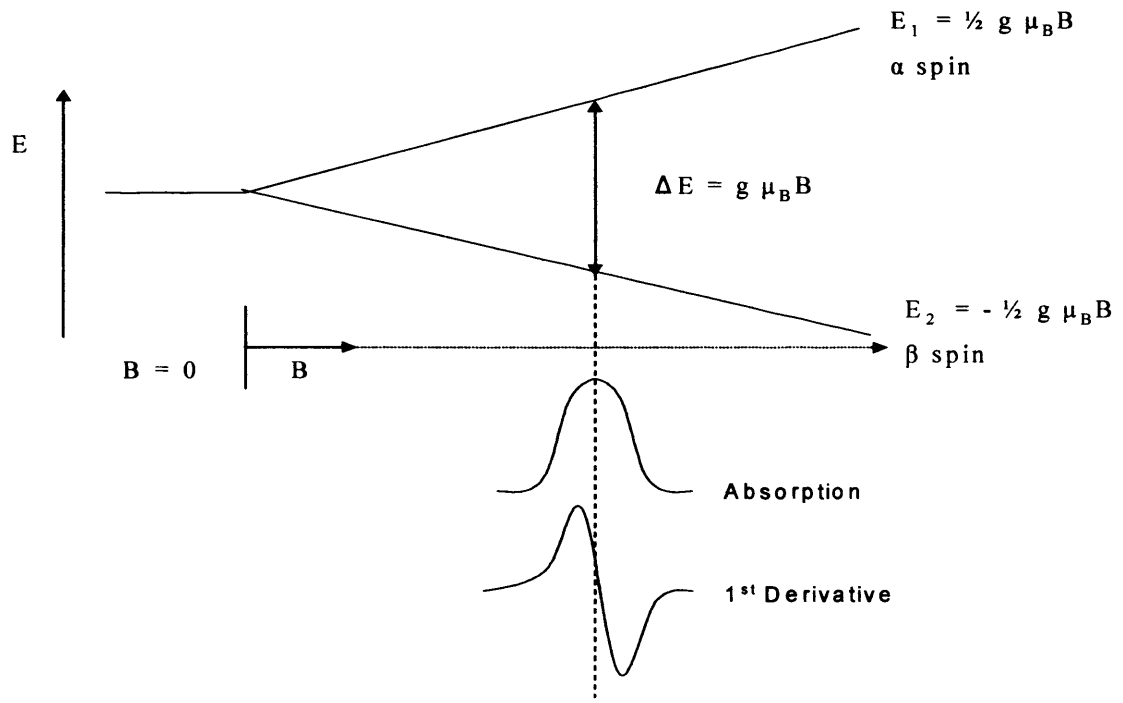

Figure 3.1 Electron Zeeman splitting

3.3 g tensor: Significance and Origin

The energy levels of an electron subjected only to the force of an applied magnetic field were given by the solutions of the simple Spin Hamiltonian, equation 3.10. However, electrons in atoms and molecules are subject to a variety of magnetic interactions, which can shift and split the simple Zeeman levels and thus the effects are reflected in the EPR spectrum. Orbital angular momentum is non-zero in the case of orbitals exhibiting p, d and f character. The spin therefore is no longer quantified or aligned along the direction of the external magnetic field, and the g value cannot be expressed by a scalar quantity, but by a tensor value. The orbital angular momentum L is associated with a magnetic momentum given by $\mu_L = \mu_B L$.

Considering a system with a doublet ($M_S = \pm ½$) non-degenerate electronic ground state and nuclei with zero nuclear magnetic moment ($\mu_n = 0$) for simplicity, for such a system the interaction with the external magnetic field can be expressed in terms of a perturbation of the general Hamiltonian by:

$$\hat{H} = g_e \mu_B \mathbf{B}\hat{\mathbf{S}} + \mu_B \mathbf{B}\mathbf{L} + \lambda \mathbf{L}\,\hat{\mathbf{S}} \qquad (3.11)$$

where $g_e\mu_B\mathbf{B}\hat{\mathbf{S}}$ = electron Zeeman term, $\mu_B\mathbf{BL}$ = orbital Zeeman term (usually quenched to zero), $\lambda\mathbf{L}\hat{\mathbf{S}}$ = spin-orbit coupling and λ = spin-orbit coupling constant which mixes the ground state wavefunction with excited states.

Spin orbit coupling is the magnetic interaction which links L and S, the extent of the interaction depends on the nature of the chemical system and the symmetry. If $|\lambda|$ is small, then $g \cong g_e$ (close to free spin) e.g. an organic radical. If $|\lambda|$ is large, then $g \neq g_e$ (large shift from free spin $g_e \pm 5$) e.g. a transition metal ion.

3.3.1 Symmetry of Real Systems

One of the main advantages of the EPR technique is that it can be applied to materials in all three of the main state phases, that is solid, liquid and gas. For those materials in the solid phase, much of the work recorded has been concerned mainly with polycrystalline materials. In recent years there has been increased interest in applying the EPR technique to single crystals, and the current literature will be reviewed and discussed in more detail in chapter 7.

Polycrystalline materials are composed of numerous small crystallites that are randomly oriented in space. The "powder" spectrum resulting from a polycrystalline material is therefore the envelope of the spectra corresponding to all possible orientations of the paramagnetic species with respect to the magnetic field. The profile of the EPR spectrum is dependent on the symmetry of the system under study, and the cases of isotropic, axial or orthorhombic symmetry are considered in the following sections.

3.3.1a Isotropic Symmetry

The g tensor for an isotropic system is characterised by a single line where $g_{xx} = g_{yy} = g_{zz}$ for nuclei with I = 0. Systems that exhibit this type of EPR spectrum have perfect cubic symmetry such as octahedral or tetrahedral symmetry. It is rare to observe an isotropic spectrum arising from a solid material but is more commonly seen in low-viscosity solutions where the observed g value, g_{iso}, is the result of averaging of the three components by rapid tumbling.

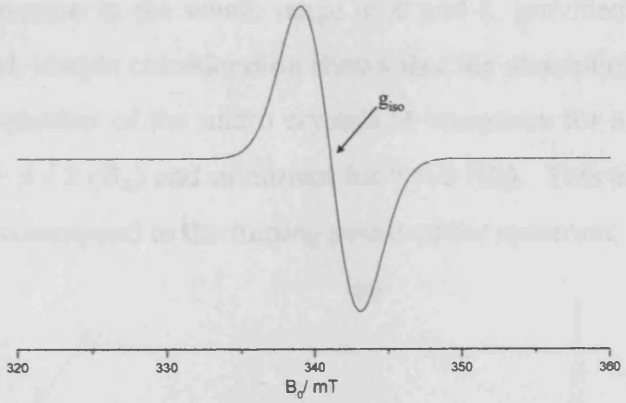

Figure 3.2 Simulated isotropic EPR spectrum for the case where I = 0.

3.3.1b Axial Symmetry

A molecule displays axial symmetry if two of the principle g values, namely x and y, are equal. The unique value is designated as $g_{\|}$ (g_{zz}) and is referred to as "g parallel" whilst the other value $g_{\perp}$ (i.e., $g_{xx} = g_{yy}$) is referred to as "g perpendicular". If z is the unique symmetry axis of the system and θ is the angle between the z axis and the magnetic field, the x and y directions are equivalent and the angle ϕ becomes meaningless.

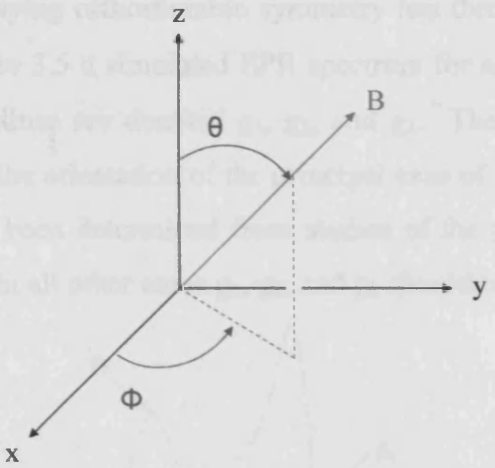

Figure 3.3 Symmetry axis of axial symmetry, where $g_{\perp} = g_x = g_y$ and $g_{\|} = g_z$.

The resonant field can then be calculated from the equation:

$$B_{res} = h\nu / \mu_B (g_{\perp}^2 \sin^2\theta + g_{\|}^2 \cos^2\theta)^{-½} \quad (3.12)$$

where $g_{\|} = g_{zz}$ and $g_{\perp} = g_{xx} = g_{yy}$ are g values measured when the axis of the paramagnetic species is respectively parallel and perpendicular to the applied magnetic field. As the powder spectrum is the envelope of the individual spectra arising from

every possible orientation in the whole range of θ and ϕ, provided the crystallites are randomly distributed, simple consideration shows that the absorption intensity which is proportional to the number of the micro crystals at resonance for a given θ value, is a maximum when $\theta = \pi / 2$ ($B_\perp$) and minimum for $\theta = 0$ ($B_\parallel$). This allows the extraction of the g values that correspond to the turning points of the spectrum.

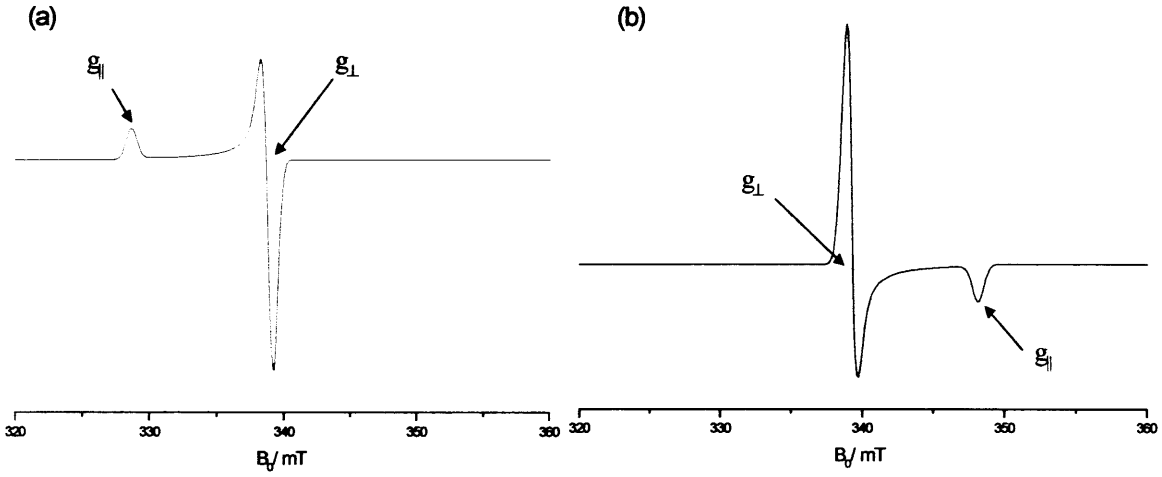

Figure 3.4 Simulated axial EPR spectra where (a) $g_\parallel > g_\perp$ and (b) $g_\perp < g_\parallel$.

3.3.1c Orthorhombic Symmetry

A system displaying orthorhombic symmetry has three distinct values of g i.e. $g_{xx} \neq g_{yy} \neq g_{zz}$. In Figure 3.5 a simulated EPR spectrum for an orthorhombic species is illustrated and the g values are denoted g_1, g_2, and g_3. The g_{xx}, g_{yy} and g_{zz} notation should only be used if the orientation of the principal axes of the system with respect to the magnetic field has been determined from studies of the paramagnetic species in a single crystal sample. In all other cases g_1, g_2, and g_3 should be used.

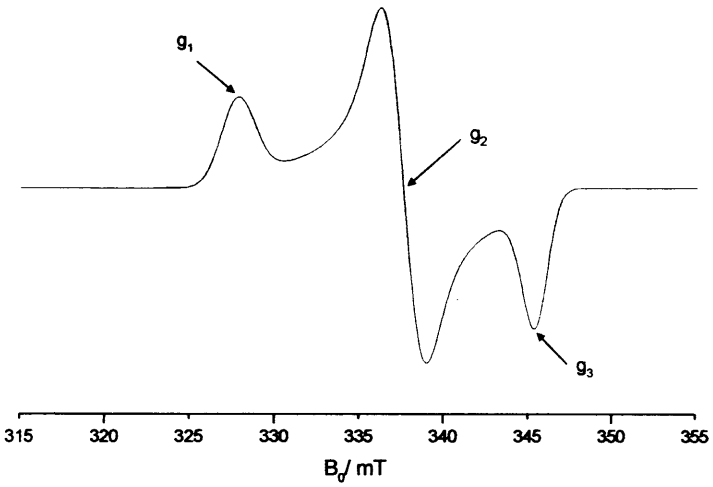

Figure 3.5 Simulated EPR spectrum for a system with orthorhombic symmetry where $g_1 \neq g_2 \neq g_3$.

3.4 Hyperfine Tensor: Significance and Origin

The interaction of an electron with an external magnetic field yields only a single line in an EPR spectrum and therefore contains very little information. The case described above is for a hypothetical situation of a free electron in space which is unaffected by other spins. However, in any real example, the electron will interact at least with its associated nucleus, and it is this interaction, termed the nuclear hyperfine interaction, which is most useful in EPR spectroscopy.

The hyperfine interaction (A) comes from the interaction between the magnetic moment of the electron with the magnetic moment of a nearby nucleus (B_{local}), therefore equation (3.9) may be modified to:

$$h\nu = g\mu_B(\mathbf{B} + \mathbf{B}_{(local)}) \tag{3.13}$$

The nuclear spin quantum number (I) has an associated magnetic moment (μ_N) written as:

$$\mu_n = g_n \mu_N I \tag{3.14}$$

where g_n = nuclear g factor (proton value), μ_N = nuclear magneton value (μ_N is smaller than μ_B by a factor of 1838, i.e. the ratio of the mass of a proton to that of an electron).

The contribution from the magnetic field and the orbitals, as well as the contribution from the magnetic field of the nucleus are considered in the more complete form of the spin Hamiltonian as shown:

$$\hat{H} = g_e \mu_B \mathbf{B}\hat{\mathbf{S}} - g_n \mu_N \mathbf{B}\hat{\mathbf{I}} + \hat{\mathbf{I}}\,\mathbf{A}\,\hat{\mathbf{S}} \tag{3.15}$$

where $\hat{\mathbf{I}}$ = nuclear spin, $\mathbf{A}$ = hyperfine term, $\hat{\mathbf{S}}$ = electron spin

The interaction between the unpaired electron and a spin active nucleus gives origin to further splitting of the lines in the spectra which gives the EPR spectrum hyperfine structure. Two types of electron spin/nuclear spin interactions occur; an isotropic interaction (A_0) and an anisotropic interaction (B_0), which will be discussed further below.

For a solid state paramagnetic species where the unpaired electron is localised upon a magnetic nucleus, each of the principal g tensor components will be split into (2nI + 1) lines, where I is the spin quantum number of the nucleus involved. For each g tensor component, the set of lines (determined by 2nI + 1) will be spaced by a splitting constant, which corresponds to the appropriate component of the anisotropic coupling, where g_1 is split by A_1, g_2 split by A_2, etc. In powder samples, the EPR spectra often

have large linewidths; consequently some hyperfine detail may not be clearly resolved, and the precise splitting constant remains uncertain.

3.4.1 Isotropic Hyperfine Coupling

This type of interaction occurs when the electron is located in a spherical s orbital. Isotropic hyperfine couplings are observed by rapidly tumbling molecules and species with high s character in the wavefunction. An electron has a non-zero probability of being at the centre of the orbital and therefore has a Fermi contact interaction with the nucleus. The spherical nature of the s orbital results in an interaction which is independent of the orientation of the orbital in which the electron is situated, i.e. the interaction is isotropic. The isotropic coupling constant, a_{iso}, is given by:

$$a_{iso} = (8 \pi / 3 \, g_e \, g_n \, \mu_B \, \mu_N) \, |\psi(0)|^2 \qquad (3.16)$$

where $|\psi(0)|^2$ is the square of the absolute value of the wavefunction of the unpaired electron evaluated at the nucleus. The high electron density at the nucleus of s orbitals gives rise to large hyperfine coupling constants, and due to the symmetry of the s orbital the coupling will be independent of direction.

The energy of an electron now depends on three different interactions: (i) the interaction of the electron itself with an applied magnetic field, (ii) the interaction of the associated nucleus with the magnetic field and (iii) the interaction between the electron and the nucleus. As an illustration of this the following section discusses the energy diagram arising for an unpaired electron due to its interaction with its associated nucleus with $I = ½$.

The energy of an electron with magnetic quantum number M_s interacting with a nucleus of quantum number M_I is given by:

$$E(M_s, M_I) = g \, \mu_B \, B \, M_s - g_N \, \mu_N \, B \, M_I + h \, a_{iso} \, M_s \, M_I \qquad (3.17)$$

For the interaction of an unpaired electron ($M_s = ½$) with a single proton ($M_I = ½$) the above equation gives rise to four different energy levels as detailed in Table 3.1

Table 3.1 Energy levels for an unpaired electron interacting with a I = ½ nucleus

	M_s	M_I
$E_1 = 1/2g\mu_B B + 1/2g_N\mu_N B - 1/4ha_{iso}$	+ ½	- ½
$E_2 = 1/2\ g\mu_B B - 1/2\ g_N\mu_N B + 1/4ha_{iso}$	+ ½	+ ½
$E_3 = -1/2\ g\mu_B B + 1/2\ g_N\mu_N B + 1/4ha_{iso}$	- ½	- ½
$E_4 = -1/2\ g\mu_B B - 1/2\ g_N\mu_N B - 1/4ha_{iso}$	- ½	+ ½

The transitions between energy levels are restricted by selection rules, which state that for a transition $\Delta M_s = \pm 1$ and $\Delta M_I = 0$. From the above, the allowed transitions are given by:

$$\Delta E_1 = E_3 - E_1 = g\mu_B B - \tfrac{1}{2} ha_{iso} \quad (3.18a)$$

$$\Delta E_2 = E_4 - E_2 = g\mu_B B + \tfrac{1}{2} ha_{iso} \quad (3.18b)$$

The spectrum therefore consists of two absorptions of equal intensity separated by the hyperfine coupling constant, as shown in Figure 3.6.

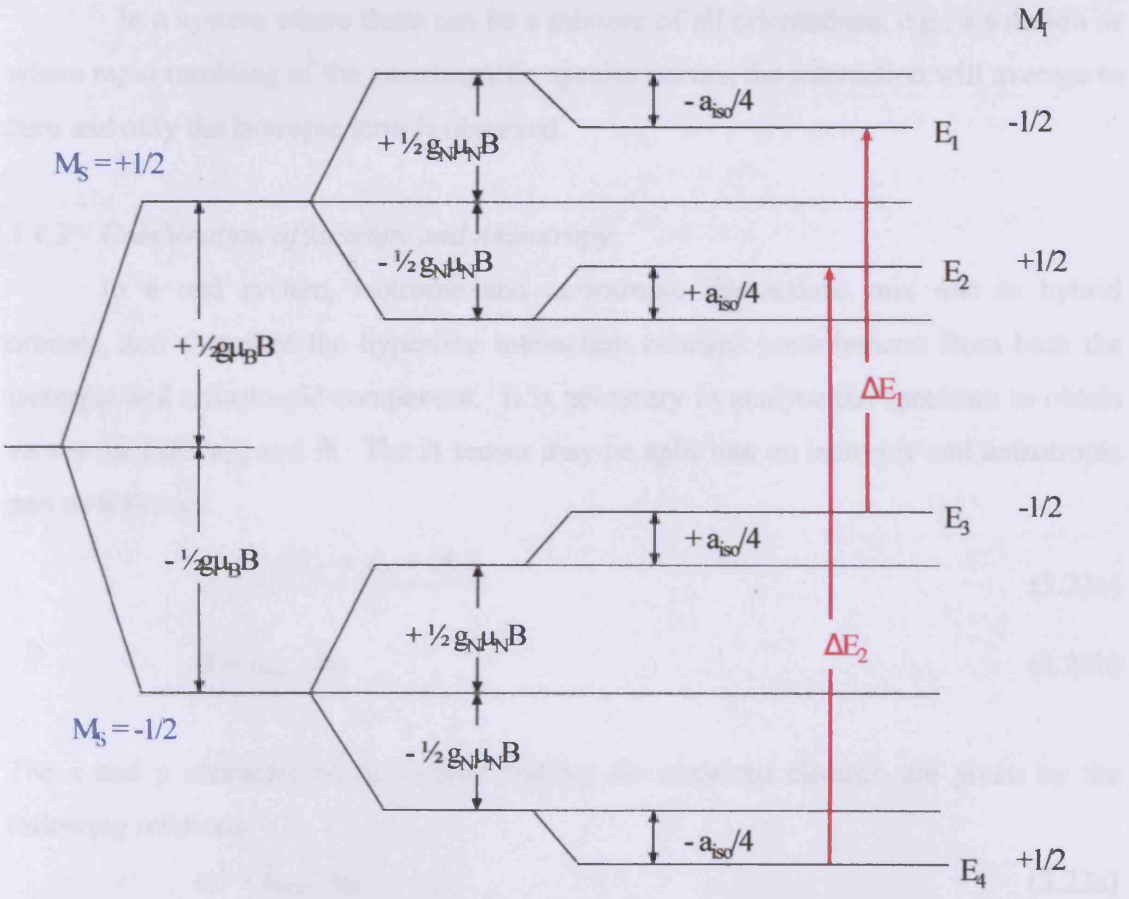

Figure 3.6 Energy level diagram for an unpaired electron interacting with a nucleus of spin I = ½.

3.4.2 Anisotropic Hyperfine Coupling

Electrons which are situated in directional orbitals, i.e., p, d, f etc., exhibit anisotropic hyperfine interactions with the nucleus. The electron is unable to approach the nucleus very closely due to the node of the orbital and therefore the field it experiences from the nucleus appears to arise from a point magnetic dipole. The interaction is referred to as dipole-dipole interaction. This interaction is anisotropic, i.e. the magnitude and sign of the interaction is dependent on the orientation of the electrons' orbital with respect to the applied magnetic field and to the separation between the two dipoles. The interaction energy is given by:

$$E = \mu_s \mu_n / r^3 - 3(\mu_s \mathbf{r})(\mu_n \mathbf{r}) / r^5 \tag{3.19}$$

where **r** is the vector relating the electron and nuclear moments, and r is the distance between the two spins. The resulting Hamiltonian is given by:

$$H_{aniso} = - g_e \mu_B g_n \mu_N (\mathbf{I.S}/ r^3 - 3(\mathbf{I.r})(\mathbf{S.r})/ r^5) \tag{3.20}$$

In a system where there can be a mixture of all orientations, e.g., a solution or where rapid tumbling of the paramagnetic species occurs, the interaction will average to zero and only the isotropic term is observed.

3.4.3 Combination of Isotropy and Anisotropy

In a real system, isotropic and anisotropic interactions mix due to hybrid orbitals, and therefore the hyperfine interaction contains contributions from both the isotropic and anisotropic component. It is necessary to analyse the spectrum to obtain values for both a_{iso} and B. The A tensor may be split into an isotropic and anisotropic part as follows:

$$a_{iso} = \frac{(A_\perp + A_\perp + A_\parallel)}{3} \tag{3.21a}$$

$$B = a_{iso} - A_\perp \tag{3.21b}$$

The s and p character of the orbital hosting the unpaired electron are given by the following relations:

$$c_s^2 = a_{iso} / A_0 \tag{3.22a}$$

$$c_p^2 = B / B_0 \tag{3.22b}$$

where A_0 and B_0 are the theoretical hyperfine coupling constants (assuming pure s and p orbitals for the elements under consideration). The terms a_{iso} and B are the experimental isotropic and anisotropic coupling constants respectively.

3.5 Point Symmetry

The cases of isotropic, axial and orthorhombic symmetry have been considered above in section 3.3. For all of these point symmetries the principal axes of the g and A tensors are coincident; however, for the lower classes of symmetry such as monoclinic and triclinic, the g and A axes may not be coincident. The relationship between these tensors, the EPR spectral characteristics and the associated point symmetries are listed in Table 3.2. These relationships indicate that each type of EPR spectrum (isotropic, axial, etc) is associated with a restricted number of point symmetries, therefore giving some indication of the structure of the paramagnetic species responsible for the EPR spectrum.

Table 3.2 Relationship between g and A tensors, EPR symmetry and the point symmetry of the paramagnetic species.

EPR Symmetry	g and A tensors	Coincidence of tensor axis	Molecular point symmetry
Isotropic	$g_{xx} = g_{yy} = g_{zz}$ $A_{xx} = A_{yy} = A_{zz}$	All coincident	O_h, T_d, O, T_h, T
Axial	$g_{xx} = g_{yy} \neq g_{zz}$ $A_{xx} = A_{yy} \neq A_{zz}$	All coincident	D_{4h}, C_{4v}, D_4, D_{2d}, D_{6h}, C_{6v}, D_6, D_{3h}, D_{3d}, C_{3v}, D_3
Rhombic	$g_{xx} \neq g_{yy} \neq g_{zz}$ $A_{xx} \neq A_{yy} \neq A_{zz}$	All coincident	D_{2h}, C_{2v}, D_2
Monoclinic	$g_{xx} \neq g_{yy} \neq g_{zz}$ $A_{xx} \neq A_{yy} \neq A_{zz}$	One axis of g and A coincident	C_{2h}, C_s, C_2
Triclinic	$g_{xx} \neq g_{yy} \neq g_{zz}$ $A_{xx} \neq A_{yy} \neq A_{zz}$	Complete non-coincidence	C_1, C_1
Axial non-collinear	$g_{xx} = g_{yy} \neq g_{zz}$ $A_{xx} = A_{yy} \neq A_{zz}$	Only g_{zz} and A_{zz} coincident	C_3, S_6, C_4 S_4, C_{4h}, C_6 C_{3h}, C_{6h}

3.6 Interpreting Real EPR Spectra

The overall shape of a powder spectrum is a combination of many different factors including:

- The presence of several species in the system that have different EPR parameters, including nuclei with different nuclear spins.
- Broadening of the lines as a result of dipolar spin-spin interactions or to rapid motion leading to loss of resolution.
- Second order effects including nuclear quadrupolar interactions that influence the regular spacing of hyperfine lines.

In order to interpret an EPR spectrum it is necessary to firstly separate it into the individual component species and then to make some assignment for these paramagnetic species. Finally, these assignments are confirmed using simulations and often theoretical calculations. There are several approaches which can be used to help in the task of interpreting a spectrum, some of which have been used throughout the course of this thesis, and these will be discussed in the following sections.

3.6.1 Measurement of g values

There are two possible ways to measure a g value; either with a reference sample (e.g. DPPH) and using the equation:

$$g = \frac{g_{ref} B_{ref}}{B} \tag{3.23}$$

or by obtaining carefully measured ν and B values directly using an NMR gaussmeter and substituting these into equation (3.9).

3.6.2 Variable power and temperature studies

By increasing the power of the microwave radiation entering the cavity, species which are easily saturated can be removed from the spectrum, thereby making it less complicated. The components of the spectrum are separated on the basis of different saturation abilities. Species with long relaxation times (T_1 and T_2) are most easily saturated, i.e., their Zeeman levels become equally populated and no EPR transition can occur. This method is often adopted for organic radicals or solid-state defects weakly coupled to the lattice.

Transition metal ions (TMIs) have much shorter relaxation times compared to organic radicals and often avoid saturation. Therefore, variable power studies on these radicals may not be useful. However, the relaxation time of each TMI will be sensitive to temperature. Performing a variable temperature study can help to interpret the spectrum by separating the different components of the spectrum based on the different dependencies of the signal intensities with temperature. This technique has been adopted several times in this study (see, for example, section 6.3.4).

3.6.3 Addition of probe molecules

Probe molecules may be used to test the different features of oxide surfaces. The addition of the probe molecule may result in changes in the line shape, line width and even g values of the paramagnetic species present, depending on the strength of the interaction between the paramagnetic species and the probe molecule. Oxygen is commonly used as a probe molecule, and has been used successfully to distinguish between the species situated in the bulk and on the surface of metal oxides.[18] Charge transfer may occur between the surface and the probe molecule giving rise to new EPR signals, or alternatively the spectrum may simply be affected by line-broadening in the presence of the probe molecule which vanishes upon outgassing.

3.6.4 Isotopic labelling

The simulated spectra shown in section 3.3 for an isotropic, axial and orthorhombic system do not include any hyperfine interactions. However, isotopic labelling can be used to produce a hyperfine pattern in a spectrum when the original sample investigated only contained species with $I = 0$ (or a very low abundance of species with $I \neq 0$). The value of the nuclear spin will determine the overall number of hyperfine lines, and the hyperfine patterns produced will be strongly dependent on the relative abundance of the $I \neq 0$ component. The effect of hyperfine coupling on an axial spectrum is shown in Figure 3.7. In Figure 3.7a an axial spectrum with $I = 0$ is shown, with $g_{\parallel} > g_{\perp}$. In Figure 3.7b, isotopic labelling with a nucleus $I = ½$ leads to splitting of the $g_{\parallel}$ and $g_{\perp}$ components into doublets; $g_{\parallel}$ is split by $A_{\parallel}$ and $g_{\perp}$ is split by $A_{\perp}$. In Figure 3.7c, a nucleus with $I = 5/2$ (for example, ^{17}O) splits the parallel and perpendicular components of the spectrum into 6 lines (number of lines = $2nI + 1$), separated by the hyperfine coupling constants $A_{\parallel}$ and $A_{\perp}$ respectively.

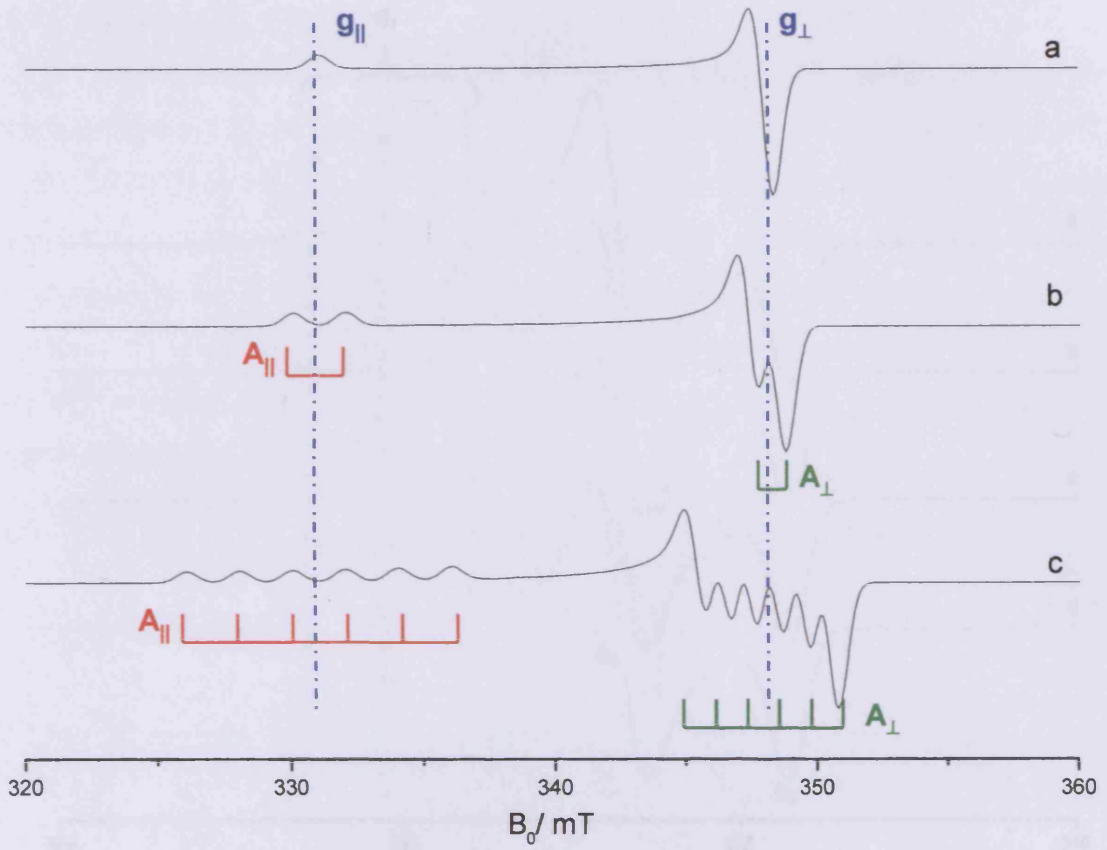

Figure 3.7 Effect of nuclear spin on an EPR species with axial symmetry. The value of I is (a) 0 (b) ½ and (c) 5/2. The g values remain constant in each of the spectra. $g_{\|}$ is split by $A_{\|}$, $g_{\perp}$ is split by $A_{\perp}$. The $A_{\|}$ and $A_{\perp}$values also remain constant.

This technique has been adopted several times throughout this thesis, see for example sections 6.3.1 and 6.3.4.

3.6.5 Spectral Simulation

Numerical methods are commonly used for EPR data acquisition, processing and evaluation. The spin Hamiltonian parameters obtained from the experimental data can be refined using computer simulation. Simulations lead to accurate values of the g and A tensors for each species contributing to the spectrum and can also provide information on their relative populations through peak deconvolution. For example, Figure 3.8a shows an orthorhombic spectrum with three signals in the g_1 component. Following in Figures 3.8b,c and d, are shown the individual orthorhombic signals which result in the spectrum shown in Figure 3.8a when added together in a linear combination.

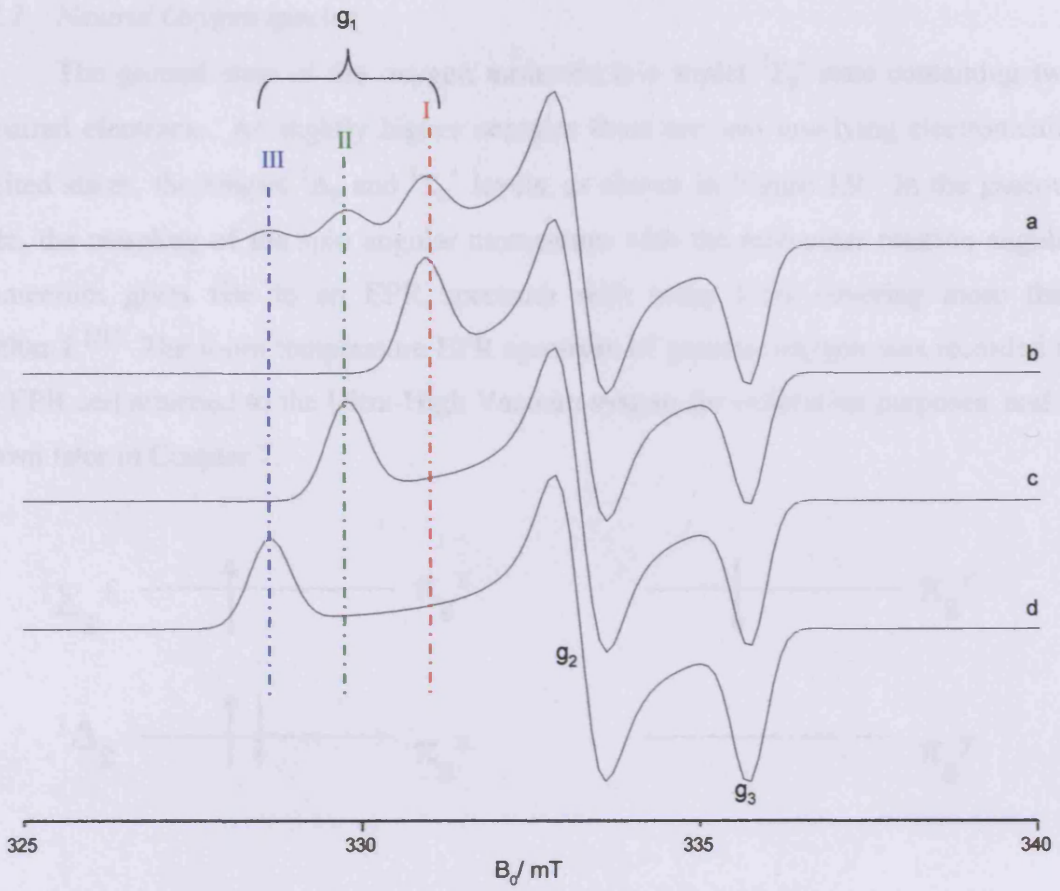

Figure 3.8 (a) Simulated EPR spectra of three superimposed orthorhombic signals (ratio 1:1:1) possessing equivalent g_1 and g_2 values, but different g_3 values. The individual (deconvoluted) signals from the three species are shown in (b), (c) and (d).

This approach has been used in Chapter 5 where the simulation software Sim32 has been used to simulate the experimental data.[19, 20]

3.7 Surface oxygen species

Throughout the course of this thesis, several surface oxygen species have been identified over the TiO_2 substrate (Chapters 5 and 6). Furthermore, a large number of potentially paramagnetic radicals can be generated during the photocatalytic process. Some of these radicals are known to be stable on the surface for several days at room temperature, while others are only detected at low temperature and decay on gentle annealing. Therefore, before presenting the experimental results on the oxygen based radicals observed later in the thesis, it if first necessary to present some of the basic background EPR theory to these radicals.

3.7.1 Neutral Oxygen species

The ground state of the oxygen molecule is a triplet $^3\Sigma_g^-$ state containing two unpaired electrons. At slightly higher energies there are two low-lying electronically excited states, the singlet $^1\Delta_g$ and $^1\Sigma_g^+$ levels, as shown in Figure 3.9. In the gaseous state, the coupling of the spin angular momentum with the molecular rotation angular momentum gives rise to an EPR spectrum with many lines covering more than 1,000mT.[21] The room temperature EPR spectrum of gaseous oxygen was recorded in the EPR cell attached to the Ultra-High Vacuum system for calibration purposes, and is shown later in Chapter 7.

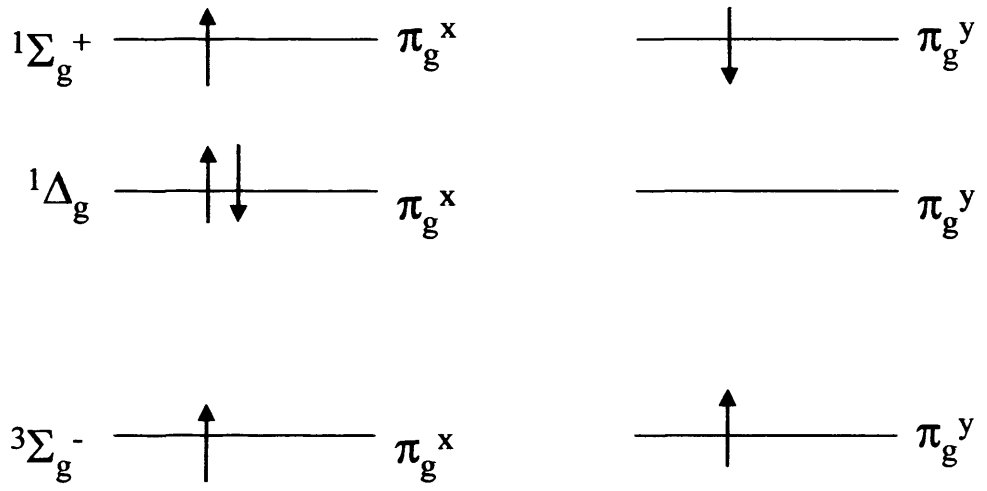

Figure 3.9 Ground state and excited state energy levels for O_2.

3.7.2 Superoxide, O_2^-, Ion

Several kinds of charged dioxygen species have been reported on surfaces, including O_2^+, O_2^-, O_2^{2-} and O_2^{3-}. All of these species are paramagnetic and should therefore give rise to an EPR signal. However, the only process that leads to a decrease of the energy of molecular oxygen is the formation of the free superoxide ion (O_2^-; -10.15kcal/mol).[22] The superoxide radical is generally described using an ionic model, in which electron transfer from the surface to the adsorbed oxygen takes place to form O_2^-; there is an electrostatic interaction between the cation at the adsorption site and the superoxide ion.[23] The unpaired electron lies in a π^* orbital which results in orthorhombic symmetry described by the g values g_{xx}, g_{yy} and g_{zz} where the z direction is along the internuclear axis of the superoxide radical and the y direction is perpendicular to the plane of the surface, as shown in Figure 3.10. In the ground state

the π_y^* and π_x^* antibonding orbitals are degenerate and no EPR signal can be resolved in the superoxide radical. It is only when the degeneracy of the two antibonding orbitals is removed, for example by an external perturbation such as an electric field, that an EPR signal can be resolved.

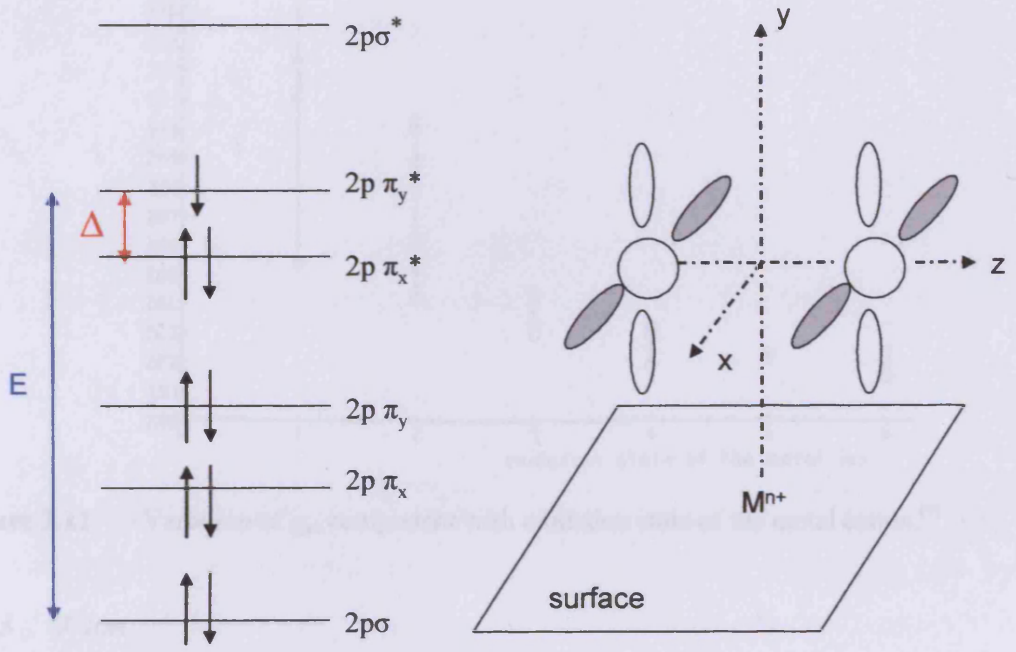

Figure 3.10 The energy level diagram for O_2^- in the ground state, and an illustration of the adsorption mode of O_2^- on a cationic surface site.

The g tensor of O_2^- has been derived for the case of superoxide impurities in the bulk of single crystal samples of alkali halides, thereby allowing the g values to be referred to as g_{xx}, g_{yy}, etc, (as opposed to g_1, g_2, etc).[24] Ignoring second order terms, the g tensor can be described by the following:

$$g_{xx} = g_e \qquad (3.23a)$$

$$g_{yy} = g_e + 2\lambda / E \qquad (3.23b)$$

$$g_{zz} = g_e + 2\lambda / \Delta, \qquad (3.23c)$$

where λ is the spin-orbit coupling constant of oxygen, E is the energy level separation between the σ_g^z and the highest occupied π^* orbital, and Δ is the energy separation between the two $2\pi^*$ antibonding orbitals due to the electric field. From these equations it can be seen that the g_{zz} component is most sensitive to the cationic field experienced by the adsorbed anion and can therefore be used as a probe of surface electrostatic interaction. For example, the magnitude of the g_{zz} component gives a measure of the

cation charge at the adsorption site (see Figure 3.11), and it can be used to establish the adsorption site in mixed metal oxide systems such as MoO_3/ Al_2O_3.

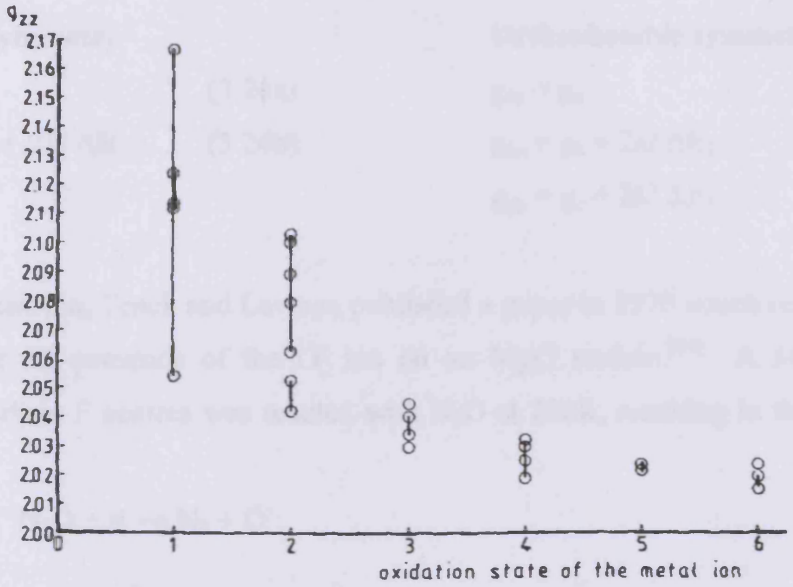

Figure 3.11 Variation of g_{zz} component with oxidation state of the metal cation.[9]

3.7.3 O^- Ion

During the early 1970's much work was carried out on the identification and characterization of oxygen radicals over metal oxide surfaces, and two detailed reviews by Che and Tench describe much of this early work in detail.[22,25] One surface oxygen radical that required several studies by different groups to satisfactorily characterize it was the O^- trapped hole species. The theoretical spectrum is dependent upon the relative energies of the O 2p orbitals, and two cases have been suggested for tetragonal and orthorhombic symmetry.

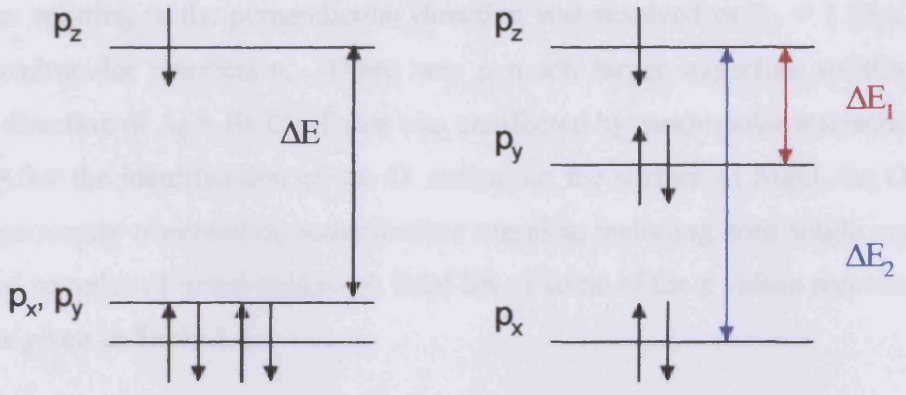

Figure 3.12 Energy level diagrams for the O^- ion in tetragonal and orthorhombic symmetry.

The energy level diagrams for the two cases are shown in Figure 3.12 and the principle g tensors are described as:

Tetragonal symmetry		**Orthorhombic symmetry**	
$g_{zz} \approx g_e$	(3.24a)	$g_{zz} \approx g_e$	(3.25a)
$g_{xx} = g_{yy} = g_e + 2\lambda/\Delta E$	(3.24b)	$g_{xx} = g_e + 2\lambda/\Delta E_2$	(3.25b)
		$g_{yy} = g_e + 2\lambda/\Delta E_1$	(3.25c)

For example, Tench and Lawson published a paper in 1970 which confirmed for the first time the presence of the O^- ion on an MgO surface.[26] A MgO sample containing surface F centres was reacted with N_2O at 298K, resulting in the following reaction:

$$N_2O + e^- \rightarrow N_2 + O^- \qquad (3.26)$$

The resulting EPR signal produced g values of $g_1 = 2.047$, $g_2 = 2.019$ and $g_3 = 2.002$.

Williamson *et al.*,[27] also reported the formation of the O^- radical on the surface of MgO by adsorption of N_2O at low temperatures onto a surface containing trapped electrons. The trapped electrons were formed by UV irradiation at low temperatures in the presence of hydrogen and the N_2O^- ion was subsequently formed on addition of N_2O. The N_2O^- ion is unstable on the surface and dissociates to form N_2 and O^- with the resulting O^- ion characterized by the axial g tensor of $g_\perp = 2.041$ and $g_\parallel = 2.0016$.

Wong and Lunsford[28] repeated the experiments of Williamson using ^{17}O-enriched molecular oxygen to gain information about the electronic structure of the ion from the hyperfine splittings. The EPR spectra of the O^- ion had a g tensor of $g_\perp = 2.042$ and $g_\parallel = 2.0013$, in good agreement with the results of Williamson *et al.*[27] The hyperfine splitting in the perpendicular direction was resolved as $A_\perp = 1.95$mT with a small quadrupolar interaction. There was a much larger hyperfine splitting in the parallel direction of $A_\parallel = 10.32$mT that was unaffected by quadrupolar interactions.

After the identification of the O^- radical on the surface of MgO, the O^- radical was subsequently observed on several other samples, including both single crystal and powdered samples of metal oxides. A brief list of some of the g values recorded for the radical is given in Table 3.3.

Table 3.3 Reported g values for the O^- radical in (bulk) and on (surface) various oxides.

	g_1	g_2	g_3	Reference
		Single crystals		
ZnO	2.0193	2.0193	2.0024	[29]
MgO	2.0385	2.0385	2.0032	[30]
	2.0386	2.0386	2.0033	[31]
KBr	2.226	2.226	1.987	[32]
		Powders or frozen solutions		
ZnO	2.021	2.021	2.0026	[33]
	(I) 2.021 (II) 2.023	(I) 2.021 (II) 2.023	2.003	[34]
MgO (Axial)	2.042	2.042	2.0013	[28]
MgO (Ortho)	2.0472	2.0193	2.0016	[35]
	2.0505	2.0297	2.0016	[35]

3.7.4 Ozonide, O_3^-, Ion

On subsequent exposure of the surface radical O^- to molecular oxygen at 298K, the O^- signal disappeared and was replaced with a new signal with g values of g_1 = 2.0147, g_2 = 2.0120 and g_3 = 2.0018, which was attributed to the ozonide, O_3^-, ion. Wong and Lunsford provided more details on the nature of the bonding in the O_3^- ion by introducing ^{17}O into the ozonide ion and gaining information from the hyperfine tensor.[36] The ^{17}O was introduced by first forming a $^{17}O^-$ ion and reacting this with $^{16}O_2$, or alternatively by adding a $^{16}O^{17}O$-N_2 mixture to the sample. On exposure of $^{17}O^-$ to $^{16}O_2$ a signal with the g values of g_1 = 2.0172, g_2 = 2.01 and g_3 = 2.0014 was observed. A hyperfine pattern composed of 6 lines centred around the g_3 component with a splitting of 2.6mT was observed. In the second experiment, when $^{16}O^-$ was reacted with ^{17}O-enriched molecular oxygen, the spectrum recorded was more complicated; three sets of 6 hyperfine lines were resolved centred around g_1 with the splittings 8.2mT, 6.5mT and 2.6mT. No splittings could be resolved in either of the other two principal directions for either experiment, suggesting that the coupling was less than ~0.5mT.[36]

The ozonide radical is known to decay to the superoxide radical if left at room temperature for a period of time. The ozonide radical prepared from $^{17}O^-$ and $^{16}O_2$ decayed to leave a superoxide radical with no trace of labelled ^{17}O, although there was a

hyperfine splitting of 7.7mT resolved for the superoxide radical formed on decay of the ozonide sample prepared from $^{16}O^-$ with $^{17}O_2$. From these results it was determined that the ozonide radical consists of three oxygen atoms in different environments on the surface, as depicted in Figure 3.13, in which O^a is originally the O^- ion. From the hyperfine splittings and the fact that there was no isotropic mixing on decay to the superoxide radical, Wong *et al.*,[36] concluded that the O^a-O^b bond breaks rather than the O^b-O^c bond.

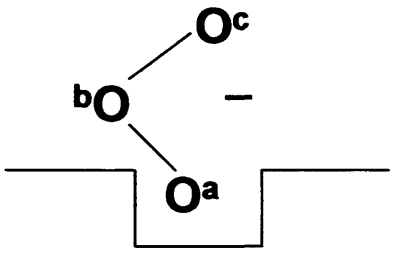

Figure 3.13 Schematic representation of the orientation of the ozonide radical on the surface of metal-oxides.

The O_3^- ion is a 19 electron radical, isoelectronic with AB_2^- type radicals such as SO_2^- that have been observed on surfaces. The correlation diagram for a 19 electron (and 17 electron) radical is shown in Figure 3.14. For radicals with sixteen or less valence electrons, the species can accommodate all of the electrons in bonding orbitals, resulting in a linear molecule (no strain from antibonding orbital occupation has to be relieved through bending of the molecule). When an extra electron is added to form a 17-electron species (such as O_2^-), it enters the $\bar{\pi}_u$ antibonding orbital. From Figure 3.14 it is seen that on bending of the molecule, the $\bar{\pi}_u$ orbital becomes increasingly built from s-orbital character, which lowers the energy of the molecule. A 19-electron species (such as O_3^-) contains an electron in the $2b_1$-orbital which only has a small dependency on bond angle.

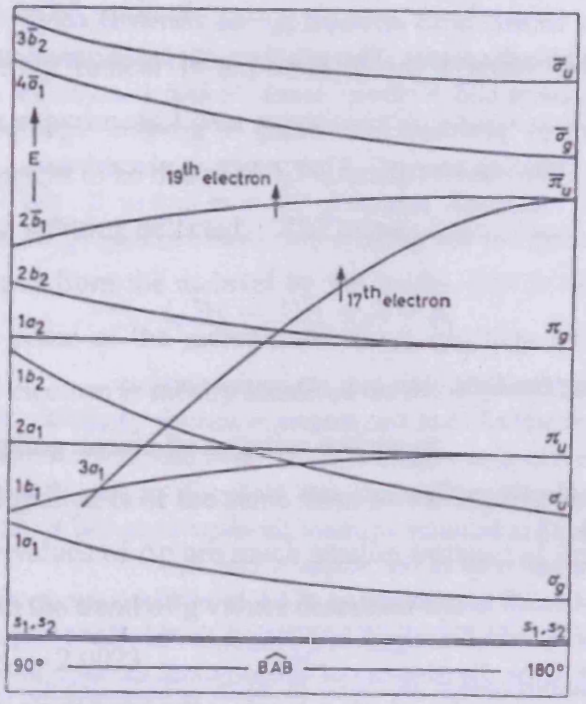

Figure 3.14 Correlation diagram for AB_2 type molecules.[13]

The rules derived by Walsh[13] state that occupation of a bonding molecule between the atoms favours a bent formation of the radical, therefore explaining the orientation of the ozonide radical as show in Figure 3.13. As seen, the energy levels of O_3^- ions are well separated and because they are not perturbed by the surface crystal field, the g tensor can be used to confirm the identity of the species.[37] The g values for the O_3^- species on different samples are listed in Table 3.4.

Table 3.4 g tensors for the O_3^- radical on various oxide surfaces.

Species	Principal Direction	g tensor	Reference
O_3^- on MgO (major site)	xx	2.002	[38]
	yy	2.0148	
	zz	2.0121	
O_3^- on MgO	xx	2.0014	[36]
	yy	2.0172	
	zz	2.0100	
O_3^- in $KClO_3$	xx	2.0035	[39]
	yy	2.0187	
	zz	2.0123	

3.7.5 Hydroperoxy, $HO_2^\bullet$, radical

The hydroperoxy radical is expected to be a more stable radical than the hydroxyl radical, but experimental data supporting its assignment is still under debate. Early EPR spectra thought to be due to $HO_2^\bullet$ radicals showed a broad asymmetric single line with no hyperfine splitting detected. The unpaired electron is expected to be in the π_x^* level, which is split from the π_y level by the proton (the x direction is taken to be perpendicular to the plane of the radical, and the z direction is taken along the O-O bond). The unpaired electron is mostly localised on the unprotonated oxygen, hence the proton hyperfine coupling should be negative and small.

The hydroxyl radical is of the same form as the superoxide radical discussed in section 3.7.2, but the values of Δg are much smaller because of the greater effect of the proton. This results in the trend of g values described by:

$$g_{zz} >> g_{yy} \sim g_{xx} \sim 2.0023 \qquad (3.27)$$

The g values from signals attributed to the hydroperoxy radical are listed in Table 3.5. The values of hyperfine splitting are more difficult to analyse because of the possibility that the g and A axes are not coincident.

Table 3.5 g values for the $HO_2^\bullet$ radical

Medium	**g tensor**				**Reference**
	g_{xx}	g_{yy}	g_{xx}	g_{av}	
H_2O_2 glass	2.0023	2.0065	2.0350	2.015	[13]
H_2O or H_2O_2	2.0085	2.0085	2.027	2.015	[13]

3.8 References

[1] J. R. Pilbrow, M.R. Lowrey, *Rep. Prog. Phys.*, **1980**, *43*, 433.

[2] D. Grucker, *Progress in Nuclear Magnetic Resonance Spectroscopy*, **2000**, *36(3)*, 241.

[3] (a) N. Chen, Y. Pan, J.A. Weil, *American Mineralogist*, **2002**, *87*, 37.

(b) N. Chen, Y. Pan, J.A. Weil, M.J. Nilges, *American Mineralogist*, **2002**, *87*, 47.

[4] E. Zavoisky, *J. Phys. U.S.S.R.*, **1945**, *9*, 211.

[5] J. Frenkel, *J. Phys. U.S.S.R.*, **1945**, *9*, 299.

[6] W. Gerlach, O.Stern, *Z. Phys.*, **1921**, *8*, 110.

[7] G. Breit, I.I. Rabi, *Phys. Rev.*, **1931**, *38*, 2082.

[8] A. Schweiger, G. Jeschke, *Principles of Pulse Electron Paramagnetic Resonance*, **2001**, *OUP*, Oxford.

[9] J.A. Weil, J.R. Bolton, J.E. Wertz, *Electron Paramagnetic Resonance: Elementary Theory and Practical Applications*, **1994**, *John Wiley and Sons*.

[10] F.E. Mabbs, D. Collison, *Electron Paramagnetic Resonance of d Transition Metal Compounds*, **1992**, *Elsevier*.

[11] J.R. Pilbrow, *Transition Ion Electron Paramagnetic Resonance*, **1990**, *Laredon Press*, Oxford.

[12] N.M. Atherton, *Electron Spin Resonance: Theory and Applications*, **1973**, *Wiley*, Chichester.

[13] P.W. Atkins, M.C.R. Symons, *The Structure of Inorganic Radicals*, **1967**, *Elsevier*, Amsterdam.

[14] M. Che, E. Giamello, in 'Spectroscopic Characterisation of Heterogeneous Catalysts' Part B, *Stud. Surf. Sci. Catal.*, **1987**, *57*, B265.

[15] J.H. Lunsford, *Adv. Catal.*, **1972**, *22*, 265.

[16] W. Gerlach, O. Stern, *Ann. d. Physik*, **1924**, *74*, 673.

[17] Heisenberg, W. (1927) 'Ueber den anschaulichen Inhalt der quantentheoretischen Kinematik and Mechanik' *Zeitschrift für Physik* **43** 172-198. English translation in (Wheeler and Zurek, 1983), pp. 62-84.

[18] C.A. Jenkins, D.M. Murphy, *J. Phys. Chem. B*, **1999**, *103*, 1019.

[19] T. Spalek, P. Pietrzyk, Z. Sojka, *J. Chem. Inf. Model.*, **2005**, *45*, 18.

[20] A. Adamski, T. Spalek, Z. Sojka, *Res. Chem. Intermed.*, **2003**, *29*, 793.

[21] M. Tinkham, M.W.P. Strandberg, *Phys. Rev.*, **1955**, *97*, 951.

[22] M. Che, A.J. Tench, *Adv. Catal.*, **1983**, *32*, 1.

[23] A.L. Linsebigler, G. Lu, J. T. Yates, *Chem. Rev.*, **1995**, *95*, 735.

[24] W. Kanzig, M.H. Cohen, *Phys. Rev. Lett.*, **1959**, *3*, 509.

[25] M. Che, A.J. Tench, *Adv. Catal.*, **1982**, *31*, 77.

[26] A.J. Tench, T. Lawson, *Chem. Phys. Lett.*, **1970**, *7*, 459.

[27] W.B. Williamson, J.H. Lunsford, C. Naccache, *Chem. Phys. Lett.*, **1971**, *9*, 33.

[28] N-B Wong, J.H. Lunsford, *J. Chem. Phys.*, **1971**, *55*, 3007.

[29] D. Gallad, A. Herve, *Phys. Lett. A*, **1970**, *33*, 1.

[30] J.E. Wertz, P. Auzins, J.H.E Griffiths, J.W. Orton, *Disc. Faraday Soc.*, **1959**, *28*, 136.

[31] W.P. Unruh, Y. Chen, M.M Abraham, *Phys. Rev. Lett.*, **1973**, *30*, 466.

[32] W. Sander, *Z. Phys.*, **1962**, *169*, 353.

[33] N. Wong, Y.B. Taarit, J.H. Lunsford, *J. Phys. Chem.*, **1974**, *60*, 2148.

[34] A.M Volodin, A.E. Cherkashin, *Kinet. Katal.*, **1982**, *22*, 598.

[35] A.J. Tench, T. Lawson, J.F.J Kibblewhite, *J. Chem. Soc. Faraday Trans.*, **1972**, *68*, 1169.

[36] N-B Wong, J.H. Lunsford, *J. Chem. Phys.*, **1972**, *56*, 2664.

[37] M. Che, in "*Magnetic Resonance in Colloid and Interface Science*", **1980**, *Reidel*, Dordrecht.

[38] A.J. Tench, *J. Chem. Soc. Faraday Trans. I*, **1972**, *68*, 1181.

[39] S. Schlick, *J. Chem. Phys.*, **1972**, *56*, 654.

[40] K.U. Ingold, J.R. Morton, *J. Am. Chem. Soc.*, **1964**, *86*, 3400.

Chapter 4

Experimental Details

4.1 Introduction

In this chapter details will be given on the materials used throughout the course of this thesis. The physical and chemical properties, the origin of the materials, and sample preparation treatments will be discussed. Furthermore, the spectrometers used to characterize the radicals identified will also be described.

4.2 TiO_2 Samples

Three polycrystalline samples of TiO_2 were used during the course of this thesis. Most of the experiments presented have been performed on the mixed phase P25 powder (~80% anatase, 20% rutile) supplied by Degussa, which has a surface area of approximately $49m^2g^{-1}$. Additional results were also obtained from a pure phase anatase sample and a rutile sample, referred to as Rutile A. This sample was synthesised by hydrolysis of an aqueous solution of $TiCl_4$ and has a surface area of $\sim135m^2g^{-1}$. The pure phase anatase and Rutile A samples were kindly supplied by Dr T.A Egerton (Newcastle University).

4.3 Single crystals

Table 4.1 lists the single crystal oxide samples which were purchased to be studied during the course of this thesis. Note that all of the TiO_2 samples were of the rutile phase, as single crystal samples of the anatase phase are not readily available. The sample treatment conditions for the single crystals are not mentioned here, but are discussed in more detail in Chapter 7.

Table 4.1 Single crystal samples of metal oxide.

Metal Oxide	Crystal Face		
TiO_2	(100)K(001)	(001)K(100)	(110)K(001)
MgO	(100)K(001)	(110)K(110)	(111)K(110)

Unfortunately, the crystals were found to contain high levels of paramagnetic impurity ions giving rise to strong and well resolved EPR signals. The TiO_2 crystals contained chromium ions which exhibited EPR signals over the magnetic field range

from 50–650mT as shown in the angular resolved investigation of a $TiO_2(110)$ sample in Figure 4.1a. The MgO crystals purchased were found to contain high levels of Mn^{2+} ions which resulted in a sextet hyperfine pattern centered around the free spin value, g = 2.0023. Similarly an angular resolved study of an MgO(111) crystal was performed and is shown in Figure 4.1b.

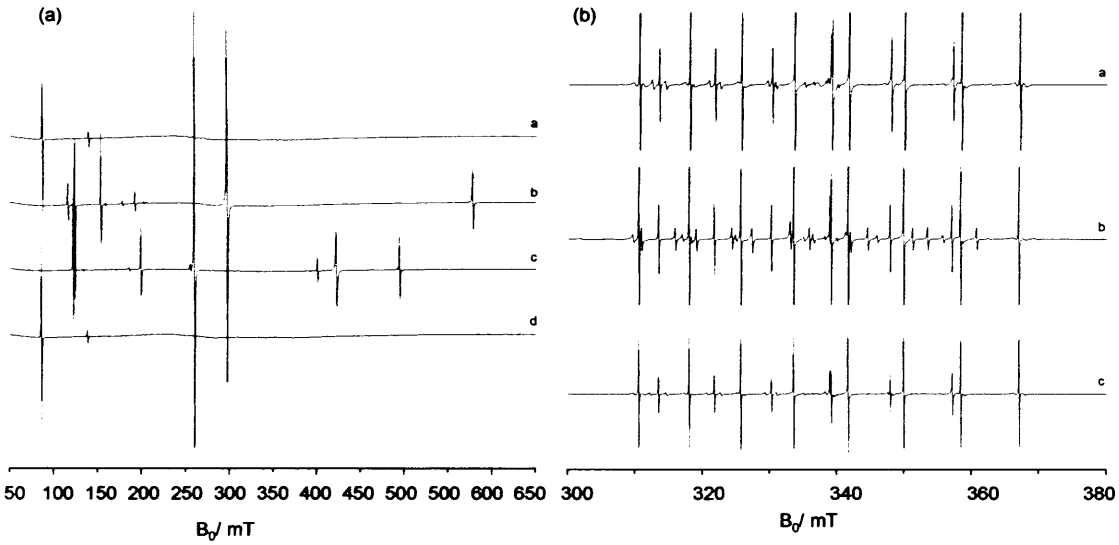

Figure 4.1 An angle resolved study of (a) the chromium impurity cations in $TiO_2(110)$ and (b) the Mn^{2+} impurity cations in MgO(111).

For the sensitivity studies performed on the UHV-EPR spectrometer discussed in Chapter 7, a series of quartz plates were used as a substrate. The plates were synthetic quartz with an epi-polish on both faces, and measured 10×10×1mm in order to maintain the same cavity filling factor as achieved during the single crystal investigations.

4.4 Methods

4.4.1 Vacuum Line

The powder TiO_2 samples were treated on the vacuum line shown in Figure 4.3. The line is constructed using 12mm bore Pyrex glass, with greased taps isolating different parts of the line. The line was connected to an Alcatel C1 series rotary vane pump and an Alcatel ATP 80/100 diffusion pump which combine to achieve base pressures of 10^{-5} Torr. Pressure measurements were made with an Alcatel ACS 100 pirani gauge. The powder samples were heated using a thermostatically controlled electric furnace, able to maintain temperatures between 323 and 1073K. The samples were heated in the bulb section of an EPR cell and then transferred to the capillary

quartz section for placement in the cavity. Gases could be added to the line from the gas reservoir and mixed in the line before exposure to the sample in the EPR cell.

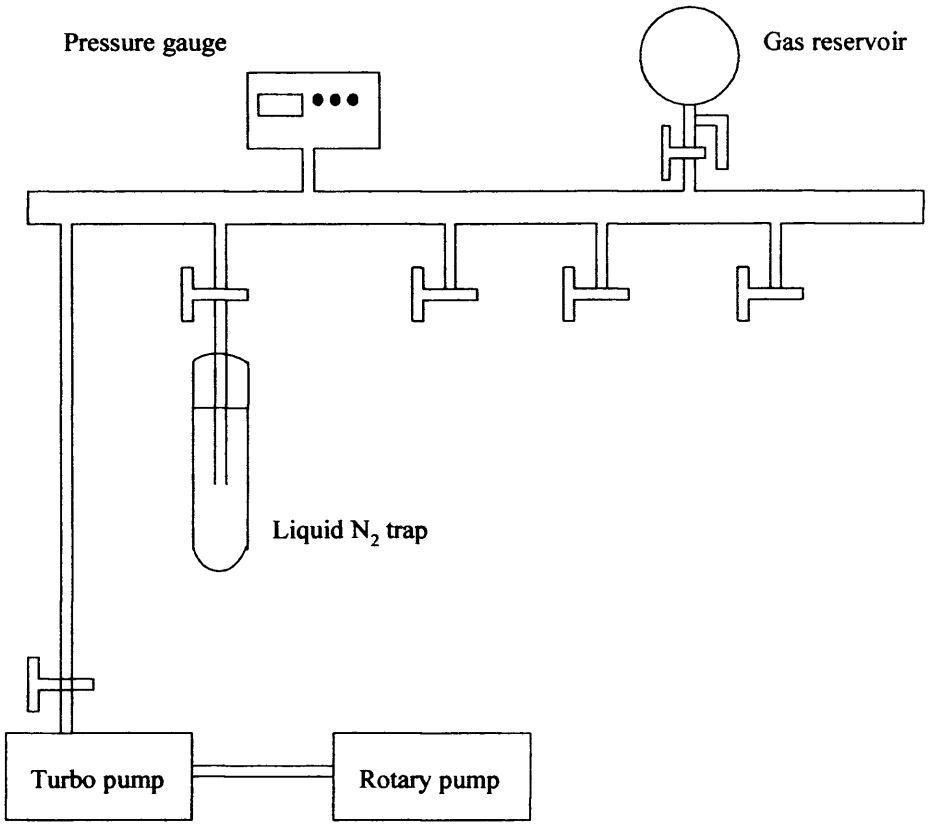

Figure 4.3 Schematic illustration of the vacuum manifold used to prepare powder samples.

4.4.2 Ultra Violet Lamp

An *Oriel Instruments UV lamp* (model n°. 66021) was used for all irradiations. The power output from the lamp could be varied between 50 and 1000W. The Hg/Xe arc lamp used has a broad band spectral output from 250nm to 2500nm; the UV output below 280nm accounts for only 4–5% of the total lamp output. In all experiments a water filter was used in order to absorb infrared frequencies and prevent sample heating by the UV beam.

Samples were treated on the vacuum line before irradiation *ex-situ* at 77K under static vacuum conditions or under small pressures of probe gases. Following irradiation the samples were rapidly transferred to the pre-cooled cavity.

4.5 Characterization

The EPR spectra reported in Chapters 5 and 6 were recorded on an X-band *Bruker EMX* spectrometer operating at 100 kHz field modulation, 10 mW microwave

power and fitted with a high sensitivity cavity (ER 4119HS). The spectrometer is equipped with a variable temperature unit to allow measurements to be performed at temperatures ranging from 120K to 298K. The g values were determined using a DPPH standard, and are accurate to ±0.001. EPR computer simulations were performed using the SimEPR32 program.

Supplemental *cw*-ENDOR measurements (Electron Nuclear DOuble Resonance) reported in Chapter 6 were also performed on a *Bruker ESP300E* series spectrometer operating at 12.5kHz field modulation and equipped with an ESP360 DICE ENDOR unit in an EN-801 ENDOR cavity. The ENDOR spectra were recorded at 10K, using 8 dB RF power from an ENI A-300 RF amplifier, 251 kHz RF modulation depth and 10 mW microwave power.

The EPR spectra of the single crystal samples were recorded on a modified X-band *Bruker EMX* spectrometer, which will be discussed in more detail in Chapter 7.

4.6 Sample Preparation

4.6.1 Reduced TiO_2

The polycrystalline TiO_2 powders (*ca.* 10 mg) were heated at 400K overnight under dynamic vacuum (10^{-4} Torr) in an EPR cell, before slowly ramping the temperature up to a final maximum temperature of 773K over a 5 hour period. The samples were then held at this temperature for a further 1 hour. This treatment results in a non-stoichiometric sample which is blue in colour, due to the excess numbers of Ti^{3+} cations present, and is hereafter referred to as a *reduced* sample.

4.6.2 Activated TiO_2

A reduced sample of polycrystalline TiO_2 is prepared as described above. Following formation of the blue powder, the sample was exposed to excess oxygen (50 Torr) at 773K. The sample was held at this temperature for 30 minutes before it was cooled under the oxygen atmosphere. The residual oxygen was subsequently evacuated at room temperature. This treatment produces a clean oxidised surface, almost completely free of any surface hydroxyl groups. Oxygen exposure at 773K results in the formation of diamagnetic surface O^{2-} lattice anions, and therefore produces a clean, reoxidised stoichiometric surface; hereafter this sample is referred to as the *activated* sample. The stoichiometry was confirmed by recording the EPR spectrum of the activated sample, which did not display any paramagnetic signal.

4.6.3 Addition of probe molecules

Oxygen was admitted to the vacuum line from the gas reservoir, shown above in Figure 4.3. The oxygen could then be exposed to the sample at various temperatures. For exposure at elevated temperatures, the sample was positioned inside the furnace before opening the EPR cell to the vacuum line. For several experiments (see chapter 5) oxygen was admitted to the sample at 77K. This was achieved by holding the sample in liquid nitrogen whilst gas was admitted from the vacuum manifold. Further, in the experiments detailed in section 5.3.4 oxygen was added to the samples at 130K. During these experiments the sample was positioned inside the cavity and brought to the required temperature using the variable temperature unit. The small quantity of oxygen was subsequently admitted to the sample from a small trap attached to the EPR sample tube, shown in Figure 4.4. The samples were run under the oxygen atmosphere and subsequently after evacuation of the excess oxygen at 298K.

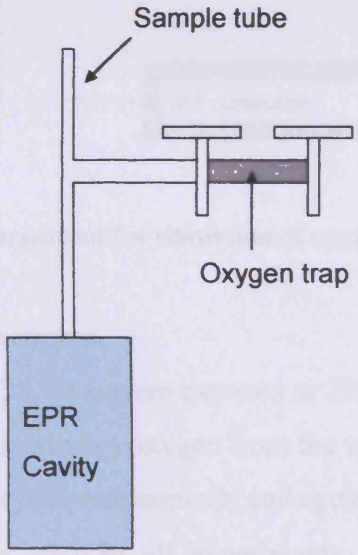

Figure 4.4 Trap for admission of oxygen to samples at 130K.

As many of the species studied during this thesis are unstable at room temperature, it was sometimes necessary to evacuate the excess oxygen at low temperatures to prevent decay of the paramagnetic species and loss of the EPR signal (Chapter 5). However, oxygen evacuation at 77K is ineffective, resulting in residual oxygen signals in the EPR spectrum and a broadening of the paramagnetic lines of interest. Therefore, during the investigation of thermally unstable radicals, the oxygen was admitted and evacuated at low temperature. For these studies the variable temperature system was used to achieve the required temperature whilst the sample was

attached to the vacuum manifold, as shown diagrammatically in Figure 4.5. Hence, oxygen could be admitted (evacuated) to (from) the sample at any temperature in the region 130–260K. The samples were then removed from the vacuum line and held in liquid nitrogen before rapid transfer to a pre-cooled cavity.

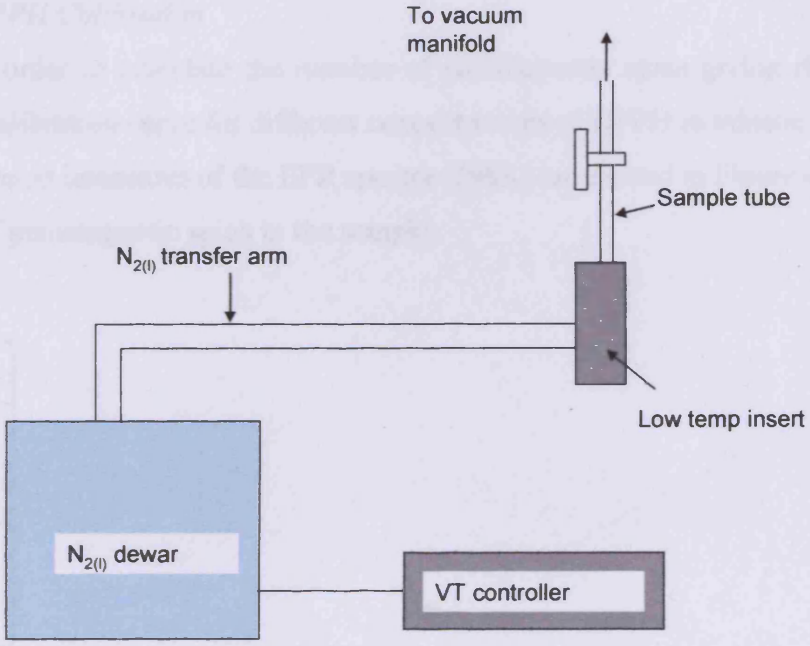

Figure 4.5 Experimental arrangement for admission of oxygen at low temperature.

4.6.4 Addition of ketone:O_2 mixtures

Activated samples of P25 TiO_2 were exposed at 298K to the following selection of ketones (in gaseous state) mixed with oxygen from the vacuum manifold; acetone:O_2, butanone:O_2, 4-heptanone:O_2, cyclopentanone:O_2 and cyclohexanone:O_2. The ketone to O_2 ratio (i.e., ketone:O_2) was ~5:1 in all experiments. The final pressure of gas admitted to the EPR cell was dependent on the room temperature vapour pressures of the particular ketone (acetone:O_2 = 180 Torr final pressure; butanone:O_2 = 70 Torr; 4-heptanone:O_2 = 11 Torr; cyclopentanone:O_2 = 13 Torr; cyclohexanone:O_2 = 18 Torr). Small volumes of the ketone were held in the bulb section of an EPR cell and were purified *via* the freeze-pump-thaw technique before expansion into the vacuum manifold. For the ketones with low vapour pressure at room temperature, the ketones were held in water baths of elevated temperatures to achieve the required vapour pressure before admission to the vacuum manifold. The vacuum manifold itself was warmed during this procedure to prevent condensation of the ketones onto the walls of

the pyrex. In all cases, the ketone pressure was in excess over oxygen during the photolysis experiments. The samples containing the co-adsorbed gases were then irradiated at 77K for a period of 30 minutes before rapid transfer to the pre-cooled EPR cavity, where the spectra were recorded at 120K.

4.6.5 DPPH Calibration

In order to calculate the number of paramagnetic spins giving rise to an EPR signal, a calibration curve for different concentrations of DPPH in toluene was recorded. The integrated intensities of the EPR spectra (298K) are plotted in Figure 4.6 against the number of paramagnetic spins in the sample.

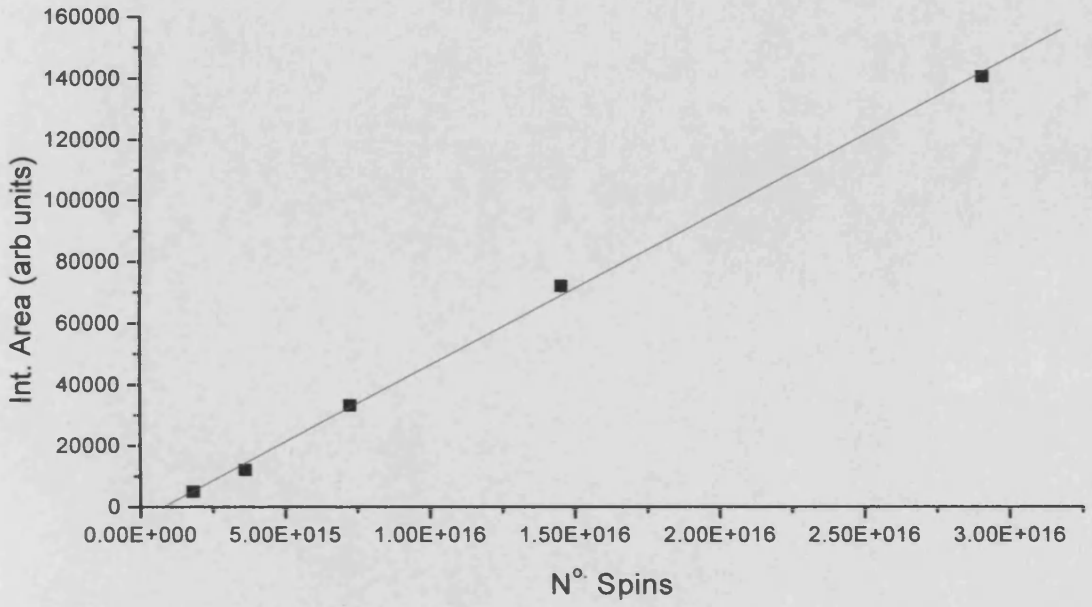

Figure 5.19 Integrated intensity of DPPH radical (solution in toluene).

4.7 Chemical suppliers

All gases used throughout this thesis were supplied by *BOC Ltd.* and were of purities individually stated in the text. The ^{17}O-labelled dioxygen gas (63% enrichment) was supplied by *Icon Services Inc.* (New Jersey) and was used without further purification. The ketones used were analytical grade supplied by *Aldrich Chemicals Ltd.* and were distilled prior to use.

The single crystal samples of TiO_2 and MgO were purchased from *PI-Kem Advanced Materials*. The two pieces of sapphire rod during the UHV investigation (see Chapter 7) were also purchased from *PI-KEM Advanced Materials*. The epi-polished quartz crystals used as substrates in Chapter 7 were supplied by *Robson Scientific*.

Chapter 5

Stabilisation of O_2^- Radicals at Oxygen Vacancy Defects on Polycrystalline TiO_2

5.1 Introduction

The photocatalytic activity of semiconductor metal oxides such as titanium dioxide (TiO_2) is of considerable interest because of its potential use in a wide range of applications such as sterilization,[1] solar energy conversion[2] and pollution control.[3] On absorption of a photon with energy equal to or greater than the band gap of the semiconductor, an electron/hole pair is generated in the bulk. These charge carriers migrate towards the catalyst surface where they can participate in redox reactions with adsorbed molecules. While the bulk properties of TiO_2 such as its band gap are clearly related to its catalytic activity, the surface properties are equally important in electron and hole mediated transfer processes.

There are several different formulations of TiO_2 that are readily available as catalysts. In particular, Degussa P25, which is a mixed-phase TiO_2 (~80/20 anatase/ rutile) is reported in several instances[4,5] to have an increased photocatalytic activity compared to the pure-phase materials. The morphology at the interface of the mixed-phase catalyst is still largely undetermined, although several bulk methods have been used in an attempt to characterize the average properties of the TiO_2 samples. The nature of the surface oxygen species formed on metal oxides is dependent on surface morphology. It was of interest to explore if EPR could be used to detect any anisotropic differences in the surface properties of the anatase and rutile polymorphs of TiO_2 and to identify the speciation of oxygen centred radicals on the TiO_2 surface.

In particular the nature of oxygen anion vacancy defect sites is of great interest as it is widely accepted that these sites largely control the surface chemistry of TiO_2. For example, in their study of the photo-oxidation of CH_3Cl over TiO_2(110), Lu *et al.*,[6] demonstrated that the photocatalytic sites responsible for the reaction were only present on the vacuum annealed surface possessing surface oxygen vacancies. Numerous further studies[7,8] have appeared in the literature describing how CO_2 can be used as a probe molecule on vacuum annealed single crystals to quantify the effects of oxygen defects. Henderson *et al.*,[9] used TPD to study the adsorption of CO_2 onto the vacuum annealed TiO_2(110) surface. Their data suggested that CO_2 preferentially adsorbs non-dissociatively onto the vacancy sites and then at five-coordinate Ti^{4+} sites. On exposure

of molecular oxygen to a surface with CO_2 adsorbed only in the vacancy sites does not lead to displacement of the CO_2 from the vacancy. Further, on heating the sample to desorb the CO_2 from the vacancy sites, the adsorbed O_2 does not move into the vacancy sites to re-oxidise the surface.

The vast majority of work in this field has however been confined to well defined single crystal surfaces. While vacancy defects are widely implicated as reactive centres in polycrystalline materials, their direct characterisation on powders has proven to be extremely difficult. In this chapter, the superoxide radical anion has been used to indirectly probe the morphology of the TiO_2 polycrystalline surface. In particular multiple adsorption sites for the anion can be identified by analysis of the orthorhombic O_2^- signal. The presence of multiple stabilisation sites is furthermore confirmed through the use of isotopically enriched $^{17}O_2$ which resolves three different A tensors for this species. This approach has previously been used to determine the hyperfine pattern arising from O_2^- on MgO[10] and further to resolve the complete A tensor of this species.[11] Among the many surface sites available for O_2^- stabilisation on TiO_2, one site in particular is unusual in terms of the stability and reactivity of the radical compared to the other sites. As will be discussed in this chapter, this site can be assigned to an oxygen vacancy. This study therefore represents the first ever identification of an O_2^- anion stabilised at an oxygen vacancy defect on polycrystalline TiO_2, and furthermore evidences the unusual reactivity displayed by the radicals when stabilised at these vacancies.

5.2 Experimental

Three samples of TiO_2 were used in the work described in this chapter, namely mixed phase P25 (largely anatase phase), a pure phase anatase sample and a high surface area rutile material, hereafter labelled Rutile A. Full experimental details have been previously given in chapter 4. However, to briefly recap the key steps in the sample preparation, *reduced samples* were prepared *via* thermal annealing to elevated temperatures under dynamic vacuum. *Activated samples* were prepared by the addition of an excess of molecular oxygen at 773K to a thermally reduced sample, followed by evacuation of the cell at room temperature. Oxygen (10 Torr) was subsequently added to the thermally *reduced samples* at a specified temperature ranging from 77K to 298K, leading to the formation of a well resolved superoxide signal. Alternatively, oxygen was added directly to the activated sample at 298K followed by UV irradiation at 77K

for 30 minutes. This treatment also results in the formation of a well resolved superoxide signal.

5.3 Results

5.3.1 Heterogeneity of Surface O_2^- Anions

Two samples of TiO_2 (P25 TiO_2) were annealed under vacuum at 573K and 723K. This treatment results in the formation of a blue coloured sample and the corresponding EPR signals shown in Figure 5.1. Both of these spectra can be regarded as composite signals arising from the presence of both bulk and surface Ti^{3+} cations, formed during thermal reduction. The EPR characteristics of these Ti^{3+} centres in TiO_2 P25 have been described elsewhere in the literature[12-14], and will not therefore be considered in detail here. The most important point of relevance to the current study is that more reduced Ti^{3+} cations are generated at the higher reduction temperatures (compare Figure 5.1a to 5.1b) as expected. At lower reduction temperatures, the Ti^{3+} signal is better resolved, and features associated with bulk ($g_\perp$ = 1.990, $g_\parallel$ = 1.957) and surface (g= 1.930)[15,16] Ti^{3+} can be clearly identified. At higher reduction temperatures, an additional isotropic signal is also seen. The isotropic signal indicates the presence of an unpaired electron located in a spherically symmetrical environment, and it has been previously assigned to medium polarised conduction electrons.[17,18] These electrons do not react with surface adsorbates, and therefore will not be considered in any further detail.

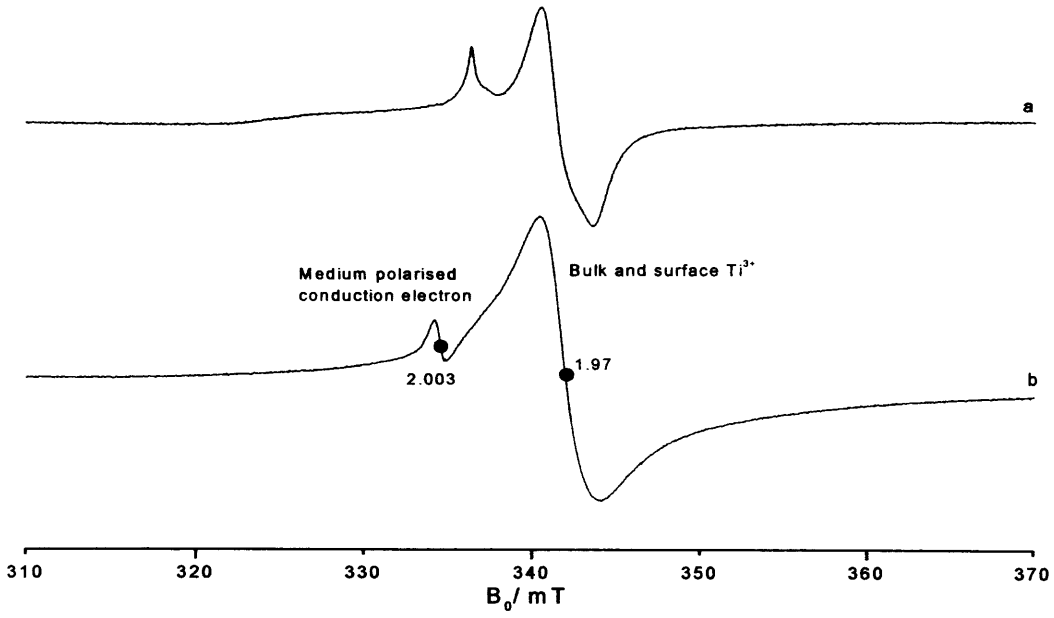

Figure 5.1 *cw*-EPR spectra [130K] of P25 TiO_2 after thermal reduction to (a) 573K and (b) 723K.

Upon exposure of $^{16}O_2$ at 298K to the above reduced samples, the EPR signals due to the reduced Ti^{3+} cations disappear immediately, and simultaneously a new EPR signal shown in Figure 5.2 appears. At the lower reduction temperature, an orthorhombic EPR signal with the g values g_{xx} = 2.005, g_{yy} = 2.01 and g_{zz} = 2.019 is observed, which can be easily and confidently assigned to the superoxide radical, O_2^-.[19] At the higher reduction temperatures, a more complex superoxide signal is formed, characterised by a well defined distribution of peaks in the g_{zz} region; notably g_{zz} = 2.019 (hereafter labelled site I), g_{zz}(site II) = 2.023 and g_{zz}(site III) = 2.026. This distribution of peaks in the g_{zz} region indicates that multiple sites are available for stabilisation of the superoxide radical on the more reduced surface.

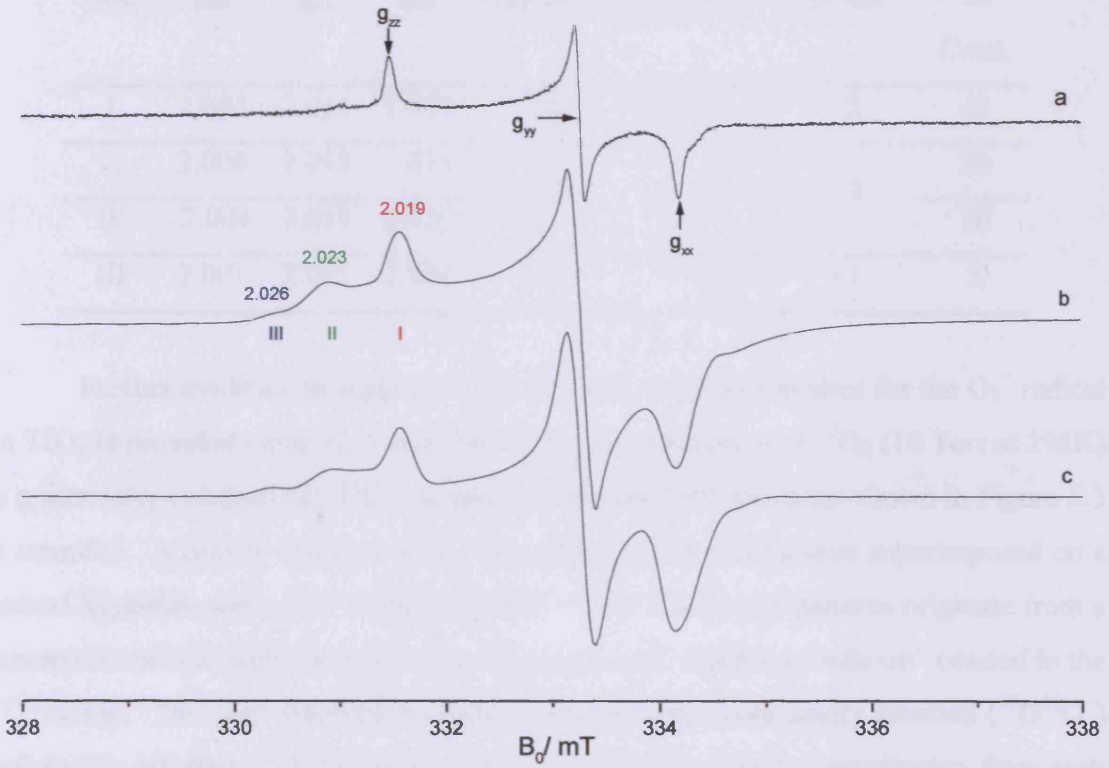

Figure 5.2 *cw*-EPR spectra [130K] of the superoxide radical on a P25 TiO_2 sample after thermal reduction at (a) 598K, (b) 723K and (c) simulation of experimental spectrum (b).

The complete set of g values for the superoxide radicals stabilised at the different sites (I, II and III) are listed in Table 5.1. It must be noted that while all three species share a common g_{yy} value of 2.011, each species possesses a slightly different g_{xx} value. For example, it is clear from Figure 5.2a that only one O_2^- species (I) exists with the well defined g values given in Table 5.1. As species II and III begin to emerge (Figure 5.2b) a broadening of the high field component of the g_{xx} peak can be observed, indicating slightly lower g_{xx} values for sites II and III. These g values were confirmed

by computer simulation (Figure 5.2c). Furthermore, the experimental spectrum was successfully simulated using the percentage contributions shown in Table 5.1. It is interesting to note, that a fourth (poorly resolved) superoxide species, labelled II′, is also present on the surface with g values intermediate between those of sites I and II. Clearly a number of stabilisation sites are available for the O_2^- anion on the TiO_2 P25 surface. However, for simplicity of discussion, these sites will hereafter be broadly classified into two main groups; site I and sites II–III.

Table 5.1 The g and A values for the various O_2^- radicals at different stabilisation sites on the P25 TiO_2 surface.

Site	g_{xx}	g_{yy}	g_{zz}	A_{xx}/ mT	A_{yy}/ mT	A_{zz}/ mT	% Cont.
I	2.005	2.011	2.019	7.64	<1	<1	43
II	2.004	2.011	2.023	7.86	<1	<1	36
II′	2.004	2.011	2.020				16
III	2.001	2.011	2.026	7.97	<1	<1	5

Further evidence in support of the different stabilisation sites for the O_2^- radical on TiO_2 is provided using 63% enriched $^{17}O_2$. On adsorption of $^{17}O_2$ (10 Torr at 298K) to a thermally reduced P25 TiO_2 sample (723K), the EPR spectrum shown in Figure 5.3 is recorded. A clearly resolved sextet hyperfine pattern can be seen superimposed on a second hyperfine pattern of 11 lines [I(^{17}O) = 5/2]. These two patterns originate from a superoxide radical with two equivalent oxygen nuclei which are "side-on" bonded to the Ti^{4+} cation. The two observed hyperfine patterns arise from singly labelled ($^{17}O^{16}O^-$) and doubly labelled ($^{17}O^{17}O^-$) ions respectively.[10] The relative contribution from each isotopomer can be calculated from $P^{16\text{-}16} = (1\text{-}p)^2$, $P^{16\text{-}17} = 2p(1\text{-}p)$ and $P^{17\text{-}17} = p^2$, where p is the level of ^{17}O-enrichment.[11] For a 63% enrichment of $^{17}O_2$ this gives $P(^{16}O_2)$ = 0.1369, $P(^{17}O^{16}O)$ = 0.4662 and $P(^{17}O_2)$ = 0.3969.

Further analysis of this spectrum on the m_I = -5, -4, -3 lines of the 11 line $(^{17}O^{17}O)^-$ pattern highlights additional structure, shown in the inset of Figure 5.3. The heterogeneity of O_2^- species is so well resolved that at least three well resolved ^{17}O A_x components in the hyperfine tensor of $^{17}O_2^-$ can be measured, and these are listed in Table 5.1. From simulations (Figure 5.3), the smallest ^{17}O A_{xx} value of 7.64mT has been assigned to the site I O_2^- species, while the largest ^{17}O A_{xx} value of 7.97mT has

been assigned to the site III O_2^- species based on the relative abundances used in the $^{16}O_2^-$ simulations. The intermediate ^{17}O A_{xx} value of 7.86mT must therefore be associated with sites II/ II'.

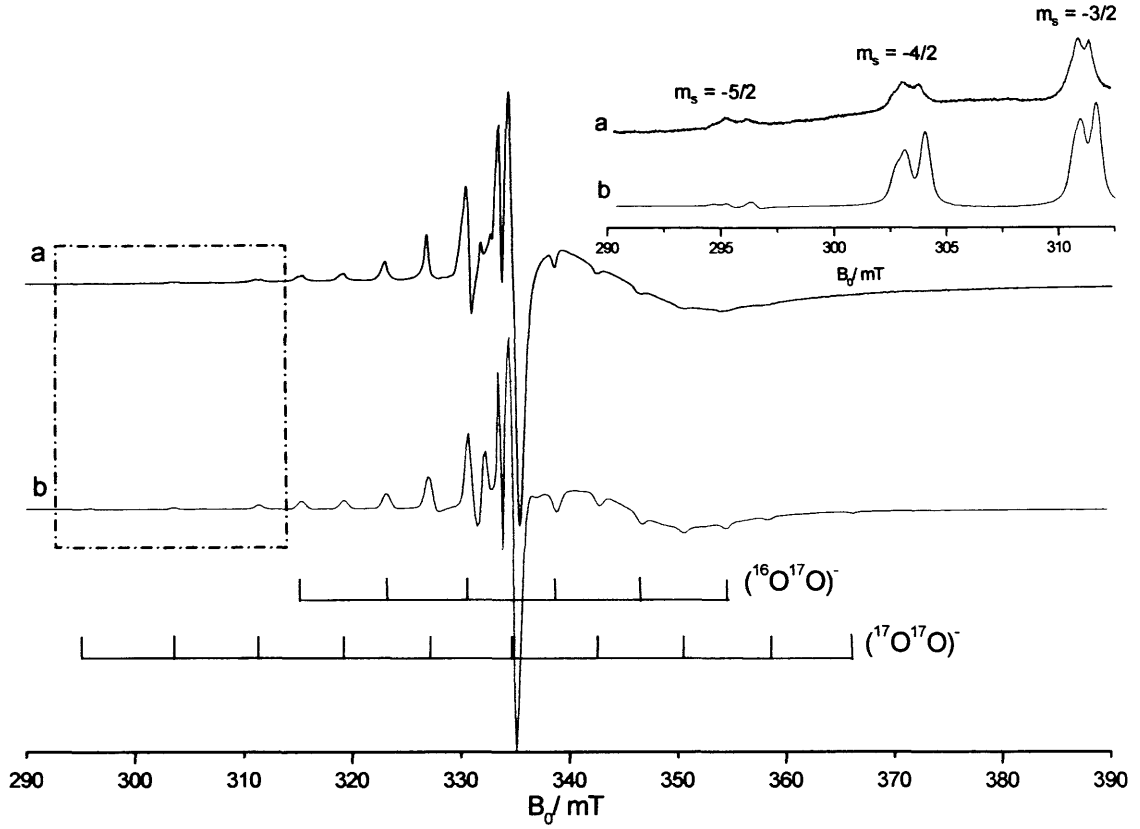

Figure 5.3 (a) Experimental [120K] and (b) simulated *cw*-EPR spectra of superoxide radicals formed by $^{17}O_2$ exposure at 298K to a thermally reduced P25 sample. The inset highlights the differences in the A_{xx} hyperfine splitting constants.

5.3.2 Thermal and photostability of surface O_2^- anions

Following formation and stabilisation of the superoxide radicals on a thermally reduced (723K) surface, the sample was gently annealed to slightly elevated temperatures (313–353K) under a dynamic vacuum of *ca.* 10^{-4} Torr. It can be clearly seen in Figure 5.4 that a preferential decay of the site I superoxide radicals, characterized by g_{zz} = 2.019, occurs during this annealing step. In the temperature regime studied here no decrease in intensity of the signals at sites II–III occurs. Correspondingly the overall integrated intensity of the superoxide spectrum decreases after each annealing step, but only by an amount which approximately equates to loss of the site I superoxide species. This result clearly demonstrates the difference in thermal stability of the site I superoxide species compared to the remaining species.

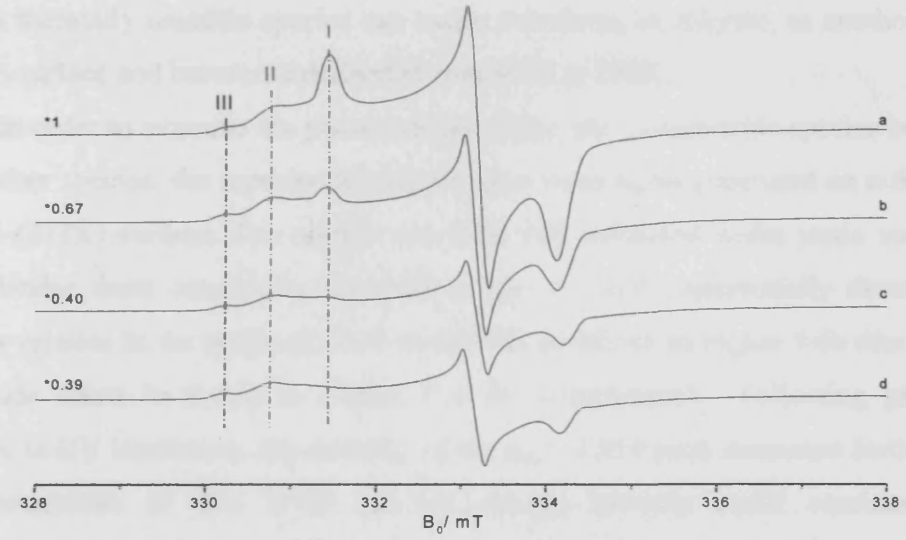

Figure 5.4 *cw*-EPR spectra [130K] of the superoxide anion on P25 TiO_2 sample after annealing to (a) 298K, (b) 313K, (c) 333K and (d) 353K. Relative intensities of the signals are given by the numbers on the left hand side.

This result was also confirmed simply by leaving the sample to stand for several days at room temperature under vacuum. The resulting series of spectra recorded for the freshly prepared sample, and after 'ageing' for 24 and 48 hours, are shown in Figure 5.5.

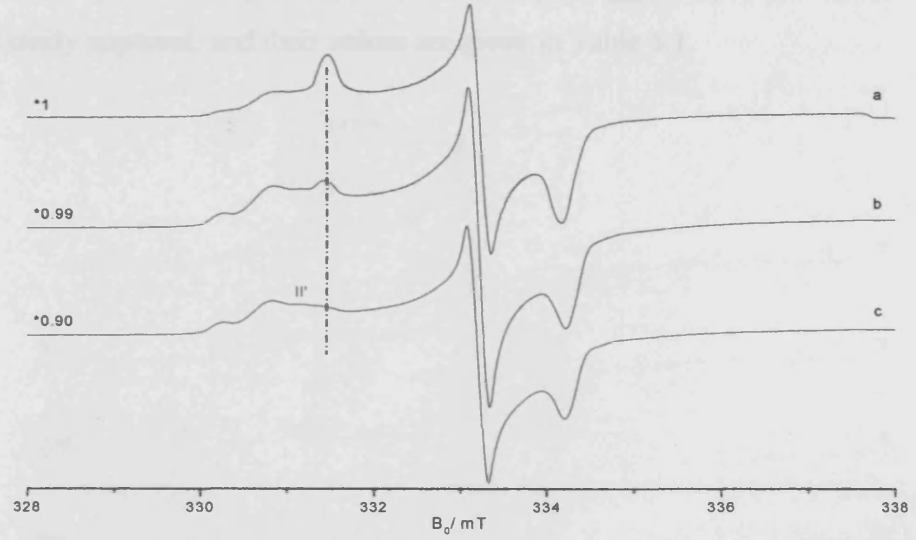

Figure 5.5 *cw*-EPR spectra [130K] of the superoxide radical on P25 TiO_2 at (a) 0 hours, (b) 24 hours and (c) 48 hours. Relative intensities of the signals are given by the numbers on the left hand side.

The systematic decrease in the intensity of the 2.019 component is analogous to the trends observed in the accelerated thermal stability test (Figure 5.4). It is interesting to note that the overall integrated intensities for the O_2^- species in Figure 5.5 remains more or less constant, despite the preferential loss of the 2.019 component. This implies

that this thermally unstable species can easily transform, or migrate, to another site on the TiO_2 surface and become stabilised at sites II-III at 298K.

In order to examine the photostability of the site I superoxide species compared to the other species, the superoxide radicals were once again generated on a thermally reduced (723K) surface. The sample was then UV irradiated under static vacuum at 77K. Under these conditions, the peak at g_{zz} = 2.019 preferentially decreased in intensity relative to the peaks at 2.023 and 2.026, as shown in Figure 5.6b (the original superoxide anion is shown in Figure 5.6a for comparison). Following prolonged exposure to UV irradiation, the intensity of the g_{zz} = 2.019 peak decreases further. The signal intensities of sites II–III did not change however under continuous UV illuminations, suggesting that these superoxide anions are not photo-labile compared to the site I superoxide species.

The preferential loss of the site I signal provides an indirect method of establishing the g_{xx} values for sites II–III. In Figure 5.2a, only the site I superoxide species is present with well defined g components of 2.019, 2.011, 2.005. Since this species dominates the spectrum of the more highly reduced sample (Figure 5.5a), the weaker g_{xx} components for sites II and III cannot be clearly resolved. However, once the dominant species I is preferentially removed, the g_{xx} components for sites II–III become easily apparent, and their values are given in Table 5.1.

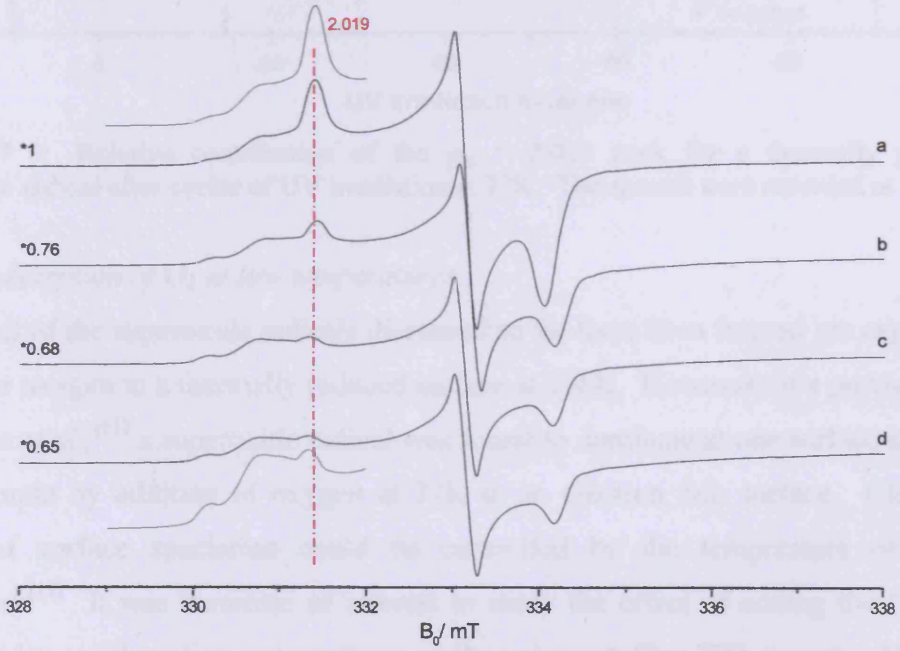

Figure 5.6 *cw*-EPR spectra [130K] of (a) the superoxide radical formed on a 773K reduced TiO_2 sample and UV irradiated (1000W) at 77K for (b) 30 minutes, (c) 2nd cycle of 30 minutes and (d) 3rd cycle of 30 minutes.

The relative contribution of the superoxide anion at site I to the overall signal intensity after each period of UV irradiation is shown in Figure 5.7. These contributions were calculated *via* deconvolution of the EPR signal into its individual components, arising from the different stabilisation sites, using the *Sim32* simulation programme.[20] From the figure it can clearly be seen that the contribution of the signal due to the superoxide anion at site I decreases steadily after each period of UV irradiation. The loss of this signal is largely responsible for the decrease in overall signal intensity reported in Figure 5.6.

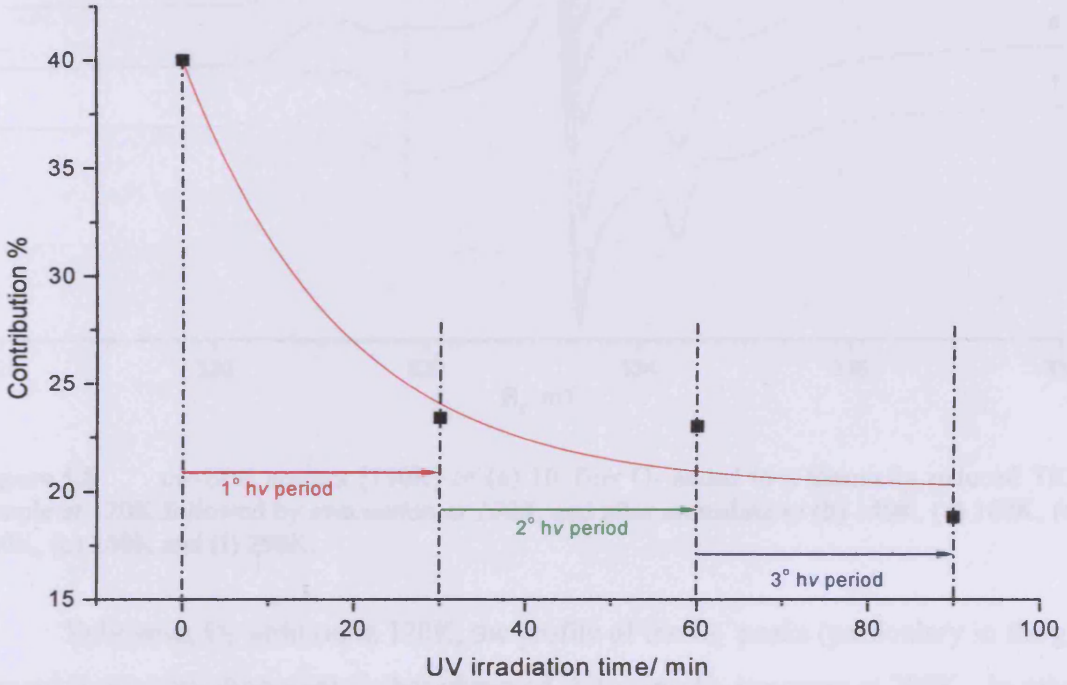

Figure 5.7 Relative contribution of the g_{zz} = 2.019 peak for a thermally generated superoxide radical after cycles of UV irradiation at 77K. The spectra were recorded at 130K.

5.3.3 Adsorption of O_2 at low temperatures

All of the superoxide radicals discussed so far have been formed *via* exposure of molecular oxygen to a thermally reduced surface at 298K. However, in a previous work by Chiesa *et al.*,[11] a superoxide radical was found to dominate at one surface site on an MgO sample by addition of oxygen at 77K to an electron rich surface. Clearly the degree of surface speciation could be controlled by the temperature of oxygen adsorption.[11] It was therefore of interest to study the effect of adding the O_2 to the surface at lower adsorption temperatures on the polycrystalline TiO_2 sample. Molecular oxygen was adsorbed onto the reduced P25 TiO_2 sample at 120K followed by

evacuation at 120K. The sample was then progressively annealed in intervals under *static* vacuum from 120K to 298K. The resulting spectra are shown in Figure 5.8.

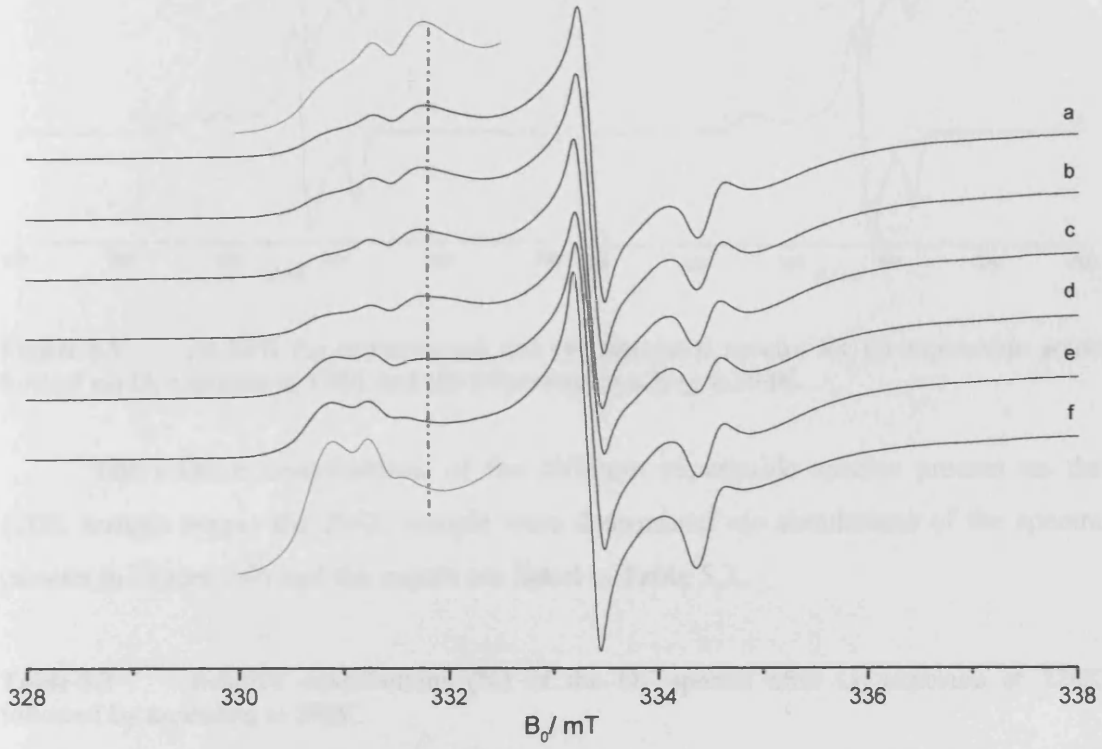

Figure 5.8 *cw*-EPR spectra [130K] of (a) 10 Torr O_2 added to a thermally reduced TiO_2 sample at 120K followed by *evacuation at 120K*, and after annealing to (b) 140K, (c) 160K, (d) 200K, (e) 240K and (f) 298K.

Following O_2 addition at 120K, the profile of the O_2^- peaks (particulary in the g_{zz} region) is not very dissimilar to that observed following O_2 exposure at 298K. In other words, the relative intensities of the species follows the approximate trend of I≈II>III>II'. Upon progressive annealing from 120K to 298K, the intensity of the g_{zz} = 2.019 peak (site I) decreases gradually so that the resulting distribution of O_2^- species follows the trend of III≈II>II'>I. Double integration of the EPR signals recorded after each annealing temperature reveals that the overall intensity of the superoxide signals remain the same from Figure 5.8a-f, which suggests that the superoxide anion is not lost from the surface. Therefore, the marked decrease in the intensity of the g_{zz} = 2.019 peak must be due to a redistribution of the superoxide anions to different sites on the surface.

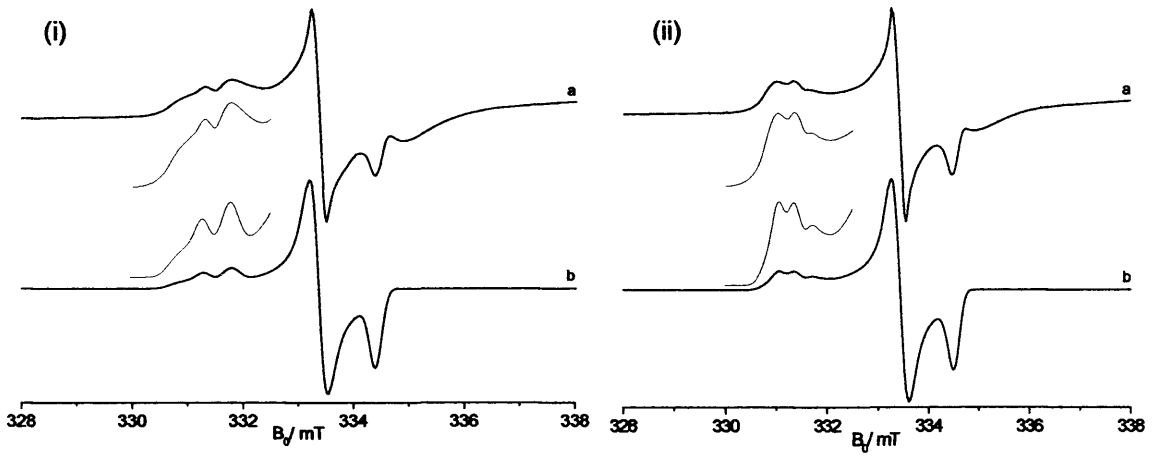

Figure 5.9 *cw*-EPR (a) experimental and (b) simulated spectra for (i) superoxide anion formed *via* O_2 exposure at 120K and (ii) following annealing to 298K.

The relative contributions of the different superoxide species present on the 120K sample *versus* the 298K sample were determined *via* simulations of the spectra (shown in Figure 5.9) and the results are listed in Table 5.2.

Table 5.2 Relative contributions (%) of the O_2^- species after O_2 exposure at 120K followed by annealing to 298K.

Temp/K	Site I	Site II	Site II′	Site III
120	31.5	31.5	10.5	26.5
298	6	32	13	49

Evacuation of oxygen at low temperatures (120K) does not completely remove all of the excess gaseous oxygen from the cell. As a result the signals shown above in Figure 5.8 may be affected by line broadening due to molecular oxygen. Therefore, the above low temperature exposure experiment was repeated but instead the oxygen was evacuated at 210K as opposed to 120K (in attempt to remove more O_2 from the cell and thereby improve spectral resolution). The resulting spectrum is shown in Figure 5.10.

A similar trend in the results can be seen in Figure 5.10 compared to those previously discussed for Figure 5.8. In other words, the relative intensity of the site I superoxide signal (at $g_{zz} = 2.019$) decreases upon annealing, whilst the relative intensity of the other peaks simultaneously increased. The overall integrated intensity of the superoxide signal remains constant on annealing, which again suggests that a selective redistribution of the superoxide anions occurs on the surface as opposed to a selective decay of the radicals.

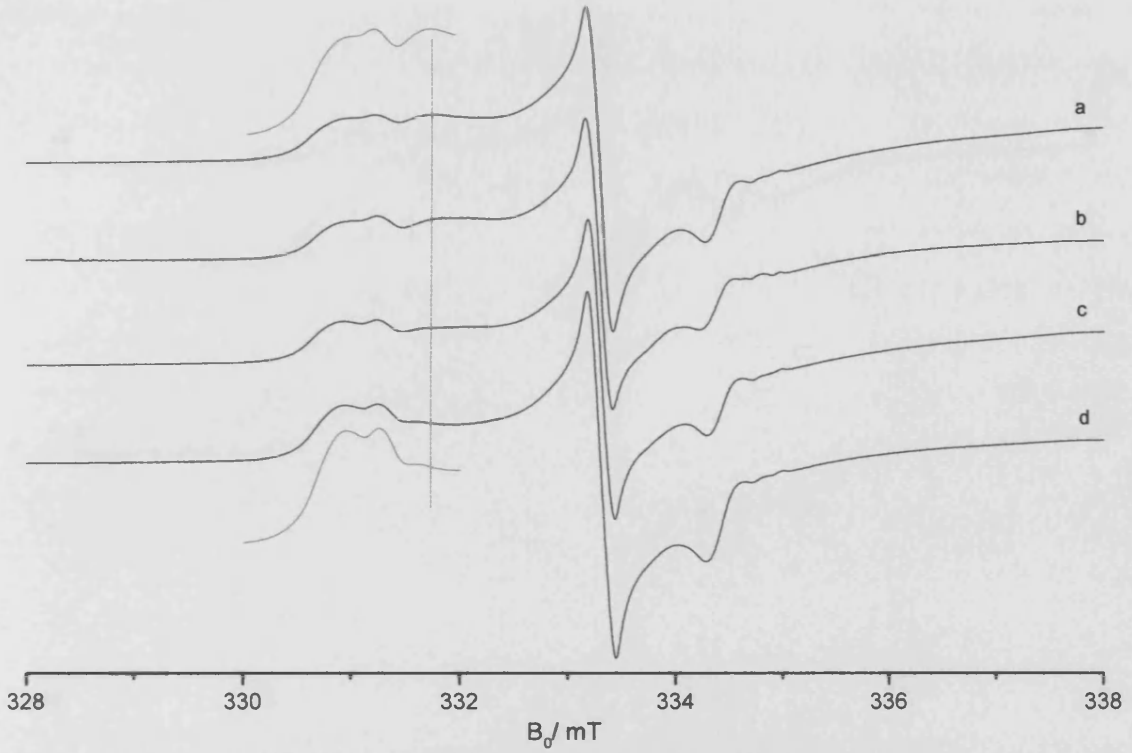

Figure 5.10 *cw*-EPR spectra [130K] of (a) 10 Torr O_2 added to a thermally reduced TiO_2 sample at 120K followed by *evacuation at 210K*, and after annealing to (b) 210K, (c) 240K and (d) 298K.

One seemingly conflicting result between the low temperature *versus* the room temperature oxygen exposure experiments pertains to the relative intensities of the site I superoxide species. According to Figure 5.2, when O_2 is exposed to a thermally reduced sample directly at 298K, the site I O_2^- species has the greatest abundance (or intensity). By contrast, according to Figure 5.8, when O_2 is exposed to a thermally reduced sample at 120K, and the sample is subsequently 'annealed' to 298K, the site I O_2^- species now has the lowest abundance. In other words, if this site I superoxide species is unstable following oxygen exposure at 120K, why is it visible and stable in Figure 5.2 at 298K? One simple explanation relates to the accessibility of the Ti^{3+} centres available for electron transfer to adsorbed O_2. While interfacial electron transfer from surface Ti^{3+} centres may be very facile at low temperatures (between 120K–210K) slightly elevated temperatures may be required to access the sub-surface Ti^{3+} centres. To test this idea further, the previous experiment described above (Figure 5.10) was repeated. However, after annealing the sample to 298K (as in Figure 5.10d) a second dose of oxygen was admitted to the evacuated cell at 298K. The resulting EPR spectrum is shown in Figure 5.11 (with the initial pre-evacuated result also shown for comparison).

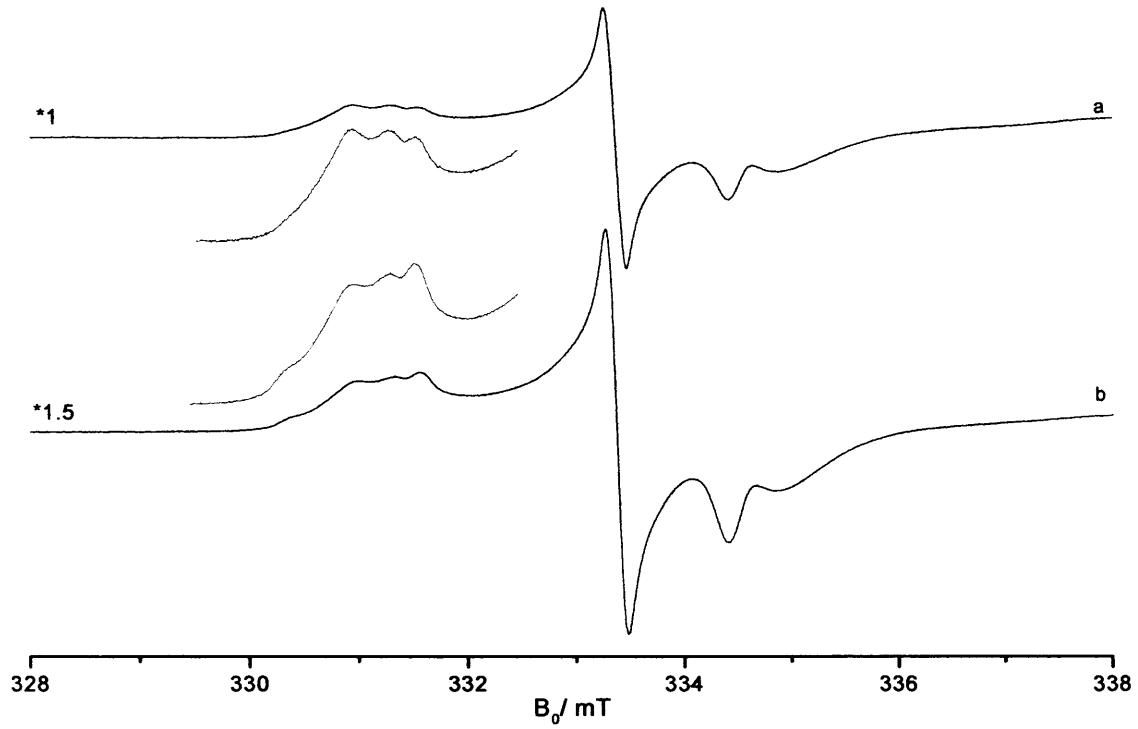

Figure 5.11 *cw*-EPR spectra [130K] of (a) 10 Torr O_2 added to a thermally reduced TiO_2 sample at 120K followed by evacuation at 210K, and after further annealing to 298K, and (b) followed by the further addition of 10 Torr O_2 at 298K.

Following additional exposure of O_2 at 298K to the low-temperature adsorption sample, an increase in the overall intensity of the superoxide signal was recorded, and in particular the contribution due to the anion stabilized at site I (characterized by g_{zz} = 2.019) increased considerably. The additional intensity in the spectrum following the second exposure to O_2 indicates that there are an increased number of superoxide anions on the surface. These additional anions were not formed after the initial O_2 exposure at 120K. A possible explanation for this is that there are a number of subsurface electrons present in the reduced sample which are not available for reaction with surface adsorbed oxygen at low temperatures. During the annealing process, an activation energy must be overcome, which drives these subsurface electrons to the surface so that they become available for reaction with the second exposure to O_2 at 298K. The results shown in Figure 5.11 explain the apparent differences in the speciation patterns found as a function of oxygen adsorption temperatures.

5.3.4 Thermal v Photogenerated O_2^-

The results presented so far have all involved the formation of O_2^- radicals on a thermally reduced surface following oxygen exposure at 120K or 298K. However, it is also of interest to consider the nature of the superoxide radicals generated *via*

photoirradiation (of an activated surface) under an oxygen atmosphere. In this experiment, oxygen (10 Torr) was admitted to a clean, oxidised TiO_2 surface followed by irradiation at 77K for a period of 30 minutes. The UV irradiation of the semiconductor results in the formation of photogenerated electrons and holes. The surface adsorbed molecular oxygen acts as an electron scavenger resulting in the generation of a superoxide radical, as shown in Figure 5.12. The g_{zz} region of this sample shows even greater complexity than the thermally generated sample, with two new peaks at g_{zz} (I′) = 2.017 and g_{zz}(II″) = 2.025. These new peaks indicate that further stabilisation sites are available for the superoxide anions on the activated surface.

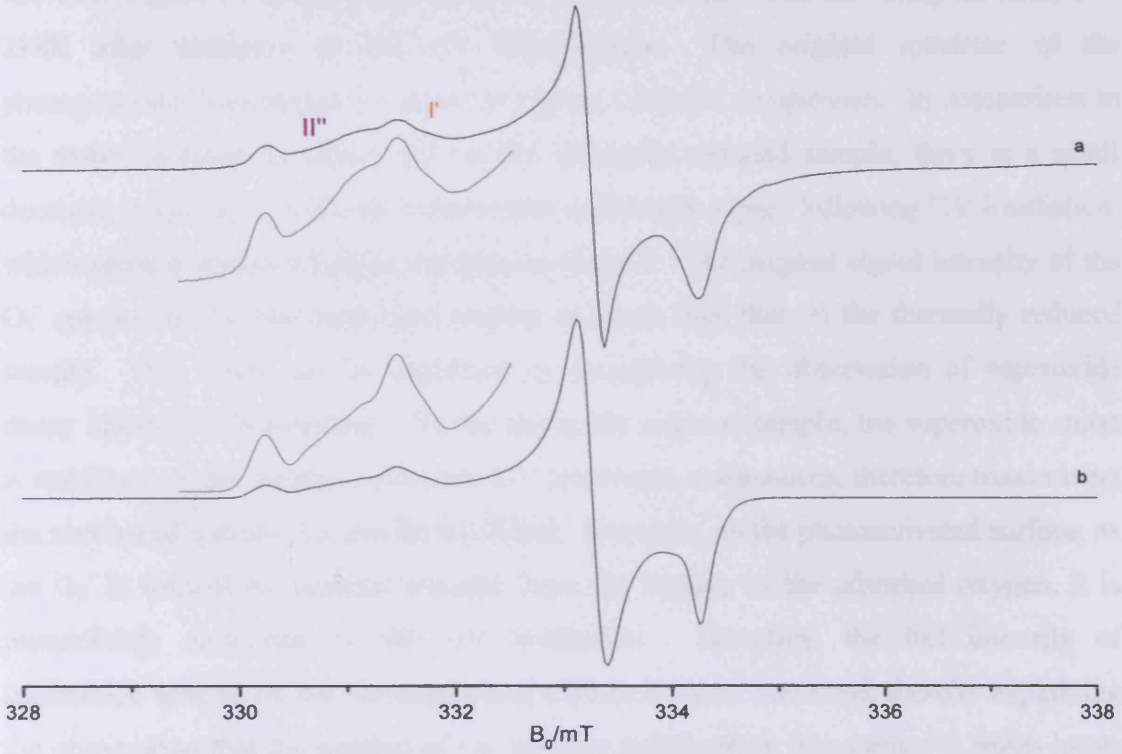

Figure 5.12 (a) experimental and (b) simulated *cw*-EPR spectra [130K] of photogenerated O_2^- anions on a P25 TiO_2 surface.

Deconvolution of the spectrum into the individual components arising from the different stabilisation sites on the surface was achieved by simulation and the results are shown in Table 5.3. It is clear that the site at g_{zz} = 2.019 accounts for only 15% of the overall signal intensity of the photogenerated superoxide radicals. In contrast, this peak (site I) contributes over 40% of the overall signal intensity on the thermally generated sample (see Table 5.3). The origin and significance of this difference in signal contribution is discussed further in section 5.4.4.

Table 5.3 Relative contributions (%) to the O_2^- signal from species at different stabilisation sites on TiO_2.

Sample	Site I	Site I′	Site II	Site II′	Site II″	Site III
Thermally reduced	43	–	36	16	–	5
Photoactivated	15	7	27	33	4	14

Following stabilisation of the photogenerated superoxide anion on the activated surface, the sample was UV irradiated under vacuum at 77K. The resulting spectrum is shown in Figure 5.13, accompanied by the signal recorded after annealing the sample to 298K after cessation of the UV illumination. The original spectrum of the photogenerated superoxide is shown in Figure 5.13a for comparison. In comparison to the result obtained in Figure 5.5 on the thermally reduced sample, there is a small decrease in intensity of the photogenerated superoxide signal following UV irradiation, which again is due to a loss of the species at site I. The original signal intensity of the O_2^- species on the photoactivated surface is lower than that on the thermally reduced sample. This result can be explained by considering the observation of superoxide decay under UV illumination. On the thermally reduced sample, the superoxide anion is stabilised on the surface before the UV irradiation commences, therefore maximising the number of species that can be stabilised. However, on the photoactivated surface, as the O_2^- is formed by electron transfer from the surface to the adsorbed oxygen, it is immediately destroyed by the UV irradiation. Therefore, the full intensity of superoxide species on the photoactivated surface is never observed, thereby explaining the observation that the number of O_2^- radicals stabilised on this surface is much lower than on the thermally reduced sample.

The new signals seen after irradiation (marked * in the figure) are assigned to photogenerated holes, O^-, which are unstable on annealing the sample to room temperature. Experimental results of Hurum *et al.*,[15,16] provide compelling evidence that photogenerated holes in particulate TiO_2 particles are initially trapped on the particle surface, while photogenerated electrons are trapped within the nanoparticles' lattice.

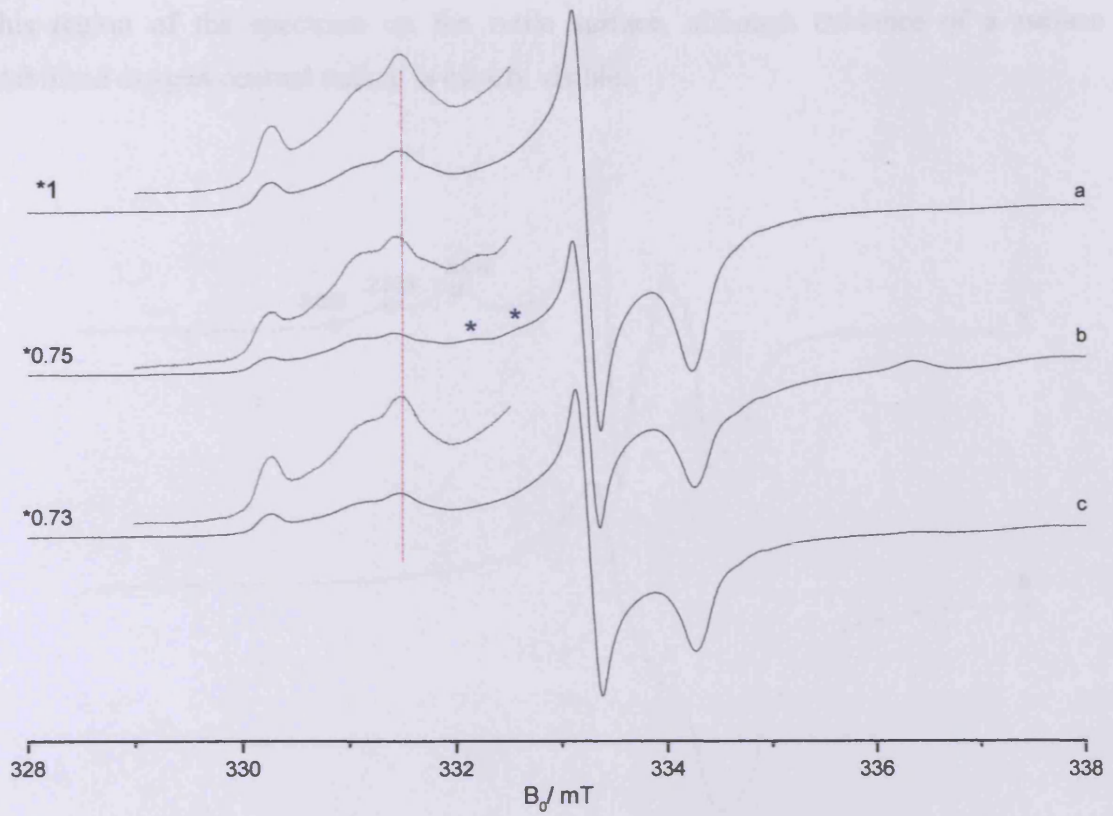

Figure 5.13 *cw*-EPR spectra [130K] of (a) photochemically generated superoxide radical followed by (b) UV irradiation at 77K for 30 mins (1000W) and (c) subsequent annealing to 298K.

5.3.5 Morphological Considerations: Anatase v Rutile

All of the results discussed so far in this chapter have been recorded on the mixed-phase Degussa P25 sample (80% anatase, 20% rutile). It is interesting to consider the differences between the two polymorphs of TiO_2, as previous work has highlighted the differences in photocatalytic reactivity between the two phases.[15,16] In particular it would be interesting to determine if the stabilisation sites on the surface discussed so far can be assigned to either of the two phases. It is also possible that a stabilisation site may exist at the interface between the two phases in the mixed-phase sample. Following thermal reduction of the pure phase Rutile A sample, the signal due to Ti^{3+} is well resolved. However, it is not visible in the spectrum of the pure phase anatase (spectra not shown for brevity) due to spin-spin broadening effects, and unfavourable spin-lattice relaxations. The EPR spectra recorded after 10 Torr O_2 addition at 298K to samples of thermally reduced pure phase anatase and rutile are shown in Figure 5.14. A superoxide radical with the g_{zz} components at 2.019, 2.023 and 2.029 can be resolved on the anatase sample. However, there are no peaks resolved in

this region of the spectrum on the rutile surface, although evidence of a surface stabilised oxygen centred radical is clearly visible.

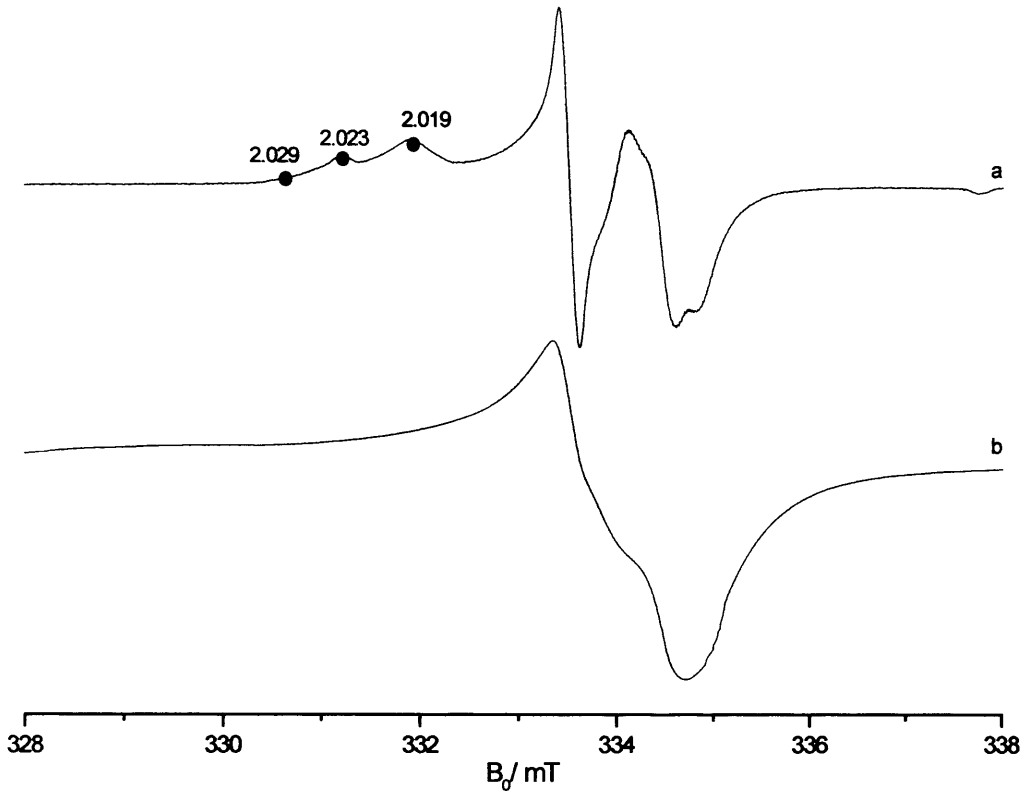

Figure 5.14 *cw*-EPR spectra [130K] of the oxygen centred radicals generated by 10 Torr O_2 addition at *298K* to thermally reduced pure phase (a) anatase and (b) rutile A.

In a previous work, this oxygen centred radical formed over thermally reduced Rutile A was assigned to the ozonide ion, O_3^-,[21] with g values $g_{xx} = 2.003$, $g_{yy} = 2.008$ and $g_{zz} = 2.011$. As previously shown in Figure 5.12, the profile of the EPR spectrum of the superoxide radical following low temperature irradiation of P25 TiO_2 under an oxygen atmosphere showed differences to the spectrum of the thermally reduced sample. It was of interest to see if this behaviour was also observed on the pure phase materials. Low temperature photoirradiation of the Rutile A under oxygen (10 Torr) resulted in the spectrum shown in Figure 5.15. The oxygen centred radical yields EPR signals with the g tensor $g_{xx} = 2.003$, $g_{yy} = 2.011$ and g_{zz} components ranging from 2.026–2.035.

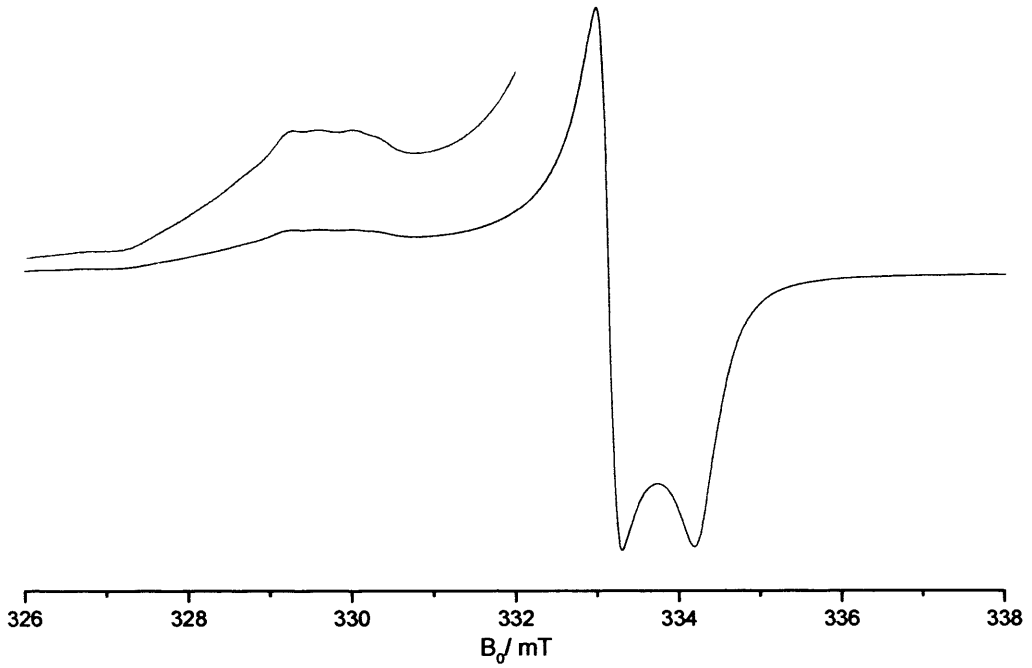

Figure 5.15 *cw*-EPR spectrum [130K] of the oxygen centred radical generated *via* UV irradiation in the presence of oxygen (10 Torr) over clean activated Rutile A.

The g values of the signal shown in Figure 5.15 do not lie in the accepted range of g values assigned to superoxide radicals on TiO_2.[19] The signal with $g_{zz} = 2.035$ has been identified as the hydroperoxy radical, HOO•, which always has a g_{zz} value of *ca.* 2.035 on TiO_2 and can therefore be used to fingerprint this species.[19,22] This radical has previously been observed over this Rutile A surface, and may be formed due to incomplete removal of surface hydroxyls following the thermal reduction of the sample.[23] It has already been discussed that the number of superoxide radicals generated *via* UV irradiation in the presence of oxygen over an activated surface is much lower than on the thermally reduced surface. Therefore, a sample of rutile was reduced to 773K followed by addition of 10 Torr oxygen at 120K and subsequent evacuation of the excess oxygen at 120K. The spectrum recorded after this treatment is shown in Figure 5.16. Although the exact value of the g_{xx} and g_{yy} component of the signals cannot clearly be determined, three signals with the g_{zz} values of 2.019, 2.023 and 2.029 are clearly resolved. These g values can be assigned to the presence of superoxide radicals. Therefore this result shows that despite the rapid rate of electron-hole recombination reported in this polymorph, charge transfer from the rutile surface to the molecular oxygen has occurred, resulting in the stabilisation of O_2^- radicals. Another signal with the g values $g_{xx} = 2.007$, $g_{yy} = 2.011$ and $g_{zz} = 2.035$ is also identified in the spectrum, which can be assigned to the HOO• species.

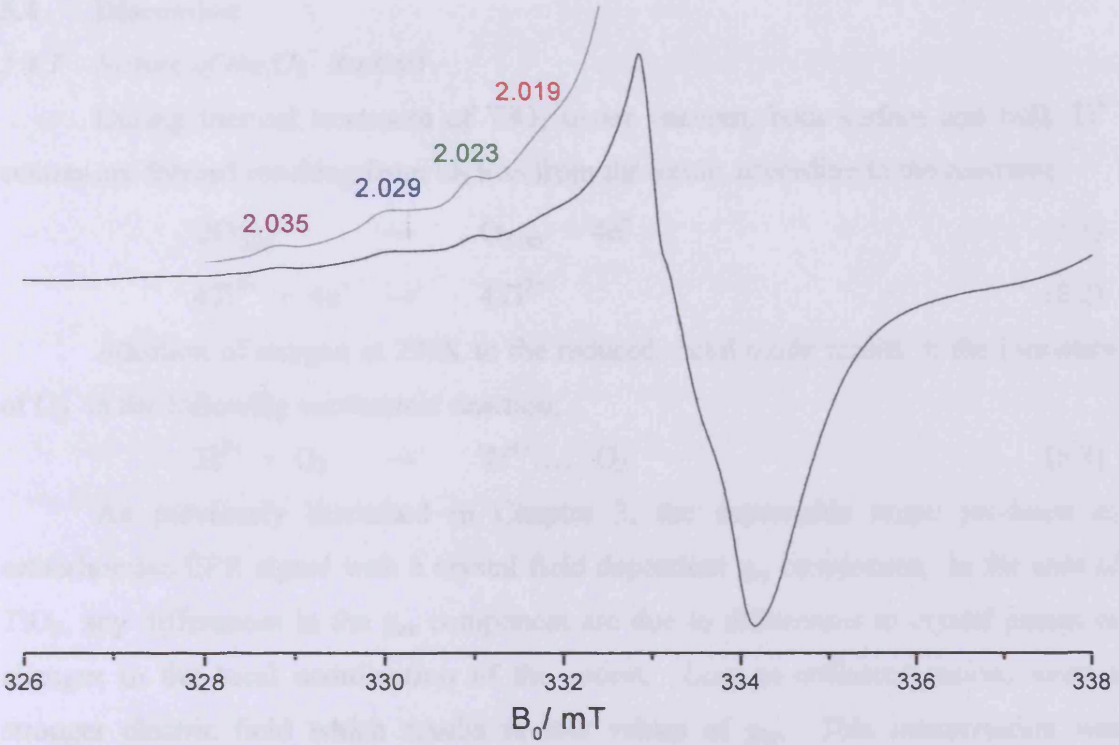

Figure 5.16 *cw*-EPR spectrum [130K] of 10 Torr O_2 admitted to a reduced sample of Rutile A at *120K*, followed by evacuation at 120K.

Table 5.4 Comparison of g values obtained for the O_2^- radical on the surface of different thermally reduced TiO_2 samples.

Polymorph	g_1 (g_{zz})	g_2 (g_{yy})	g_3 (g_{xx})	Ref
Anatase	(I) 2.019	2.01		This study
	(II) 2.023	2.01	2.004	
	(III) 2.029	2.01		
Anatase	2.019	2.009	2.003	[24]
Anatase	2.024	2.009	2.003	[25]
Rutile	(I) 2.019			This study
	(II) 2.023	unresolved		
	(III) 2.029			
Rutile	2.022	2.011	2.008	[26]
Rutile	2.030	2.008	2.004	[18]

5.4 Discussion

5.4.1 Nature of the O_2^- Radical

During thermal treatment of TiO_2 under vacuum, both surface and bulk Ti^{3+} centres are formed resulting from O_2 loss from the oxide, according to the reactions:

$$2O^{2-}_{(latt)} \rightarrow O_{2\,(g)} + 4e^- \quad (5.1)$$

$$4Ti^{4+} + 4e^- \rightarrow 4Ti^{3+} \quad (5.2)$$

Addition of oxygen at 298K to the reduced metal oxide results in the formation of O_2^- in the following exothermic reaction:

$$Ti^{3+} + O_2 \rightarrow Ti^{4+}.....O_2^- \quad (5.3)$$

As previously discussed in Chapter 3, the superoxide anion produces an orthorhombic EPR signal with a crystal field dependent g_{zz} component. In the case of TiO_2, any differences in the g_{zz} component are due to differences in crystal planes or changes in the local coordination of the cation. Low co-ordinated cations exert a stronger electric field which results in low values of g_{zz}. This interpretation was suggested based on the effect of coordination on the Madelung constant[27] and was later confirmed through experimental and quantum chemical calculations performed on the O_2^- radical on MgO.[28]

The effect of surface coordination can be seen in the two samples of P25 TiO_2 annealed to different reduction temperatures, as observed in Figure 5.2. At a reduction temperature of 573K only one component is observed in the g_{zz} region, at g_{zz} = 2.019, which indicates that at this temperature there is only one site available for stabilisation of the superoxide radical. On increasing the reduction temperature to 773K four sites are available for stabilisation as evidenced by the four peaks in the g_{zz} region; g_{zz}(I) = 2.019, g_{zz} (II) = 2.023, g_{zz}(II') = 2.020 and g_{zz} (III) = 2.026. The general trend in these results shows that at low reduction temperatures sites with a low g_{zz} value (g_{zz} (I) = 2.019) are present and as the thermal reduction temperature increases more stabilisation sites with higher g_{zz} values become available for adsorption. Therefore, as the reduction temperature increases, more sites with lower effective cationic charge become available. This trend can be explained by considering the electrostatic forces that attract the molecular oxygen to the surface before charge transfer from the Ti^{3+} cations takes place. As the $Ti^{4+}....O_2^-$ are held together electrostatically, it is thermodynamically favourable for the O_2 to adsorb at sites of higher electrostatic interaction (i.e. low coordinated sites).

Similar results have been obtained by Shvets and Kazansky,[29] who found that two types of O_2^- could be observed at 77K on titanium supported on silica. Two g_{zz} values of 2.026 and 2.020 were resolved with the relative intensity of the peaks found to be dependent on the concentration of TiO_2 present in the sample. Shvets *et al.*,[29] assigned the g_{zz} value at 2.026 to O_2^- adsorbed on tetrahedrally coordinated titanium ions formed at low TiO_2 content, whereas the g_{zz} value at 2.020 was related to O_2^- adsorbed on titanium ions in square pyramidal coordination prevailing at higher concentration. The Ti samples were prepared by impregnation of silica gel (surface area $500m^2/g$) by $TiCl_4$ hydrochloride solution, resulting in an amorphous phase of Ti/SiO_2. It must be stressed here that the morphology of the surface has a large effect on the g values of oxygen centred radicals, and therefore the results of Shvets and Kazansky[29] can only be qualitatively compared to the results in this chapter.

5.4.2 Information from the ^{17}O Hyperfine Tensor

The g tensor can only give limited information on the nature of the oxygen species. However, further details can be obtained from the hyperfine tensor and the use of oxygen isotopically enriched in ^{17}O has been used on many different oxides for this purpose. The nucleus of ^{17}O has a spin of I = 5/2, so that a diatomic species could give 6×6, i.e. 36 lines for every principle direction of the hyperfine tensor. However, in the spectrum recorded of O_2^- on MgO,[10] the hyperfine tensor showed a pattern consistent with equivalent oxygen nuclei. A singly labelled superoxide radical $(^{17}O^{16}O)^-$ should give a hyperfine pattern of 6 lines and a doubly labelled superoxide radical $(^{17}O^{17}O)^-$ should give an 11 line pattern for each principle direction of the hyperfine tensor. The sign and absolute direction of the hyperfine tensor cannot be obtained unambiguously from a powder spectrum, but in the following discussion the largest hyperfine value is defined to be along A_{xx}, which is the orbital containing the unpaired electron and lies in the same direction as g_{xx}.

Tench and Holroyd[10] reported an investigation of oxygen adsorption on the surface of MgO with a large concentration of surface F centres. The spectrum resolved after addition of $^{16}O_2$ was complex and interpreted in terms of a superoxide radical in several well defined sites of varying thermal stability. On adsorption of oxygen enriched to 58% $^{17}O_2$ a spectrum with a rich hyperfine structure was obtained. The lines were centred around g_{xx} and g_{yy} and were assigned to the species $^{17}O^{16}O^-$ and $^{17}O^{17}O^-$ with a measured hyperfine splitting of 7.7 ± 0.2mT. A further set of lines appeared

about g_{zz} with a splitting of 1.5 ± 0.2mT. The data was therefore fitted using a completely asymmetrical tensor of the form $A_{xx} = 7.7 \pm 0.2$, $A_{yy} = 0 \pm 0.4$ and $A_{zz} = 1.5 \pm 0.2$mT.[10] No values for additional hyperfine patterns due to speciation of superoxide radicals were reported by the authors,[10] although it was stated that experiments performed at Q-band confirmed the existence of several sites for oxygen species on the surface.

The first investigation of $^{17}O_2$ adsorbed on thermally reduced TiO_2 samples was performed by Naccache *et al.*[18] Two different anatase samples, one obtained by flame hydrolysis of the chloride (labelled by the authors as A1)[18] and the other prepared by precipitation from a solution of the chloride using NaOH and NH_4OH (labelled A2), were reduced in vacuum to form the paramagnetic Ti^{3+} cation. On exposure of the samples to $^{16}O_2$ at 77K an orthorhombic signal characteristic of O_2^- was formed. Sample A1 only showed one signal in the g_{zz} region, whereas sample A2 showed two g_{zz} values of 2.024 and 2.020 indicating two sites on the surface. When the experiment was repeated using oxygen enriched to 58% $^{17}O_2$ a well resolved hyperfine structure was obtained, with a hyperfine coupling constant of 7.7mT in the A_{xx} direction for both samples.[18]

Adsorption of $^{16}O_2$ at 77K onto a thermally reduced rutile sample resulted in two orthorhombic EPR signals, with the g_{zz} values 2.030 and 2.020, which were also assigned to superoxide.[18] This observation confirms the result shown in Figure 5.16 that O_2^- radicals can be stabilised on the rutile surface following oxygen exposure at *low temperature*. The signal observed by Naccache *et al.*,[18] at 2.030 was unstable on warming the sample to 298K. Using $^{17}O_2$ enriched oxygen, the authors[18] observed a hyperfine pattern on the rutile surface. A detailed analysis of the spectrum resolved two sets of hyperfine lines with $A_{xx} = 7.6$ and 7.2mT corresponding to the species with $g_{zz} = 2.030$ and 2.020 respectively.[18] This observation corroborates the result shown in Figure 5.3 (and the data listed in Table 5.1) for the different hyperfine couplings corresponding to the speciation of $^{17}O_2^-$ on the anatase surface.

This data comprehensively proved that the species observed was not O^- as previously thought,[18] since both the anatase and rutile samples showed hyperfine structures which could only be attributed to a diatomic ion. On both the anatase A2 sample, and to a lesser extent on the rutile sample, a line was observed at $g = 2.003$ in addition to the hyperfine lines assigned to the O_2^- ion. This line appeared during oxygen adsorption but was not affected by $^{17}O_2$ and was therefore considered unlikely

to be due to an O^- ion. Although the authors[18] found it difficult to get an unambiguous assignment of this line, they proposed that it probably arose from the localization of a conduction electron in the lattice by the adsorbed oxygen.

The hyperfine tensor can also be used to estimate the spin density on the oxygen atoms. Assuming that the unpaired electron is in an axially symmetrical π_g orbital, the axial hyperfine tensor can be separated into an isotropic part (a_{iso}) and an anisotropic traceless tensor of the form;

$$(A_\perp, A_\perp, A_\parallel) = a_{iso} + (-B, -B, 2B) \quad (5.4)$$

where

$$a_{iso} = (2A_\perp + A_\parallel)/ 3 \quad (5.5)$$

The isotropic and anisotropic terms are then given by $a_{iso} = A_0 c_{2s}^2$ and $B = B_0 c_{2p}^2$, where c_{2s}^2 and c_{2p}^2 are the spin densities of the unpaired electron in the 2s and 2p orbitals of the oxygen atoms, and A_0 and B_0 are the hyperfine constants for pure 2s and 2p oxygen orbitals. Several values for A_0 and B_0 have been used previously, but the discussion hereafter uses the values of $A_0 = -165.1$ and $B_0 = -5.138$mT as described in Morton.[30] The 2s spin density arises from a spin polarization mechanism and there are only small values involved, therefore only the 2p populations need to be calculated. In the following discussion, only the A_{xx} value is used; A_{yy} and A_{zz} are assumed to be zero. Whilst this is strictly not true, the values of A_{yy} and A_{zz} are predicted to be small (close to zero), and for the purposes of the following discussion it is convenient to assume zero hyperfine coupling in the perpendicular directions.

From the hyperfine splitting constants A_{xx} resolved for the case of $^{17}O_2$ adsorbed on the surface of thermally reduced P25 TiO_2 [7.64mT (site I), 7.86 (site II/II') and 7.97mT (site III)], a_{iso} and B can be calculated. From the relationship between B and c_{2p}^2 given above, the corresponding total spin density on the O_2^- anion at the different sites can be calculated, and are listed in Table 5.5. These values can be compared to the spin density calculated from ^{17}O hyperfine splittings for diatomic oxygen species on other metal oxide systems (Table 5.5). A total spin density value close to unity indicates that the electron is almost completely localized on the two oxygen atoms. This result confirms the ionic nature of the $[Ti^{4+}....O_2^-]$ centres studied in this investigation.

Table 5.5 Total spin density for diatomic oxygen species on metal oxide systems

System	A_{xx}	A_{yy}	A_{zz}	A_{iso}	Total spin density	Ref.
TiO_2(anatase)	(I) 7.64	...	...	2.55	0.99	This study
	(II/II') 7.86			2.62	1.02	
	(III) 7.97			2.66	1.03	
MgO	-7.7	0	+15	-2.07	0.9	[10]
CaO	-7.7	...	...	-2.57	1.00	[31]
SnO_2	-8.05	...	...	-2.68	1.04	[32]
TiO_2(anatase)	7.7	...	...		1.00	[18]
TiO_2(rutile)	-7.6	...	...	-2.53	0.98	[18]
WO_3/ SiO_2	-7.4	...	...	-2.47	0.96	[33]

5.4.3 Nature of the g_{zz} = 2.019 stabilisation site

Throughout this chapter several stabilisation sites for the superoxide radical have been identified on the mixed-phase P25 TiO_2. As discussed above, the value of the g_{zz} component is an indication of the degree of coordination of the stabilisation site. However, studies on the polycrystalline samples are unable to determine the exact position or identity of the sites on the surface. The results discussed in this chapter have highlighted the different thermal and photoreactive stabilities of the superoxide radical at the different sites, and this data can now be used to make some predictions on the likely candidates responsible for site stabilisation.

In particular, the superoxide radical at site I (characterized by g_{zz} = 2.019) has exhibited different behaviour compared to the superoxide radicals on the stabilisation sites II–III. In Figure 5.2 it was shown that the superoxide radical forms preferentially at the 2.019 site at low reduction temperatures. Following this, in Figures 5.4 and 5.5, the superoxide radical at the 2.019 site was seen to decay preferentially under thermal annealing and under UV irradiation. It will be shown later (section 6.3.3) that this radical also undergoes preferential chemical reactivity with adsorbed acetone. These results all suggest that the nature of the stabilisation site responsible for this signal is substantially different compared to the other sites on the surface and therefore deserves further attention.

The low value of the g_{zz} component for site I points towards a stabilisation site of low coordination. During the annealing process of the TiO_2 sample under vacuum,

oxygen atoms are removed from the surface resulting in vacancy sites. The Ti^{3+} cations adjacent to the vacancy are therefore sites of low coordination, and thus it is proposed that the superoxide radical responsible for the signal at 2.019 is adsorbed at a vacancy site on the surface. This proposal is supported by experimental data on single crystal surfaces provided by other groups. For example, Lu *et al.*,[34,35] performed a series of photodesorption experiments on a rutile TiO_2(110) surface to elucidate the nature of the adsorbed oxygen species on the defective surface. Following oxygen exposure to a sample previously annealed to 900K under UHV conditions, the maximum coverage of O_2 was <0.12ML. The coverage of oxygen vacancy sites on the surface had previously been reported to be ~0.08–0.1ML. Therefore this suggested that the O_2 molecules were probably adsorbed at these vacancy sites. Differences in the geometric configuration of the adsorbed O_2 at oxygen vacancy sites are likely to result in drastically different bonding characteristics and electronic interactions with the substrate, leading to quite distinct photoactivities. The relative photoactivities of the superoxide anions will be discussed further in section 5.4.6.

Henderson[9] proposed a model for oxygen adsorption on the vacuum annealed TiO_2(110) surface based on TPD and ELS results. The oxygen vacancies created during the annealing process were shown by STM to be isolated vacancies along the bridging oxygen rows, as shown in Figure 5.17(a).

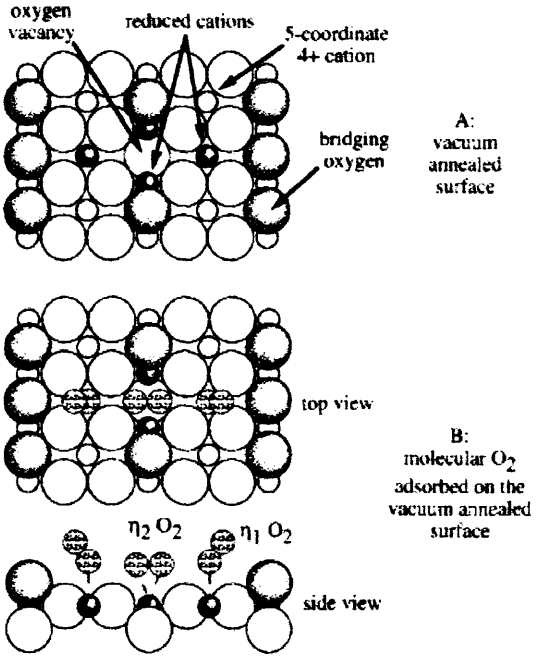

Figure 5.17 Schematic model for the bonding of O_2 to the vacuum annealed TiO_2(110) surface. Model A shows the top view of the TiO_2(110) surface with an oxygen vacancy site. Model B shows top and side (along the [001] direction) views of O_2 molecules bonded at vacancy and non-vacancy sites.[9]

The electrons associated with the vacancy were localized on the titanium atoms situated directly around the vacancy site creating Ti^{3+} cations. From DFT studies, in combination with STM images, Henderson *et al.*,[9] proposed that the five-coordinate Ti^{4+} sites adjacent to the vacancy were actually only *partially* reduced, but still possessed sufficient electron density to facilitate charge transfer to adsorbed O_2. This resulted in three O_2 molecules sharing the two electrons associated with each vacancy site, as shown in Figure 5.17(b). The adsorption model proposed consisted of one O_2 molecule adsorbed in a 'side-on' manner with η^2 bonding directly over the vacancy.[9] The remaining two O_2 molecules were adsorbed in an 'end-on' manner at the in-plane 5-coordinate Ti^{4+} cations directly adjacent to the vacancy. During TPD experiments, the 'end-on' bonded O_2 at the Ti^{4+} sites were observed to molecularly desorb, whereas the 'side-on' bonded O_2 at the vacancy site dissociated, leading to reoxidation of the vacancy and a reactive oxygen adatom on the surface.[9]

It is pertinent to state at this point that the results obtained in this thesis do not fully corroborate the proposal of three oxygen molecules per vacancy as suggested by Henderson.[9] The 11-line hyperfine pattern recorded for the superoxide anion using isotopically enriched $^{17}O_2$ (Figure 5.3) is proof that the diatomic radicals on the surface of TiO_2 possess exactly equivalent oxygen nuclei. This can only arise if the oxygen is 'side-on' bonded to the surface. No EPR evidence was observed to support the assignment of 'end-on' bonded molecular oxygen species as proposed by Henderson,[9] which would result in two different hyperfine coupling constants in the A_{xx} direction.

From oxygen uptake curves, Henderson[9] also suggested that the first 4×10^{13} molecules/cm^2 of oxygen adsorb irreversibly at vacancy sites (and subsequently dissociate to fill the vacancies). This proposal explains the trend shown in Figure 5.2, where superoxide anions form initially at site I on the surface, i.e., an oxygen vacancy site. Further, Henderson *et al.*,[9] observed that any subsequent oxygen exposure resulted in adsorption of oxygen molecules that did not evolve in the TPD experiments until temperatures of 410K, and were assigned to adsorption sites other than vacancies. This confirms the observations shown in Figure 5.4 which showed the decay of the superoxide anion preferentially at site I at low annealing temperatures, but the anions stabilised at sites II–III, which can be attributed to sites other than vacancies, are stable on the surface to temperatures of 353K.

On the basis of their TPD and ELS data, Henderson *et al.*,[9] concluded that there are two main thermal channels for O_2 adsorption on the vacuum annealed TiO_2(110)

surface at 120K, which subsequently lead to either molecular desorption at 410K or irreversible decomposition with O vacancy filling. There is competition between these two processes, and it was shown that at oxygen adsorption temperatures below 150K the molecular adsorption channel was predominant. At the low adsorption temperatures, the O_2 molecules adsorbed through a precursor-mediated process, and gave rise to the evolution of signals in the TPD spectra at 410K, which, as described above, have been assigned to oxygen adsorbed at non-vacancy sites. The dissociative channel was favoured at adsorption temperatures above 150K, and again these adsorption sites have been assigned to oxygen adsorbed at vacancy sites (see Figure 5.18). These assignments by Henderson *et al.*,[9] explain the observations in Figures 5.8 and 5.10, where oxygen adsorption onto the thermally reduced surface at low temperatures (115K) led to an increased relative contribution from the species at sites II–III (Table 5.3), i.e. the oxygen is more likely to adsorb at the non-vacancy sites at low adsorption temperatures (the molecular desorption channel of Henderson). In contrast, when oxygen is exposed to the surface at 298K, the distribution of sites shows that the oxygen has preferentially adsorbed at the vacancy site (see Figure 5.2 and Table 5.1).

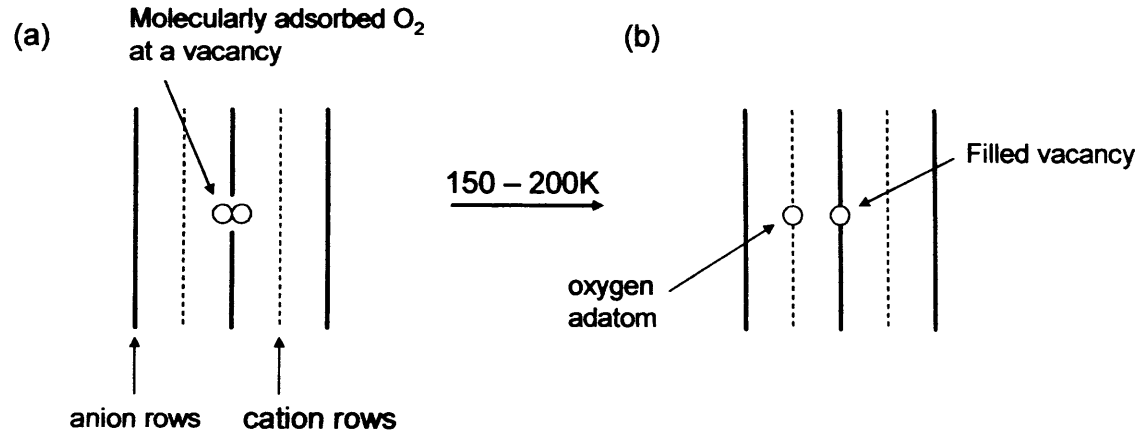

Figure 5.18 (a) molecular adsorption of O_2 at a vacancy site at temperatures < 150K and (b) O_2 dissociation at the surface resulting in a filled vacancy site and an oxygen adatom. The surface shown in (b) is not able to undergo further oxygen adsorption.

5.4.4 Defect Concentration

Further data which suggests that the stabilisation site at 2.019 is due to an oxygen vacancy is provided by considering the relative contributions of the different superoxide radicals to the overall signal intensity. As mentioned previously, the 2.019 peak accounts for 40% of the overall signal intensity on the thermally reduced sample

compared to only 15% for the photochemically produced superoxide. The main difference between the two samples is the nature of the surface (i.e., the stoichiometry).

During thermal annealing under vacuum, oxygen atoms are removed from the surface creating large numbers of Ti^{3+} defects (or low coordinated sites). On exposure to molecular oxygen at 298K, electron transfer occurs from the Ti^{3+} to the oxygen forming the superoxide ion. The large electrostatic interaction between a low coordinated Ti^{3+} cation and the molecular oxygen explains the preferential formation of the superoxide radical at the 2.019 site. In contrast, the photochemically produced superoxide is formed on a clean, activated surface. This surface has been re-oxidised and should therefore contain only a small number of surface defects. TPD and STM data provided by Epling *et al.*,[36] showed that following exposure of molecular oxygen at 300K to a TiO_2(110) surface previously annealed in vacuum to 850K, the surface contained less than 1% oxygen vacancy sites. Therefore, the superoxide radicals formed *via* the photochemical method on the oxidised surface are less likely to be stabilised at oxygen vacancy sites explaining the decrease in relative contribution of the superoxide signal at 2.019.

The absolute number of O_2^- radicals on the TiO_2 surface was determined by double integration of the EPR signal and comparing this value to a calibration curve based on standard samples of DPPH (see Chapter 4 for experimental details). The area of the superoxide radical can be estimated to be $\sim 2.7\times10^{-20} m^2$ (from an O-O bond distance of 1.3Å and assuming each oxygen atom to be approximated by a circle). A total surface area for each sample can also be calculated from the weight of each sample used and the known surface area of $49 m^2 g^{-1}$ for the P25 used in this study. Therefore, from the calibration curve it is possible to calculate the number of spins present on the surface and subsequently determine the percentage of surface coverage.

For example, the superoxide signal shown in Figure 5.2b generated *via* the thermal method arose due to a total number of paramagnetic spins of $\sim 1.25\times10^{16}$, which equates to a surface coverage of 0.03%. This is compared to the superoxide signal generated *via* photoirradiation in the presence of oxygen shown in Figure 5.11b, which arises from a surface coverage of 0.02%.

5.4.5 Photoactivity

It was shown in Figure 5.5 that the intensity of the superoxide signal at site I (g_{zz} = 2.019) decreased under the influence of low temperature UV irradiation, indicating that this species is photo-labile. The intensities of the signals due to the superoxide anion stabilised at the alternative sites on the surface were unchanged following irradiation, which suggests that the superoxide anions at these sites are not active for photodesorption.

Previous studies have shown that oxygen adsorption onto the surface of TiO_2 can lead to molecular oxygen species which show differences in photoreactivity. For example, Lu *et al.*,[34,35] studied the photooxidation process of CO to CO_2 on a TiO_2(110) surface. On the annealed TiO_2(110) sample, two adsorption states for the oxygen were identified, which were termed α-O_2 and β-O_2 by the authors and are shown in Figure 5.19.[34,35] Following oxygen adsorption at 105K onto the annealed sample, the surface was subsequently exposed to a saturation coverage of CO in order to study the photooxidation process of CO to CO_2. The results showed that oxygen adsorbed in the α-O_2 state was active for photooxidation processes but had a much smaller cross section for photodesorption. Oxygen adsorbed in the β-O_2 state however, was not active for photooxidation of CO but had a much larger cross section for photodesorption.

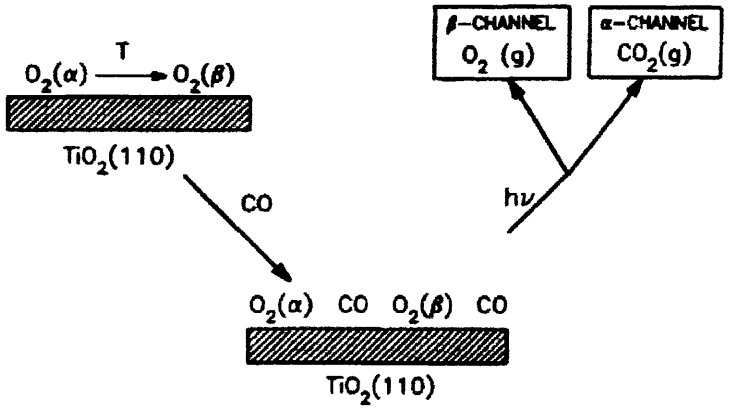

Figure 5.19 Schematic illustration of the two oxygen adsorption channels on TiO_2(110).[34]

Using isotopically labelled $^{18}O_2$, they detected molecular desorption of the adsorbed oxygen on exposure to the photon source.[34,35] The group plotted the photodesorption yield of molecular oxygen as a function of the oxygen exposure at 105K and determined that the adsorption was accurately described by a Langmuir adsorption profile. The threshold energy for photodesorption of oxygen was found to be 3.1eV corresponding to the bandgap energy of rutile, suggesting the photodesorption

is a substrate-excitation mediated process *via* the capture of photogenerated holes by the adsorbed oxygen complex.

The above results of Lu *et al.*,[34,35] support the results discussed earlier in this chapter regarding the differences in photoreactivity of the superoxide radicals at the different stabilisation sites on the surface. As we have seen, the superoxide radical giving rise to the EPR signal with the g_{zz} component at 2.019 preferentially decays under the influence of UV irradiation. It is therefore likely based on the above discussion that this superoxide radical can be assigned to oxygen adsorption in the α-O_2 state as described by Lu *et al.*[35] The authors assigned the α-O_2 state as molecular oxygen chemisorbed at oxygen vacancy defect sites. This supports the earlier assignment discussed in section 5.4.3 that the signal at 2.019 is due to a superoxide anion stabilised at a vacancy site on the surface.

Further evidence for the presence of two different oxygen adsorption channels on thermally reduced TiO_2 was provided by the TPD experiment of Perkins and Henderson[37] performed on a TiO_2(110) sample dosed with oxygen and water overlayers. On UV irradiation of a vacuum annealed TiO_2(110) surface that had previously been exposed to a saturation coverage of molecular oxygen, TPD experiments showed that some of the adsorbed oxygen still remained after the cessation of the irradiation. This observation was explained by a dissociation of the oxygen molecules on the surface to fill in the bridging oxygen vacancies that were generated during the vacuum annealing process.

The photodesorption was found to be made up of two contributions.[37] The first was from O_2 adsorbed in association with bridging oxygen vacancy sites; these sites were deactivated by a single oxygen exposure and did not contribute to further photodesorption on subsequent adsorption/ desorption cycles. The second contribution was accessible irrespective of the status of the bridging oxygen vacancies. These observations by Perkins *et al.*,[37] agree with those of Yates *et al.*,[38] that show two different forms of oxygen adsorption on TiO_2(110) at low temperatures.

Although there have been many experimental studies on the nature of oxygen adsorption on the TiO_2(110) rutile surface, there are comparatively very few studies on the anatase polymorph. Bonapasta and Filippone[39] performed a theoretical study on the effects of surface oxygen vacancies on the adsorption, photoreduction and chemical activity of O_2 on the TiO_2(100) anatase surface. They considered a 2-coordinate oxygen vacancy at the surface of the crystal lattice, termed V_O, in which two electrons are left in

the defect state. The bonding and electronic structures of the adsorbed O_2 molecule on the surface were investigated by consideration of three systems: (i) an O_2 molecule located in the vacuum region away from the surface, (ii) an O_2 molecule adsorbed on the surface and (iii) an O_2^- radical adsorbed on the perfect surface and at a surface vacancy.

In the first system there were no electronic levels introduced in the bandgap of the anatase, as would be expected for a non-interacting molecule. In the second system however, there was an acceptor level induced at 0.23eV above the valence band. There was a weak bond formed between the O_2 molecule and a Ti^{4+} cation, resulting in Ti-O bond distances of 2.28Å and 3.11Å. In the third system, there was electron transfer from the surface to the adsorbed O_2 resulting in the formation of an O_2^- radical. On the perfect surface, both of the O atoms of the O_2^- molecule were calculated to be bonded to the same Ti surface atom in a symmetric configuration with two strong Ti-O bond distances of 2.07Å. Bonapasta and Filippone[39] suggested that this strong bond could hinder the participation of O_2^- species in reactions with other molecules. However, in chapter 6 it will be shown that surface stabilised superoxide anions on the surface of P25 TiO_2 can react with adsorbed acetone.

When an O_2 molecule was adsorbed at a 2-coordinate vacancy site on the anatase (100) surface, each O atom of the molecule was calculated to be bonded to one of the two Ti atoms neighbouring the vacancy with Ti-O bond lengths of 1.91Å and 1.86Å. The energy required to break the molecule from the surface was increased compared to the energy previously calculated for the perfect surface. An important conclusion drawn by Bonapasta and Filippone[39] related to the relative photoactivity of the superoxide complex on the perfect surface and at the vacancy site. Photoreduction of the $O_{2(ads)}^{-1}$ on the perfect surface was observed to be incomplete, meaning that this species was not photo-labile. However, the calculations showed that the release of O_2^- radicals under the influence of photoirradiation was strongly favoured in the presence of surface vacancies and by photogenerated electrons. This result again strongly supports the assignment of the signal at $g_{zz} = 2.019$ to a superoxide radical stabilised at a vacancy site on the TiO_2 surface.

5.4.6 Superoxide diffusion

It was seen earlier that oxygen adsorption at room temperature onto a thermally reduced TiO_2 surface (see Figure 5.2) resulted in a different distribution of superoxide radicals on the surface compared to the case when a reduced sample was exposed to oxygen at 120K followed by annealing to room temperature (see Figures 5.8 and 5.9). In particular, oxygen adsorption at room temperature leads to superoxide speciation at four well defined sites [g_{zz}(I) = 2.019, g_{zz}(II) = 2.023, g_{zz}(II′) = 2.020 and g_{zz}(III) = 2.026] with the order of site abundance being I>II> II′>III. However, the distribution of the superoxide radicals after annealing a sample exposed to oxygen at 120K to 298K under static vacuum is seen to be in the order III>II>II′>I (Table 5.2). As the overall intensity of the superoxide signal remains constant during the annealing process, it is concluded that migration of the superoxide must occur across the surface between the different stabilisation sites.

The migration of superoxide radicals across a solid oxide surface has previously been demonstrated by Dyrek *et al.*,[40] on the CoO-MgO surface. The superoxide anions formed over this surface were initially stabilised at two different Co^{3+} cations, giving rise to two slightly different O_2^- species, labelled A and B. On gentle annealing of the sample, species A and B transformed into another O_2^- radical, labelled species C, which was assigned to superoxide radicals stabilized on Mg^{2+} cations.

In Figure 5.7 it was demonstrated that the superoxide anions on the TiO_2 surface have a tendency to change their localization over time, even when not subjected to thermal treatment. It was seen that immediately after the superoxide anion was formed and stabilized on the surface following oxygen exposure at 298K, the distribution in abundance of the superoxide radicals were in the order of site I>II>>II′>III. On subsequent recording of the signal on consecutive days, the dynamics of the O_2^- radical on the surface at room temperature had led to changes in the distribution of the signal in the g_{zz} region. Redistribution of superoxide radicals on the surface as a function of time has also been witnessed on the $O_2^- - Mg^{2+}$ system (CoO-MgO), as shown in Figure 5.20.[40] The number of adsorption sites and their variety increased after several days of maintaining the sample at room temperature, as evidenced by the gradual spreading of the values of the g_{zz} component, a decreasing overall intensity and finally the disappearance of the EPR signal.

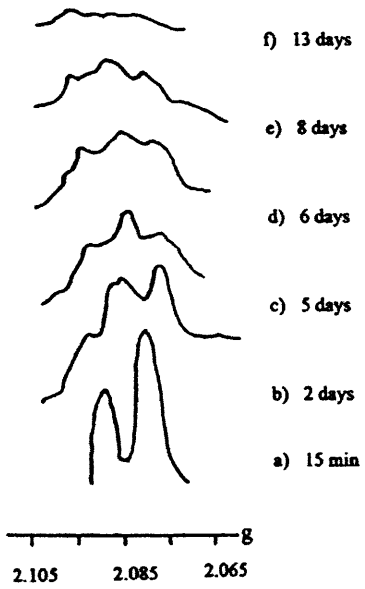

Figure 5.20 Evolution of the g_{zz} component of O_2^- stabilized on Mg^{2+} at room temperature as a function of time.[40]

Previous work on oxygen adsorption onto single crystals of $TiO_2(110)$ has shown there to be two different adsorption pathways for oxygen on the reduced sample. Henderson *et al.*,[9] reported that at temperatures below 150K oxygen adsorbs with a high initial sticking probability suggestive of precursor-mediated kinetics. Evidence was found for a temperature dependency between molecular and dissociative adsorption, with dissociative adsorption being favoured at adsorption temperatures above 150K.[9] Adsorption at 120K resulted in oxidation of the surface oxygen vacancies but as the adsorption temperature was increased, there was increased dissociation of the molecule leading to oxidation of the vacancy sites and removal of electron density necessary for charge transfer formation of the O_2 species. The shift toward dissociative behaviour with increasing adsorption temperature was postulated to be as a result of more favourable kinetics for O_2 dissociation with increasing temperature, suggesting that it is an activated process.[9]

From data provided by ELS measurements, combined with results from DFT calculations, Henderson *et al.*,[9] proposed that the molecularly adsorbed oxygen species bind to the surface in an η^1 configuration resulting in molecular desorption above 410K. The adsorbed species that resulted in dissociation and vacancy filling were thought to be originally bound in an η^2 configuration.[9] Further, on annealing the sample after oxygen adsorption at 120K, two possible pathways were identified as being available for the adsorbed oxygen; (i) molecular desorption at temperatures above 410K and (ii)

irreversible dissociation of the oxygen molecule resulting with oxygen vacancy filling and adsorbed adatoms.

Migration of adsorbed oxygen species was also found to occur between the two α-O_2 and β-O_2 adsorption states identified by Lu *et al.*,[34,35] on a 900K annealed rutile surface. When oxygen was exposed to the surface at low adsorption temperatures (105K) this resulted in a higher population of α-O_2 states on the surface. These could be converted to the β-O_2 state by annealing the substrate to temperatures >250K. Above 400K the β-O_2 was dissociated to atomic oxygen, resulting in titration of the oxygen vacancy sites. These results indicate that the oxygen adsorbed in the β-O_2 state is more strongly bound to the surface. The authors suggested that the thermal conversion process between the two modes of oxygen adsorption was due to an alteration of the O_2 adsorption configuration at an anion vacancy defect.[34,35]

These observations of Lu *et al.*,[34,35] support the results shown in Figure 5.8, which showed that after annealing a sample exposed to oxygen at low temperatures, the relative distribution of the O_2^- radicals on the surface changed from adsorption at vacancy sites to non-vacancy sites. From Figure 5.4, it was shown that the O_2^- anions stabilised at the non-vacancy sites were stable on the surface at 353K, whereas those stabilised at the vacancy site had decayed at temperatures of 333K. These observations support the earlier assignment of vacancy adsorbed O_2^- to the α-O_2 states (and non-vacancy adsorbed O_2^- to the β-O_2 state) as described by Lu *et al.*,[34,35] and also that non-vacancy adsorbed species are more strongly bound to the surface. It must be noted that the results of Lu *et al.*,[34,35] were performed on the rutile surface, therefore the stabilisation and conversion temperatures quoted may be quantitatively different for the results presented here on the anatase surface; however, the trend of observations remains important.

Schaub *et al.*,[41] performed a detailed STM study on the diffusion of oxygen vacancies across the TiO_2(110) surface to elucidate four possible mechanisms of diffusion. They found experimental evidence to suggest that the O vacancy diffusion proceeds exclusively along the [110] direction perpendicularly to the bridging oxygen rows. The diffusion was not seen to occur on a surface in the absence of adsorbed molecular oxygen, therefore the process was determined to be an adsorbate-mediated mechanism. One of the diffusion mechanisms suggested involved the dissociation of an adsorbed oxygen molecule. An O_2-vacancy complex was formed at the surface and subsequently dissociated. One of the O atoms of the complex filled the vacancy while

the other was ejected laterally onto a neighbouring Ti row as an O adatom. The O adatom was observed to be highly reactive and subsequently abstracted an O atom from a neighbouring bridging oxygen row to form an adsorbed O_2 molecule. Thus, the final configuration on the surface was an O_2 molecule remaining in the original Ti row and an oxygen vacancy in a neighbouring row of bridging oxygen rows. The overall process is illustrated schematically in Figure 5.21.

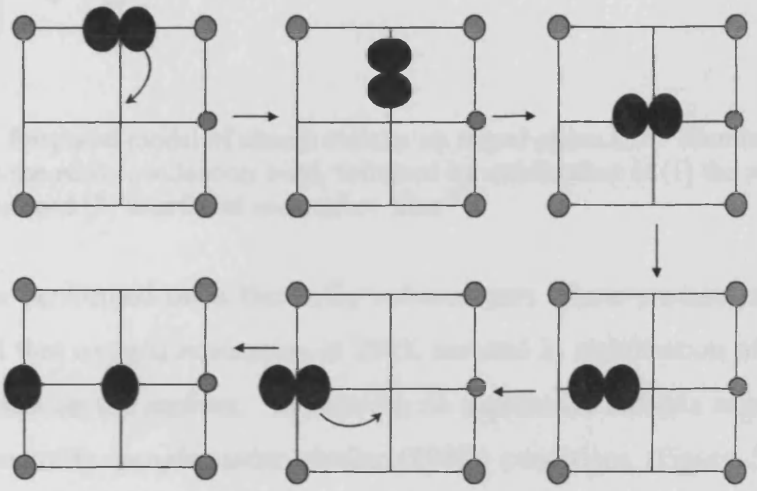

Figure 5.21 Schematic representation of the suggested vacancy migration mechanism. Small grey dots represent lattice oxygen, large black dots represent adsorbed oxygen.[41]

5.4.7 Interfacial sites

The chemistry of the interfacial sites between the anatase and rutile phases of mixed-phase Degussa P25 has attracted much attention in the past. The interfacial sites can affect the recombination of photogenerated charge carriers and therefore affect the resulting photocatalytic activity. Notably, the photocatalytic activity of the mixed-phase was widely reported to be enhanced compared to that of either of the pure phases. The first papers published on this topic proposed that the enhanced activity was due to the transfer of photogenerated electrons on the anatase phase to lower energy trapping sites on the rutile phase, thereby reducing the recombination rate of the charge carriers.[42-44] However, Hurum *et al.*,[15,16] performed a series of EPR investigations on P25 TiO_2 and provided an alternative explanation for the chemistry of the mixed-phase sample. The authors[15,16] proposed that the photogenerated electrons migrated from the rutile phase to the anatase phase on the basis that the anatase trapping site is lower in energy than the rutile conduction band, as shown in Figure 5.22.

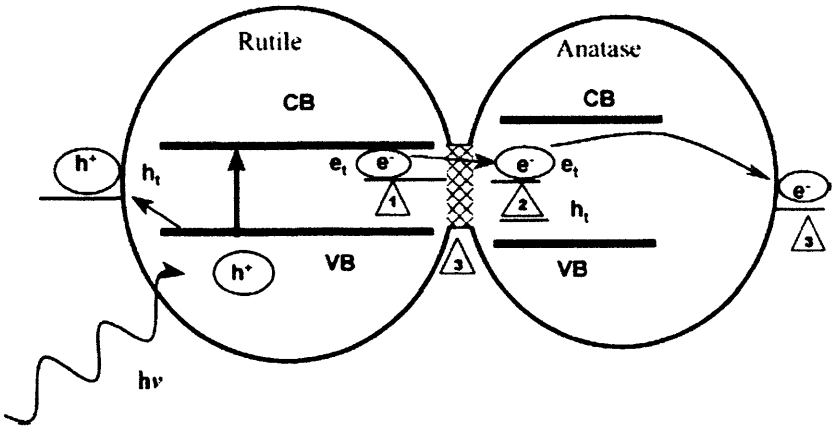

Figure 5.22 Proposed model of charge transfer on mixed-phase P25. Illumination promotes an electron into the rutile conduction band, followed by stabilisation in (1) the rutile lattice, (2) the anatase lattice and (3) interfacial and surface sites.[16]

Studies performed on a thermally reduced pure phase anatase sample (Figure 5.14a) showed that oxygen adsorption at 298K resulted in stabilisation of O_2^- anions at well-defined sites on the surface. In contrast, no superoxide radicals were observed on the pure phase rutile sample under similar (298K) conditions (Figure 5.14b). From these results, it is determined that the O_2^- species on the P25 TiO_2 material are stabilised at surface sites on the anatase phase of the material. This assignment provides confirmation of the proposed model of charge transfer events in mixed-phase P25, as described by Hurum *et al.*[15,16]

5.5 Conclusion

The surface chemistry of TiO_2 has been widely studied in the past. From studies of single crystal samples, the structure of the perfect and defective surfaces are well understood. STM experiments image the surface and reveal that the thermally annealed surface contains large numbers of oxygen vacancy sites, which are commonly associated with the high catalytic activity of this material. Using EPR it has been shown that there are several stabilisation sites available for the superoxide anion on the reduced polycrystalline surface, identified by differences in the g_{zz} component of the orthorhombic EPR signal.

Oxygen exposure at room temperature preferentially leads to stabilisation of O_2^- at vacancy sites on the surface, identified by a g_{zz} value of 2.019. The vacancy stabilised superoxide radicals were seen to be thermally unstable at temperatures of 333K, whereas O_2^- radicals stabilised at non-vacancy sites were stable on the surface at

temperatures of 353K. Superoxide radicals at the vacancy site exhibited low temperature photo-lability, which was not observed for the non-vacancy bound species. The *relative* contribution to the overall signal intensity from vacancy stabilised superoxide radicals decreased when oxygen was exposed to the reduced surface at low temperatures. Changes in the profile of the g_{zz} component identified on annealing a sample exposed to oxygen at 120K to 298K, indicated that O_2^- radicals undergo migration between the different stabilisation sites on the surface in this temperature regime. Sub-surface electrons in the thermally reduced TiO_2 sample remained un-reacted following low temperature oxygen adsorption until further exposure to molecular oxygen at room temperature.

The number of O_2^- radicals on the photoactivated surface was lower than on the thermally reduced surface due to the immediate decay of the radical under the influence of the UV irradiation. Differences in the adsorption behaviour of molecular oxygen over the two polymorphs of TiO_2 (anatase and rutile) were identified. In particular, the superoxide radical was stabilised on the anatase surface at all oxygen adsorption temperatures. By comparison, $HOO^{\bullet}$ radicals were formed on the rutile surface at room temperature; O_2^- was only stabilised on this sample following oxygen exposure at low temperature.

Finally, it has been shown that the speciation of superoxide radicals on the TiO_2 surface can be manifested in both the g and A tensors of the spin Hamiltonian. Three different couplings in the A_{xx} direction were resolved due to the location of the unpaired electron in the π_x^* orbital. These results demonstrate how EPR can be used to identify different stabilisation sites for adsorbed radicals on the surface of polycrystalline samples, and emphasize the need to perform detailed investigations of the single crystal samples in order to make accurate assignments for these sites on the surface.

5.6 References

[1] P. C. Maness, S. Smolinski, D. M. Blake, Z. Huang, E. J. Wolfrum, W. A. Jacoby, *App. and Envt. Microbiol.*, **1999**, *65*, 4094.

[2] M. Gratzel, *Nature,* **2001**, *414*, 338.

[3] M.A. Fox, M.T. Dulay, *Chem. Rev.*, **1993**, *93*, 341.

[4] M.R. Hoffman, S.T. Martin, W. Choi, D.W. Bahnemann, *Chem. Rev.*, **1995**, *95*, 69.

[5] A.L. Linsebigler, G. Lu, J.T. Yates, Jr., *Chem. Rev.*, **1995**, *95*, 735.

[6] G. Lu, A.L. Linsebigler, J. T. Yates, Jr., *J. Phys. Chem.*, **1995**, *99*, 7626.

[7] S. Funk, U. Burghaus, *Phys. Chem. Chem. Phys.*, **2006**, *8*, 4805.

[8] K. Fink, *Phys. Chem. Chem. Phys.*, **2006**, *8*, 1482.

[9] M. Henderson, W.S. Epling, C.L. Perkins, C.H.F Peden, U. Diebold, *J. Phys. Chem. B*, **1999**, *103*, 5328.

[10] A.J. Tench, P. Holroyd, *Chem. Comm.*, **1968**, *8*, 471.

[11] M. Chiesa, E. Giamello, M.C. Paganini, Z. Sojka, D.M. Murphy, *J. Chem. Phys.*, **2002**, *116*, 4266.

[12] R.F. Howe, M. Grätzel, *J. Phys. Chem.*, **1985**, *89*, 4495.

[13] R.F. Howe, M. Grätzel, *J. Phys. Chem.*, **1987**, *91*, 3906.

[14] Y. Nakaoka, Y. Nosaka, *J. Photochem. and Photobiol. A*, **1997**, *110*, 299.

[15] D.C. Hurum, A.G. Agrios, K.A. Gray, T. Rajh, M.C. Thurnauer, *J. Phys. Chem. B*, **2003**, *107*, 4545.

[16] D.C. Hurum, A.G. Agrios, S.E. Crist, K.A. Gray, T. Rajh, M.C. Thurnauer, *J. Elect. Spec. and Rel. Phen.*, **2006**, *150*, 155.

[17] E. Serwicka, M.W. Schlierkamp, R.N. Schindler, *Z. Naturforsch*, **1981**, *36*, 226.

[18] C. Naccache, P. Meriaudeau, M. Che, A.J. Tench, *Trans. Faraday Soc.*, **1971**, *67*, 506.

[19] M. Che, A.J. Tench, *Adv. Catal.*, **1983**, *32*, 1.

[20] A. Adamski, T Spalek, Z. Sojka, *Res. Chem. Intermed.*, **2003**, *29*, 793.

[21] A.L. Attwood, D.M Murphy, J.L. Edwards, T.A. Egerton, R.W. Harrison, *Res. Chem. Intermed.*, **2003**, *29*, 449.

[22] M. Che, A.J. Tench, *Adv. Catal.*, **1982**, *31*, 77.

[23] A.L. Attwood, *PhD Thesis*, **2003**, Cardiff.

[24] M. Setaka, S. Fukazawa, Y. Kirino, T. Kwan, *Chem. Pharm. Bull.*, **1968**, *16*, 1240.

[25] M. Dufaux, M. Che, C. Naccache, *C.R. Acad. Sci.*, **1969**, *268*, 2255.

[26] C.A. Jenkins, D.M. Murphy, *J. Phys. Chem. B*, **1999**, *103*, 1019.

[27] E. Garrone, A. Zecchina, F.S. Stone, *Phil. Mag. B*, **1980**, *42*, 683.

[28] E. Giamello, P. Ugliengo, E. Garrone, *J. Chem. Soc., Faraday Trans. I*, **1989**, *85*, 1373.

[29] V.A. Shvets and V.B. Kazansky, *J. Catal.*, **1972**, *25*, 123.

[30] J.R. Morton, *Chem. Rev.*, **1964**, *64*, 453.

[31] M. Che, A.J. Tench, S. Coluccia, A.J Zecchina, *J. Chem. Soc. Faraday Trans. I*, **1976**, *72*, 1553.

[32] P. Meriaudeau, C. Naccache, A.J. Tench, *J. Catal.*, **1971**, *21*, 208.

[33] A. Kazusaka, L.K. Yong, R.F. Howe, *Chem. Phys. Lett.*, **1978**, *57*, 592.

[34] G.Lu, A. Linsebigler, J.T. Yates Jr., *J. Chem. Phys.*, **1995**, *102*, 3005.

[35] G.Lu, A. Linsebigler, J.T. Yates Jr., *J. Chem. Phys.*, **1995**, *102*, 4657.

[36] W.S. Epling, C.H. F. Peden, M.A. Henderson, U. Diebold, *Surf. Sci.*, **1998**, *412*, 333.

[37] C.L. Perkins, M.A. Henderson, *J. Phys. Chem. B*, **2001**, *105*, 3856.

[38] C.N. Rusu, J.T. Yates Jr., *Langmuir*, **1997**, *13*, 4311.

[39] A. Amore Bonapasta, F. Filippone, *Surf. Sci.*, **2005**, *577*, 59.

[40] K. Dyrek, A. Adamski, Z. Sojka, *Spect. Acta A.*, **1998**, *54*, 2337.

[41] R. Schaub, E. Wahlstrom, A. Ronnau, E. Laegsgaard, I. Stensgaard, F. Besenbacher, *Science*, **2003**, *299*, 377.

[42] R.I. Bickley, T. Gonzalez-Carreno, J.S. Lees, L. Palmisano, R.J.D. Tilley, *J. Solid State Chem.*, **1991**, *92*, 178.

[43] T. Ohno, K. Sarukawa, K. Tokieda, M. Matsumura, *J. Catal.*, **2001**, *203*, 82.

[44] A.K. Datye, G. Riegel, J.R. Bolton, M. Huang, M.R. Prairie, *J. Solid State Chem.*, **1995**, *115*, 236.

Chapter 6

Free radical pathways in the decomposition of ketones over polycrystalline TiO_2; The role of organoperoxy radicals.

6.1 Introduction

Photocatalytic oxidation of organic pollutants is extensively used for the remediation of waste water and as a means of indoor air purification.[1] In particular, growing attention is now placed on the study of volatile organic compounds (VOCs) as they have been shown to be a major contributing factor in the formation of lower atmosphere ozone and are considered to be harmful to human health over long-term exposure.[2] Heterogeneous photocatalytic oxidation has proven itself to be a promising technique for the remediation of both aqueous and gaseous VOCs. The experimental conditions are mild, requiring only a UV or near-UV light source in the presence of a semiconductor to oxidise the VOCs into carbon dioxide and water. On absorption of a photon with energy equal to or greater than the band gap of the semiconductor, an electron/hole pair is generated in the bulk. These charge carriers migrate towards the catalyst surface where they participate in redox reactions with the adsorbed organic molecules. Since the early work of Fujishima and Honda,[3] the use of titanium dioxide (TiO_2) in UV assisted catalysis has proven to be of significance due to its ready availability, low cost and high corrosion resistance. As a result, numerous studies have appeared in the literature describing the mechanism of photooxidation over TiO_2.

In many of these studies, surface (and desorbed gaseous) radical intermediates have been proposed and implicated in the photooxidation mechanism.[4-6] Nevertheless, it is clear from several studies that the presence of oxygen and water is crucial in controlling the reaction pathways often *via* the intermediacy of active oxygen species.[7-9] Among the many studies devoted to photooxidation over polycrystalline and single crystal TiO_2,[10] acetone has received considerable attention.[11-20] Coronado *et al.*,[11] used simultaneous FTIR analysis and DRIFT spectroscopy to study the gas-phase species and surface of the TiO_2 powder following UV irradiation of adsorbed acetone. Their data suggested that on prolonged exposure of acetone vapour to the TiO_2 surface, interaction of surface hydroxyl groups with acetone molecules occurred through hydrogen bonding. The DRIFT results provided evidence of both formaldehyde and acetaldehyde formation, which they believe are plausible intermediates of acetone photocatalytic oxidation.[11] In a very thorough series of studies, Henderson[12,13] used

TPD and photodesorption to identify the nature of the surface intermediates formed on the $TiO_2(110)$ surface following acetone photooxidation. It was proposed that the photooxidation involves a thermal reaction between surface adsorbed acetone and an adsorbed oxygen species forming an $\{acetone\text{-}oxygen\}_{(a)}$ complex.[13] Photodecomposition of this complex was shown to occur *via* photogenerated charge carriers in the substrate through a mechanism involving methyl radical ejection from the surface and conversion of the complex to surface bound acetate. Despite the growing evidence for the role of active oxygen species in such reactions, surprisingly few studies have been devoted to exploring the radical nature of these intermediates.

One of the most direct means of identifying radical intermediates in surface reactions is to use Electron Paramagnetic Resonance (EPR) spectroscopy, which has been successfully applied to study a range of radicals on both hydrated and dehydrated polycrystalline TiO_2 powders.[21-34] In many of these studies ionic oxygen centred radicals including O^-, O_3^- and particularly O_2^- were reported, with specific relevance to photoadsorption phenomena or as probes to identify the distribution of radicals formed on the surface. However, other types of oxygen based radicals have received far less attention,[20-22] and these include the series of thermally unstable peroxyacyl radicals (of general formula $RCO_3^{\bullet}$)[21] and peroxy radicals (of general formula $ROO^{\bullet}$)[20] which were identified on TiO_2 following low temperature UV irradiation under co-adsorbed aldehyde:O_2 and acetone:O_2, respectively. Che was one of the first pioneers in this field, and established that a peroxy ($ROO^{\bullet}$) based radical could be formed using co-adsorbed ethylene:O_2 mixtures on TiO_2.[22] Because these transient radical species[18,20,22] are so thermally unstable, they are often not easily detected and can be completely missed during the experimental observation. Instead the more thermally stable superoxide radical (O_2^-) may exist as the sole remaining EPR visible species at room temperature, which may be only partially responsible for the photooxidation process.

In the present chapter it will be demonstrated that a series of reactive oxygen species, particularly organo-peroxy radicals, are responsible for the decomposition of various ketones over polycrystalline (P25) TiO_2 both in dark and in radiative conditions. As will be shown, these radicals can be formed not only through hole mediated processes, but also through electron mediated processes following irradiation of the TiO_2 substrate, and the type of organoperoxy radical observed depends on the adopted experimental conditions, particularly the oxygen pressure. Despite the general importance of organoperoxy radicals in the oxidation of aldehydes and ketones in

solution, their role in heterogeneous photocatalysis has not been seriously considered or demonstrated until now.

6.2 Experimental

Two samples of TiO_2 were used throughout this work, namely Degussa P25 and Rutile A. Full experimental details have been given previously in Chapter 4 (pg 89). In brief, samples of *activated* TiO_2 were prepared on the vacuum manifold, as described in section 4.6.2. The activated sample was subsequently exposed to the probe gases mixed with oxygen (acetone:O_2, butanone:O_2, 4-heptanone:O_2, cyclopentanone:O_2 and cyclohexanone:O_2) at 298K from a vacuum manifold. The ketone to O_2 ratio (i.e., ketone:O_2) was ~5:1 in all experiments. The samples containing the co-adsorbed gases were then irradiated at 77K for a period of 30 minutes before rapid transfer to the pre-cooled EPR cavity, where the spectra were recorded at 120K. The direct reactivity of thermally and photochemically generated surface superoxide radicals (O_2^-) towards the ketones was also examined. In both cases, the ketone was exposed to the surface radicals at 77K, and then slowly annealed at elevated temperatures (210-220K) in the EPR cavity.

6.3 Results

6.3.1 Identification of a transient peroxy radical on activated TiO_2 (butanone:O_2)

Photoirradiation of polycrystalline and nanocrystalline TiO_2 (anatase or rutile) under an oxygen atmosphere will result in the formation of surface oxygen radicals as widely reported.[11,25,27] The same surface reactivity also occurs in the mixed phase P25 TiO_2 material.[20,23,25] The dominant radical formed *via* photoinduced interfacial electron transfer from surface Ti^{3+} centres to adsorbed O_2, is the superoxide radical anion O_2^-. This radical is easily characterised from its g tensor components (g_{xx} = 2.005, g_{yy} = 2.011 and a number of g_{zz} components in the region 2.017–2.026) and its well known stability at room temperature (i.e., the radical persists for several days under vacuum). A more detailed description on the EPR features of this radical has previously been given in Chapter 5.

By comparison, photoirradiation of polycrystalline TiO_2 containing a mixture of butanone and oxygen results in a dramatically different EPR spectrum (Figure 6.1).

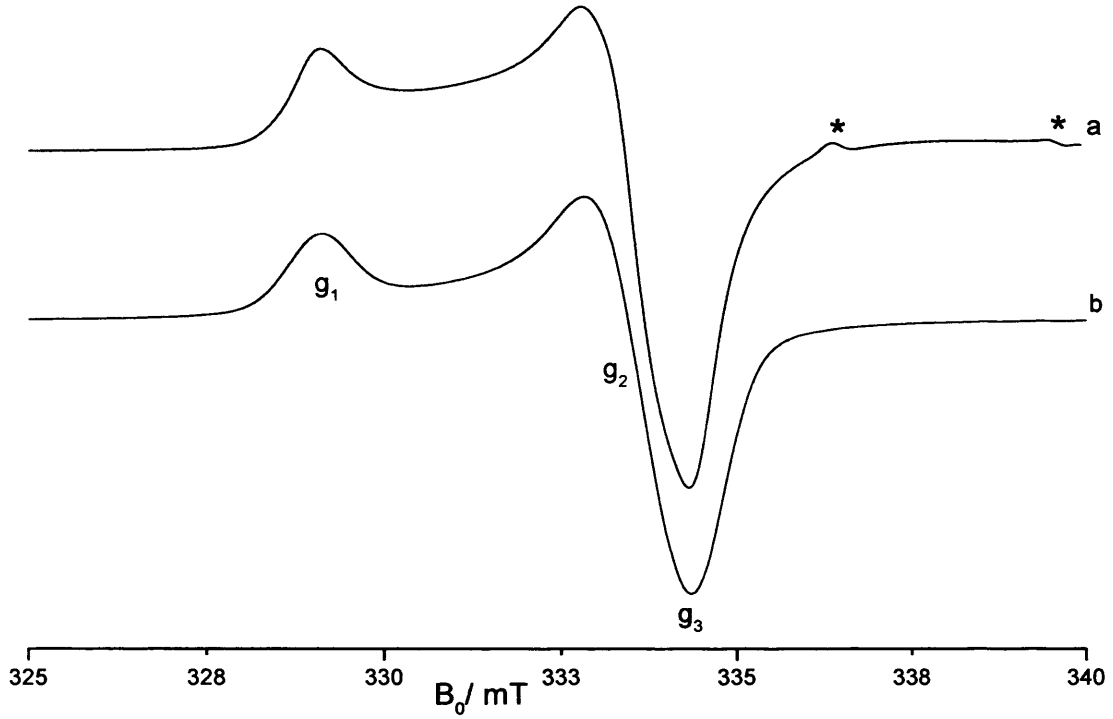

Figure 6.1 Experimental (a) and simulated (b) *cw*-EPR spectrum [120K] of photoirradiated (activated) TiO_2 (P25) containing co-adsorbed butanone:O_2 in a 5:1 ratio. The irradiation was performed at 77K.

This EPR spectrum was not observed following irradiation of TiO_2 containing adsorbed butanone only or following irradiation of (frozen) butanone. The spectrum was only observed when molecular oxygen was present, and importantly under butanone rich conditions (ie., > 5:1 butanone:O_2 ratio). At higher O_2 pressures (i.e., < 5:1 butanone:O_2 ratio), an EPR signal typical of the superoxide anion (Chapter 5) was instead obtained. The simulated EPR spectrum for this new signal is shown in Figure 6.1b and the resulting g values are listed in Table 6.1. The weak high field features at g = 1.991 and g = 1.973 (labelled * in Figure 6.1a) can be easily attributed to bulk Ti^{3+} cations at substitutional and lattice sites,[25,35] formed during low temperature irradiation, and were not included in the simulations.

As seen from Table 6.1, the g values for the superoxide anion (O_2^-) are significantly different compared to those observed for the new radical (g_1 = 2.0345, g_2 = 2.009, g_3 = 2.003) in Figure 6.1. According to the ionic model of the superoxide radical anion, originally proposed by Kanzig and Cohen for bulk halides,[36] the magnitude of the g_{zz} component is largely controlled by the local electric field gradient at the surface site (Ti^{4+}), which removes the degeneracy of the two π^* antibonding orbitals to an extent which depends on the strength of the local field gradient at the adsorption site. For TiO_2 these g_{zz} values usually fall within the range of 2.026 – 2.018,[37] with minor

variations in the g_{zz} distribution depending on the sample treatment and the physicochemical characteristics of the sample (eg., phase, morphology, particle size, *etc.*,). However, one does not usually observe g_{zz} values as high as 2.035 for ionic surface superoxide radicals on activated TiO_2. The g values of the new radical are more consistent with those expected of a peroxy type radical ($ROO^{\bullet}$). It is well known for example that the g values for $ROO^{\bullet}$ radicals are largely independent of the nature of the attached -R group, and commonly observed values are cited as $g_1 = 2.035$, $g_2 = 2.008$ and $g_3 = 2.003$.[38] This was also confirmed by Che[22] who reported the formation of an unstable peroxy radical over TiO_2 using ethylene:O_2 mixtures, with g values very similar to those found in this case (Table 6.1). Furthermore, the identification of the $CH_3COCH_2OO^{\bullet}$ peroxy radical over TiO_2 using acetone:O_2 mixtures was recently reported and an almost identical set of g values was obtained (Figure 6.2).[20] Therefore, based on the preceding observations and discussions it is clear that a peroxy type radical ($ROO^{\bullet}$) is also formed in the butanone:O_2 case.

Table 6.1 g values and ^{17}O hyperfine parameters for oxygen centred radicals and organoperoxy species on polycrystalline TiO_2. Values in italics could not be accurately obtained.

Species	g_1	g_2	g_3	$A_{\|\|}$(i)	$A_{\|\|}$(ii)	ρ	comments	Ref.
Ti^{3+} (bulk / surface)	$g_\perp = 1.990$; $g_{\|\|} = 1.957$							[25]
O_2^-	I 2.019	2.011	2.005	$A_{xx} = 7.64$			*Chapter 5*	
	II 2.023	2.011	2.004	$A_{xx} = 7.86$				
	III 2.026	2.011	2.001	$A_{xx} = 7.97$				
$CH_3COCH_2OO^{\bullet}$	2.0345	2.007	2.001	9.45	5.52	0.61	*Acetone:O_2*	[20]
$CH_3CH_2COCH_2OO^{\bullet}$	2.0345	2.009	2.003	9.92	5.85	0.64	*Butanone:O_2*	
$CH_3OO^{\bullet}$	2.034	*2.007*	*2.003*				*$CH_3^{\bullet}$ + O_2*	
$CH_3CO_3^{\bullet}$	2.016	2.008	2.003				*Acetaldehyde:O_2*	[21]
$CH_3CO_3^{\bullet}$	2.012	*2.008*	*2.003*				*$CH_3CO^{\bullet}$ + O_2*	
$HO_2^{\bullet}$	2.025	2.010	2.003				*on TS1*	[39]
$HO_2^{\bullet}$	2.034	2.008	2.002				*on TiO_2*	[39]
[acetone-O_2^-]$_{(a)}$	I 2.035	2.008	2.003					
	II 2.032	2.008	2.003					

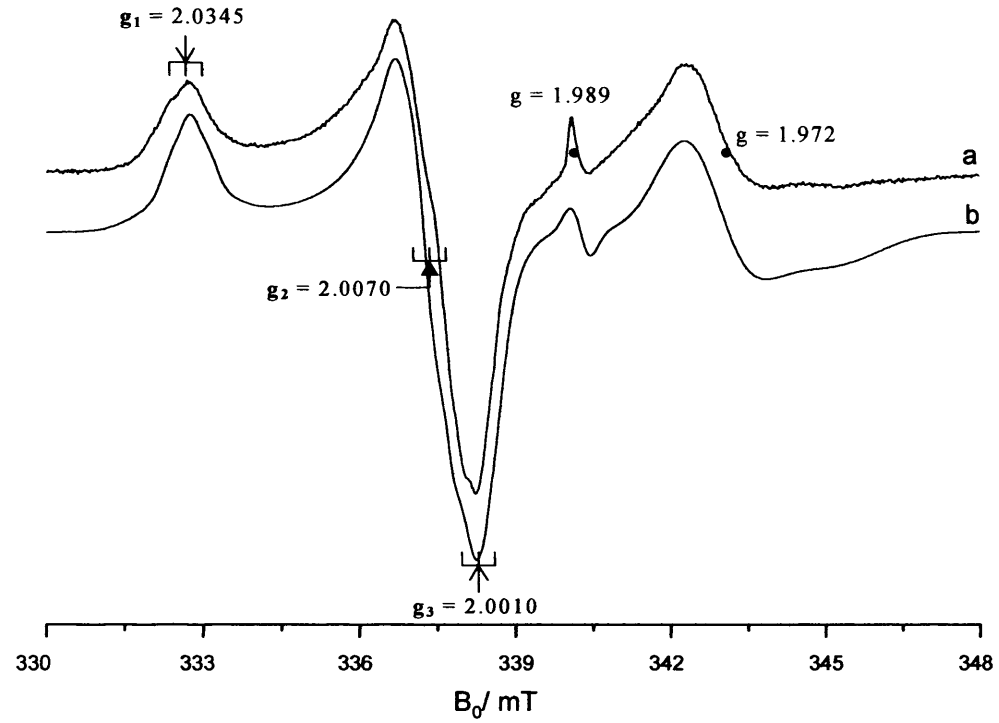

Figure 6.2 Experimental and simulated *cw*-EPR spectrum [10K] of photoirradiated (activated) TiO_2 (P25) containing co-adsorbed acetone:O_2 in a 10:1 ratio. The irradiation was performed at 100K.[20]

Further confirmation for this assignment can be obtained using isotopically enriched $^{17}O_2$. The hyperfine pattern for ^{17}O labelled ROO$^\bullet$ is distinctively different compared to other possible surface oxygen derived radicals such as O^-, O_2^-, O_3^- or even OH$^\bullet$ (i.e., they each produce a characteristic ^{17}O hyperfine pattern(s)). Due to the inequivalent spin densities on the two oxygen nuclei of the peroxy species, two different sets of sextets are observed (i.e., corresponding to R^{17}OO$^\bullet$ and RO^{17}O$^\bullet$), whereas only a single dominant sextet is found for the superoxide species indicating equal spin densities on the two oxygen nuclei of $^{17}O_2^-$. In the latter case a minor 11 line hyperfine pattern will also be observed if higher ^{17}O enrichment is used (i.e., $^{17}O^{17}O^-$). The experimental EPR spectrum of photoirradiated TiO_2 containing co-adsorbed butanone:$^{17}O_2$ is shown in Figure 6.3. Based on the relative abundance of the different isotopomers ($^{16}O_2$, $^{16}O^{17}O$ and $^{17}O_2$) for a 63% enriched $^{17}O_2$ sample, the experimental spectrum was satisfactorily simulated (Figure 6.3b). Analysis of the resulting simulation revealed the expected ^{17}O hyperfine couplings of $^{17O}A_{\|}$ (i) = 9.92mT (i.e., for RO^{17}O$^\bullet$) and $^{17O}A_{\|}$ (ii) = 5.85mT (ie., for R^{17}OO$^\bullet$) centred on the g_3 component at 2.003. This confirms the identity of the radical as an ROO$^\bullet$ type species. By comparison, the sextet hyperfine pattern for $^{17}O_2^-$ on TiO_2 is 7.6mT.[37] See also the references given in Chapter 5.

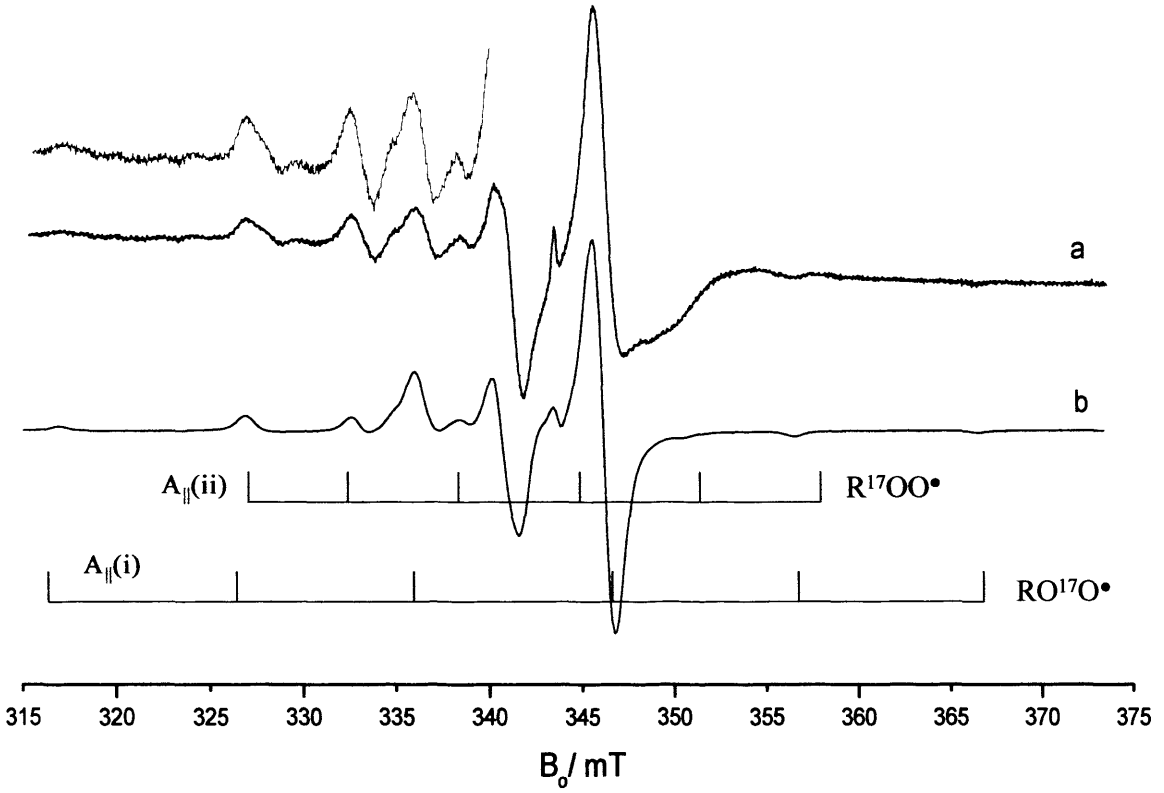

Figure 6.3 Experimental (a) and simulated (b) *cw*-EPR spectrum [120K] of photoirradiated (activated) TiO_2 (P25) containing co-adsorbed butanone:$^{17}O_2$ in a 5:1 ratio (63% isotopic enrichment of ^{17}O). The irradiation was performed at 77K.

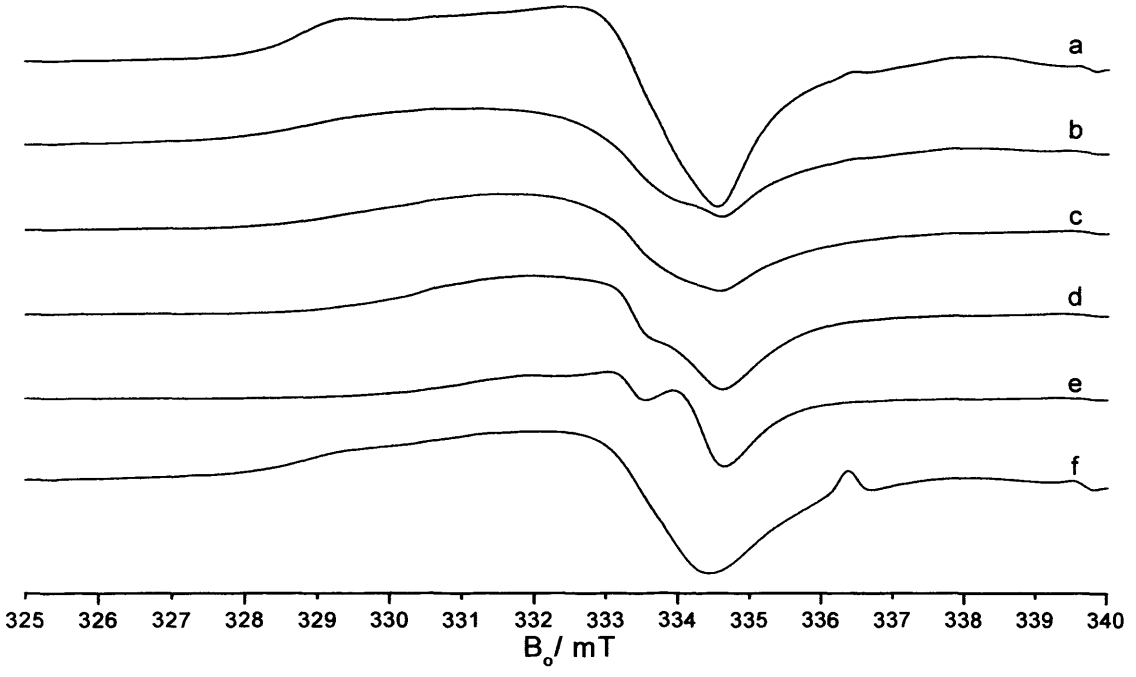

Figure 6.4 Experimental *cw*-EPR spectra of dehydrated TiO_2 (P25) after photoirradiation at 77K in the presence of co-adsorbed butanone and oxygen recorded at (a) 125, (b) 150, (c) 180, (d) 220, (e) 260K and (f) re-irradiated at 77K .

The surface organoperoxy radical in the butanone:O_2 case is not thermally stable on the TiO_2 surface. Gentle annealing of the sample from 120K to 300K leads to the progressive decrease and eventual destruction of the $ROO^{\bullet}$ EPR signal intensity, as shown in Figure 6.4. The signal can be reformed by photo-irradiation of the sample (containing butanone:O_2) at 77K. At 298K, only a weak EPR signal due to the background localised conduction electrons is observed.

6.3.2 Formation of transient peroxy radicals with other ketones

The formation of similar transient peroxy radicals was also examined with other ketones, including 4-heptanone, cyclopentanone and cyclohexanone. The resulting EPR spectra are shown in Figure 6.5. For comparison, the EPR spectra for the $ROO^{\bullet}$ radicals formed with acetone and butanone are also shown. The profile of the spectra, in particular the g values, are identical in all cases, with the slight exception of the g_3 component for the 4-heptanone:O_2 case (Figure 6.5c; labelled *). This small distortion in the g_3 value is due to the slightly higher concentration of the localised conduction electrons in the sample.

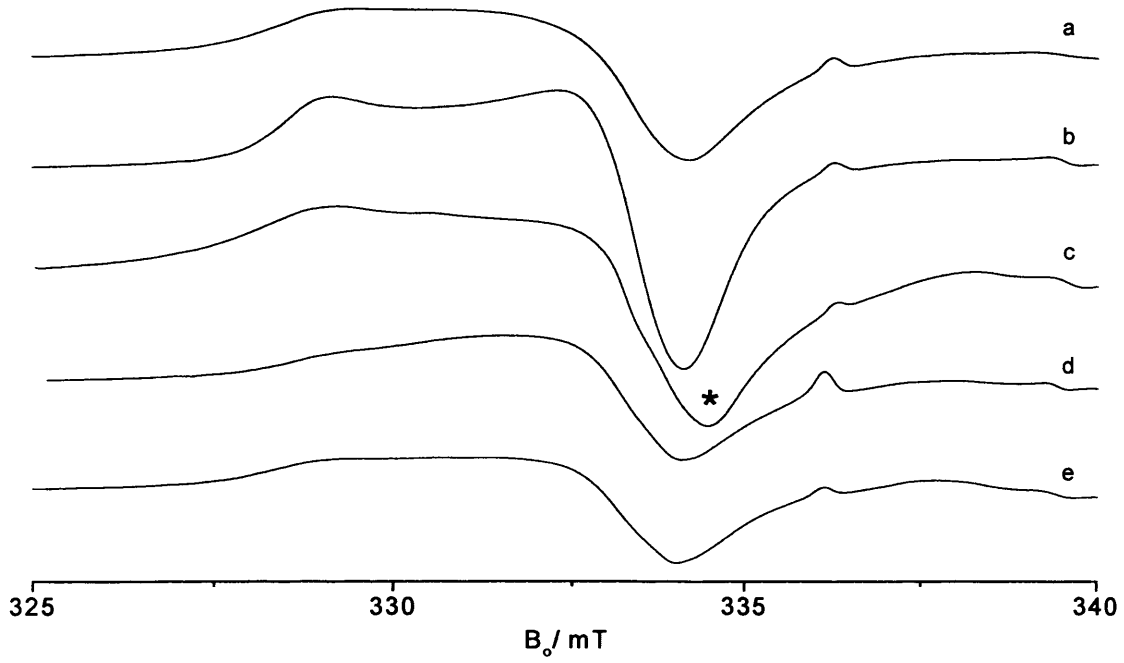

Figure 6.5 Experimental *cw*-EPR spectra [120K] of activated TiO_2 (P25) after photoirradiation at 77K in the presence of co-adsorbed (a) acetone:O_2, (b) butanone:O_2, (c) 4-heptanone:O_2, (d) cyclopentanone:O_2 and (e) cyclohexanone:O_2.

Furthermore, the temperature evolution of the EPR spectra for each radical in Figure 6.5 followed an identical trend to that shown in Figure 6.4 for butanone. In other words, all of the radicals decayed rapidly at temperatures greater than 200K. The decay of the radical formed on coadsorption of cyclohexanone and oxygen is shown in Figure 6.6. These results therefore indicate that a family of transient organoperoxy radicals (of general formula $ROO^{\bullet}$) are clearly formed during the low temperature (77K) photo-irradiation of ketones over dehydrated TiO_2 in the presence of molecular oxygen.

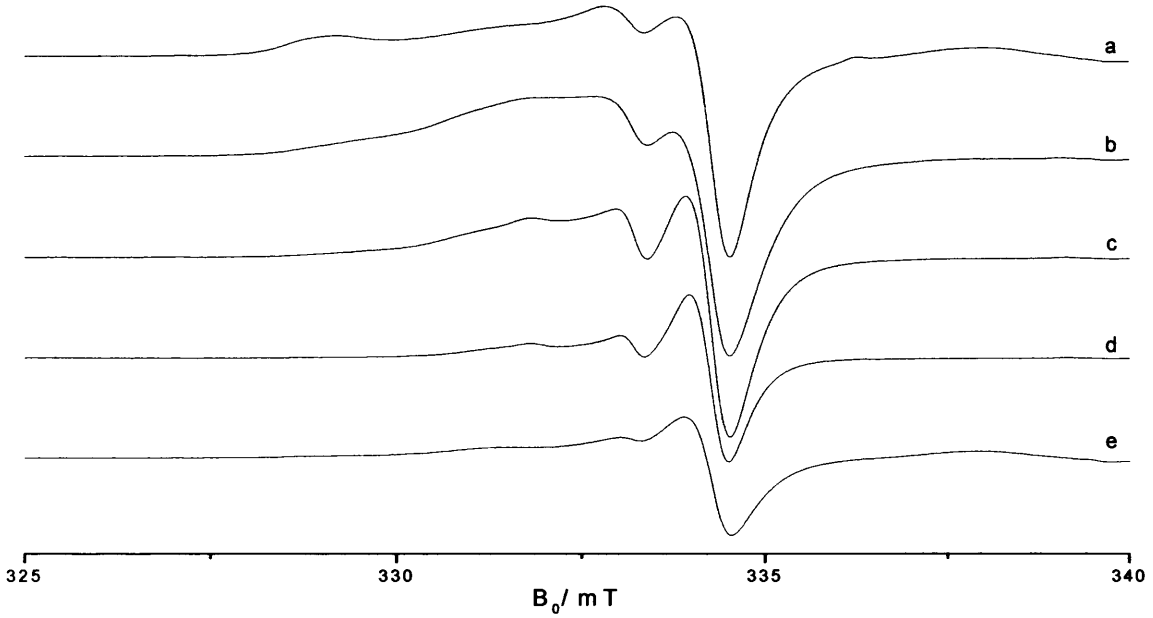

Figure 6.6 *cw*-EPR spectrum of dehydrated TiO_2 (P25) after photoirradiation at 77K in the presence of co-adsorbed cyclohexanone and oxygen recorded at (a) 120, (b) 200, (c) 240, (d) 290K and (e) 120K after annealing.

6.3.3 Superoxide reactivity with adsorbed acetone

Ionic superoxide radicals can be easily generated on TiO_2 by a number of methods including (a) by contact with H_2O_2,[39] (b) by direct O_2 adsorption on thermally reduced samples,[20,21,23] and by far the most commonly used method (c) by photoadsorption.[18,26,27,40-42] In methods (b-c) the radicals are formed at the gas-solid interface and they are reasonably stable at room temperature provided the sample is kept under vacuum and free from other surface adsorbates[23] particularly OH groups and water. In this study, the superoxide radicals were formed either by method (b), involving O_2 exposure to the reduced TiO_2 sample, or by method (c) involving photoirradiation of adsorbed oxygen on an activated TiO_2 sample. In both cases the EPR profiles for the resulting O_2^- radicals were generally similar. A typical EPR spectrum of the O_2^- radical generated on reduced P25 TiO_2 is shown in Figure 6.7a. The

spectrum is characterised by a well resolved set of features in the g_{zz} region with at least three distinct components at 2.019, 2.023 and 2.026. Exposure of this superoxide radical to acetone at 300K, results in the immediate and irreversible disappearance of the EPR signal. However, when the sample was exposed to acetone at 77K (as opposed to direct exposure at 300K) and the temperature was slowly raised from 200K - 220K, the EPR spectrum changed (Figure 6.7b-e). Two new signals, characterised by the g values of 2.035 and 2.032 appear at the expense of the O_2^- signal. After annealing to 300K, all of the EPR signals are once again completely destroyed.

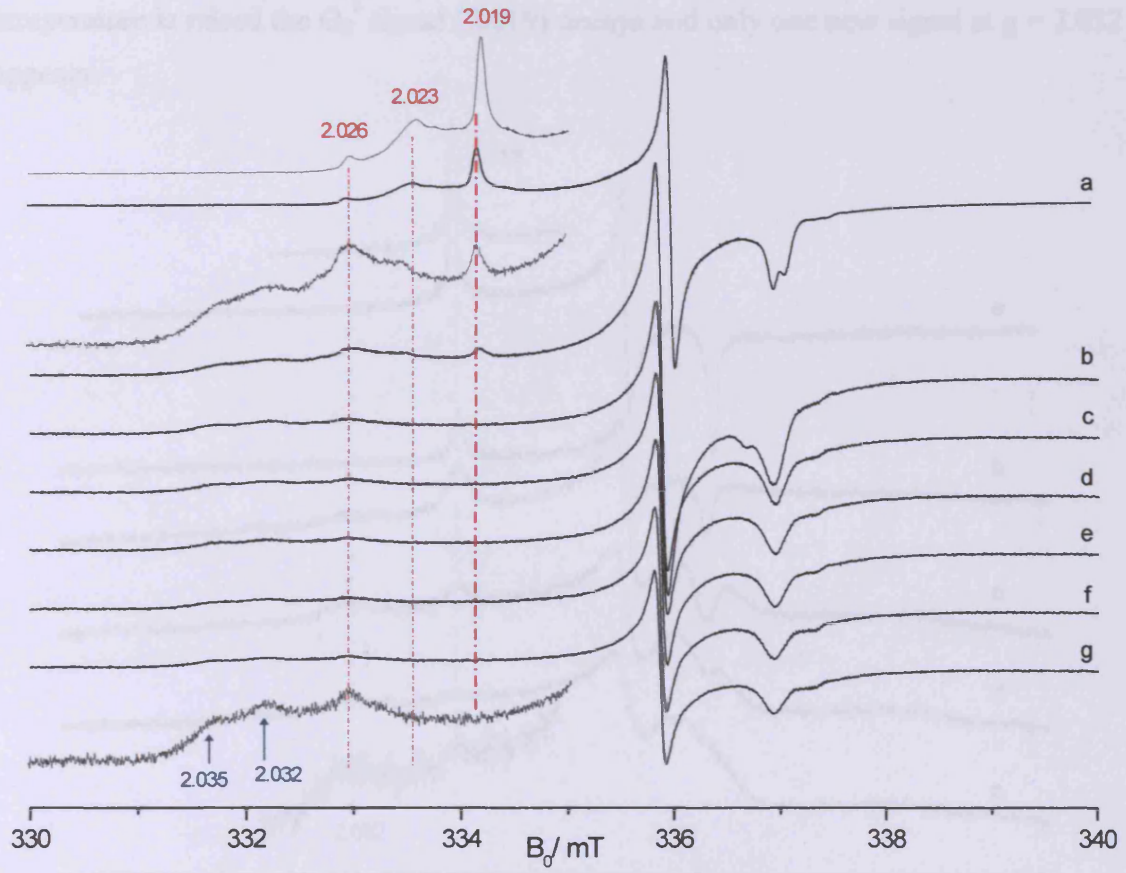

Figure 6.7 *cw*-EPR spectra of (a) superoxide radicals formed by O_2 exposure to a reduced TiO_2 sample. Acetone (18 Torr) was then admitted to the EPR cell at 77K, and the spectra were recorded at (b) 210, (c) 212, (d) 214, (e) 216, (f) 218 and (g) 220K.

The series of EPR spectra shown in Figure 6.7 evolve between the temperatures of 210K to 220K during which the different O_2^- species appear to react differently and *selectively* with acetone. As stated above, three different O_2^- species can be identified in the EPR spectrum, at g_{zz} = 2.019 (species I), 2.023 (species II) and 2.026 (species III). The first two O_2^- species (I and II) preferentially react with acetone, while the third O_2^- species (III) remains unreacted. Simultaneously, the two new signals at g = 2.035 and 2.032 appear in the spectrum at the expense of the two O_2^- species I and II.

The selectivity of the O_2^- radical is further evidenced when the experiment is repeated on a sample reduced to a lower temperature; therefore creating less defects and fewer reduced Ti^{3+} centres on the surface. A sample of (P25) TiO_2 was thermally reduced under vacuum to 573K and subsequently exposed to 10 Torr oxygen at 298K for 10 minutes. The excess oxygen was evacuated at this temperature. This treatment results in the formation of a superoxide signal as expected, but there is only one peak visible in the g_{zz} region at 2.019. On exposure of acetone (18 Torr) to the sample at 77K, followed by annealing, the spectra in Figure 6.8 were recorded. Notably, as the temperature is raised the O_2^- signal (2.019) decays and only one new signal at g = 2.032 appears.

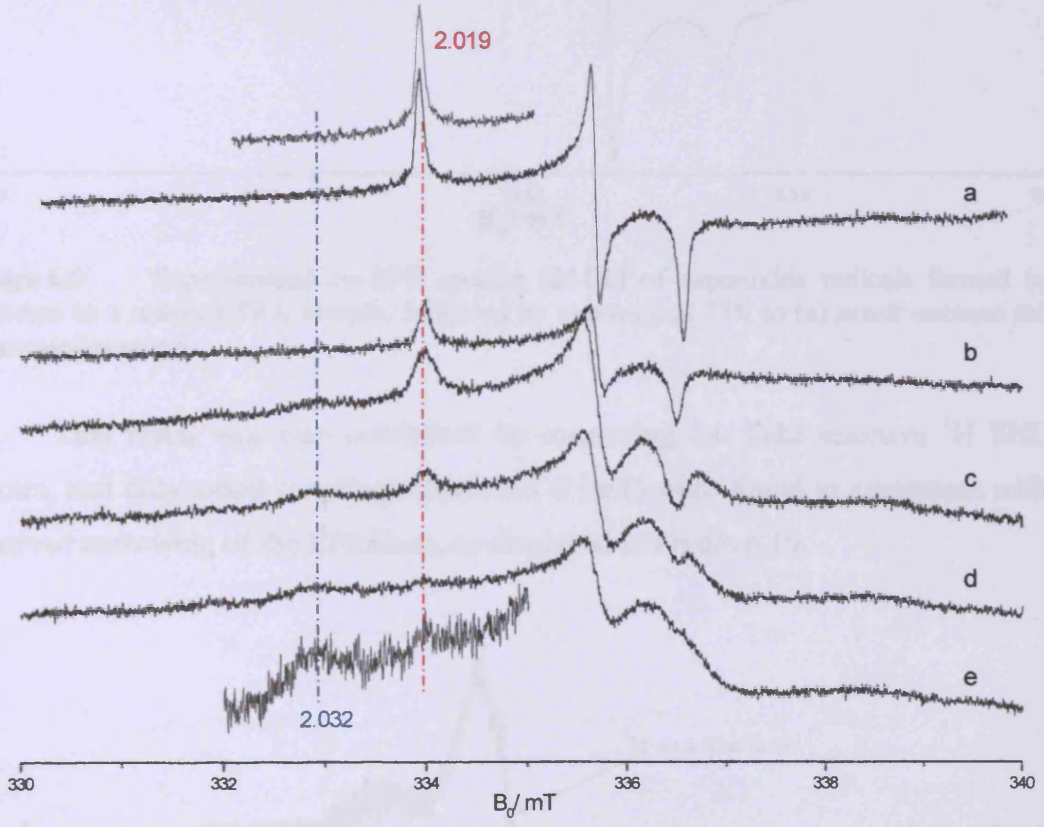

Figure 6.8 Experimental *cw*-EPR spectra of (a) the superoxide radical formed on a 573K reduced (P25) TiO_2 surface. The superoxide was then exposed to acetone (18 Torr) and annealed to (b) 210, (c) 212, (d) 214K and (e) 216K.

The series of spectra shown in Figure 6.8 suggest that the reaction between the surface adsorbed superoxide and acetone is an activated process. It is often not possible to make an assignment of a new radical based on g values alone, but information on the hyperfine couplings can aid in this process. Therefore to examine the proton hyperfine couplings in more detail, the experiment was repeated using perdeuterated d^6-acetone. The resulting spectrum is shown in Figure 6.9 along with the accompanying protic

acetone result for comparison. While a narrowing of the EPR lines can clearly be observed, no large couplings typical of $HO_2^{\bullet}$ can be found, despite the agreement with the g values (2.034).

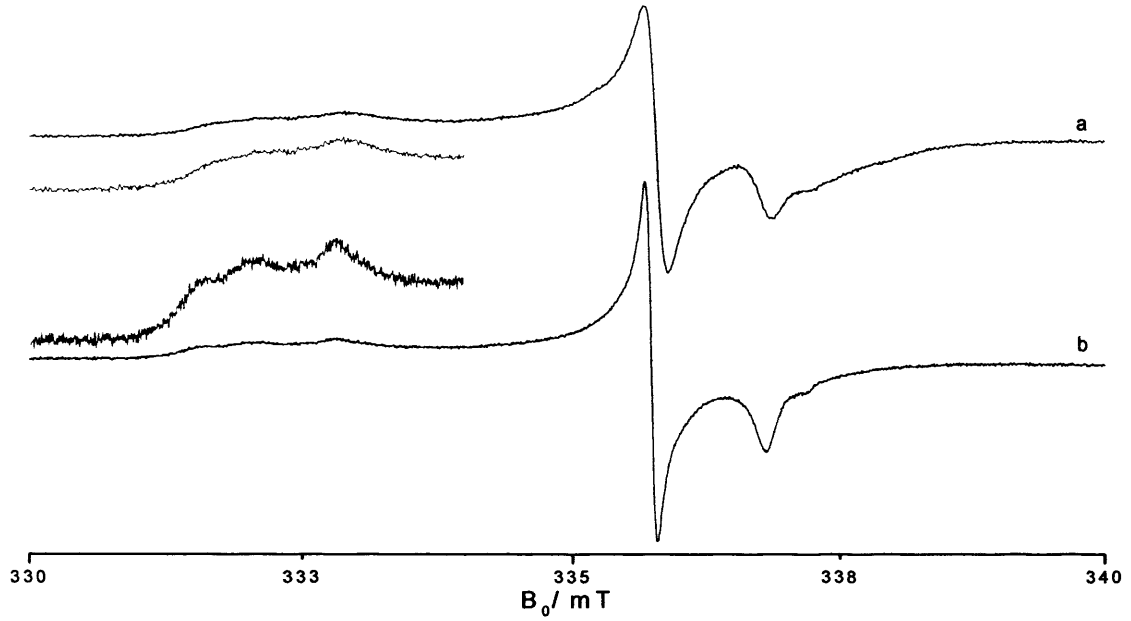

Figure 6.9 Experimental *cw*-EPR spectra [214K] of superoxide radicals formed by O_2 exposure to a reduced TiO_2 sample, followed by exposure at 77K to (a) *protic*-acetone and (b) *deuterated*-acetone.

This result was also confirmed by measuring the field selective ^1H ENDOR spectra, and only small couplings (less than 0.1mT) were found in agreement with the observed narrowing of the EPR lines, as displayed in Figure 6.10.

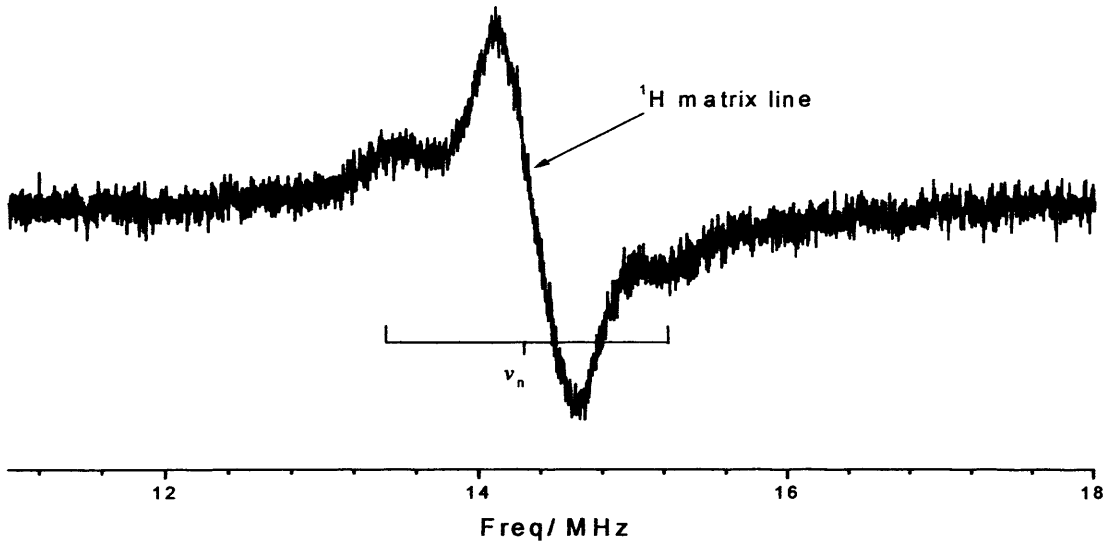

Figure 6.10 *cw*-^1H ENDOR spectrum of the radical formed by O_2 exposure to a reduced TiO_2 sample, followed by acetone exposure at 77K and subsequent annealing at 215K. The spectrum was recorded at 10K and at a magnetic field position of 335.8mT.

To examine the ^{17}O hyperfine couplings in more detail, the experiment was also repeated using ^{17}O labelled oxygen. The characteristic sextet hyperfine pattern of $^{17O}A_x \approx 7.7$mT for adsorbed $^{17}O_2^-$ (and the minor 11 line pattern of $^{17}O^{17}O^-$, due to the 63% enrichment used in our experiments) could be easily observed at temperatures between 120K and 210K. After exposure to acetone, the same sextet hyperfine pattern was observed (Figure 6.11). In other words, the unpaired spin density in the two oxygen nuclei of the new radical species remains equivalent, and this conclusively eliminates the possibility of an assignment based on a pure ROO$^\bullet$ type radical.

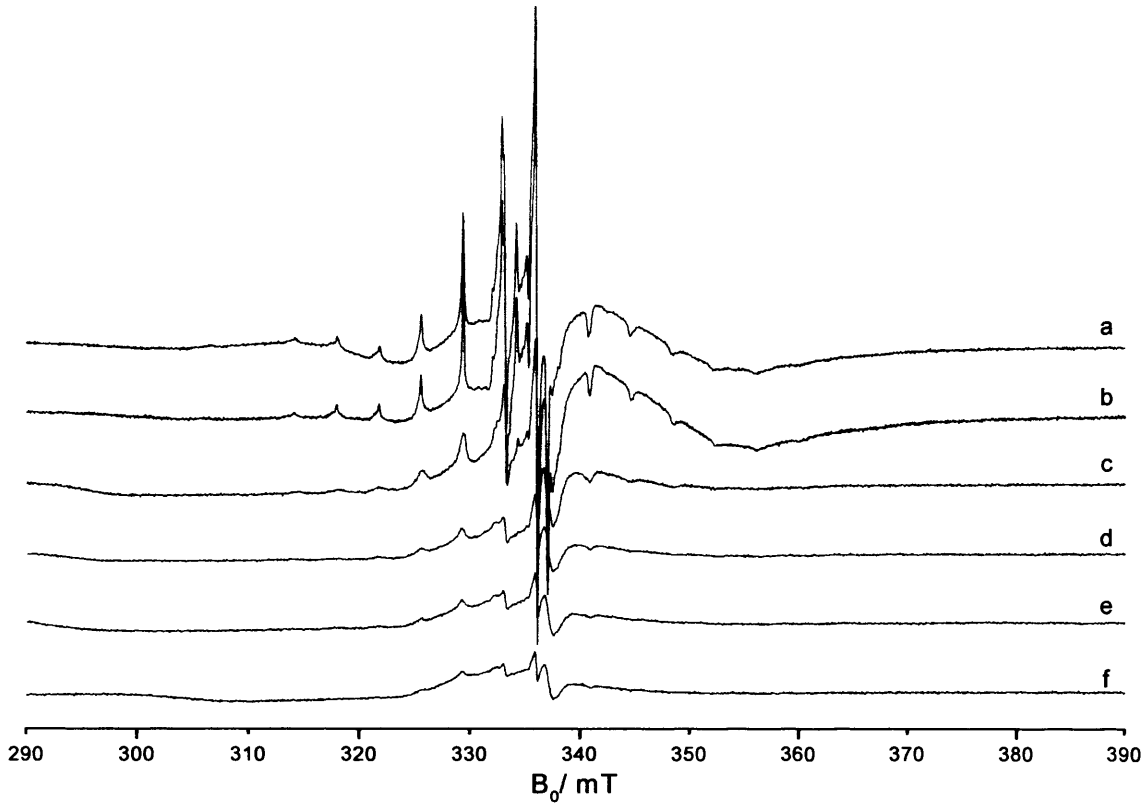

Figure 6.11 *cw*-EPR spectra of (a) superoxide radical formed by addition of 10 Torr $^{17}O_2$ (63% enrichment) to a reduced TiO_2 sample. Acetone (18 Torr) was then admitted to the EPR cell at 77K, and the spectra were recorded at (b) 120, (c) 200, (d) 210, (e) 214 and (f) 220K.

The reaction leading to the formation of the new radical at ~2.034 also occurs equally well with O_2^- radicals formed *via* photoadsorption. An activated sample of (P25) TiO_2 was prepared and exposed to acetone (18 Torr) at 77K in the usual manner. On annealing the sample under the acetone atmosphere there is a decay in the intensity of the superoxide signal, accompanied by the appearance of the new signal at ~2.034, as shown in Figure 6.12. The intensity of the new signal at 2.034 is much lower than that produced by reaction with a thermally generated superoxide, and this can be explained by the fact that there are less superoxide radicals on the surface of the photogenerated sample available for reaction with the acetone.

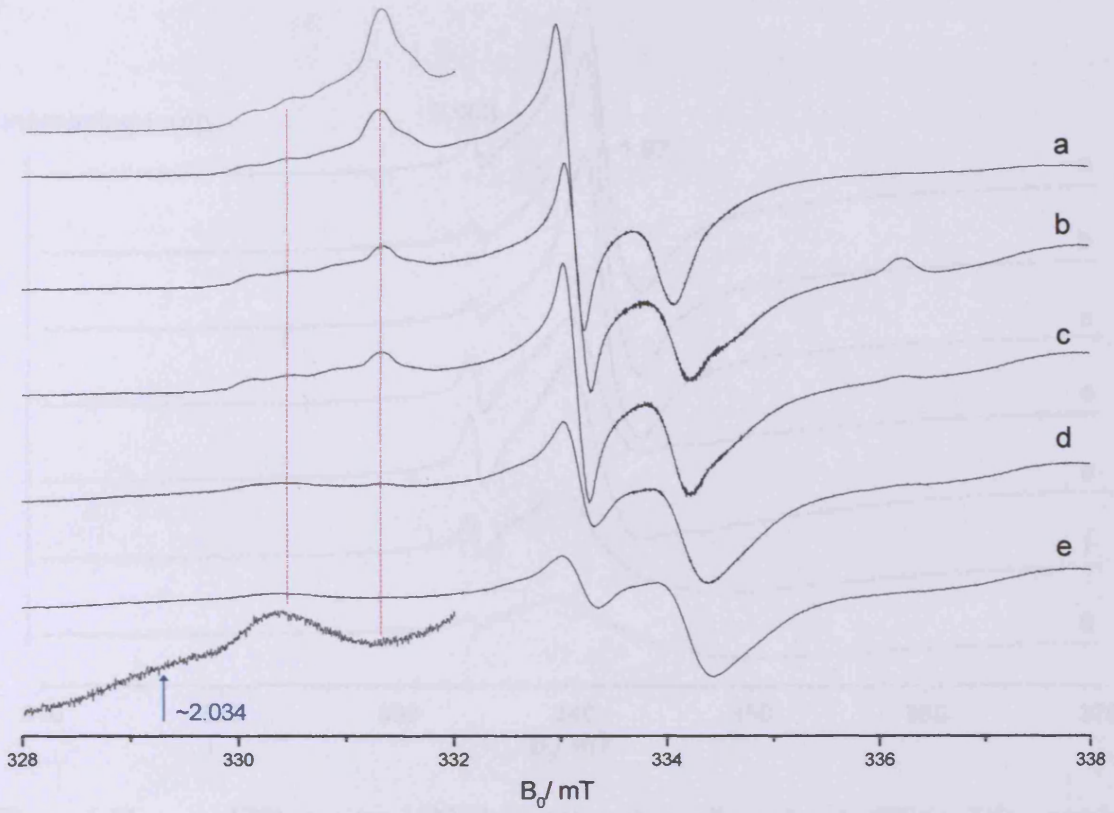

Figure 6.12 Experimental *cw*-EPR spectra [125K] of (a) photogenerated superoxide radical. Acetone (18 Torr) was exposed to the sample at 77K followed by annealing to (b) 125, (c) 210, (d) 220 and (e) 240K.

6.3.4 Acetone reactivity with reduced TiO_2

The results from the preceeding section demonstrate the reactivity between acetone and adsorbed superoxide radicals (either on a reduced or an activated surface). Owing to the non-stoichiometric nature of the reduced surface, one must also consider the direct reactivity of acetone with surface defects such as Ti^{3+} centres. The EPR spectrum of the reduced P25 TiO_2 sample is shown in Figure 6.13. The broad signal at $g_{\perp}$ = 1.966 and $g_{\parallel}$ = 1.95 can be attributed to a mixture of bulk and surface Ti^{3+} centres,[43] while the sharp signal close to free spin can be assigned to a medium polarised conduction electron spin resonance signal observed in the reduced sample.[21,44] Acetone was then admitted to the EPR cell at 77K and the temperature slowly raised. No significant changes were detected in the spectra until 210K (Figure 6.13d); at this temperature, the EPR signal intensity due to Ti^{3+} significantly decreased. Following annealing at 298K (Figure 6.13g), only the EPR signal of the residual bulk Ti^{3+} centres remain. All of the EPR spectra shown in Figure 6.13 were recorded at 120K, following annealing at the specified temperatures, since the EPR signal of Ti^{3+} is very dependent on spin lattice relaxation processes.

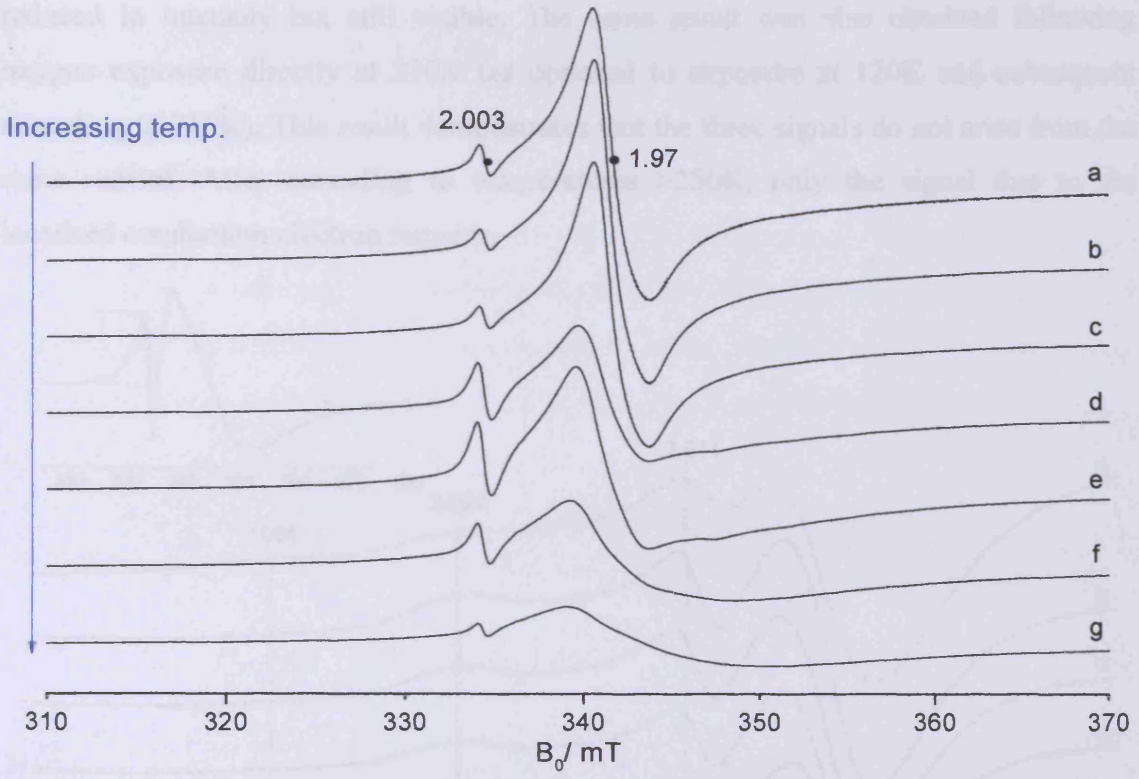

Figure 6.13 *cw*-EPR spectra [120K] of (a) a thermally reduced (773K) TiO_2 sample. Acetone (18 Torr) was then admitted to the EPR cell at 77K, and the temperature raised to (b) 125, (c) 180, (d) 210, (e) 220, (f) 260K and (g) 298K.

The loss of surface Ti^{3+} centres can be attributed to a reaction with acetone (by electron transfer from surface Ti^{3+} centres to the adsorbed substrate). The details of this reaction will be discussed further in section 6.4.4. The decay of the Ti^{3+} cations can be observed in the EPR spectrum, but no further EPR signal is identified due to the product of the reaction between Ti^{3+} and acetone.

It was of interest to explore the reactivity (if any) of the new radicals with molecular oxygen, to see if the new radicals could be identified indirectly *via* their reactivity. Therefore, in a separate experiment the acetone was exposed to the reduced surface at 77K, and the temperature was raised to 210K (as described above). Molecular oxygen was then subsequently exposed to this sample *in situ* at 120K and/or 210K. The resulting EPR spectra recorded at variable temperatures are shown in Figure 6.14. It is essential that these experiments were carried out *in situ* to avoid any reaction of O_2 with Ti^{3+}, since molecular oxygen is a far more efficient electron acceptor compared to acetone. At least three well defined peaks can now be identified in the EPR spectrum with g values of 2.034, 2.024 and 2.011 (Figure 6.14). These peaks are completely absent in Figure 6.13. After annealing the sample to 210K, the g = 2.034 signal disappears, the g = 2.024 signal remains, and the g = 2.012 signal is dramatically

reduced in intensity but still visible. The same result was also obtained following oxygen exposure directly at 210K (as opposed to exposure at 120K and subsequent annealing to 210K). This result demonstrates that the three signals do not arise from the same radical. After annealing to temperatures >250K, only the signal due to the localised conduction electron remains.

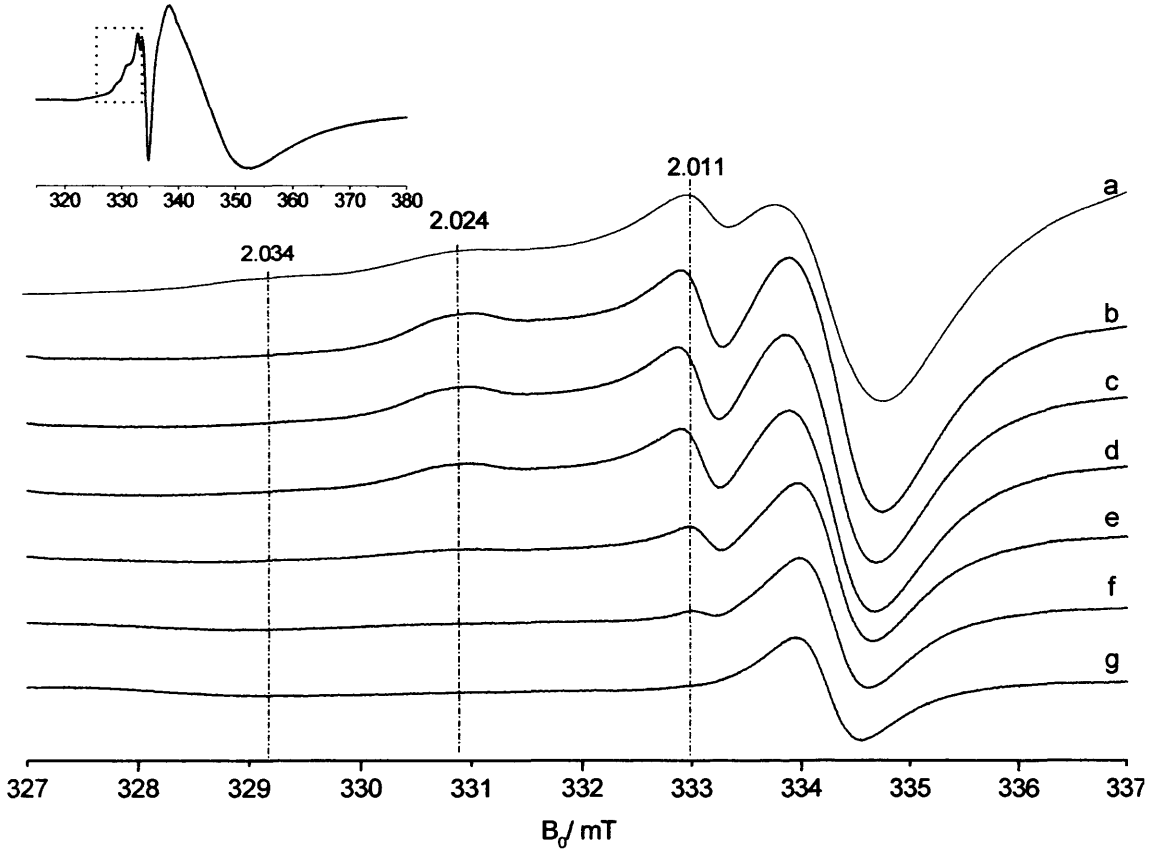

Figure 6.14 *cw*-EPR spectra [120K] recorded after O_2 (5 Torr) exposure at 77K to a reduced TiO_2 sample containing preadsorbed acetone. The TiO_2/acetone sample had been previously annealed to 210K (allowing acetone to react with the Ti^{3+} centres) and recooled to 77K before oxygen exposure. The sample was then annealed to (a) 125, (b) 210, (c) 215, (d) 220, (e) 230, (f) 240 and (g) 260K. Inset shows full width spectrum.

As stated earlier, extreme care must be exercised in the assignment of oxygen radicals based purely on (one) g values alone. Therefore the above experiment was subsequently repeated using ^{17}O labelled dioxygen. The new radicals observed may have a significantly different ^{17}O hyperfine pattern compared to $^{17}O_2^-$, and if they are indeed formed on TiO_2, they should be visible through their ^{17}O patterns. The resulting spectrum is shown in Figure 6.15. For clarity only the low field region of the EPR spectrum is shown. Unfortunately, the resolution of the spectrum is poor owing to the slight over-pressure of molecular oxygen admitted to the EPR cell at 120K. Nevertheless a complex hyperfine pattern can be clearly seen which definitely arises

from more than one type of oxygen centred radical. The hyperfine pattern due to the singly and doubly labelled superoxide species ($^{16}O^{17}O^-$ and $^{17}O_2^-$) is shown in the stick diagram with the unmistakable 7.7mT splitting. A characteristic hyperfine splitting of 5.5mT and 9.5mT can also be identified in the spectrum and this clearly confirms the existence of a surface alkylperoxy radical ($ROO^\bullet$). A number of other poorly resolved ^{17}O hyperfine patterns are also visible in the EPR spectrum, labelled with the * symbol (which are not attributed to singly or doubly labelled $^{17}O_2^-$ or $RO^{17}O^\bullet/R^{17}OO^\bullet$). These additional lines must originate from a third (different) type of oxygen centred radical.

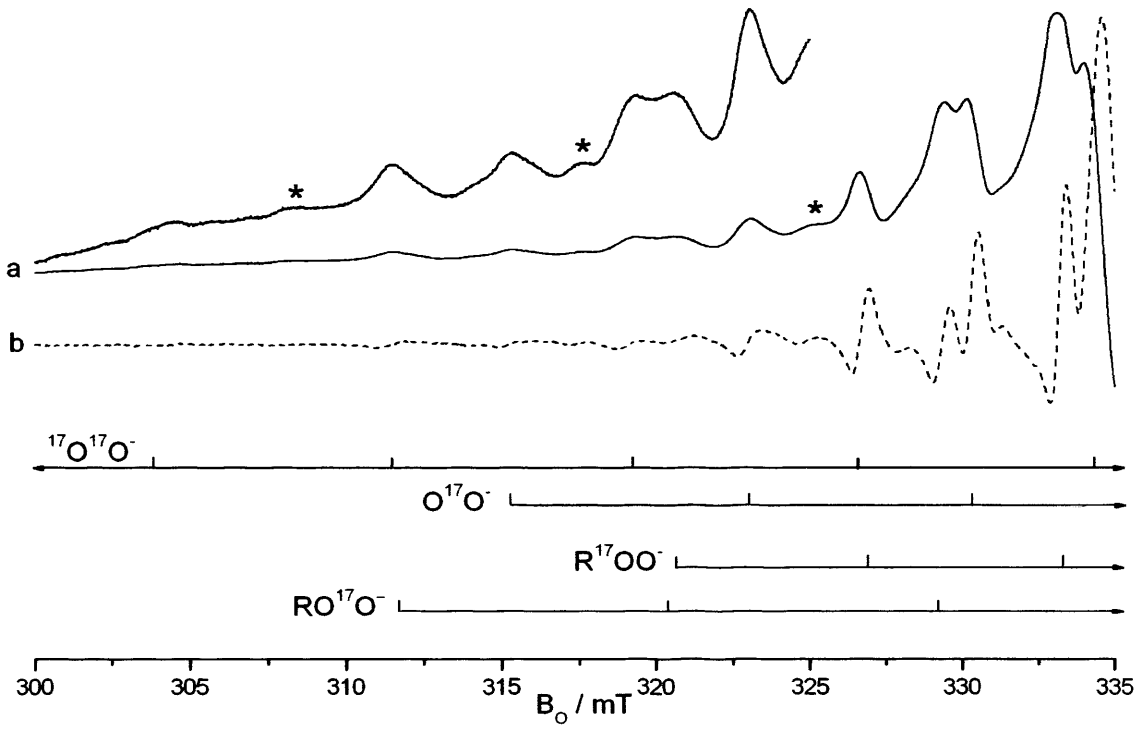

Figure 6.15 *cw*-EPR spectrum [120K] after $^{17}O_2$ (5 Torr) exposure at 77K to a reduced TiO_2 sample containing preadsorbed acetone. The TiO_2/acetone sample had been previously annealed to 210K and recooled to 77K before oxygen exposure. (a) first derivative, and (b) second derivative spectrum.

Finally it is important to note, that while all of the above experiments were conducted on a thermally reduced TiO_2 surface, the exact same results were also obtained on the activated TiO_2 surface (with the exception of the $^{17}O_2$ work, which was not attempted on an activated sample). In the latter case, the surface Ti^{3+} centres were photogenerated in the presence of adsorbed acetone at 120K. Molecular oxygen was subsequently exposed to the sample (under dark conditions), and the same series of EPR spectra shown in Figure 6.14 were reproducibly obtained. The spectra from these results have not been included for brevity, as they are qualitatively the same as those

produced on the thermally generated sample and provide no further mechanistic information.

6.4 Discussion

Acetone (and other ketones investigated in this study) can react and decompose with the reduced and activated surface of dehydrated TiO_2, both in the presence and absence of oxygen, and both under dark or radiative conditions. A series of radical intermediates have been identified in the decomposition pathways. These radicals have been assigned as organoperoxy species. The particular organoperoxy species which is observed depends on the adopted experimental conditions. A summary and discussion of these reactions, based on the above EPR findings, is given below.

6.4.1 The role of alkylperoxy radicals.

The mechanism of surface alkylperoxy radical formation was discussed recently for the case of co-adsorbed acetone:O_2 on TiO_2.[20] In the first step, UV irradiation of the oxide produces bulk and surface trapped holes, O^-. Electron transfer from the adsorbed ketone to the surface trapped hole occurs, producing an adsorbed cation radical. This quickly deprotonates by H^+ transfer to the surface oxide, forming an intermediate radical which subsequently reacts with molecular oxygen to form the adsorbed alkylperoxy radical observable by EPR. These steps are summarised in equations (6.1-6.2) below for acetone:O_2:

$$CH_3COCH_{3(a)} + O^-_{(s)} \rightarrow CH_3COCH_2^{\bullet}{}_{(a)} + OH^-_{(s)} \quad (6.1)$$

$$CH_3COCH_2^{\bullet}{}_{(a)} + O_{2(a)} \rightarrow CH_3COCH_2OO^{\bullet}{}_{(a)} \quad (6.2)$$

A similar reaction mechanism must also be responsible for the formation of the alkylperoxy radicals originating from the other ketones investigated here (i.e., butanone, 4-heptanone, cyclopentanone and cyclohexanone). In the acetone case, H^+ transfer can occur from either methyl group, leading to only one type of radical ($CH_3COCH_2OO^{\bullet}$). However, for butanone it is possible for the electron transfer to occur from either the α- or β-carbon, leading to two possible alkylperoxy radicals (namely $^{\beta}CH_3{}^{\alpha}CH_2CO^{\alpha}CH_2OO^{\bullet}$ or $^{\alpha}CH_3CO^{\alpha}CH_2{}^{\beta}CH_2OO^{\bullet}$ respectively). These two radicals cannot be confidently discriminated based only on the powder EPR spectrum. Nevertheless, since the protons on the α-position of carbonyl compounds and particularly the methyl group are more acidic, it is anticipated that proton transfer

should occur preferentially from these positions. Therefore, the radical structure formed by photo-irradiation of TiO_2 containing co-adsorbed butanone:O_2 can be assigned to $CH_3CH_2COCH_2OO^{\bullet}$. These results clearly demonstrate that transient organoperoxy ($ROO^{\bullet}$) type radicals can be involved in the photooxidation of ketones over P25 TiO_2. Control experiments establish that in the absence of the semiconductor, no peroxy radical is formed, which provides evidence that the photocatalysis of co-adsorbed ketones:O_2 over TiO_2 is a surface initiated mechanism. Henderson[13] has already shown that the photooxidation of acetone on $TiO_2(110)$ single crystal surfaces correlates with the excitation of the TiO_2 substrate rather than the adsorbed molecule itself. In other words, direct photolysis of adsorbed acetone does not appear to contribute significantly to the photooxidation of acetone (confirmed in this study). The formation of these radicals are clearly hole mediated and therefore this pathway is operative only under radiative conditions. The intermediates are transient and are only observed at low temperatures.

It is well known that the unpaired spin density in peroxy radicals is localized primarily in the p_z orbitals of the two oxygen atoms, which are aligned parallel to each other, as depicted in Scheme 6.1.[45] The anisotropic hyperfine couplings arising from the spin density in the p_z orbitals is axially symmetric, with $A_{\|} = (a + 2B)\rho$ and $A_{\perp} = (a - B)\rho$ where ρ is the spin density in the p_z orbital.[45] An estimate of the p_z orbital spin density can be calculated using the expression $\rho(i) = |A_{\|}(i)|/ 15.4mT$, where $15.40mT = |a + 2B|$. From this expression, and using the simulated hyperfine couplings, the spin density on the terminal oxygen of the butanone derived peroxy radical was estimated to be 0.64. This falls inside the range of typical spin densities (0.61 – 0.70) for carbon-based peroxy radicals.[45]

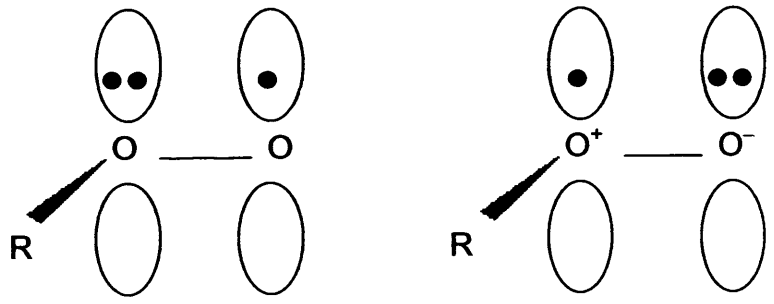

Scheme 6.1 The two major resonance structures of a typical peroxy based radical

Based on the nearly constant value for the sum of the two $A_{\|}$ couplings for carbon-based organoperoxy radicals ($ROO^{\bullet}$), only a small amount of delocalization of

the spin occurs onto the R group.[45] Nevertheless, it is known that the nature of the -R group can affect the stability and reactivity of peroxy radicals. As the electron withdrawing power of the -R group increases, the positive charge on the inner oxygen increases and simultaneously the spin density on the terminal oxygen increases. This produces an increase in the hyperfine coupling on the terminal oxygen, $A_{\|}(i)$. This trend is observed with the aliphatic ketones used in this study, as seen by increased terminal spin densities (ρ) for 2-butanone versus acetone (Table 6.1).

6.4.2 Identification of an organoperoxy signal

The new EPR signals in the g = 2.035-2.032 region formed on reaction of acetone with a superoxide radical (Figure 6.7) are unusual in two respects; (i) they are thermally unstable, since they are irreversibly lost on warming to 300K, and (ii) the g values of 2.035-2.032 are not typical g_{zz} values for a normal ionic superoxide radical on TiO_2. While O_2^- species are known to be stable on dehydrated TiO_2 surfaces,[46,47] the radical is destabilised on a hydrated or partially hydrated surface.[23,48] As was shown in a previous study, on partially hydrated rutile, some of the low temperature photoadsorbed O_2^- radicals were still observed upon warming the sample to 300K, but under identical conditions using P25, the O_2^- radicals were completely absent after annealing to 300K.[23] The destabilisation of the O_2^- radicals was attributed to the formation of hydroperoxy radicals ($HO_2^{\bullet}$),[23] which can subsequently undergo a series of disproportionation reactions leading to H_2O_2 formation.[49,50] The g values for the thermally unstable $HO_2^{\bullet}$ species on P25 was $g_1 = 2.034$ ($g_2 = 2.008$, and $g_3 = 2.002$).[23] However, the organoperoxy radicals identified earlier, are also thermally unstable upon warming to 300K, and they also have a g value of $g_1 = 2.0345$ ($g_2 = 2.007$, and $g_3 = 2.003$).[20] Therefore, g values alone are not sufficient to make a definitive assignment on the nature of the new signals observed in Figure 6.7; this requires information on the hyperfine couplings.

The terminal ^1H couplings of $HO_2^{\bullet}$ in TS-1 were reported as $^HA_1 = 1.3$mT, $^HA_2 = 1.0$ mT and $^HA_3 = 1.0$ mT[39] while the α-H couplings of $ROO^{\bullet}$ were found to be significantly smaller with $^HA_1 = 0.34$mT, $^HA_2 = 0.10$ mT and $^HA_3 = 0.29$ mT.[20] The ^{17}O hyperfine pattern of $ROO^{\bullet}$ was also observed in this study as $^{17O}A_{\|}(i) = 9.92$ mT and $^{17O}A_{\|}(ii) = 5.85$ mT. For the hydroperoxy species, the unpaired electron is expected to be in the π^*_x level which is split from the π^*_y level by the proton, similar to the situation in O_2^-, but due to the presence of the proton the Δg shift should be smaller.[51] Since the

unpaired electron is largely confined to the unprotonated oxygen, the hyperfine coupling should be negative and relatively small (a_{iso} ~1.1mT).

6.4.3 The role of superoxide radicals

In the photoirradiation process, holes and electrons are both produced which can become trapped at the surface to form O^- centres (these are involved in the formation of the organoperoxy radicals discussed above) and Ti^{3+} centres. In the presence of molecular oxygen, interfacial electron transfer from Ti^{3+} to O_2 is very facile (even at 77K) producing surface stabilised superoxide radicals (O_2^-). Subsequent exposure of these radicals to acetone leads to the irreversible destruction of the EPR signal due to O_2^-. An intermediate radical (or paramagnetic complex), which is thermally unstable at temperatures above *ca.* 250K, responsible for the signals at g = 2.035 and 2.032 is involved in this reaction. The reaction occurs equally well with O_2^- radicals formed *via* photoadsorption or formed on a reduced TiO_2 (under dark conditions). The interaction of acetone with O_2^- in this complex is clearly sufficiently strong to perturb the g values away from normal O_2^- values and also reveal a small ^1H coupling to acetone, but insufficient to alter the unpaired electron spin densities in the oxygen atoms as manifested in the ^{17}O hyperfine pattern. The latter observation implies that both oxygen nuclei remain equivalent in this surface complex.

The combined EPR observations (g, ^HA, ^{17}O, stability, *etc.*) support a preliminary assignment based either on an $[H...O_2^-]$ type species or more probably an $[O_2^-...C{=}O(CH_3)_2]$ type species. In the former hypothesis, Lewis acid-base pairs may be responsible for the deprotonation of adsorbed acetone leading to the formation of surface hydroxyls:

$$Ti^{4+}\text{-}O^{2-} + CH_3COCH_3 \rightarrow Ti^{4+}\text{-}OH^- + CH_3COCH_2^- \quad (6.3)$$

$$Ti^{4+}\text{-}OH^- + O_2^- \rightarrow Ti^{4+}\text{-}[OH^-.....O_2^-] \quad (6.4)$$

These surface hydroxyls may then interact with the adsorbed O_2^- radical to form a hydroperoxy type species (i.e., $[H...O_2^-]$ rather than a pure $HO_2^\bullet$ species) and it is simply this species which is responsible for the g = 2.035-2.032 signals in the EPR spectrum which subsequently disappear upon warming to 300K. While this interpretation cannot be discounted, based on other evidence available in the

literature[12,13] it is believed that the $[O_2^-...C{=}O(CH_3)_2]$ species is a more plausible explanation.

In a very thorough series of papers, Henderson investigated the photooxidation of acetone over a rutile $TiO_2(110)$ surface under ultra high vacuum (UHV) conditions.[12,13] It was proposed that the primary photocatalytic pathway involves ejection of methyl radicals from the surface. Initially a thermal reaction was proposed to occur between acetone and an adsorbed oxygen species (either O_2^- or O/O^-) to form an acetone-oxygen complex labelled $\{\text{acetone-oxygen}\}_{(a)}$. This complex photodecomposed *via* photogenerated charge carriers in the TiO_2 through a mechanism involving methyl radical ejection from the surface and conversion of the complex to surface bound acetate. The steps are summarised below:

$$O_2 + Ti^{3+} \rightarrow O_2^- + Ti^{4+} \quad (6.5)$$

$$O_2^- + \eta^1\text{-acetone} \rightarrow\rightarrow \{\text{acetone-oxygen}\}_{(a)} \quad (6.6)$$

$$\{\text{acetone-oxygen}\}_{(a)} + UV \rightarrow \text{acetate}_{(a)} + CH_{3(g)} \quad (6.7)$$

It was also shown by Coronado *et al.*,[11] and Henderson[12,13,46] that a reaction intermediate in the thermal and photochemical reactions of acetone on TiO_2 may involve nucleophillic attack of an $O_2^{\delta-}$ species on an acetone molecule leading to adsorbed acetate. Oxygen surface coverage was found to be important in this reaction compared to acetone coverage,[46] since a surface rich in molecularly adsorbed O_2 preferentially yielded acetate. This is an important result as it demonstrated that electron mediated pathways involving TiO_2 can also be involved in the photooxidation of acetone over TiO_2. Based on these reports it is conceivable that the $[\text{acetone-}O_2^-]_{(a)}$ surface complex observed in this work (similar to equation 6.6) could indeed be formed by O_2^- nucleophillic attack on acetone. Although its precise structure/identity is not clear, a tentative assignment at this stage is that the weak O_2^- nucleophile attacks the electrophillic carbon atom of the highly polarised carbonyl group in a 'side-on' manner, rather than an 'end-on' manner. The resulting interaction with acetone is likely to be weak at 210K. If the oxygen of the carbonyl group interacts with a suitable electrophile (a proton), attack by the weak O_2^- nucleophile could be enhanced, and this weak interaction may reduce the strength of the electrostatic $Ti^{4+}...O_2^-$ interaction thereby leading to an increased g_{zz} value (e.g., from g = 2.019 to g = 2.035). This model also

explains the small observed ^{1}H couplings and ^{17}O hyperfine patterns since a "side-on" bonded superoxide would possess equivalent oxygen nuclei.

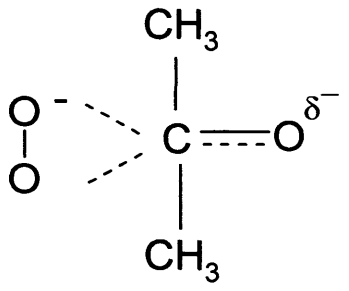

Scheme 6.2 Proposed structure of the [acetone-O_2^-]$_{(a)}$ surface intermediate.

While the exact structure of this paramagnetic intermediate requires further theoretical work, it is clear from the current EPR results that superoxide radicals formed by interfacial electron transfer from Ti^{3+} centres are responsible for the decomposition of adsorbed acetone *via* a thermally unstable [acetone-O_2^-]$_{(a)}$ surface complex. The suggested structure shown in Scheme 6.2 best fits the observed EPR features, and the HREELS data of Henderson[46] that shows the C-O bonds in the surface adsorbed {acetone-oxygen} complex are midway between single and double bonds. Interestingly, the selective reactivity observed by the different O_2^- species towards acetone indicates that different surface sites responsible for superoxide stabilisation display different chemical reactivities. This result may be considered along with the different thermal and photostabilities of superoxide radicals at different stabilisation sites (Chapter 5), and in particular the assignment of reactive radicals stabilised at oxygen vacancy sites.

6.4.4 The role of reduced Ti^{3+} centres

It was seen earlier that reduced Ti^{3+} centres not only react with molecular oxygen, but they can also react directly with adsorbed acetone. The Lewis acidity of the Ti^{4+} centres on activated P25 was explored by Martra[52] using CO as an IR probe, and different acidities were identified depending on the differences in the geometric arrangement of the O^{2-} anions around the Ti^{4+} centre. The reduced Ti^{3+} cation should show enhanced Lewis acidity compared to Ti^{4+}, and should react with the carbonyl group of acetone. In the absence of molecular oxygen (or in acetone rich conditions), transient radical anions can be formed on the reduced surface according to equation 6.8:

$$Ti^{3+} + CH_3COCH_3 \rightarrow Ti^{4+} + \{CH_3COCH_3^{\bullet-}\}^* \qquad (6.8)$$

The anion radical most likely produced, labelled $\{CH_3COCH_3^{\bullet-}\}^*$, was not detected by EPR. Since back electron transfer is highly unlikely, owing to the relative redox potential of the acetone-TiO_2 conduction band, fast dissociation of the anion intermediate must occur (hence the * symbol indicating an unstable intermediate). Assuming electron transfer to adsorbed acetone results in π^*_{CO} anti-bonding orbital occupation, this being the lowest unoccupied molecular orbital, fragmentation patterns similar to those obtained by direct UV irradiation might be expected leading to C-C bond scission. Although only the π^*_{CO} anti-bonding orbital is populated by electron transfer, while the n_O non-bonding state remains populated, the lability of the adsorbed $\{CH_3COCH_3^{\bullet-}\}^*$ species is still expected to be higher compared to the gas phase equivalent, since some partial σ-electron donation from the carbonyl oxygen to the surface cations will also occur which can cause some time-averaged depopulation of the C-C bonding orbitals. The resulting $CH_3^\bullet$ (methyl) and $CH_3CO^\bullet$ (acyl) radicals (see equation 6.9), which to date have only been trapped and identified by EPR in matrix isolation experiments at low temperatures[53], were not observed in Figure 6.13.

$$\{CH_3COCH_3^{\bullet-}\}^* \rightarrow CH_3^\bullet + CH_3CO^\bullet \qquad (6.9)$$

However, some strong candidates for the assignments for the reaction products of $CH_3^\bullet$ and $CH_3CO^\bullet$ with oxygen can be proposed. A series of peroxy radicals ($ROO^\bullet$) have already been identified in this chapter formed by reaction of alkyl radicals with O_2, and a series of peroxyacyl radicals ($RCO_3^\bullet$) over TiO_2 containing co-adsorbed aldehydes:O_2 have previously been identified.[21] In the latter case the radicals were formed by reaction of photogenerated acyl radicals ($RCO^\bullet$) with O_2. Since acyl radicals are σ species with the unpaired electron density located primarily in an sp hybrid orbital of the carbonyl carbon,[54] they are expected to undergo rapid radical addition reactions. However, unlike the $\{CH_3COCH_3^{\bullet-}\}^*$ intermediate formed during acetone adsorption on reduced TiO_2, the acyl species does not possess any significant anti-bonding orbital occupation and is therefore not expected to decompose by intramolecular dissociation to any great extent. Based on this evidence, it is possible for peroxyacyl radicals, in addition to peroxy radicals, to form on the reduced TiO_2 surface containing adsorbed acetone *via* the $\{CH_3COCH_3^{\bullet-}\}^*$ intermediate. As discussed earlier superoxide radicals on TiO_2 have g_{zz} values within the range 2.026 – 2.018; this suggests the g = 2.024 signal is most likely due to O_2^- formed on residual Ti^{3+} centres (unreacted Ti^{3+}

remaining after acetone contact at 210K). The peroxyacyl ($RCO_3^{\bullet}$) radical was identified, on photoirradiated TiO_2 containing co-adsorbed aldehyde:O_2, and produces g values of $g_1 = 2.016$ ($g_2 = 2.008$ and $g_3 = 2.003$);[21] this suggests that the closely related $g = 2.012$ signal could be assigned to $CH_3CO_3^{\bullet}$ formed by O_2 reaction with $CH_3CO^{\bullet}$ (see equation 6.11). Finally, as discussed earlier, organoperoxy radicals typically have g values close to 2.0345, for example for the photogenerated acetone derived $CH_3COCH_2OO^{\bullet}$ radical; this suggests that the $g = 2.0345$ signal could be assigned to a peroxy species such as $HO_2^{\bullet}$ or $CH_3OO^{\bullet}$ ($CH_3COCH_2OO^{\bullet}$ is only formed under radiative conditions, and so can be discounted). The rate at which organoperoxy radicals react and decay is dependent upon the electron withdrawing/donating character of the -R group. Electron donating groups such as $-CH_3$ are therefore expected to increase the terminal oxygen spin density, resulting in relatively higher reaction rates, compared to -H. Since the $g = 2.034$ signal in Figure 6.14 decays at lower temperatures (~150K) compared to $HO_2^{\bullet}$ (stable up to 250K[23]), this would suggest that this signal could be more appropriately assigned to the $CH_3OO^{\bullet}$ species (equation 6.10). It is also well known that ionic species such as O_2^- are effectively immoblised on metal oxide surfaces at temperatures below 300K, whereas the neutral peroxy radicals will possess some mobility (even at low temperatures) which facilitates and enables further reactions.

$$CH_3^{\bullet} + O_2 \rightarrow CH_3OO^{\bullet} \quad (6.10)$$

$$CH_3CO^{\bullet} + O_2 \rightarrow CH_3COOO^{\bullet} \quad (6.11)$$

These reactions can occur on both the reduced TiO_2 surface and also on the photoirradiated TiO_2 surface. While these methyl and acyl radicals can undergo further reactions, in the presence of molecular oxygen, a series of organoperoxy radicals are formed (according to equations 6.10 and 6.11). These radicals were identified by EPR based on their g values, thermal stabilities and ^{17}O hyperfine patterns. These signals are only visible at low temperatures, since they are very thermally unstable. Indeed Coronado *et al.*,[11] studied the photocatalytic oxidation of acetone over polycrystalline TiO_2 by FTIR, and it was suggested that the acetone molecule breaks after the attack of the photogenerated charge carriers to yield a two-carbon molecule and a single carbon one. In this work evidence has been provided for the formation of a two carbon ($CH_3CO^{\bullet}$) and single carbon ($CH_3^{\bullet}$) fragment, indirectly *via* the formation of the organoperoxy radicals according to 6.10 and 6.11.

6.4.5 Decomposition of acetone via radical pathways at low temperature

The above EPR data has provided strong evidence for the involvement of free radical pathways in the decomposition of ketones over polycrystalline (P25) TiO_2. Depending on the experimental conditions adopted different radical intermediates have been identified. Both of the photogenerated charge carriers can result in the decomposition of acetone. The trapped holes can lead to $CH_3COCH_2^{\bullet}{}_{(a)}$ which subsequently reacts with adsorbed molecular oxygen to form the thermally unstable organoperoxy radicals $CH_3COCH_2OO^{\bullet}{}_{(a)}$ (pathway I in Scheme 6.3). By comparison, the trapped electrons (Ti^{3+}) can react with molecular oxygen producing O_2^- radicals which subsequently undergo a further reaction with acetone to form a thermally unstable radical complex, $[acetone\text{-}O_2^-]_{(a)}$ (pathway III). This latter complex can also be classified as an organoperoxy radical. This reaction is observed using preadsorbed O_2^-, simulating the reactions that occur in oxygen rich conditions. The same results are obtained regardless of whether the O_2^- is generated on a reduced TiO_2 surface or by photoadsorption on an activated surface. By adopting acetone rich conditions, the trapped electron (Ti^{3+}) reacts directly with acetone to produce an unstable $\{CH_3COCH_3^{\bullet-}\}^*$ intermediate which subsequently disproportionates to yield $CH_3^{\bullet}$ and $CH_3CO^{\bullet}$ radicals (pathway II). The latter species undergo secondary reactions with molecular oxygen to form the organoperoxy radicals $CH_3OO^{\bullet}$ (alkylperoxy) and $CH_3COOO^{\bullet}$ (peroxyacyl). These transient species were identified primarily on the basis of their g values and the ^{17}O hyperfine patterns. All of these competing reaction pathways are summarised below in Scheme 6.3.

Apart from the expected EPR observations of the stable Ti^{3+} and O_2^- species, all of the unstable radicals highlighted in bold (square dashed brackets) were directly observed in this work at low temperatures using controlled experimental conditions. However, the relative rates of each reaction pathway do not appear to be equivalent. For example, under continuous UV illumination the strongest EPR signal observed is due to the $CH_3COCH_2OO^{\bullet}{}_{(a)}$ intermediate on activated TiO_2 containing co-adsorbed acetone:O_2. The radicals formed by pathways II and III may be present, but in minor amounts. The intermediates formed *via* pathways II and III are simply controlled by the O_2 pressure.

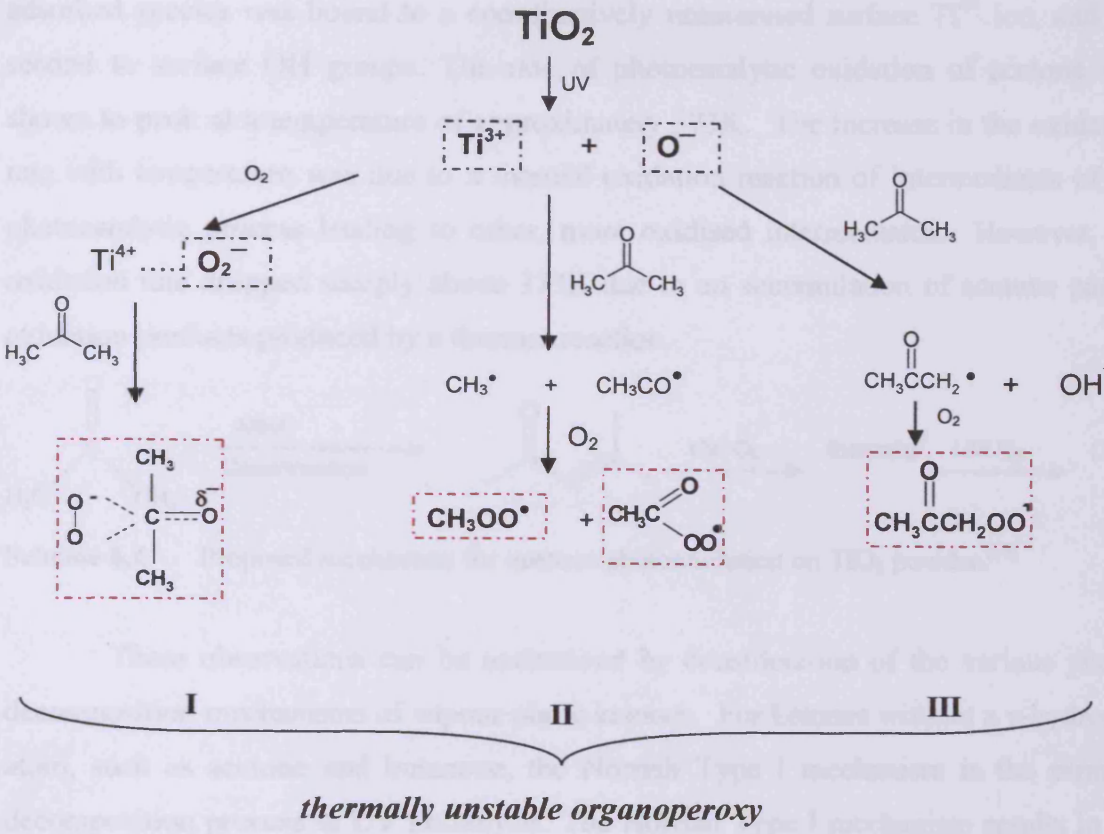

Scheme 6.3 Observed radical pathways in the decomposition of acetone.

6.4.6 Decomposition of acetone via radical pathways at elevated temperature

The radical pathways considered in Scheme 6.3 above explain the series of results discussed in section 6.3 for the decomposition of acetone at low temperature. However, the photocatalytic oxidation of acetone over TiO_2 has been studied by several groups at room temperature (or elevated temperatures) and alternative pathways for decomposition have been suggested. For example, Xu *et al.*,[55] used solid state NMR to elucidate the mechanism of the photocatalytic oxidation of acetone over TiO_2 powder at 298K. They found that the mechanism of oxidation depends significantly on surface morphology because of the possibility of forming different chemisorbed species. The oxidation route of acetone on TiO_2 powder in their study was observed through mesityl oxide $[(CH_3)_2C{=}CHCOCH_3]$ fragmentation to formic acid (CHOOH), which forms titanium formate with a surface OH group and then the final oxidation product CO_2 (Scheme 6.4). The dependence on photocatalytic oxidation rate with acetone concentration was shown by Vorontsov *et al.*,[56] to be fitted using a Langmuir-Hinshelwood equation that incorporates two different surface adsorption sites. This theoretical assumption was corroborated by the results from an FTIR study of TiO_2 oxidation performed in acetone at 313K, which showed two bands for $\nu_{C=O}$. The first

adsorbed species was bound to a coordinatively unsaturated surface Ti^{4+} ion, and the second to surface OH groups. The rate of photocatalytic oxidation of acetone was shown to peak at a temperature of approximately 373K. The increase in the oxidation rate with temperature was due to a thermal oxidation reaction of intermediates of the photocatalytic process leading to other, more oxidised intermediates. However, the oxidation rate dropped sharply above 373K due to an accumulation of acetone partial oxidation products produced by a thermal reaction.

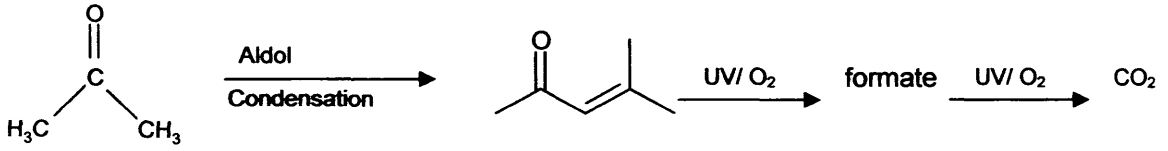

Scheme 6.4 Proposed mechanism for acetone photooxidation on TiO_2 powder.[55]

These observations can be understood by consideration of the various photo-decomposition mechanisms of vapour phase ketones. For ketones without a γ-hydrogen atom, such as acetone and butanone, the Norrish Type I mechanism is the primary decomposition process in UV photolysis. The Norrish Type I mechanism results in the rupture of the C-C bond adjacent to the carbonyl group. If the two alkyl groups are different, both the bond cleavage processes shown in (6.12a) and (6.12b) below may occur, but preference is shown for dissociation of the weakest bond when the incident light is of long wavelength. This selectivity between the two processes decreases when the energy of the quantum increases.

$$RCOR' + h\nu \rightarrow R + COR' \quad (6.12a)$$

$$\rightarrow RCO + R' \quad (6.12b)$$

As the incident quantum energy increases, the energy of the products of (6.12a) and (6.12b) also increases, resulting in the formation of a larger fraction of non-thermally equilibrated RCO radicals. These radicals rapidly undergo decomposition, $RCO^* \rightarrow R + CO$, in an early vibration following formation. This explains why these radicals have never before been detected *via* EPR spectroscopy.

Ketones with a γ-hydrogen atom, such as 4-heptanone, preferentially undergo the alternative Norrish Type II decomposition, which is illustrated schematically in Scheme 6.5. The photoelimination process goes *via* a cyclic, six-membered ring intermediate, with an alkene and an enol form of a ketone as primary products. Although the ring is a convenient representation of the process, alternative stepwise

processes are also possible. The spatial arrangement and charge distribution within the carbonyl group in the excited π^* state in theory favours bond formation between the γ-hydrogen atom and the oxygen of the carbonyl group. There is no known case of a saturated aliphatic ketone with γ-hydrogen atom not participating in this Type II photo-elimination process.

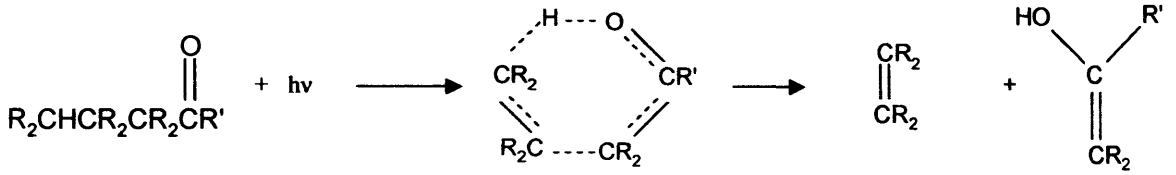

Scheme 6.5 The Norrish Type II mechanism

There are two possible dissociation processes open for the two cyclic ketones, cyclopentanone and cyclohexanone, used in this study. The major primary photochemical reaction in the gas phase at low pressures is decarbonylation which proceeds *via* an intramolecular elimination mechanism. During this process, cleavage of the C-C bond adjacent to the carbonyl group results in a diradical intermediate. After loss of CO through vibrational losses, the remaining fragment can undergo either intramolecular combination or self-disproportionation. Several of these alternative pathways are displayed in Scheme 6.6 for the case of cyclohexanone.

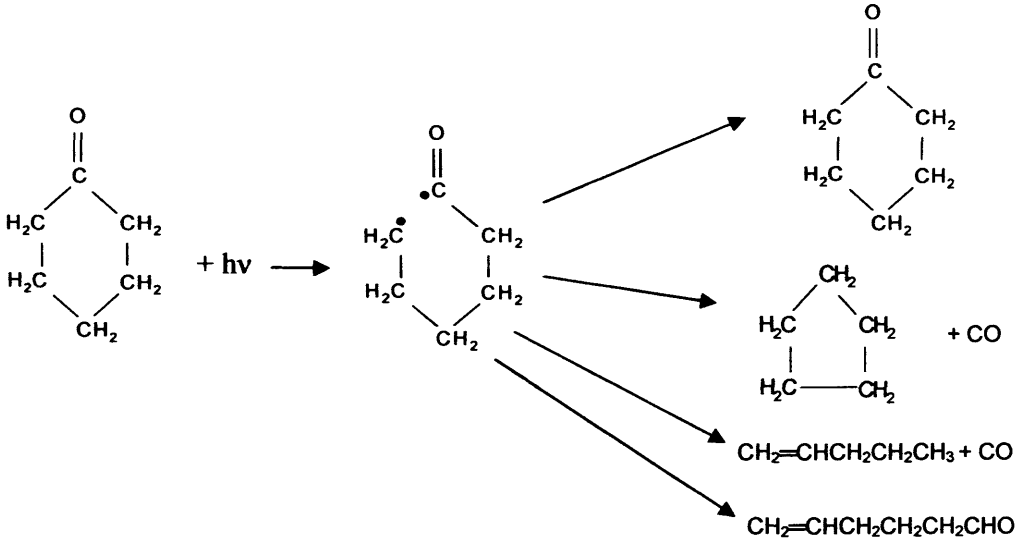

Scheme 6.6 Alternative modes of photodecomposition for the cyclic ketones, illustrated for the case of cyclohexanone.

6.4.7 Effect of water adsorption

The series of reactions discussed in section 6.3 certainly occur on the dehydrated (reduced and activated) TiO_2 (P25) surface. Water and surface hydroxyls undoubtedly play an important role in the photooxidation of organic substrates over TiO_2. Indeed,

previous work has shown the significant differences between the thermal stabilities of O_2^- radicals on hydrated anatase *versus* hydrated rutile,[23] and even the difficulties of detecting O_2^- on the hydrated surface. If the series of organoperoxy radicals identified in this work do exist on the hydrated surface they may prove extremely difficult to detect.

Some authors have shown that the presence of H_2O can lead to an increase in the rate of photooxidation[1,11,57], whereas others have shown that the adsorbed H_2O decreases photocatalytic activity by poisoning the surface of the catalyst[15,16,19]. For example, in the study of the photocatalytic oxidation of ethane to CO_2 and H_2O on different TiO_2 catalysts, Park *et al.*,[58] showed that the photocatalytic activity was increased on addition of up to 5 Torr of water vapour to the system but it started to decrease again on any further addition of water vapour. The authors[58] explained these findings based on the effect of water vapour on oxygen uptake. When only a small amount of water vapour was introduced to the system both water and oxygen could be adsorbed onto the surface of the photocatalyst to produce reactive $^{\bullet}OH$ radicals under irradiation, which itself led to an increase in activity. However, when excess water vapour was added the effective adsorption sites were occupied completely by water molecules, therefore decreasing the photo-induced uptake of oxygen and consequently lowering activity.

Henderson[59] performed a UHV experiment on the effect of water adsorption on both oxidised and reduced surfaces of TiO_2(110) in the presence of acetone. His results showed that co-adsorbed water could have a significant impact on the surface coverage of acetone depending on the redox state of the TiO_2 surface. On reduced surfaces, at high water coverages the preadsorbed acetone was displaced into multilayer states. In contrast, pre-oxidised surfaces exhibited a greater resistance against acetone displacement by water as a result of the formation of an [acetone-oxygen] surface complex. These results were explained in part by the adsorption binding energies of water and acetone on the surface.[59] Water is able to adapt its adsorption structure by hydrogen bonding to neighbouring molecules and to the oxide surface, and this appears to lessen the influence of dipole-dipole repulsions which might otherwise lower the water molecules' desorption energy. However, acetone molecules adsorb to the TiO_2(110) surface in a restricted geometry *via* an η^1-configuration through lone pair electrons on the oxygen atom. This aligns the molecular dipoles in opposition with those of its neighbouring molecules resulting in greater sensitivity to surface coverage.

Anpo *et al.*,[60] proposed that the adsorption of water vapour onto the surface of TiO_2 causes structural changes in surface band bending, which unfavourably accelerates

the recombination of photogenerated electrons and holes, and thus gives rise to low photoefficiency. An alternative explanation was put forward by Phillips and Raupp who suggested that water is used to supply hydroxyl groups, which are consumed by trapping holes to generate OH radicals in the process of reaction[61].

It will be of interest in the future to repeat some of the experiments discussed throughout this chapter in the presence of water vapour to determine the effect of surface adsorbed hydroxyls on the reaction mechanism of photooxidation.

6.5 Conclusion

Whilst the reactions between surface radicals derived from O_2, H_2O or OH groups and adsorbed substrate have received considerable attention over the years in relation to heterogeneous photocatalysis, the participation of organic radicals involving OH, OOH, O/O_2, and $ROO^{\bullet}$ has received considerably less attention. Despite the well known participation of organoperoxy species ($ROO^{\bullet}$) in the oxidation of organic compounds, their involvement in heterogeneous mechanisms has scarcely been considered to date. Using EPR, it has been shown that a number of different organoperoxy species are involved in the heterogeneous decomposition of ketones (including acetone, 2-butanone, 4-heptanone, cyclopentanone and cyclohexanone) over dehydrated polycrystalline TiO_2 (P25). These species are generated by charge-transfer events associated with the charge carriers in TiO_2 generated by photon absorption. Some of the organoperoxy species can also be formed and identified on thermally reduced TiO_2 (under dark conditions). The trapped holes (O^-) are involved in the surface decomposition reactions by hole transfer to the adsorbed ketones; subsequent reactivity of the adsorbed cation radical with molecular oxygen leads to the formation of the peroxy species $ROO^{\bullet}$. In the specific case of co-adsorbed butanone:O_2 the organoperoxy species has been identified as $CH_3CH_2COCH_2OO^{\bullet}$ based on the analysis of the g and A components. By comparison, the reduced Ti^{3+} centres were also directly and indirectly involved in the oxidative decomposition pathways of adsorbed ketones. Ti^{3+} involvement occurs either through the generation of stable inorganic (O_2^-) radicals or through the participation of unstable organic intermediates ($\{CH_3COCH_3^{\bullet-}\}^*$) which disproportionates to form methyl ($CH_3^{\bullet}$) and acyl ($CH_3CO^{\bullet}$) radicals. These latter radicals were indirectly identified through their reactivity with molecular oxygen forming the corresponding organoperoxy radicals ($CH_3OO^{\bullet}$ and $CH_3CO_3^{\bullet}$). In an oxygen rich environment, Ti^{3+} reacts preferentially with molecular oxygen forming

superoxide radicals (as opposed to $\{CH_3COCH_3^{\bullet-}\}^*$ which forms under acetone rich conditions). The O_2^- anions selectively react with the adsorbed acetone (depending on the temperature) to form an associated $[\text{acetone-}O_2^-]_{(a)}$ surface complex, which can also be classified as an organoperoxy type species. All of these radical intermediates are thermally unstable, and cannot be observed at temperatures above 250K. This may partly explain why they have not been widely studied to date, and at least emphasises the need to perform the experiments at low temperatures if a complete picture of the decomposition pathways is to emerge.

References

[1] M. El-Mazaawi, A.N Finken, A.B Nair, V.H Grassian, *J. Catal.*, **2000,** *191*, 138.

[2] S.B. Kim, H.T. Hwang, S.C Hong, *Chemosphere*, **2002**, *48*, 437.

[3] A. Fujishima, K. Honda, *Nature*, **1972**, *37*, 238.

[4] A.L. Linsebigler, G. Lu, J.T. Yates, Jr., *Chem. Rev.*, **1995**, *95*, 735.

[5] P.V. Kamat, *Chem. Rev.*, **1993**, *93*, 267.

[6] M.A. Fox, M.T. Dulay, *Chem. Rev.*, **1993**, *93*, 341.

[7] T. Tatsuma, S. Tachibana, A. Fujishima, *J. Phys. Chem. B*, **2001**, *105*, 6987.

[8] R. Nakamura, S. Sato, *J. Phys. Chem. B*, **2002**, *106*, 5893.

[9] S. H. Szczepankiewicz, A.J. Colussi, M.R. Hoffmann, *J. Phys. Chem. B*, **2000**, *104*, 9842.

[10] U. Diebold, *Surf. Sci. Rep.*, **2003**, *48*, 53.

[11] a) J.M. Coronado, S. Kataoka, I. Tejedor-Tejedor, M.A. Anderson, *J. Catal.*, **2003**, *219*, 219; b) J.M. Coronado, M.E. Zorn, I. Tejedor-Tejedor, M.A. Anderson, *Appl. Catal., B,* **2003**, *43*, 329.

[12] M.A. Henderson, *J. Phys. Chem.*, **2004**, *108*, 18932.

[13] M.A. Henderson, *J. Phys. Chem. B*, **2005**, *109*, 12062.

[14] a) W. Xu, D. Raftery, *J. Catal.*, **2001**, *204*, 110; b) W. Xu, D. Raftery, J.S. Francisco, *J. Phys. Chem., B,* **2003**, *107*, 4537.

[15] a) J. Peral, D.F. Ollis, *J. Catal.*, **1992**, *136*, 554; b) M.L. Sauer, D.F. Ollis, *J. Catal.*, **1994**, *149*, 81.

[16] a) A.V. Vorontsov, E.N. Kurkin, E.N. Savinov, *J. Catal.*, **1999**, *186*, 318; b) A.V. Vorontsov, I.V. Stoyanova, D.V. Kozlov, V.I. Simagina, E.N. Savinov, *J. Catal.*, **2000**, *189*, 360

[17] D. Kozlov, D. Bavykin, E. Savinov, *Catal. Lett.*, **2003**, *86*, 169.

[18] J.C. Yu, J. Lin, D. Lo, S.K. Lam, *Langmuir,* **2000**, *16*, 7304.

[19] S.B. Kim, S.C. Hong, *Appl. Catal. B,* **2002**, *35*, 305.

[20] A.L. Attwood, J.L. Edwards, C.C. Rowlands, D.M. Murphy, *J. Phys. Chem. A,* **2003**, *107*, 1779.

[21] C.A. Jenkins, D.M. Murphy, *J. Phys. Chem. B*, **1999**, *103*, 1019.

[22] A.R. Gonzalez-Elipe, M. Che, *J. Chim. Phys.*, **1982**, *79*, 355.

[23] A. Attwood, D.M. Murphy, J. Edwards, T.A. Egerton, R.W. Harrison, *Res. Chem. Interm.*, **2003**, *29*, 449.

[24] C. Murata, H. Yoshida, J. Kumagai, T. Hattori, *J. Phys. Chem.*, **2003**, *107*, 4364.

[25] D.C. Hurum, A.G. Agrios, K.A. Gray, T. Rajh, M.C. Thurnauer, *J. Phys. Chem.*, **2003**, *107*, 4545.

[26] A) T. Berger, M. Sterrer, O. Diwald, E. Knozinger, D. Panayotov, T.L. Thompson, J.T. Yates, Jr. *J. Phys. Chem.*, **2005**, *109*, 6061; b) T. Berger, M. Sterrer, O. Diwald, E. Knozinger, *Chemphyschem.*, **2005**, *6*, 2104.

[27] a) J.M. Coronado, A.J. Maira, J.C. Conesa, K.L. Yeung, V. Augugliaro, J. Soria, *Langmuir*, **2001**, *17*, 5368. b) M.J. Lopezmunoz, J. Soria, J.C. Conesa, V. Augugliaro, *Stud. Surf. Sci. Catal.*, **1984**, *82*, 693.

[28] Y. Nakaoka, Y. Nosaka, *J. Photochem. Photobiol. A: Chem.*, **1997**, *110*, 299.

[29] J. Yanez, C.L. Sevilla, D. Becker, M.D. Sevilla, *J. Phys. Chem.*, **1987**, *91*, 487.

[30] O.I. Micic, Y. Zhang, K.R. Cromack, A.D. Trifunac, M.C. Thurnauer, *J. Phys. Chem.*, **1993**, *97*, 13284.

[31] Y. Nosaka, K. Koenuma, K. Ushida, A. Kira, *Langmuir*, **1996**, *12*, 736.

[32] a) M. Kaise, H. Nagai, K. Tokuhashi, S. Kondo, S.Nimura, O. Kikuchi, *Langmuir*, **1994**, *10*, 1345. b) M. Kaise, C. Nishihara, H. Nozoye, H. Shindo, S. Nimura, O. Kikuchi, *J. Chem. Soc. Chem. Comm.*, **1993**, 4, 395.

[33] a) R.F. Howe, M. Gratzel; *J. Phys. Chem.*, **1985**, *89*, 4495. b) R.F. Howe, M. Gratzel, *J. Phys. Chem.*, **1987**, *91*, 3906.

[34] M. Anpo, T. Shima, Y. Kubokawa, *Chem. Lett.*, **1985**, 1799.

[35] P. Meriaudeau, M. Che, P.C. Gravelle, S. Teichner, *Bull. Soc. Chim. France*, **1971**, *1*, 13.

[36] W. Kanzig, M.H. Cohen, *Phys. Rev. Lett.*, **1959**, *3*, 509.

[37] M. Che, A.J. Tench, *Adv. Catal.*, **1983**, *32*, 1.

[38] M.D. Sevilla, D. Becker, M.J. Yao, *J. Chem. Soc., Faraday Trans.*, **1990**, *86*, 3279.

[39] K.L. Antcliff, D.M. Murphy, E. Griffiths, E. Giamello, *Phys. Chem. Chem. Phys.*, **2003**, *5*, 4306.

[40] J.M. Coronado, A.J. Maira, J.C. Conesa, J. Soria, *NATO Science Series, II: Mathematics, Physics and Chemistry*, **2002**, *76*, 297.

[41] R. Konaka, E. Kasahara, W.C. Dunlap, Y. Yamamoto, K.C. Chien, M. Inoue, *Free Radical Biology & Medicine*, **1999**, *27*, 294.

[42] D. Dvoranova, V. Brezova, M. Mazur, M.A. Malati, *Applied Catalysis, B: Envirn.*, **2000**, *37*, 91.

[43] C.P. Kumar, N.O. Gopal, T.C. Wang, M-S. Wong, S.C. Ke, *J. Phys. Chem. B*, **2006**, *110*, 5223.

[44] E. Serwicka, M.W. Schlierkamp, R.N. Schindler, *Z. Naturforsch.*, **1981**, *36a*, 226.

[45] D.C. McCain, W.E. Palke, *J. Magn. Reson.*, **1975**, *20*, 52.

[46] M.A. Henderson, W.S. Epling, C.H.F. Peden, C.L. Perkins, *J. Phys. Chem. B*, **2003**, *107*, 534.

[47] P. Meriadeau, J.C. Vedrine, *J. Chem. Soc., Faraday Trans. 2* **1976**, *72*, 472

[48] A.R. Gonzalez-Elipe, G. Munuera, J. Soria, *J. Chem. Soc., Faraday Trans. 1*, **1979**, *75*, 748.

[49] K. Ishibashi, Y. Nosaka, K. Hashimoto, A. Fujishima, *J. Phys. Chem. B*, **1998**, *102*, 2117.

[50] A. Linsebigler, G. Lu, J.T. Yates, *J. Phys. Chem.*, **1996**, *100*, 6631.

[51] P.W. Atkins, M.C.R. Symons, *The structure of inorganic radicals*, Elsevier Publishing Company, Amsterdam, **1967**.

[52] G. Martra, *Appl. Catal. A: General*, **2000**, *200*, 275.

[53] a) Y.A. Dmitriev, *J. Low Temp. Phys.*, **2005**, *139*(5/6), 541.; b)Y.A. Dmitriev, *J. Low Temp. Phys.*, **2005**, *31*, 423.

[54] J.E. Bennett, B. Mile, *Trans. Faraday Soc.*, **1971**, *67*, 1587.

[55] W. Xu, D. Raftery, J.S. Francisco, *J. Phys. Chem. B*, **2003**, *107*, 4537

[56] A.V. Vorontsov, E.N. Kurkin, E.N. Savinov, *J. Catal.*, **1999**, *186*, 318

[57] S. Chen, X. Cheng, Y. Tao, M. Zhao, *J. Chem. Tech. Biotech.*, **1998**, *73*, 264

[58] D-R Park, J.Zhang, K. Ikeue, H. Yamashita, M. Anpo, *J. Catal.*, **1999**, *185*, 114

[59] M.A. Henderson, *Langmuir*, **2005**, *21(8)*, 3443

[60] M. Anpo, K. Chiba, M. Tomonari, S. Collucia, M. Che, M.A. Fox, *Bull. Chem. Soc. Jpn.*, **1994**, *64*, 543

[61] L.A. Phillips, G.B. Raupp, *J. Mol. Catal.*, **1992**, *77*, 297

Chapter 7

Development of a UHV-EPR Assembly for Studies of Single Crystal Oxide Surfaces

7.1 Introduction

Magnetic resonance, including nuclear magnetic resonance (NMR) and electron paramagnetic resonance (EPR), constitute a class of spectroscopy which has grown in importance over the past 70 years. NMR is frequently used in the fields of chemistry and biology, and with the advent of magnetic resonance imaging (MRI) in 1973 it serves as an important diagnostic tool in medical studies. Both techniques provide information on structure, composition and additionally on the dynamics of molecules in solution. The sensitivity of the NMR technique extends to 10^{17} nuclei,[1] whereas most modern EPR spectrometers can detect down to 10^{12} spins. For a single crystal of dimensions 10×10mm, a monolayer would equate approximately to 10^{15} spins. Therefore EPR is a suitable technique to study monolayers or fractions of monolayers on single crystal samples. The improved sensitivity of EPR spectrometers compared to NMR spectrometers can be attributed in part to the difference in the values of the magnetic moments of electrons and nuclei (i.e., $9.27402\times10^{-24}JT^{-1}$ and $5.05079\times10^{-27}JT^{-1}$ respectively) which determines the population difference between the energy levels, and thus the sensitivity of the technique.

Surface science studies must be performed under ultra-high vacuum conditions in order to maintain a surface free from contaminants over the time scale of the experiment. The first UHV-EPR experiment was reported by Bagdonat *et al.*,[2] in 1973 on the investigation of semiconductors and thin films on insulating substrates. Since that time several UHV-EPR experiments have been performed by different groups investigating many different systems, including defects on cleaved Si surfaces[3-5] and the adsorption of paramagnetic gases on the surface of thin-films.[6,7]

The initial aim of the investigation described in this chapter using UHV-EPR spectroscopy was to study the surface chemistry of single crystal samples of metal oxides. The previous chapters of this thesis have detailed the importance of different stabilisation sites on the surface of polycrystalline samples of TiO_2. Experimental results suggest that the chemistry at the surface is affected by surface electronics, in particular at vacancy sites. It has been well documented that surface defect sites play an

important role in surface chemistry, but it is impossible to identify the nature of these defects on polycrystalline samples. Therefore, it is necessary to study single crystals that have a well-defined morphology and crystal structure, thereby providing the possibility to acquire a deeper understanding of the results previously obtained on the powdered samples, as described in Chapters 5 and 6.

7.2 A Brief Review of UHV-EPR Studies

7.2.1 NO_2 Adsorption on Different Substrates

One of the first UHV-EPR investigations was carried out by Nilges *et al.*,[8] who reported the adsorption of NO_2 onto a Cu/Vycor substrate. In their study, a thin film of Cu containing ~10^{18}–10^{19} metal spins was evaporated onto the inner surface of a cylindrical cavity. No EPR signal was recorded of the clean copper film. However, after exposing the sample to 0.1–1 Torr NO_2 at room temperature a well-resolved EPR spectrum was observed implying that the Cu on Vycor could be oxidized by NO_2 to form Cu^{2+}.[8] The resulting EPR spectrum of NO_2 was made up of two contributions. Firstly, the specific spatial orientation of the electron orbital in which the unpaired electron was located led to a dependency of the electron spin resonance on the orientation of the molecule in the external magnetic field. In other words, the isotropic g value of the free electron was transformed into an anisotropic g tensor which gave rise to a splitting of the resonance lines. The hyperfine interaction of the unpaired electron with the nuclear spin (I = 1) of the nitrogen atom as the second contribution may be described by the A tensor and finally led to an appearance of the spectrum exhibiting three well separated parts.

Two g-tensors and corresponding hyperfine tensors could be resolved from the spectrum, which were assigned to two different Cu^{2+} complexes.[8] When small samples of Cu wire were placed in the EPR cavity followed by the admission of NO_2 to the sample, three different EPR signals were resolved: (a) a symmetric singlet with g = 2.19, (b) an asymmetric signal with $g_{\parallel}$ = 2.41 and $g_{\perp}$ = 2.09, and finally (c) a second asymmetric signal with g values of $g_{\parallel}$ = 2.34 and $g_{\perp}$= 2.11. The three signals arose due to different stages of oxidation of the metal wire. No hyperfine splitting could be resolved for any of these signals, and this was attributed to the fact that, on the pure metal, adjacent sites become paramagnetic so they can exchange narrow the hyperfine splitting. On the Cu/Vycor system only spectra from separated Cu^{2+} ions were seen with negligible exchange interaction. Nilges *et al.*,[8] concluded that this study should

be applicable to other metal films and to the preparation and study of "clean" oxide surfaces as well as "supported metal" surfaces.

Following the above paper, Farle *et al.*,[9] reported on an investigation of NO_2/H_2O adsorbed on clean Cu(111) single crystals under UHV conditions. In accordance with results described further below, no EPR signal could be resolved for only NO_2 adsorbed directly onto the metal substrate. Only when the sample was cooled under approximately 5 Torr NO_2/H_2O did an EPR signal develop. The NO_2/H_2O gas mixture condensed at the cooled copper surface forming nitric acid and solvating Cu^{2+} ions. When this aqueous solution of Cu^{2+} and NO_3^- ions froze out during evacuation of the chamber the axially symmetric $Cu(NO_3)_2$ complex was formed in an environment of frozen water. No hyperfine structure from the Cu^{2+} was observed but the EPR signal was observed to exhibit angular dependency, as shown in Figure 7.1. Therefore this excluded the possibility of a random orientation of the molecules on the surface. From computer simulations it was determined that the $Cu(NO_3)_2$ molecules were adsorbed on the surface with their molecular planes inclined preferentially normal to the plane of the Cu (111) surface.[9]

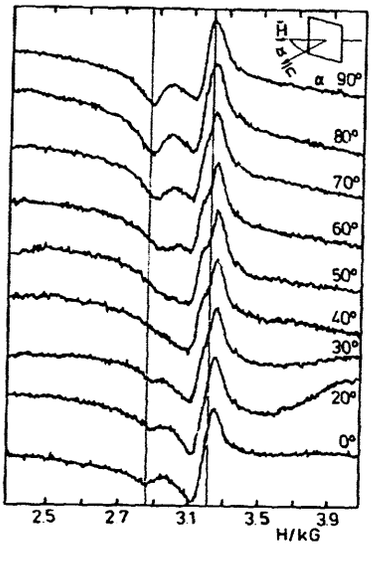

Figure 7.1 Experimental EPR spectra of $Cu(NO_3)_2$ on Cu(111) at various angles with respect to the magnetic field.[9]

The interest in the information gathered from EPR investigations performed under UHV conditions increased significantly at this time, and led to an increase in the number of publications in this area. Zomack and Baberschke[10] published for the first time in 1986 an experiment where the traditional surface analytical methods of LEED and AES were combined with EPR in UHV. No EPR signal was resolved after

adsorbing a low dosage of NO_2 on the clean Ag(110) crystal, whereas a well-resolved resonance appeared after pre-adsorption of a few layers of krypton (>10L, ~3 layers).[10] The explanation provided for this observation was that the Korringa-correlation[11] effects were present on the monolayer sample. That is, the interaction between the electrons at the Fermi energy of the metal substrate and the electron spin on the molecule were so strong that the average residence time of the electron spin on the molecule was strongly reduced. This led to a strong increase of the line width such that the spectrum disappeared into the background noise.[12] In Zomack's experiment, the local moment was completely decoupled from the metal by the krypton layer.[10]

Investigation of the EPR line shapes at different coverages led to information on the molecular orientation of the adsorbate. At low coverages of NO_2 only two of the molecular axes contributed to the spectrum, which led to the conclusion that the NO_2 lies flat on the krypton surface. As the coverage increased, the third molecular direction contributed to the signal, but the resolution of the hyperfine lines was lost when the coverage increased above several layers.[10]

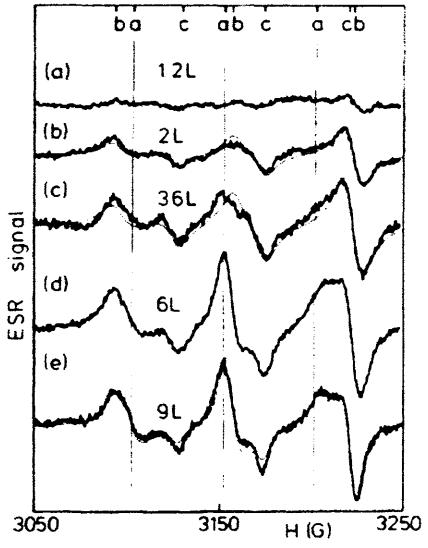

Figure 7.2 EPR spectra of NO_2 on xenon films on a Ag(111) substrate at 20K. 3L corresponds approximately to one monolayer.[13]

This investigation was extended by utilising two additional rare gases, argon and xenon.[13] By comparison to the initial results of NO_2 on krypton, an EPR signal could only be resolved for NO_2/Xe or NO_2/Ar when almost a monolayer of the rare gas had been pre-adsorbed onto the metal surface (Figure 7.2). Again, from computer simulations, the molecule was found to lie flat on the surface, only showing a random

distribution of all three orientations when several layers of rare gas were adsorbed.[13] This observation was as a result of the Stranski-Krastanov or type-II growth mode of the xenon (argon) films. In this growth mode the first adsorbed layer forms a complete two-dimensional film and 3D islands start growing on top of this. The mismatch of the lattice constants between the Ag(111) and bulk xenon promotes this type of growth.

The above work prompted investigation of thin films on single crystals. Katter *et al.*,[12] considered the EPR spectra obtained upon the adsorption of NO_2 onto a clean Au(111) single crystal and a NiAl(110) single crystal. Following this, the group grew a thin film several monolayers thick of NiO(111) on the Au(111) surface and a γ–Al_2O_3(111) film was prepared on the NiAl(110) surface.[12] From previous work on the NO_2/Au(111) system it had been determined that the NO_2 molecule had its molecular plane oriented perpendicularly towards the surface plane, and the molecule was bound to the surface with both oxygen atoms.[14] No EPR signal was resolved from the system with only monolayer coverage of NO_2, but on multilayer adsorption a strong well resolved solid state spectrum was recorded.[12]

The line width of the EPR spectra recorded using different surface concentrations of NO_2 on the Au(111) surface were used in conjunction with data from Kittel and Abrahams[15] to determine the intermolecular distance between the adsorbed species.[12] A surface concentration of 5×10^{-2} M resulted in a line width of 1.72mT which translates to an intermolecular distance of 8.2Å. A decrease in surface concentration to 1×10^{-6} M led to a line width of 0.57mT and an increase in the intermolecular distance of 50%.[12]

On direct adsorption of NO_2 onto a NiAl(110) surface an angular dependency in the EPR signal was observed, which was not observed for the NO_2/Au(111) system. NO_2 reacts with NiAl(110) leading to several N containing species with unpaired electrons on the eventually oxidised surface. At an orientation of 0° (between the sample plane and the applied magnetic field) Katter *et al.*,[12] recorded a spectrum which resembled a three-dimensionally random NO_2 adsorbate. However, at 90° there was an extra triplet overlapping the spectrum of a randomly oriented NO_2 distribution, indicating that there was a chemically different NO_2 species present on the surface which was oriented with its molecular plane relative to the surface plane.

In the case of NO_2/γ-Al_2O_3/NiAl(110) the EPR signals recorded for different surface coverages led to the conclusion that there was a combination of three-dimensional random and two-dimensional distributions, which was attributed to the

coexistence of a physisorbed multilayer on top of a monolayer of molecules in direct contact with the $Al_2O_3(111)$ surface.[12] However, there were several deviations of the computer simulations from the experimental data when only a statistical distribution was considered, which were suspected to be a consequence of molecular motion in the system. The investigation of temperature dependent spectra indicated characteristic changes of the line shapes as a function of temperature which could be related to the dynamics in the adsorbate systems.

The investigation of surface adsorbed species on clean metal surfaces and oxide films was continued by Katter *et al.*,[16] in their study of the adsorption of di-*tert*-butyl nitroxide (DTBN) on Au(111) and NiO(111). As seen previously, no EPR signal could be recorded of DTBN on the clean Au(111) surface, even at multilayer coverages corresponding to dosages of 50L. An EPR signal was first resolved at a dosage of 100L which corresponds to 20 layers, shown in Figure 7.3. The interaction between the substrate and the adsorbate was weakened by pre-adsorbing xenon onto the surface of the clean Au(111). The results of the investigation showed that the DTBN molecules were influenced by the substrate even through a monolayer of xenon, but that this interference was negligible through multilayers.[16]

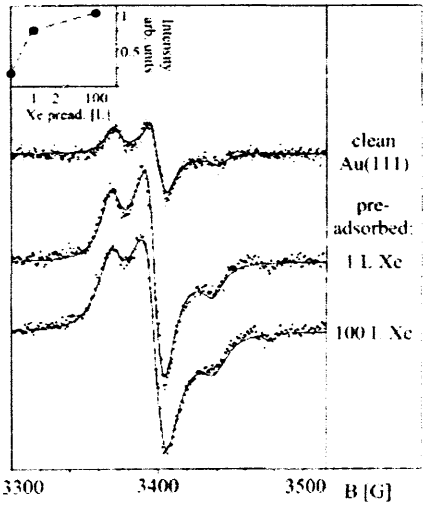

Figure 7.3 EPR spectra of DTBN/Au(111) with preadsorbed xenon.[16]

The suppression of the EPR signal through interactions between the adsorbate and the substrate was even more long range in the case of DTBN/NiO(111)/Au(111). For this system, no EPR signal could be recorded until dosages corresponding to 80 layers were used and the enhancement of the signal from dosing with xenon was less pronounced. Information on the rotational and translational motion in the multilayers

was however resolved on annealing of the sample from 35K to 165K, as shown by changes in the hyperfine structure.[16]

In contrast to the results discussed thus far, the research of Schlienz *et al.*,[17] contained EPR spectra of submonolayer coverages of NO_2 on Al_2O_3. A 5Å thick film of γ-Al_2O_3(111) was grown on a NiAl(110) single crystal. As in previous studies, an increase in the line-width was observed as the coverage of the adsorbate increased. This was attributed to a decrease in the distance, r, between NO_2 molecules leading to increased dipolar interaction, described by $\Delta B \approx 1/r^3$. On gentle annealing of the sample to ~100K, a decrease of the EPR line-width and signal intensity to levels below detection was observed over a period of minutes. The decrease of the concentration of NO_2 was caused by the reaction of paramagnetic NO_2 monomers to the diamagnetic N_2O_4 dimer ($2NO_2 \leftrightarrow N_2O_4$).[18] The dimerization was assumed to be a diffusion controlled reaction, for which a theoretical relation between the rate constant and diffusion coefficient is available.[19] From the EPR signals recorded in Schlienz's study,[17] a diffusion coefficient for NO_2 across Al_2O_3 of $D \sim 10^{-15} cm^2 s^{-1}$ was calculated.

7.2.2 Fatty acid films

There have been several papers published on the study of self-assembled fatty acid films on oxide surfaces utilising EPR spectroscopy under UHV conditions. From the lineshape of the EPR spectrum an insight into the rotational motion of the films can be gained. Risse *et al.*,[20-22] performed a study on the self-assembly of stearic acid ($C_{18}H_{36}O_2$) films on an Al_2O_3 thin film substrate grown on a NiAl(110) single crystal. The stearic acid molecules were labelled with *n*-doxyl stearic acid (*n*-DXSA) as probe molecules. These nitroxides, with an oxazolidinyl ring as the paramagnetic group connected to different positions of the aliphatic chain, are well-known as paramagnetic probes. The study identified both concentration and temperature dependence on the lineshape of the resolved EPR signals. Notably, for concentrations lower than 10% the spin labels could be considered to be magnetically independent. The temperature dependence of the lineshape identified two trends in molecular motion of the stearic acid molecules. Changes in the linewidth above 200K were due to the motion of the protons in the surroundings of the spin label. At temperatures above 315K the lineshape changes were indicative of the motion of the spin labels connected to the alkyl chains, which are themselves anchored to the Al_2O_3 substrate.[20-22]

7.2.3 *MgO Thin Films*

Most recently, Sterrer *et al.*,[23] have performed an ultra-high vacuum EPR investigation of the surface colour centres on thin films of MgO(001) on Mo(001) substrates. The oxygen vacancies on the surface can donate or accept electrons from adsorbates at the surface, and consequently play an important part in catalysis. Their research characterized the surface F centres in terms of their electronic and geometric structure and investigated their influence on adsorbed species. The Zeeman interaction of the colour centres could be described using a symmetric (3×3) g tensor, which would be different for all orientations of the colour centre with respect to the orientation of the static magnetic field. The authors[23] identified differences in the g tensor and linewidths of the F centres at different sites on the crystal. For example, the g value of the F centre at an edge site was resolved as $g_{iso} = 2.0001 \pm 0.00005$, $\Delta g = 0.00040$, $\Delta B = 0.110$mT whereas that at a corner site was resolved as $g_{iso} = 2.0001 \pm 0.00005$, $\Delta g = 0.00027$ and $\Delta B = 0.106$mT. These g values could not be resolved from studies on powder samples which contain all possible orientations with respect to the static magnetic field. The angular dependency of the linewidth, shown in Figure 7.4, could therefore be used as an identification of the geometric properties of paramagnetic defects at crystal surfaces, and it was determined that paramagnetic colour centres generated on the surface of MgO thin films are located predominantly at the edges of the MgO facets.[23]

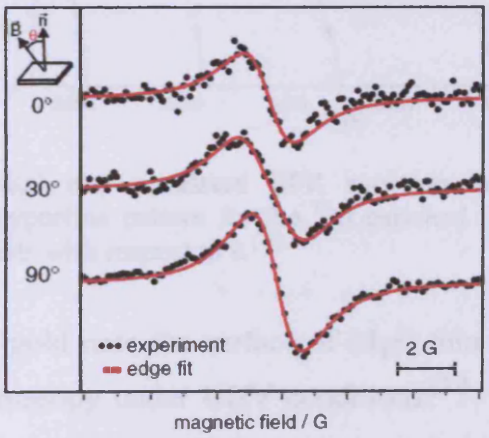

Figure 7.4 Experimental and simulated EPR spectra of colour centres on MgO(001)/Mo(001).[23]

Yulikov *et al.*,[24] recently published a paper on the binding of single gold atoms onto thin MgO(001) films, grown on a Mo(001) substrate. The authors combined EPR and low temperature STM under UHV conditions to ascertain the location of isolated Au atoms on the MgO film. Upon deposition of 2.8×10^{12} Au atoms on to the

MgO(001) film, a four line EPR spectrum was recorded due to the hyperfine interaction of the electron with the gold atoms. From angular resolved measurements, axially symmetric g and A tensors of $g_{\|}$ = 1.9904, $A_{\|}$ = 1410 MHz and $g_{\perp}$ = 2.0652, $A_{\perp}$ = 1402MHz were resolved.[24] All of the low coordinate sites (e.g. edges, corners, kinks, etc) were rejected as possible adsorption sites for the Au atoms as none of the principle components of the tensor were collinear with the surface normal. However, the terrace sites are collinear with the parallel component of the matrix and it was therefore concluded that Au atoms were adsorbed on these terrace sites. Further, when a film enriched with ^{17}O was used [I(^{17}O) = 5/2] a six line hyperfine pattern superimposed onto the original four line signal was resolved, shown in Figure 7.5. From these observations it was concluded that the Au atoms were adsorbed on top of oxygen ions on the terraces of the MgO film.[24]

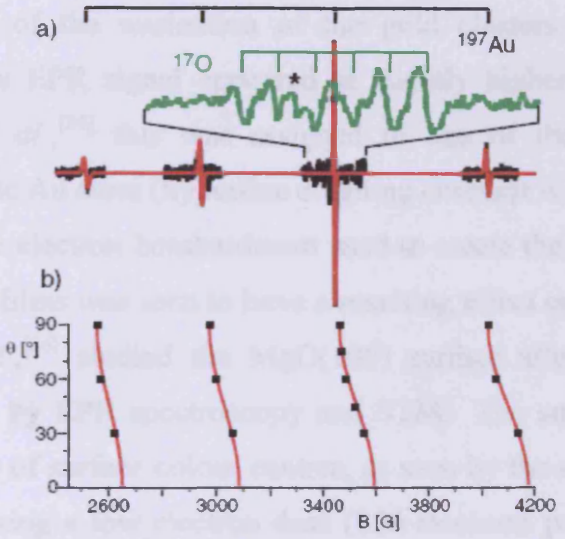

Figure 7.5 (a) experimental and simulated EPR spectrum of Au atoms adsorbed on MgO(001)/Mo(001). The hyperfine pattern for the ^{17}O enriched film is indicated (b) angular dependence of the EPR signals with respect to θ.[24]

The adsorption of gold onto the surface of MgO thin films was studied further *via* STM and EPR spectroscopy under UHV conditions.[25] A 4ML thick MgO(100) thin film was prepared on top of a Ag(001) single crystal and was treated with 100eV electron bombardment. The electron bombardment resulted in the formation of surface colour centres at edges, corner and kinks of the MgO facets that were visible in the STM images as bright spots. An EPR spectrum recorded for a MgO(100) film on a Mo(001) substrate showed a sharp isotropic signal at $g \approx 2$, which was assigned to paramagnetic colour centres located at edge sites of the MgO surface,[25] as shown in the top of Figure 7.6.

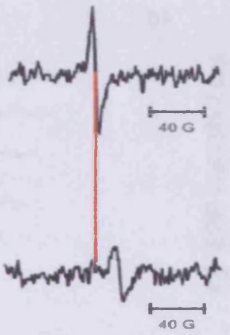

Figure 7.6 EPR ($g \approx 2$) of MgO(100)/Mo(001) after low dose electron bombardment (top); after deposition of 0.015ML Au at 30K (bottom).[25]

On subsequent exposure of the film to 0.035ML Au atoms at 5-8K, Au atoms and dimers could be resolved in the STM images.[25] Additionally, small Au clusters nucleated on top of the surface colour centres. After deposition of Au (0.015ML, 30K) onto the MgO surface [Mo(001) substrate], the EPR signal due to the colour centre was quenched as a result of the nucleation of the gold clusters [Figure 7.6(bottom)]. Simultaneously, a new EPR signal appeared at slightly higher field. Based on the results of Yulikov *et al.*,[24] this was assigned to one of the lines in the quartet characteristic of a single Au atom (hyperfine coupling constant A~ 1400MHz).[25]

The dose of the electron bombardment used to create the surface colour centres on the thin MgO(100) films was seen to have a resulting effect on the electronics of the centres. Sterrer *et al.*,[26] studied the MgO(100) surface after increasing doses of electron bombardment by EPR spectroscopy and STM. The surface prior to electron bombardment was free of surface colour centres, as seen by the absence of any lines in the EPR spectrum. Using a low electron dose (150 electrons per surface oxygen ion; $150e^-/O^{2-}$), the resonance line at free spin due to singly occupied surface colour centres (F_s^+) at MgO edges appeared. The intensity of this EPR line increased up to an electron dosage of 1000 e^-/O^{2-} but decreased for higher exposures, as shown in Figure 7.7a. A plot of peak-peak value against electron dosage (Figure 7.7b) indicated that the decay of the F_s^+ centres could be described by first-order kinetics in this regime.[26]

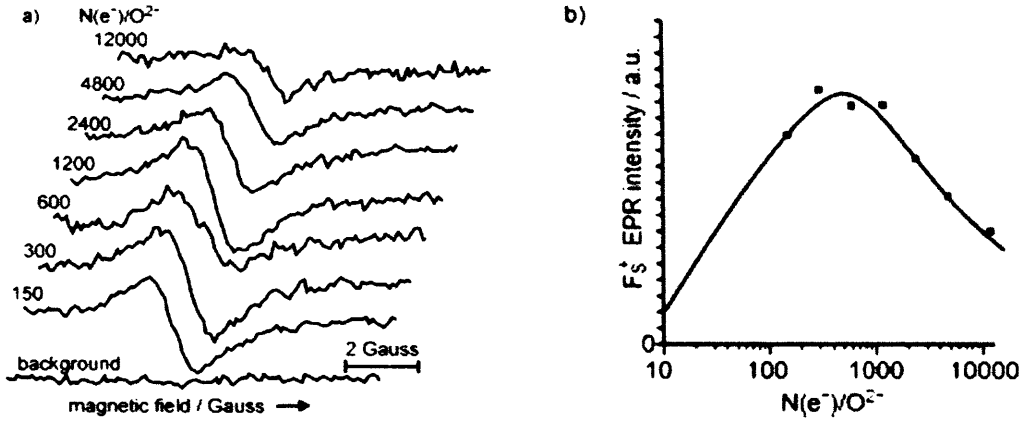

Figure 7.7 (a) EPR spectra of MgO(100) film after 100eV electron bombardment at increasing dosage levels (b) peak-to-peak intensity of EPR signal as a function of dosage.[26]

7.2.4 Outlook

To date, no UHV-EPR studies have been performed on single crystal sample of metal oxides (only thin films, as described above). Further, no attempt has been made to study TiO_2 using EPR spectroscopy under UHV conditions. In Chapters 5 and 6, a detailed account of paramagnetic defects and oxygen centred radical stabilised over polycrystalline TiO_2 was given. In particular, evidence was provided for the identification of oxygen vacancy sites on the surface of the polycrystalline material. Through extensive studies of single crystal samples of TiO_2 using conventional surface science techniques a great deal of information has been gathered on the nature of the TiO_2(110) surface.[27] Therefore, it is appropriate at this stage to investigate the TiO_2(110) surface using UHV-EPR spectroscopy in order to combine the knowledge from the polycrystalline material with the detailed accounts on the single crystal.

7.3 Experimental

The EPR investigations described hereafter under ultra-high vacuum conditions were performed on an Omicron Multiprobe® Surface Science Ultra-High Vacuum (UHV) system. Only the important details on the system relevant to the EPR studies are included below; additional supplementary material describing the basic requirements of UHV conditions are discussed further in Appendix 1.

7.3.1 The EPR Spectrometer and Magnet

A Bruker EMX spectrometer operating at X-band frequencies (~9.5GHz) was used during this investigation. The control unit of the spectrometer is equipped with a Bruker ER036TM teslameter which can provide accurate measurements of field inhomogeneities down to 10^{-4} mT, giving g values accurate to 4 decimal places. The magnet assembly was slightly modified to make it compatible with the restricted space around the UHV chamber. These modifications included the re-positioning of the microwave bridge to sit in a vertical position on a support plate fixed to the back of the magnet. The waveguide points in a horizontal direction towards the cavity, as shown in Figure 7.8.

Furthermore, the entire bridge and magnet was supported on specially constructed wheels, shown in Figure 7.9, to retract the magnet and bridge from the UHV system. The magnet used with the Bruker EMX spectrometer is a Bruker ER072 8" magnet coupled to a Bruker ER081 power supply. The magnet operates in the range 50-950mT. The movement of the magnet is required during periods of bake-out when the entire Omicron© Multiprobe system is enclosed in bake-out covers. The cavity must be disconnected from the bridge and lowered down from around the EPR quartz dewar before the magnet can be retracted.

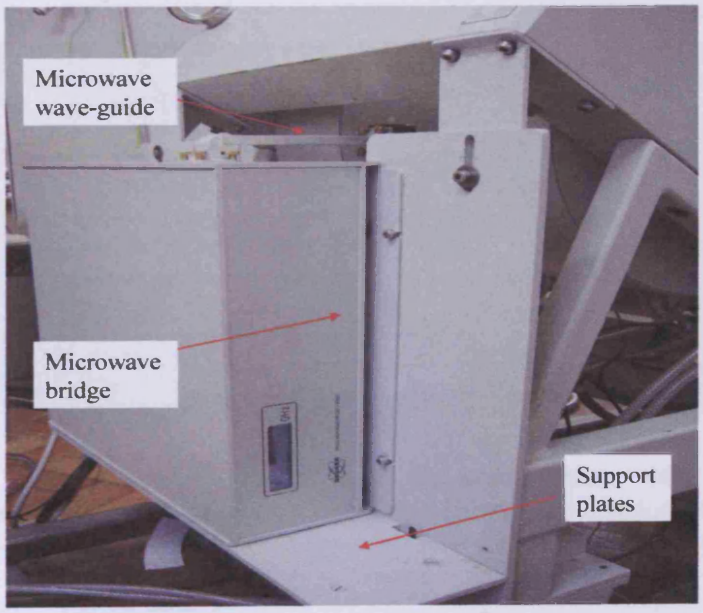

Figure 7.8 Microwave bridge for the EMX spectrometer. The bridge sits in a vertical position on support plates attached to the back of the magnet.

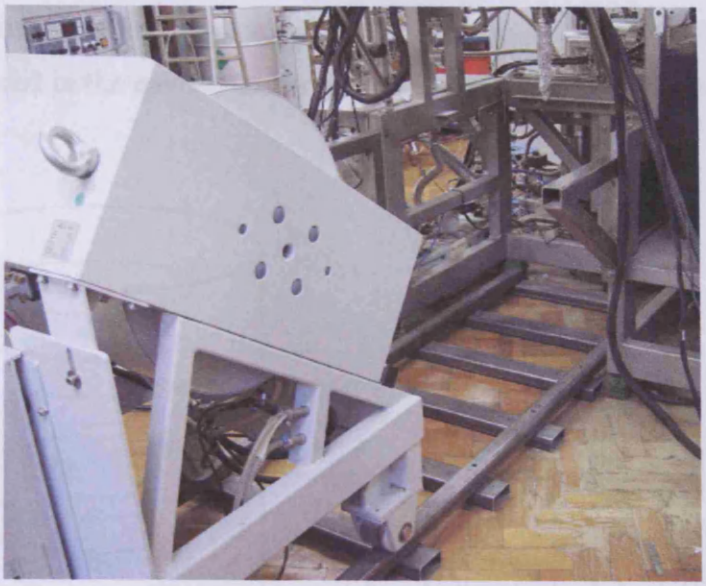

Figure 7.9 The rail system on which the magnet and bridge are situated. The magnet can be rolled into position under the UHV chamber and removed again during bake-out.

7.3.2 The EPR Cavity

The cavity used with the Bruker EMX spectrometer is an ER4103TM wide bore cylindrical resonator, as shown in Figure 7.10. The maximum sample diameter that can be accommodated by this cavity is 17mm, which yields a four-fold signal increase over the standard ER4102ST cavity. The samples used during this investigation have a maximum width of 10mm for reasons that will be discussed further in the following sections.

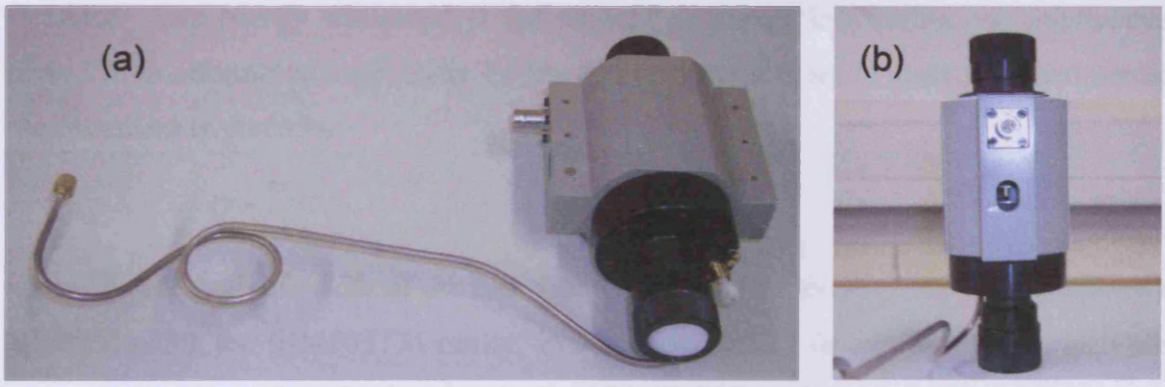

Figure 7.10 (a) The ER4103TM cavity used in combination with the Bruker EMX spectrometer for the study of single crystals showing (b) the modulation cable attachment and transmission window.

The ER4103TM cavity operates in the TE_{011} mode with the microwave field profiles shown in Figure 7.11. The microwaves resonate inside the cavity and amplify

the signals originating from the sample. At resonance all of the microwaves entering the cavity are stored in the cavity, i.e., none are reflected back to the source.

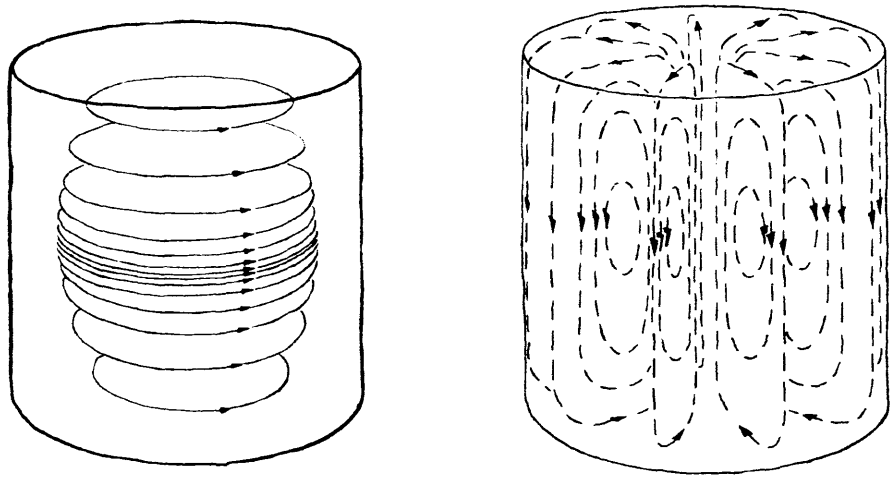

Figure 7.11 Microwave field profiles of a cylindrical cavity operating in the TE_{011} mode.

A measure of the efficiency of the storage of microwaves within the cavity is given by the cavity quality or Q factor, which can be defined according to Equation 7.1:

$$Q = \frac{[2\pi(energy\ stored)]}{energy\ dissipated\ per\ cycle} \tag{7.1}$$

An increase in the sensitivity of the cavity is demonstrated by an increase in the Q factor. The energy dissipated is the amount of energy lost during one microwave period. An alternative expression for the Q factor, which lends itself to experimental measurement is given by:

$$Q = \frac{\nu_{res}}{\Delta\nu} \tag{7.2}$$

where $\Delta\nu$ is the half-width of the resonance. Quality factors of ~5000 were frequently achieved using the ER4103TM cavity, in comparison to Q factors of ~2000 which are more commonly achieved using the standard ER4102ST cavity.

To avoid dielectric loss from the microwave electric field, it is important to position the sample in a region of maximum magnetic and minimum electric field. Dielectric losses inside a cavity lead to a reduction of the Q-factor due to the increase in energy dissipated per period. The electric and magnetic components of the microwaves are 90° out of phase, therefore a region of minimum electric field corresponds to a region of maximum magnetic field. The arrangement of the cavity during an EPR

measurement is shown diagrammatically in Figure 7.12. The cavity is placed into position around the quartz dewar and then supported in place by two clamps directly below the bottom of the cavity.

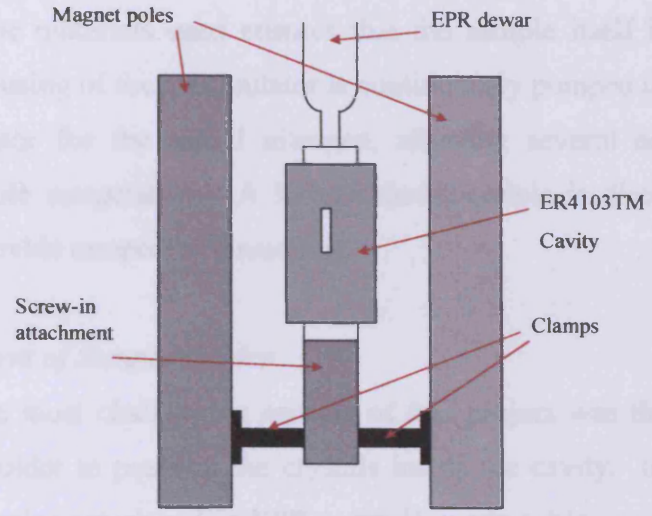

Figure 7.12 Diagrammatic representation of the positioning of the cavity.

7.3.3 Accessories

The single crystals are coupled to a vertical manipulator which has a 540mm z-translation. This allows the samples to be placed into position in front of the X-ray gun for XPS studies and then lowered into the EPR dewar. The manipulator can be rotated a complete 360° to enable angular selective studies of the crystals to be performed (Figure 7.13).

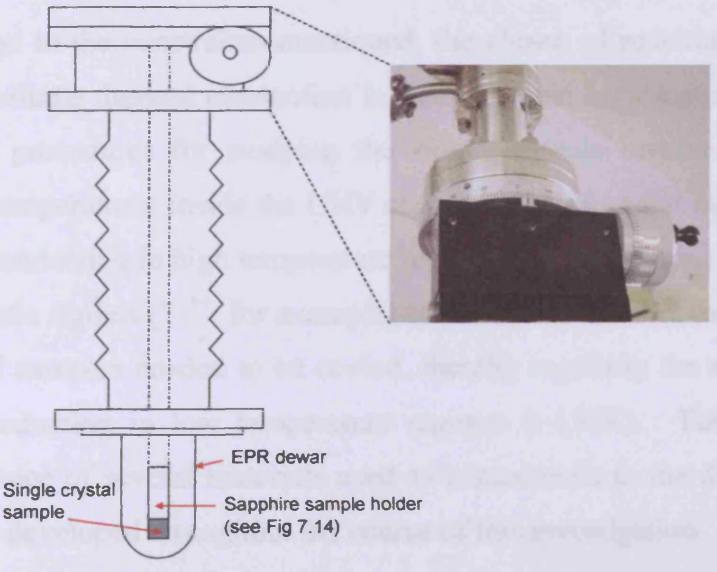

Figure 7.13 The 360° rotational vernier system to allow complete angular resolved studies of the single crystals.

Single crystal samples may be resistively heated by passing a current through the manipulator. Additionally, samples can be cooled *via* liquid nitrogen cooling of the manipulator. Liquid nitrogen is poured into the housing of the manipulator and collects in the 0.6m length. This cools the bottom of the manipulator and the good thermal conductance of the materials used ensures that the sample itself is also substantially cooled. As the housing of the manipulator is continuously pumped under vacuum it acts as a good insulator for the liquid nitrogen, allowing several accumulations to be recorded at a stable temperature. A K-type thermocouple is directly attached to the manipulator to provide temperature readings.

7.3.4 Development of Sample Holder

One of the most challenging aspects of this project was the development of a suitable sample holder to position the crystals inside the cavity. In conventional EPR spectroscopy, samples are placed in EPR suprasil quartz tubing and positioned directly inside the cavity. However, in this project the single crystal samples needed to be attached to the bottom of the manipulator inside the UHV chamber. Most importantly, the sample holder had to be designed to satisfy the requirements of UHV conditions and also the constraints of an EPR cavity. UHV conditions require that the materials used are clean and do not out-gas over long periods of time; suitable materials include tantalum, copper or stainless steel. However, metals cannot be placed in the microwave field of the EPR cavity, therefore preventing the use of a sample holder made purely of metal.

In addition to the constraints mentioned, the choice of material for the sample holder had to facilitate thermal conduction in both low and high temperature regimes. The preparation procedures for studying the single crystals involved annealing the crystals to high temperatures inside the UHV chamber; therefore the sample holder had to be thermally conducting in high temperature regimes (~700K). Additionally, as some of the paramagnetic signals (Ti^{3+}, for example) cannot be resolved at room temperature, the single crystal samples needed to be cooled, thereby requiring the sample holder to be thermally conducting in low temperature regimes (~150K). Table 7.1 lists the thermal conductance of several materials used as components in the different versions of sample holder developed throughout the course of this investigation.

Table 7.1 Thermal conductivity values

Material	Thermal Conductivity (298K) $W.m^{-1}.K^{-1}$	Ref.
Copper	385	[28]
Quartz (273K)	6.8 – 12	[28]
Sapphire	18	[28]
Tantalum	57.5	[28]
Tungsten	173	[28]
Shapal M	100	[29]
Boron Nitride	15 - 50	[29]

The first design of a sample holder, shown in Figure 7.14a, was a very simple arrangement used purely to test the tuning characteristics of the cavity and other aspects of the system. A $TiO_2(110)$ crystal was glued into a small groove etched out of a thin quartz rod, which was attached to the bottom of the vertical manipulator by a wire hoop. Using this design, the EPR cavity could be easily tuned and critically coupled with the entire sample inside the active part of the cavity. However, the poor thermal conductance of this design prevented its use for any further studies during the rest of the investigation.

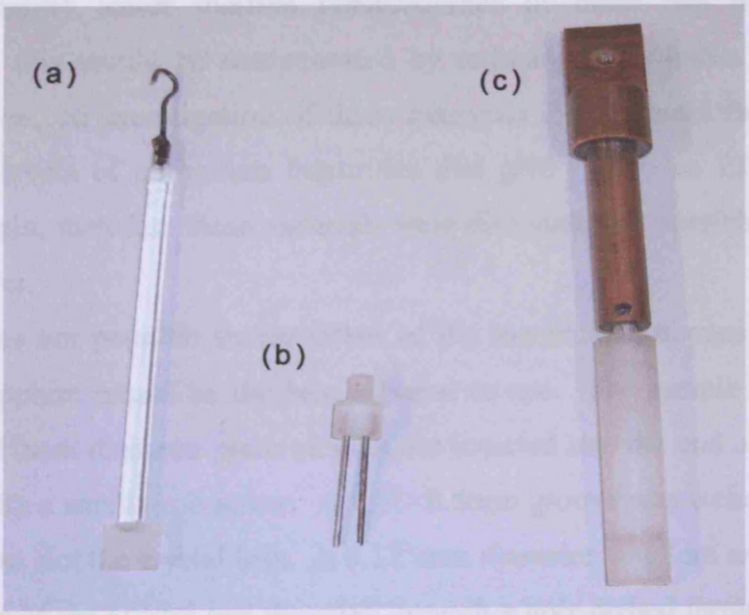

Figure 7.14 The various sample holders that have been developed during the course of this investigation (a) quartz rod (b) sapphire with tungsten rods and (c) copper and sapphire.

The second design of sample holder developed, shown in Figure 7.14b, was based on the design described by Katter *et al.*[12] It incorporated a small piece of sapphire slotted into the base of a copper block that was attached directly to the end of the manipulator. The copper block can be seen in Figure 7.14c. Two small holes were drilled at the bottom of the sapphire, into which two tungsten rods were fixed in place with aluminium foil. The crystal was held in place by a length of 0.125mm tantalum wire wrapped around the crystal and spot welded to each of the tungsten rods. Although this design incorporated the use of metal it was not seen to have a large detrimental effect on the cavity Q-value.

This design again allowed the cavity to be critically coupled when loaded with the sample. However, initial testing concluded that the cooling of the sample was insufficient to resolve the paramagnetic Ti^{3+} species of interest in this study. It was determined that the tungsten rods were not providing sufficient cooling to the sample, hence it was necessary to remove the tungsten rods from the design and replace them with a component that improved the overall thermal conductance. It should be mentioned that the design of Katter *et al.*,[12] was used in conjunction with liquid helium cooling, and therefore the authors were able to achieve temperatures of ~30K. However, this sample holder did not work efficiently with the liquid nitrogen cooling used in this investigation. Several materials were considered as possible options for use in the new design, including the machinable ceramics boron nitride and Shapal M. Despite the slightly lower thermal conductivities of these two materials it was considered that this would be compensated by reducing the number of joints in the design. However, on investigation of these materials it was found that both samples contained low levels of chromium impurities that give rise to an EPR signal in the region of free spin, therefore these materials were discounted as possible components of the sample holder.

As it was not possible to use either of the machinable ceramics tested, it was decided that sapphire would be the best material to use. The sample holder therefore incorporated a 10mm diameter piece of sapphire inserted into the end of the copper and held in place with a small grub screw. A 1.05×0.5mm groove was etched out of the end of the sapphire to slot the crystal into. A 0.125mm diameter tantalum wire was wrapped around the sides of the crystal and threaded through a hole drilled through the sapphire. The crystals themselves have small grooves cut around all four sides to allow intimate contact between the wire and the crystal.

Although the thermal conductivity of the sample holder had been dramatically improved in this design, it still proved to be ineffective. Due to the diameter of the sapphire rod, the microwave field was significantly distorted so that only 3mm of the sample could be inserted into the critically coupled cavity. Therefore, a new sapphire rod was purchased with a 4mm diameter (Figure 7.15); this allowed 10mm of the crystal, plus an additional 5mm of sapphire, to be critically coupled inside the cavity.

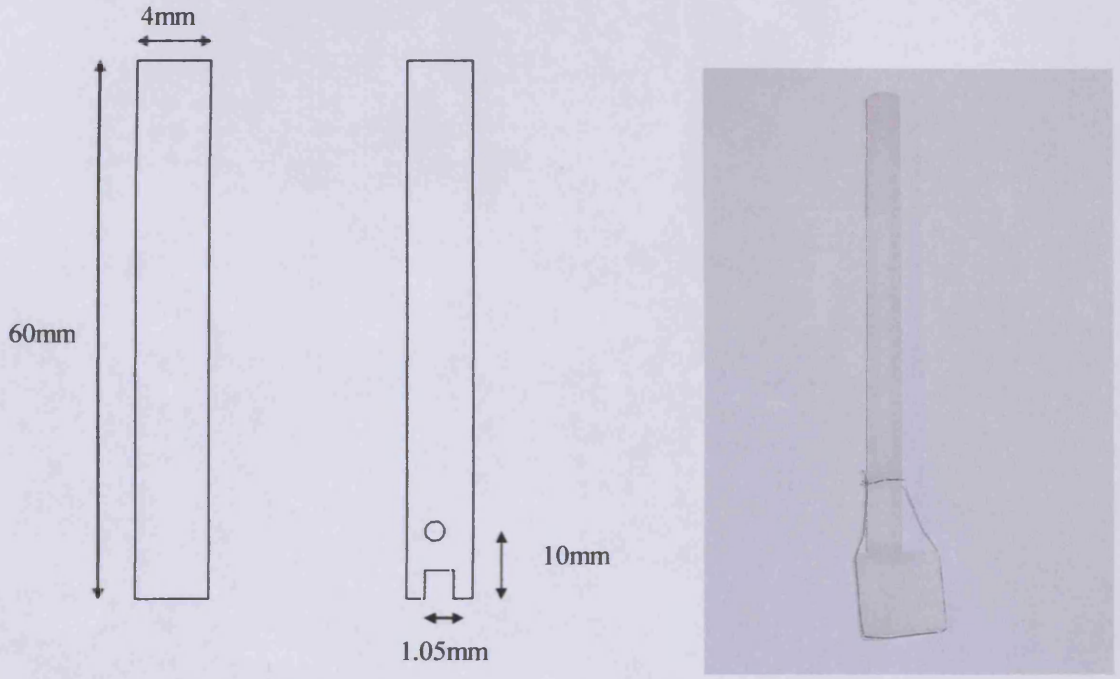

Figure 7.15 Dimensions of 2nd sapphire rod

7.3.5 Surface Science Capabilities

The EPR system used to study the single crystal samples in this investigation is incorporated in an Omicron Multiprobe® Surface Science Ultra-High Vacuum (UHV) system, shown in Figure 7.16. The system consists of four chambers which are equipped with most of the important surface science analytical techniques including X-ray Photoelectron Spectroscopy (XPS), Ultraviolet Photoelectron Spectroscopy (UPS), Low Energy Electron Diffraction (LEED), Ion Scattering Spectroscopy (ISS), Scanning Tunnelling Microscopy (STM) and Atomic Force Microscopy (AFM). For ease of discussion throughout this chapter the four chambers are referred to as the Analysis (A), Central (C), Preparation (P) and Scanning Tunnelling Microscopy (STM) chambers. All of the chambers can be isolated from each other and are independently pumped. Samples can be moved between the chambers by a series of manipulators so that they

may be studied using all of the available techniques. The surface science capabilities of the A chamber will be briefly discussed in the following, and further information on the C and P chambers is included in Appendix 1.

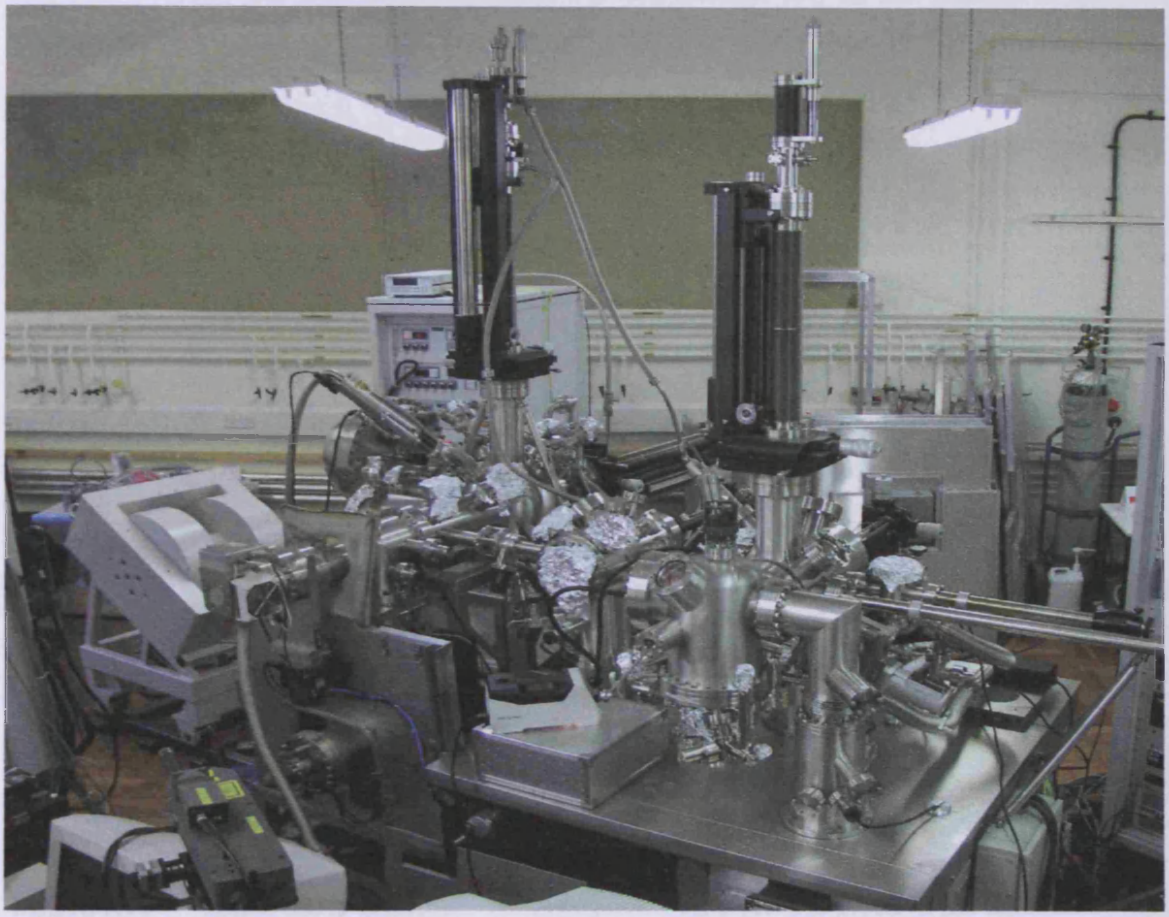

Figure 7.16 The multi-chamber Omicron Multiprobe® Surface Science Ultra-High Vacuum (UHV) system. The EPR magnet is shown in the left of the picture.

7.3.6a The A Chamber

Samples to be studied by Electron Paramagnetic Resonance (EPR) are situated in the A chamber. The A chamber is additionally equipped with X-ray Photoelectron Spectroscopy (XPS), Ultraviolet Photoelectron Spectroscopy (UPS), Low Energy Electron Diffraction (LEED), and Ion Scattering Spectroscopy (ISS). This chamber also houses two ion sputtering guns which can be used for sample cleaning, and a charge neutraliser that can be used on non-conducting samples when they are being studied by XPS. Gases can be admitted into the chamber through leak valves and the composition in the chamber can subsequently be monitored by a mass spectrometer.

Figure 7.17 shows a view inside the A-chamber. Through the centre of the chamber can be seen the end of the vertical manipulator with a sample attached on a

quartz rod (previously shown in Figure 7.14a). In the top right hand side of the picture the X-ray gun with its aluminium foil window can be seen and adjacent to this is the ISS gun. Pointing in directly from the right is the analyser for the XPS, and just underneath this can be seen the charge neutraliser. At the bottom left of the picture is a metal evaporator and pointing in from the left at the back of the picture is the filament for the mass spectrometer.

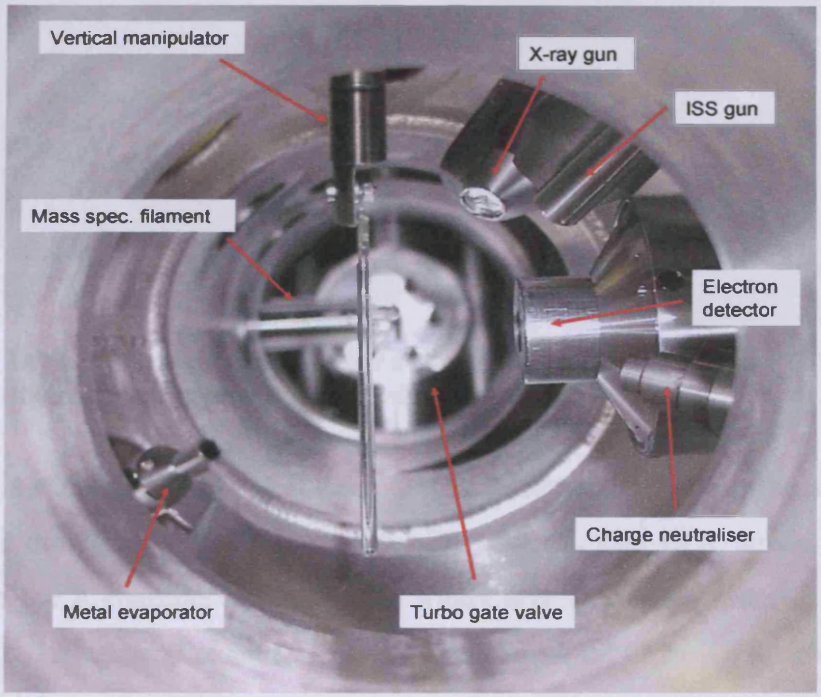

Figure 7.17 Inside the A-chamber. A description of the parts is given in the text.

The A chamber is serviced by two manipulators, one with vertical movement and the other with horizontal movement (note that samples cannot be moved between the manipulators in this chamber). Samples on the vertical manipulator can be studied using all of the techniques listed above, with the exception of LEED; samples on the horizontal manipulator by all with the exception of EPR. Base pressures of 2×10^{-10}mbar can be achieved in the A chamber through a combined pumping system consisting of rotary, turbo, ion and titanium sublimation pumps.

7.3.6b EPR Dewar

The samples to be studied by EPR are lowered into a quartz dewar below the A chamber. The dewar can be isolated from the A chamber *via* a seal at the lower extent of the 540mm z-translation, as shown in Figure 7.18.

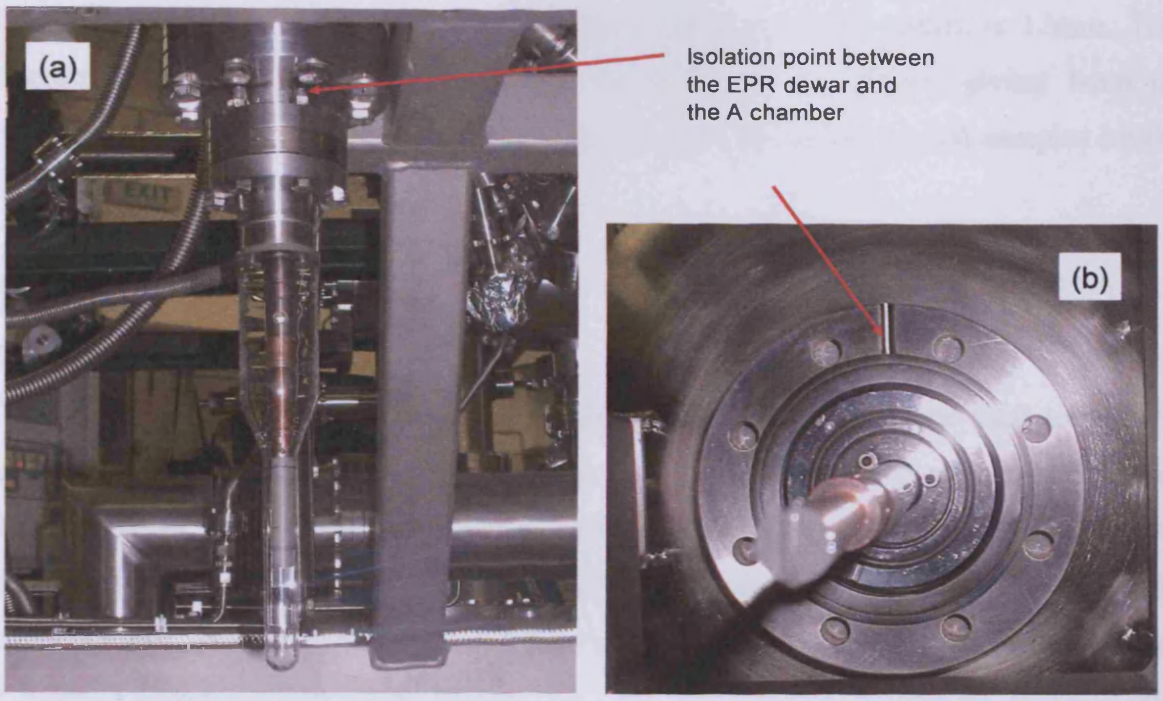

Figure 7.18 The EPR quartz dewar situated at the bottom of the A chamber (b) is taken from directly below the A-chamber, with the quartz dewar removed for clarity.

This is accompanied by a further 10mm z-translation below the seal to enable accurate positioning of the sample in the EPR cavity. The EPR dewar is separately pumped from the A chamber by a series of rotary and turbo pumps and can reach base pressures of 1×10^{-7}mbar. Pressures of gas can be admitted to the EPR dewar through a leak valve which enables EPR measurements to be taken *in-situ* in positive pressures of gas. The isolation of the EPR dewar from the A chamber prevents any UHV components from being exposed to high pressures of gas which may decrease the lifetime of the components and simultaneously compromise the base pressure in the main chamber.

The dimensions of the quartz dewar were required to be very precise in order to satisfy the strict limitations of the system. In order to achieve maximum filling factor, the dewar needed to extend the full length of the cavity, but there also needed to be enough clearance under the bottom of the dewar for the magnet to pass underneath during retraction. The clearance between the lowest extent of the EPR dewar and the magnet was measured to be 2mm. Careful consideration had to be paid to the chosen diameter of the dewar also. The inner diameter of the ER4103TM cavity is 20mm, therefore an outer diameter of 14mm was selected for the EPR dewar, giving 3mm of clearance in all directions inside the cavity. This clearance is necessary to allow accurate positioning of the cavity around the dewar. The suprasil quartz used for the

EPR dewar is 1mm thick, therefore the inner diameter of the quartz is 12mm. The maximum sample size used during this investigation was 10mm, giving 1mm of clearance in all directions for accurate positioning of the single crystal samples inside the EPR dewar.

7.4 Results and Discussion

7.4.1 Sensitivity studies

In order to establish whether the EPR spectrometer could be used to resolve surface sites on single crystals, the absolute sensitivity of the cavity system had first to be determined. Two methods for determining the sensitivity of UHV-EPR cavities are described in the literature[9,12] and both of these techniques were employed in this investigation. They include using molecular oxygen and DPPH to determine the minimum detection limit of the system.

The method described here of measuring the sensitivity of the cavity through changes in the EPR spectrum of molecular oxygen is taken from the studies of Farle *et al.*,[9] reported in 1985. The EPR dewar was isolated from the main chamber and filled with a static pressure of molecular oxygen gas. The room temperature O_2 signal was detected over a field of 300–930mT at decreasing gas pressures until no EPR signal could be resolved, thus giving a measure of the detection limit of the cavity. The complete gas phase oxygen signal is displayed in Figure 7.19. One resonance peak of the oxygen signal is shown in the inset of Figure 7.19 at a pressure of 3.8×10^{-3}mbar. This resonance, which accounts for only 4% of the overall oxygen signal detected, could not be resolved at lower oxygen pressures.

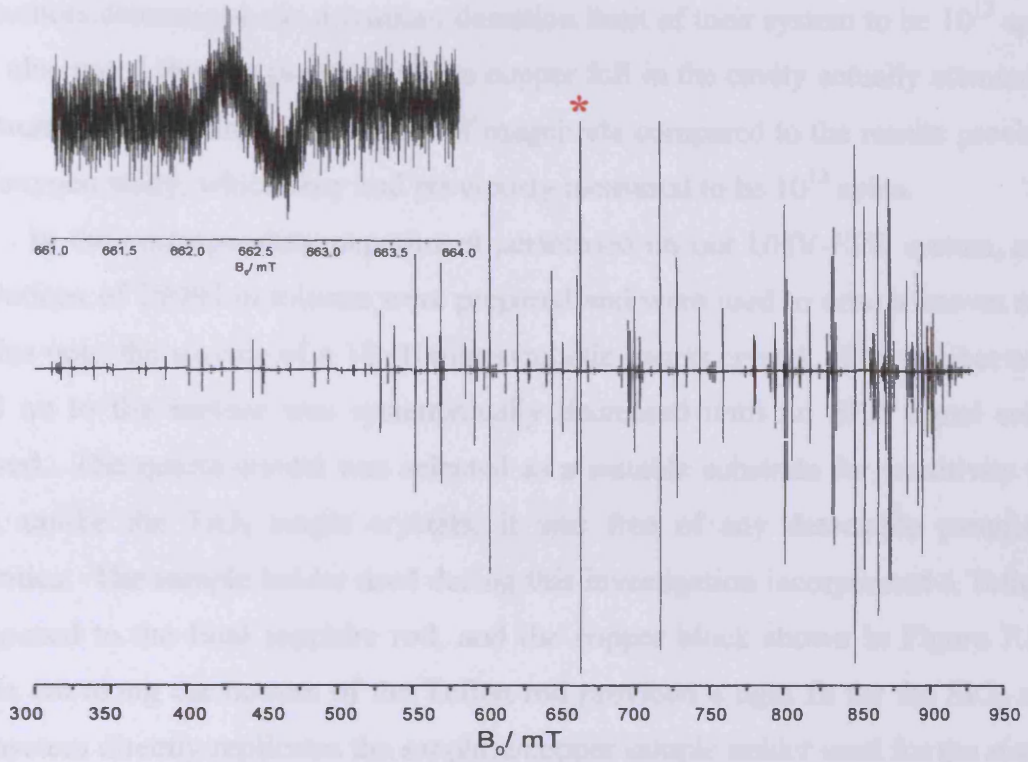

Figure 7.19 X-band EPR spectrum [300K] of gas phase O_2 recorded at 9.41GHz. The inset shows the peak marked * recorded at a pressure of 3.8×10^{-3}mbar

The volume of the active resonant cavity was measured to be $8.5cm^3$, and with this information the minimum number of spins that can be detected by the cavity can be calculated using the equation given by:

$$PV = n'RT \qquad (7.3)$$

where P is the minimum pressure of oxygen which results in a detectable EPR signal, V is the volume of the active cavity, n′ is the uncorrected number of moles, R is the gas constant and T is the temperature at which the spectrum was recorded. Hence, using the value of $R = 62.363 lTorrmol^{-1}K^{-1}$ (and adjusting the other values accordingly), n′ is calculated to be 1.3×10^{-9}. Taking into account that this signal accounts for only 4% of the complete oxygen spectrum, the corrected number of moles was calculated to be $n = 1.36\times10^{-9}$. Therefore, using Avogadro's constant, the minimum number of spins in the cavity giving a detectable EPR signal was calculated to be 8.2×10^{14}. The importance of this figure will be discussed further below.

The second method for determining the sensitivity of the EPR cavity was based on that described by Katter *et al.*[12] In their experiment, Katter *et al.*,[12] dosed a 4×7mm polycrystalline copper foil with a known concentration of 2,2-diphenyl-1-pycrylhydrazyl hydrate (DPPH) in benzene solution. The benzene evaporated off the surface of the copper leaving behind a surface coverage of a known number of spins.

The authors determined the minimum detection limit of their system to be 10^{13} spins.[12] They also noted that the presence of the copper foil in the cavity actually attenuated the minimum detection limit by an order of magnitude compared to the results provided by their oxygen study, which they had previously measured to be 10^{12} spins.

In the corresponding experiment performed on our UHV-EPR system, a series of solutions of DPPH in toluene were prepared and were used to dose a known number of spins onto the surface of a 10×10mm synthetic quartz crystal. The number of spins dosed on to the surface was systematically decreased until no EPR signal could be resolved. The quartz crystal was selected as a suitable substrate for sensitivity testing since, unlike the TiO_2 single crystals, it was free of any detectable paramagnetic impurities. The sample holder used during this investigation incorporated a Teflon rod, as opposed to the final sapphire rod, and the copper block shown in Figure 7.14. A groove cut along the bottom of the Teflon rod provided a tight fit for the SiO_2 crystal. This system directly replicates the sapphire/copper sample holder used for the studies of single crystal metal oxides discussed later in this chapter, therefore it provided a direct measure of the characteristics of the system in operational mode. Previous investigations had shown that the intensity of the EPR signal arising from the DPPH was more or less independent of pressure in the EPR dewar, therefore the spectra were recorded under atmospheric pressures and are shown in Figure 7.20. It can clearly be seen from Figure 7.20c that the minimum concentration of DPPH spins dosed on to the surface of the quartz which still resulted in a resolvable EPR signal was 2.5×10^{14} spins.

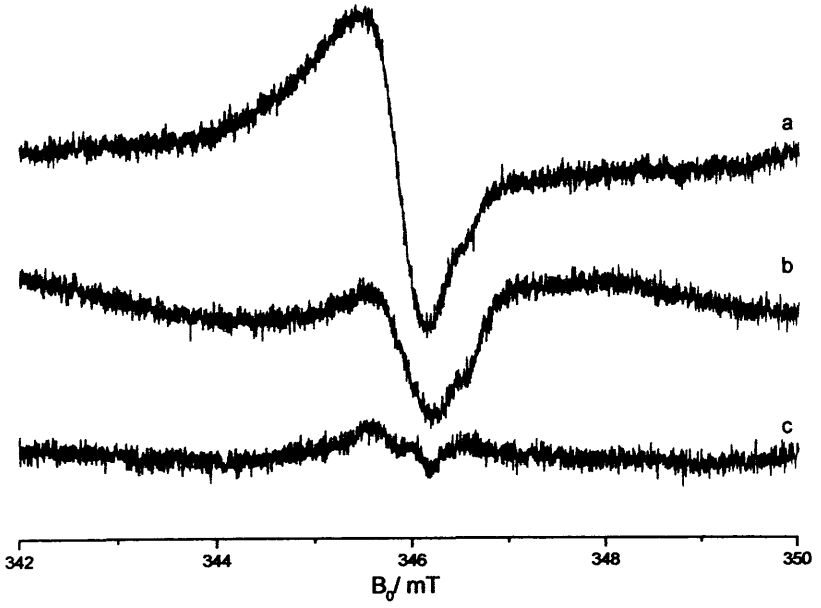

Figure 7.20 *cw*-EPR spectra of (a) 2×10^{15} (b) 5×10^{14} and (c) 2.5×10^{14} spins DPPH dosed onto a quartz 10×10mm crystal.

In a previous set of experiments using a different sample holder, a spectrum was recorded of DPPH on synthetic quartz at a concentration of 1.1×10^{14} spins (spectrum not shown for brevity). No EPR signal due to the DPPH could be resolved at this concentration. This result suggests that the lower detection limit of the system as determined from the DPPH investigation is in the region of $1.1\times10^{14} - 2.5\times10^{14}$ spins.

Taking the average of these two lower detection limits (*via* molecular oxygen and DPPH) suggests that the spectrometer can detect 5.4×10^{14} spins using the assembly described in this chapter. It is worth considering the significance of this value in relation to the number of paramagnetic species expected on a single crystal oxide surface, such as TiO_2. The unit cell on the TiO_2(110) face, which contains one Ti atom, has a surface area of $1.924\times10^{-19}m^2$ as shown in Figure 7.21. Therefore, on a $1cm^2$ crystal a monolayer consists of 5.2×10^{14} Ti atoms. Taking into account that the EPR spectrometer can resolve signals from both faces of the crystal simultaneously (unlike more conventional UHV techniques such as XPS and STM), the surface area of the crystals studied in this investigation was actually $2cm^2$. Therefore, a monolayer of paramagnetic Ti^{3+} species on each face of the crystal would result in 1.04×10^{15} spins.

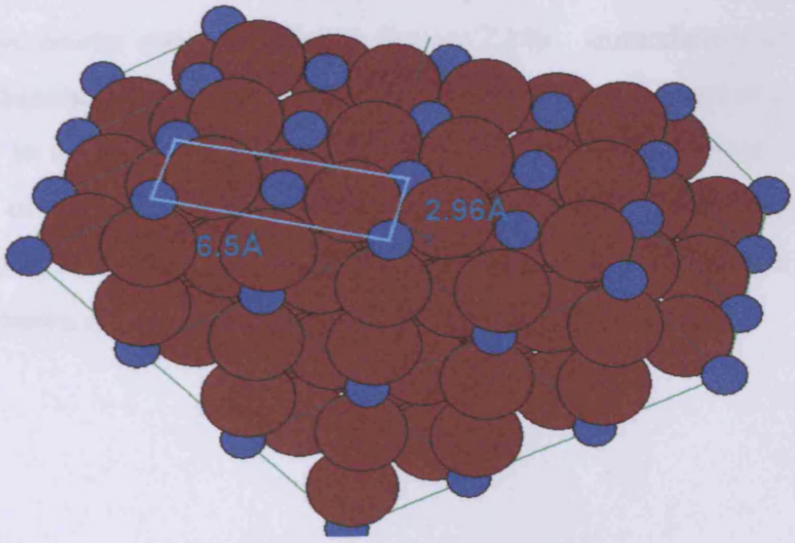

Figure 7.21 TiO_2 (110) unit cell. Blue balls: Ti atoms, red balls: O atoms.

This suggests that, in principle, a monolayer coverage of Ti^{3+} cations could be detected by our UHV-EPR spectrometer under ideal conditions. If the linewidth of the Ti^{3+} signal is broadened (due to spin orbit coupling effects, for example, not seen in the DPPH case) or if the temperature is not sufficiently low enough to quench unfavourable spin lattice relaxation effects, detection of Ti^{3+} cations on reduced TiO_2 single crystals

may prove very difficult. The experiments performed on $TiO_2(110)$ are described in the next section.

7.4.2 A UHV-EPR Investigation of $TiO_2(110)$

One of the main objectives of the work performed on the UHV- EPR system was the study of single crystal metal oxides. These systems have been the focus of many surface science investigations over the past few decades utilising techniques such as XPS, STM and LEED to determine geometrical structure and chemical composition. As discussed in Chapter 5, the nature of the vacancies and surface defects of metal oxides play a large role in determining their subsequent chemical activity. EPR has been used extensively to study these defects on polycrystalline forms of metal oxides, and it is the aim of this investigation to study the same defects on the single crystals in order to locate accurately the position of the defects on the surface. For instance, it has already been proposed in Chapter 5 that the superoxide radical with $g_{zz} = 2.019$ on the thermally reduced P25 surface is stabilised at a vacancy site on the surface. Absolute confirmation of this assignment could be provided by spectra obtained on the single crystal surface.

A $TiO_2(110)$ sample was placed in the A chamber utilising the sapphire/ tungsten sample holder shown earlier in Figure 7.14b. Immediately after placing the crystal in the chamber, the chamber underwent bake-out for 65 hours at a temperature of 388K in order to remove adsorbates (in particular H_2O) from the system. A series of EPR spectra of the $TiO_2(110)$ sample were subsequently recorded under UHV conditions at different angles of the crystal with respect to the direction of the applied field, and are shown in Figure 7.22.

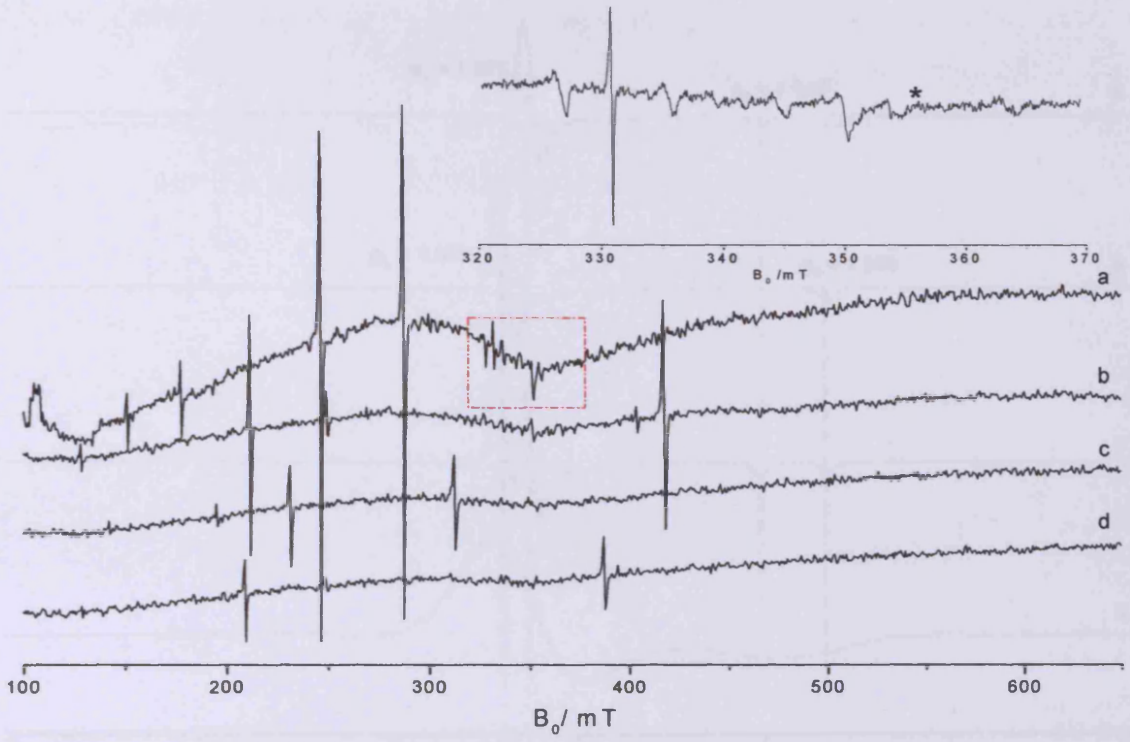

Figure 7.22 *cw*-EPR spectra [298K] of TiO_2(110) recorded under UHV conditions at varying angles of the sample with respect to the applied field. The region of the spectra enclosed in the box is expanded in the inset.

The predicted/calculated position of a Ti^{3+} signal is labelled * in the inset of Figure 7.22. Bulk and lattice Ti^{3+} have slightly different g values in polycrystalline TiO_2(rutile), with $g_\perp = 1.975$ and $g_\parallel = 1.940$. Under conditions of poor resolution, the spectra may be broadened substantially, which hinders a clear identification of the species. Nevertheless, a resonance in the region of g = 1.97 should be expected for a Ti^{3+} cation in a single crystal sample, as shown by the simulated spectra shown in Figure 7.23. As can be seen from Figure 7.22, there is no clearly observable peak at g = 1.97 which suggests that there are no Ti^{3+} cations in this sample, which is to be expected for a stoichiometric TiO_2(110) single crystal. The intense peaks at all field values in the spectra are due to chromium impurities in the crystal. Cr-doped TiO_2 has been extensively studied in the past,[30-33] due to its use in chemical sensors and its increased photoelectrochemical properties over the pure oxide; no further investigation of the impurities were made of the single crystals in this study.

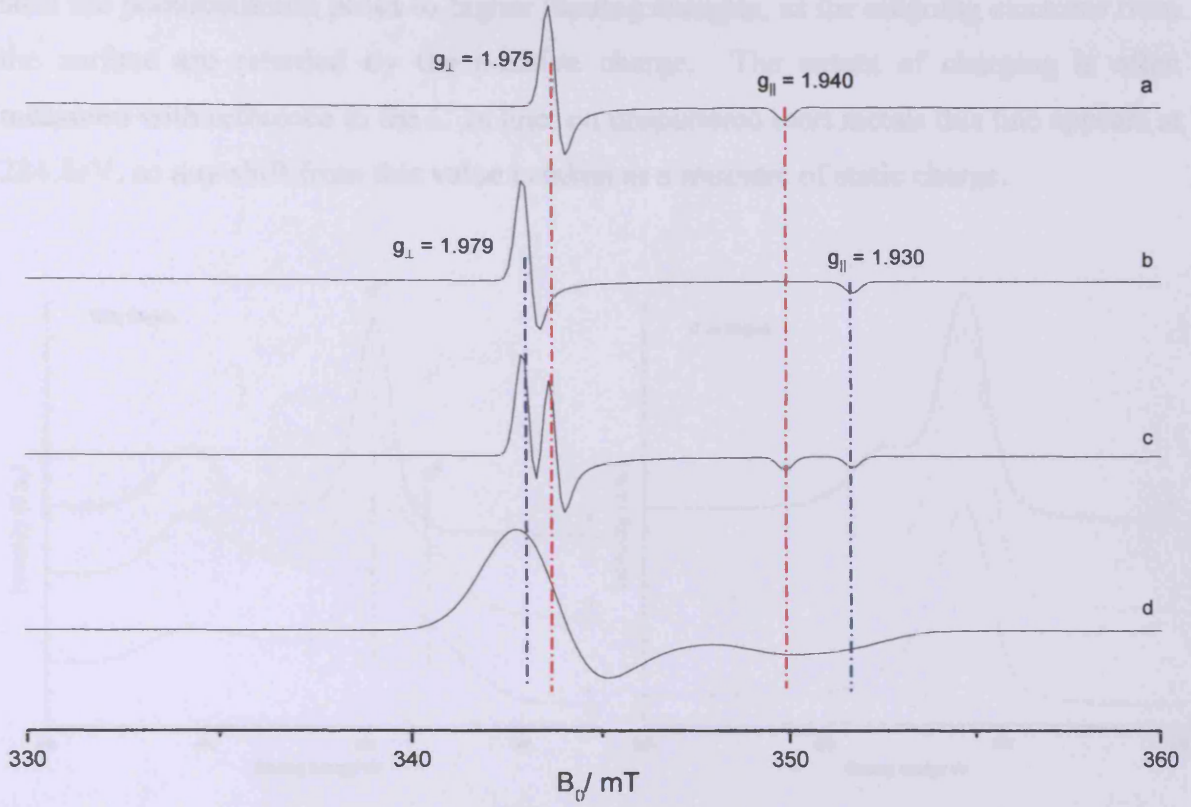

Figure 7.23 Simulated EPR spectra for an axial Ti^{3+} centre (a) bulk (b) surface (c) bulk and surface, $\Delta B = 0.4mT$ and (d) bulk and surface, $\Delta B = 2.0mT$.

The crystal was subsequently treated with several cycles of Ar^+ sputtering to remove surface contamination and to induce reduction of the surface cations from Ti^{4+} (stoichiometric) to Ti^{3+} (reduced). This technique has been used extensively in the past to create high concentrations of surface paramagnetic defects.[34] The first 30 minute Ar^+ treatment used a 600eV source and a gas pressure of 5×10^{-6}mbar. For the second Ar^+ sputter cycle, the source energy was increased to 1000eV. All other parameters were set to produce a flat profile of the sputtering gun across the surface of the crystal [Ext = 515eV, Focus = 820V, I_o= 10mA]. The XPS spectra in the binding energy regions of the Ti 2p and O 1s photoemission lines (Ti $2p_{1/2}$ 464.5eV; Ti $2p_{3/2}$ 458.7eV; O 1s 530.1eV)[35] were recorded after each sputter treatment and are shown in Figure 7.24.

The binding energy of the photoelectron peaks in the XPS spectrum of TiO_2(110) are affected by steady-state charging, and therefore the position of the photoemission lines are shifted slightly from those values given above. This steady-state charging arises due to an accumulation of electrons in the sample (TiO_2 is an insulator in the stoichiometric state), and is a balance between electron loss due to emission and acquisition of electrons from the vacuum. The effect of this charge is to

shift the photoemission peaks to higher binding energies, as the outgoing electrons from the surface are retarded by the positive charge. The extent of charging is often measured with reference to the C 1s line; on unsputtered inert metals this line appears at 284.8eV, so any shift from this value is taken as a measure of static charge.

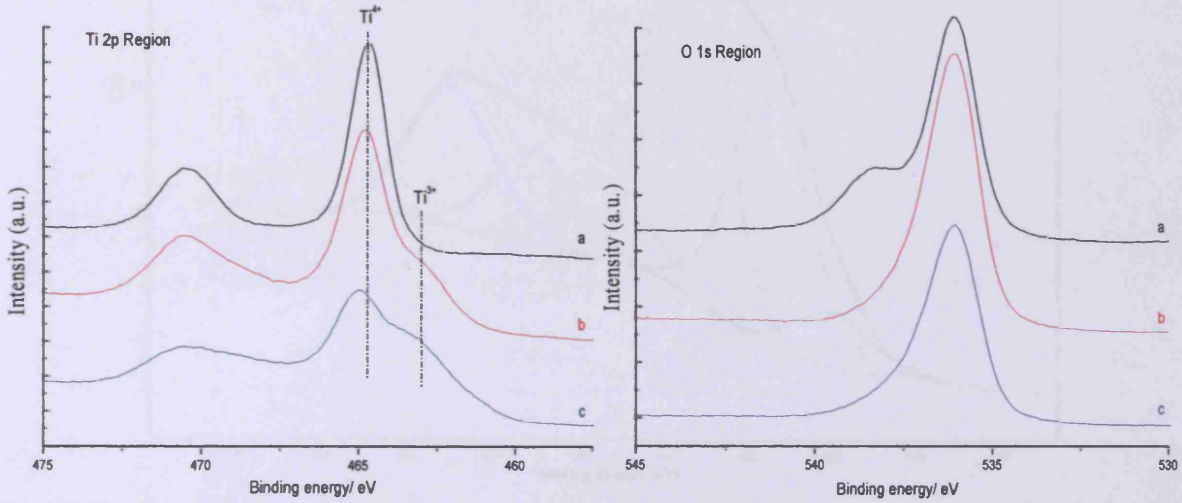

Figure 7.24 Ti 2p and O 1s XPS spectra of TiO_2(110) crystal after (a) no treatment (b) 600eV Ar^+ sputter cycle and (c) a further 1000eV Ar^+ sputter cycle. All spectra were recorded on the same face of the crystal.

As can be seen from Figure 7.24, the profiles of the Ti $2p_{3/2}$ and $2p_{1/2}$ peaks and the O 1s peak change dramatically after each surface treatment. Spectrum (a) in the Ti 2p and O 1s regions show the XPS spectra obtained from the as-received stoichiometric sample. The large shoulder at 538.2eV on the high binding energy side of the O 1s peak indicates that the crystal is covered with a level of surface contamination. This surface contamination is gradually removed during the cycles of Ar^+ treatment, as evidenced by the decrease in the area of the high binding energy shoulder. Most importantly, the Ar^+ treatment also led to surface reduction *via* removal of O atoms. During the sputtering process, two electrons remain in the lattice on removal of the O atoms, which are taken up by the neighbouring Ti^{4+} cations to create surface Ti^{3+}. The Ti^{3+} can be seen in the Ti 2p region, as shoulders on both the Ti $2p_{3/2}$ and Ti $2p_{1/2}$ peaks at 461.5 and 467.1eV. After the 1000eV Ar^+ treatment there is also a very small trace of Ti^{2+} cations present at 460.0 and 465.3eV. The presence of Ti^{3+} and Ti^{2+} cations on the surface after 1000eV Ar^+ sputtering is confirmed by the results of a peak-fitting procedure (shown in Figure 7.25).

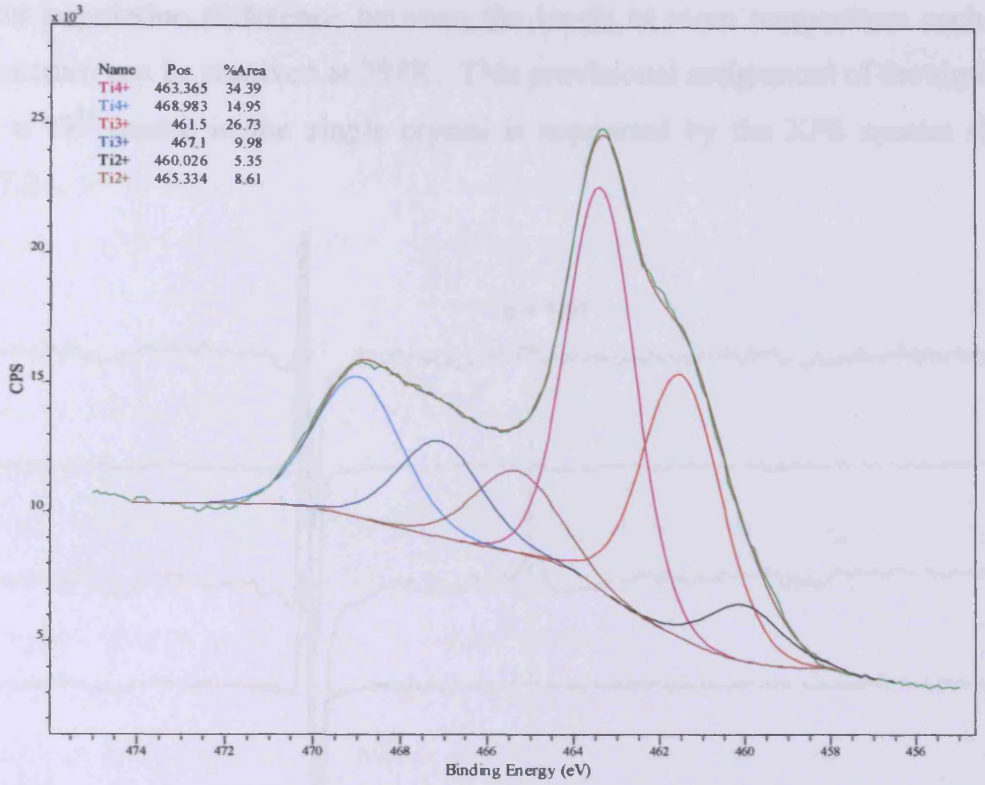

Figure 7.25 Deconvolution of XPS spectra of $TiO_2(110)$ crystal after 1000eV Ar^+ sputter.

The EPR spectra of the $TiO_2(110)$ crystal recorded after the cycles of sputtering treatments are shown in Figure 7.26 below. The signals displayed in Figure 7.26(a) and 7.26(b) were recorded at 298K. The sharp signal at 350mT is due to chromium impurities in the crystal. Following the 1000eV Ar^+ sputter treatment the crystal was cooled using liquid nitrogen to 137K and the EPR signal was recorded at this temperature. It should be noted here, that the temperature quoted was measured by the thermocouple at the end of the manipulator, before contact with the copper block of the sample holder. It was determined from external measurements that the thermal conductance through the copper and sapphire was extremely good, although this thermocouple reading gave no indication of the actual temperature of the sample. The resulting spectrum is shown in Figure 7.26(c). It can be seen that a signal at this position was more strongly resolved at the low temperatures, thereby suggesting that it was possible that this signal could be assigned to Ti^{3+} cations. Following this measurement, the sample was left for several hours to reach 298K before re-recording the EPR spectrum at this temperature. The signal at g = 1.97 decreased in intensity, although it was still visible. Although Ti^{3+} cations in the polycrystalline sample can only be resolved by EPR at low temperatures, it is possible that in the single crystal the splitting of the t_{2g} energy levels due to the tetragonal distortion of the lattice creates a

sufficient population difference between the levels at room temperature such that an EPR spectrum can be resolved at 298K. This provisional assignment of the signal at g = 1.97 to a Ti^{3+} centre in the single crystal is supported by the XPS spectra shown in Figure 7.24.

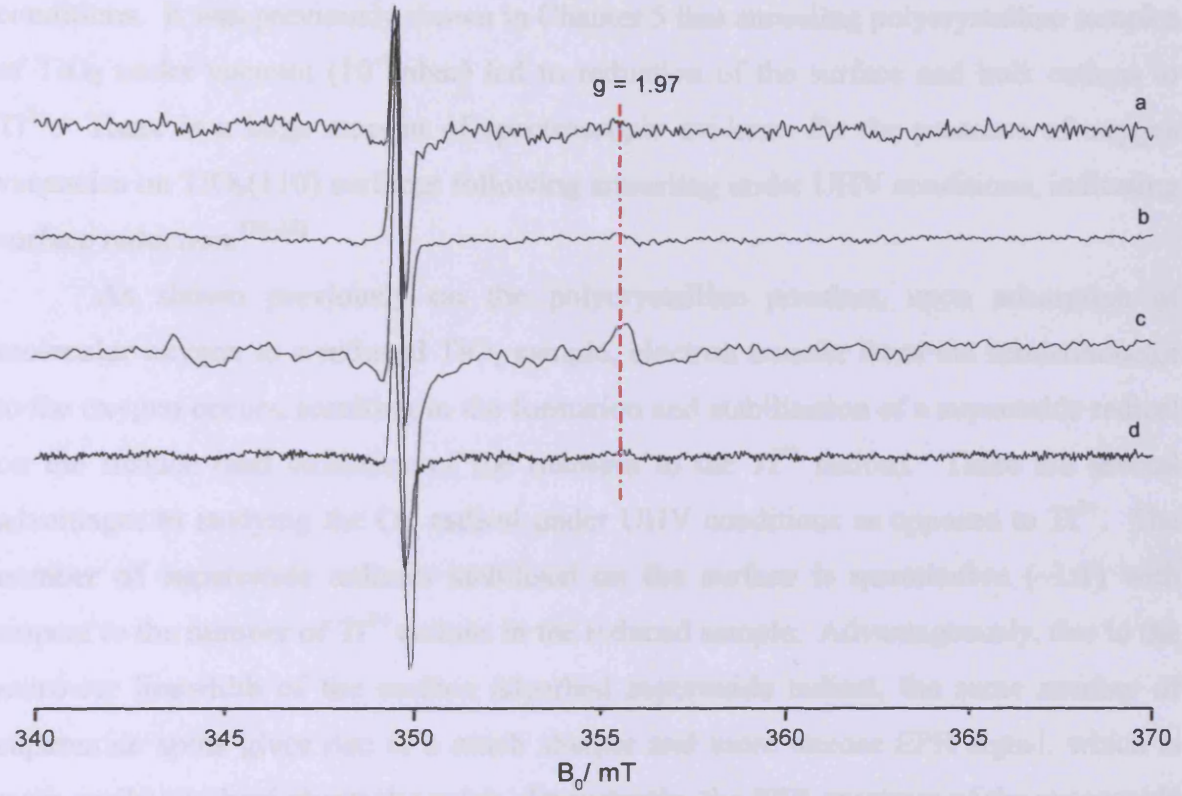

Figure 7.26 *cw*-EPR spectra of TiO_2(110) sample after (a) 600eV Ar^+ sputter (b) a further 1000eV Ar^+ sputter treatment, recorded at 298K. Spectrum (c) is sample (b) recorded at 137K. Spectrum (d) is sample (c) annealed and recorded at 298K. [ν = 9.8GHz]

In the above series of experiments, all 10mm of the sample (plus an additional 7mm of the sample holder) were located inside the active part of the cavity. This experimental arrangement maximises the number of spins in the cavity and therefore greatly enhances the possibility of resolving an EPR spectrum. However, the signal at 1.97 in Figure 7.26 is very weak and the assignment of Ti^{3+} centres to this signal would need further confirmation. In order to achieve more intense spectra it was determined that the cooling of the sample would need to be made more efficient. Therefore, following the series of experiments discussed above, several improvements were made to the system. Notably a new design of sample holder (shown in Figure 7.14c) was developed and the liquid nitrogen cooling was made more efficient, thus improving the thermal conductivity to the sample. A second sample of TiO_2(110) was studied using XPS spectroscopy, and the Ti 2p and O 1s photoemission lines are shown in Figure

7.27. The crystal was sputtered for 30 minutes with 600eV Ar^+ ions to induce reduction of the surface cations to the paramagnetic Ti^{3+} state; using the lower energy beam of Ar^+ ions ensured that the surface was not reduced to the diamagnetic Ti^{2+} state. Following the sputter treatment, the sample was annealed to 723K under UHV conditions. It was previously shown in Chapter 5 that annealing polycrystalline samples of TiO_2 under vacuum (10^{-4}mbar) led to reduction of the surface and bulk cations to Ti^{3+}. There is a large amount of spectroscopic evidence for the presence of oxygen vacancies on TiO_2(110) surfaces following annealing under UHV conditions, indicating surface reduction.[36-38]

As shown previously on the polycrystalline powders, upon adsorption of molecular oxygen to a reduced TiO_2 sample, electron transfer from the semiconductor to the oxygen occurs, resulting in the formation and stabilisation of a superoxide radical on the surface (and oxidation of the titanium to the Ti^{4+} cation). There are several advantages to studying the O_2^- radical under UHV conditions as opposed to Ti^{3+}. The number of superoxide radicals stabilised on the surface is quantitative (~1:1) with respect to the number of Ti^{3+} cations in the reduced sample. Advantageously, due to the narrower linewidth of the surface adsorbed superoxide radical, the same number of superoxide spins gives rise to a much sharper and more intense EPR signal, which is more easily resolved above the noise. Importantly, the EPR spectrum of the superoxide radical can be recorded at 300K, thereby removing the issue of insufficient sample cooling experienced during the study of the Ti^{3+} cation. Thus, a pressure of 5×10^{-6}mbar O_2 was admitted into the UHV chamber, and the EPR and XPS spectra were recorded of the sample. It was proposed that the intensity of any signal arising from paramagnetic Ti^{3+} cations in the EPR spectra created during the sputter and anneal treatment would decrease in the presence of molecular oxygen. Simultaneously, the relative contribution of Ti^{3+} cations to the Ti 2p photoemission lines should decrease following reaction between the semiconductor and the surface adsorbed oxygen.

The photoemission lines in the Ti 2p region of the TiO_2(110) crystal after each treatment are shown in the left panel in Figure 7.27. The as-received crystal (spectrum(a)) shows two symmetric photoemission lines at 461.1eV and 467eV due to the Ti $2p_{3/2}$ and $2p_{1/2}$ emissions respectively. The presence of a shoulder on the low binding energy side of each photoemission line after sputtering the crystal with 600eV Ar^+ ions for 30 minutes indicates the presence of Ti^{3+} cations. The overall intensity of

both photoemission lines in the Ti 2p region decreased after the annealing treatment, but there was no further change in the oxidation state of the crystal.

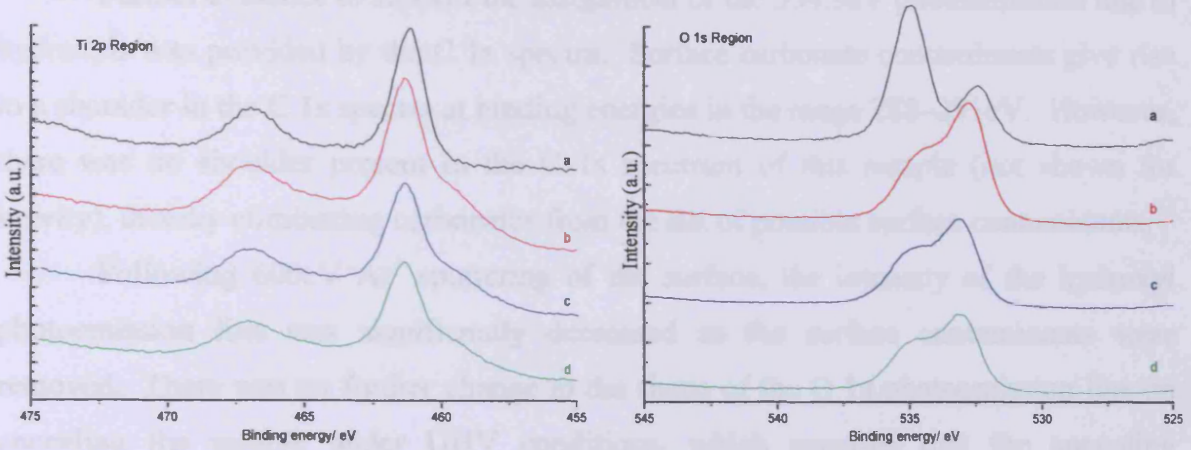

Figure 7.27 XPS spectra of $TiO_2(110)$ after (a) no UHV treatment (b) 600eV Ar^+ sputtering for 30 minutes (c) annealing to 723K under UHV conditions and (d) addition of 5×10^{-6}mbar O_2. All spectra were recorded on the same face of the crystal.

On exposure of O_2 to the crystal, the profile of the Ti 2p peaks remained the same, suggesting there was no transfer of electrons from the TiO_2 crystal to the surface adsorbed oxygen resulting in the formation of superoxide anions. Additionally, this result implies that there was no re-oxidation of the crystal in the oxygen environment at room temperatures. Previous work by Li *et al.*,[39,40] has shown that re-oxidation of reduced $TiO_2(110)$ crystals can only take place by annealing the crystal to elevated temperatures in an oxygen atmosphere.

Two photoemission lines at 532.4eV and 534.9eV were resolved in the O 1s spectra of the as-received $TiO_2(110)$ sample, indicating that there were two types of oxygen species present on the surface of the crystal. The amount of surface charging on this sample was measured from the C 1s line to be 2.6eV, which remains approximately constant throughout the range of binding energies. Therefore the line at 532.4eV was assigned to the O^{2-} anions of the TiO_2 crystal lattice. Common contaminants on the surface of TiO_2 are hydroxyls and carbonates, and it is possible from the O 1s spectra to identify which of these oxygen species are responsible for the peak at 534.9eV. The photoemission lines from the hydroxyl and carbonate species are found in the binding energy range of 531–532eV and 530.5–531.5eV respectively.[41] When the measured surface steady-state charge of 2.6eV is taken into account, these binding energy ranges increase to 533.6–534.6eV (hydroxyls) and 533.1–534.1eV (carbonates). From this

data, the photoemission line at 534.9eV from the as-received TiO_2(110) sample was assigned to surface hydroxyls.

Further evidence to support the assignment of the 534.9eV photoemission line to hydroxyls was provided by the C 1s spectra. Surface carbonate contaminants give rise to a shoulder in the C 1s spectra at binding energies in the range 288–291eV. However, there was no shoulder present in the C 1s spectrum of this sample (not shown for brevity), thereby eliminating carbonates from the list of possible surface contaminants.

Following 600eV Ar^+ sputtering of the surface, the intensity of the hydroxyl photoemission line was significantly decreased as the surface contaminants were removed. There was no further change to the shape of the O 1s photoemission line on annealing the sample under UHV conditions, which suggests that the annealing temperatures used during this experiment were insufficient to promote desorption of surface contaminants. The absence of any change in profile of the O 1s peak after exposure of molecular oxygen to the crystal, in combination with the results from the Ti 2p region, indicate that there was no re-oxidation of the crystal at the temperatures used in this experiment.

The EPR spectra of the TiO_2(110) crystal after the several surface treatments are shown in Figure 7.28. The paramagnetic Ti^{3+} cation has a g value of ~1.97, which is indicated in the figure. It should be noted here that the microwave frequency during these measurements was 9.4GHz, which has shifted considerably from the 9.8GHz at which the spectra in Figure 7.26 were recorded. This shift in frequency explains the difference in the magnetic field at which the Ti^{3+} EPR signal is expected. As previously mentioned, the cylindrical cavity is very sensitive to sample positioning within the cavity, and it is suggested that differences in the positioning of the samples inside the cavity between the spectra shown in Figures 7.26 and 7.28 have resulted in this large shift in resonance frequency.

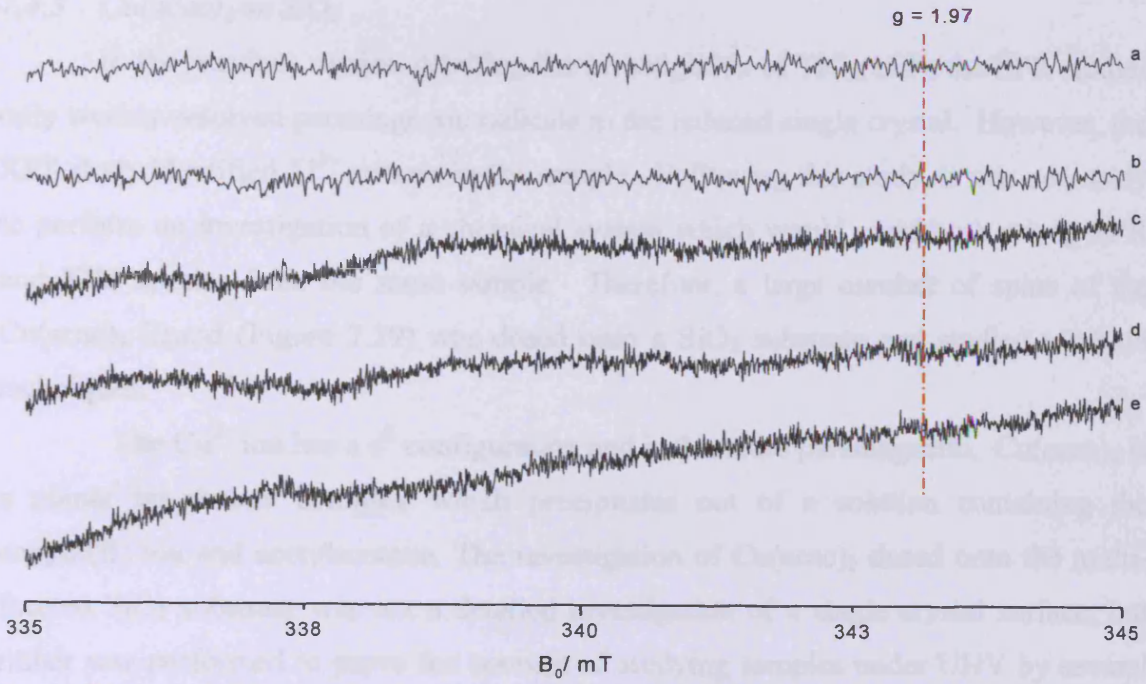

Figure 7.28 *cw*-EPR spectra of TiO_2(110) (i) as-received at (a) 298K and (b) 136K (ii) after sputtering and annealing treatment at (c) 136K and (d) 298K and (e) under 5×10^{-6}mbar O_2 [136K]. [ν = 9.4GHz]

It is evident from the figure that there is no signal detected in this region of the spectrum, indicating that despite the sputtering and annealing treatments, no paramagnetic species could be resolved. This could be as a result of several experimental limitations. The Ti 2p photoemission line in the XPS spectrum clearly shows a large contribution from Ti^{3+} cations, therefore the number of paramagnetic spins in the sample should be above the minimum detection limit of the spectrometer. However, during these series of experiments, due to the unfavourable tuning characteristics of the large sapphire piece, only 5mm of the sample could be successfully tuned inside the cavity. Therefore, the benefit of the superior thermal conduction to the sample provided by using the copper/ sapphire sample holder (Figure 7.14c) compared to the tungsten/ sapphire sample holder (Figure 7.14b) are cancelled out by the inability to position 10mm of the sample inside the resonant cavity.

Unfortunately, at this time during the stage of the investigations there was insufficient time remaining to repeat the experiment detailed here using the smaller sapphire rod. The improved tuning characteristics provided by the smaller rod would allow more of the sample to be located inside the cavity during a measurement, and the efficient cooling of this design would maximise the opportunity to resolve temperature dependent paramagnetic species, such as Ti^{3+}.

7.4.3 Cu(acac)$_2$ on SiO$_2$

In the previous section detailing the investigation of $TiO_2(110)$, the EPR studies only weakly resolved paramagnetic radicals in the reduced single crystal. However, the XPS study identified Ti^{3+} cations in the sample. Following this study, it was necessary to perform an investigation of a chemical system which would yield both strong EPR and XPS spectra from the same sample. Therefore, a large number of spins of the $Cu(acac)_2$ ligand (Figure 7.29) was dosed onto a SiO_2 substrate and studied *via* both techniques.

The Cu^{2+} ion has a d^9 configuration and is therefore paramagnetic. $Cu(acac)_2$ is a planar bis-chelate complex which precipitates out of a solution containing the copper(II) ion and acetylacetone. The investigation of $Cu(acac)_2$ dosed onto the multi-faceted SiO_2 substrate was not a detailed investigation of a single crystal surface, but rather was performed to prove the concept of studying samples under UHV by several techniques.

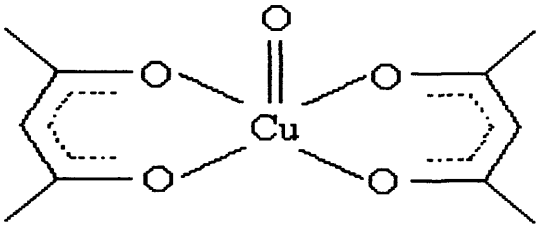

Figure 7.29 The $Cu(acac)_2$ ligand dosed onto SiO_2 substrate.

A solution of $Cu(acac)_2$ was prepared in di-chloro-methane (DCM) and a volume containing 1×10^{17} spins was delivered to the surface of the SiO_2 substrate. All of the EPR and XPS studies of this system were recorded at room temperature, meaning the thermal conductance properties of the sapphire piece were not required; therefore the Teflon rod described in section 7.4.1 was used. The EPR spectra were initially recorded under atmospheric conditions at room temperature, and are displayed at various incident microwave power in Figure 7.30. The perpendicular component of the Cu^{2+} signal can clearly be resolved at ~345mT (g = 2.002), but the parallel component cannot be resolved in this spectrum.

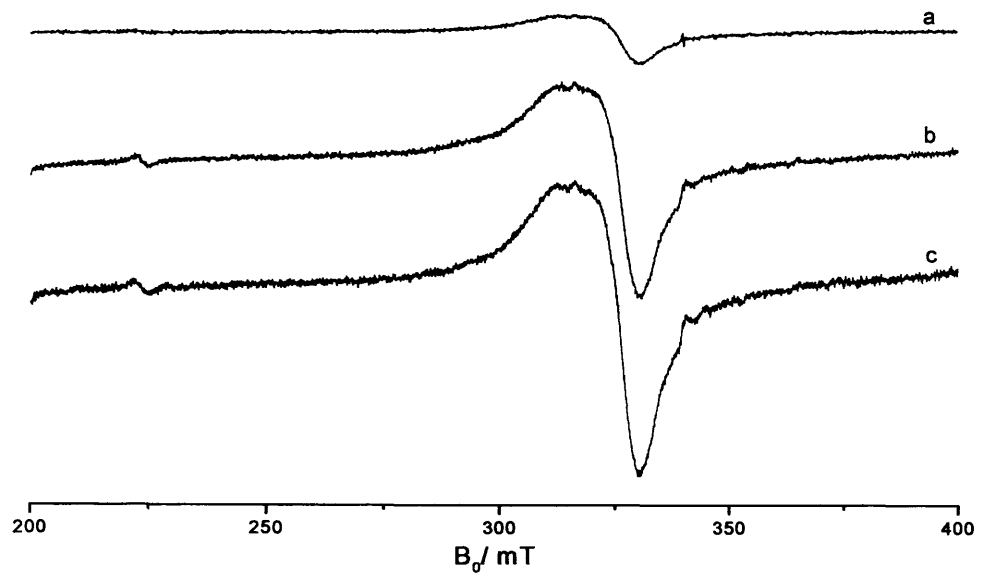

Figure 7.30 *cw*-EPR spectra [298K] of $Cu(acac)_2$ dosed onto SiO_2 substrate recorded at (a) 1mW (b) 20mW and (c) 40mW incident microwave power.

A previous spectrum was recorded of $Cu(acac)_2$ on SiO_2 at the same dosing level of 1×10^{17} spins, and is shown in Figure 7.31. As can be seen, the perpendicular component of the EPR spectrum can clearly be resolved. In addition to this peak, there are additional features at low field in the region of the parallel component. The four peaks in this region of the spectrum do not correspond to the parallel hyperfine pattern, but are in fact due to an amorphous distribution of the $Cu(acac)_2$ ligand on the SiO_2 substrate. The EPR spectrum contains peaks arising from all possible orientations of the ligand with respect to the magnetic field, thereby the g and A values of the parallel component of the signal cannot be clearly resolved.

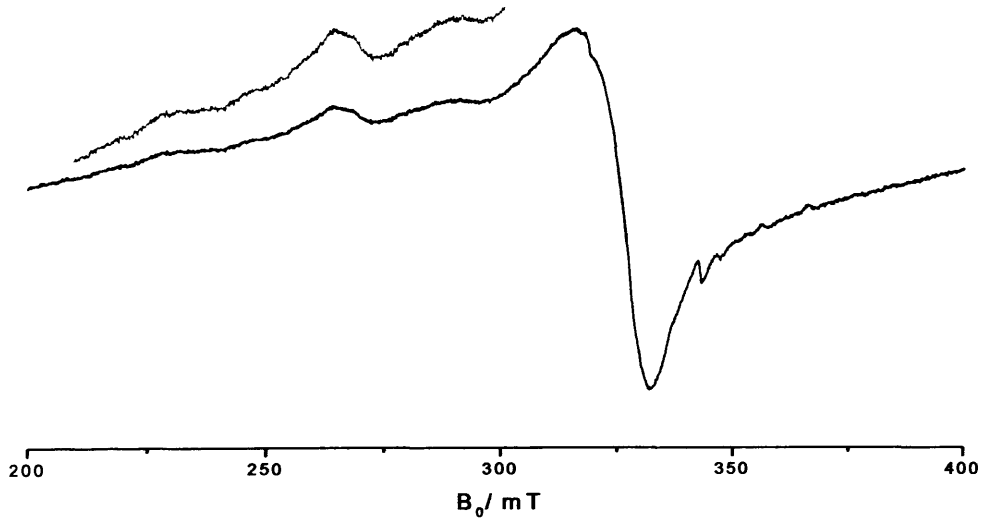

Figure 7.31 *cw*-EPR spectrum [298K] of $Cu(acac)_2$ dosed onto SiO_2 substrate recorded at 50mW incident microwave power.

The dosing procedure used for this sample involved delivering half of the required volume of the solution to each face of the crystal in one delivery, and allowing the solvent to evaporate under atmospheric conditions. However, the sample giving the EPR spectra shown previously in Figure 7.30 was prepared under more controlled conditions. Smaller volumes of the solution were delivered to the crystal per delivery, and following this the sample was placed into a closed system in order to slow down the evaporation process. This resulted in a more even distribution of the $Cu(acac)_2$ ligand to the surface of the substrate. The EPR spectra recorded of this sample (Figure 7.30) more closely resembles the situation on a single crystal, where at one orientation of the crystal with respect to the magnetic field, only one resonance can be resolved.

After the EPR spectra shown in Figure 7.30 were recorded, the EPR dewar was pumped down to a pressure of 10^{-6}mbar before breaking the seal between the EPR dewar and the main A chamber. The pressure in the A chamber did not increase above 10^{-8}mbar during this process. The sample was then raised into position to be studied by XPS spectroscopy. The sample was rotated so that one face of the crystal was perpendicular to the detector, thus maximising the number of core-level electrons detected and optimising signal intensity. A survey spectrum, scanning binding energies of 0–1280eV was recorded, as shown in Figure 7.32. Photoemission lines arising from the SiO_2 substrate were recorded at 110eV (Si $2p_{3/2}$) and 538eV (O 1s).[42] The survey spectrum also identified a level of carbon surface contamination, as evidenced by the photoemission line at 292eV (C 1s).

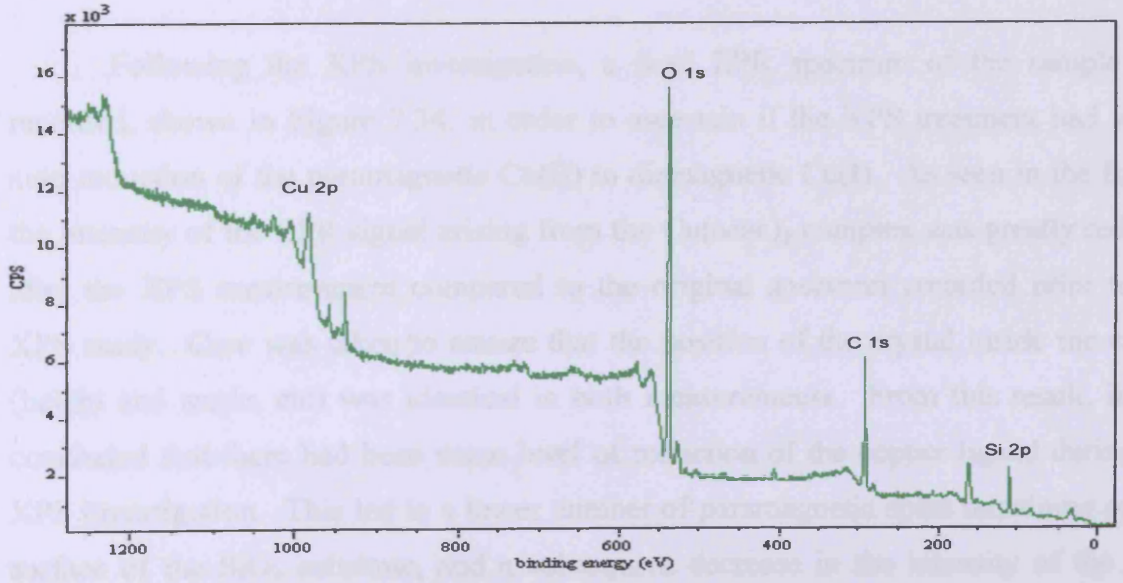

Figure 7.32 XPS survey scan of $Cu(acac)_2$ on SiO_2. The y-axis is reported in counts per second.

Following the survey spectrum, a detailed scan of the Cu 2p region was recorded, as shown in Figure 7.33. Photoemission lines due to Cu $2p_{3/2}$ and $2p_{1/2}$ were resolved at 938.5V and 958.2eV respectively. No shoulders were detected on either of the photoemission peaks, indicating that there was only one oxidation state of Cu on the SiO_2 surface.

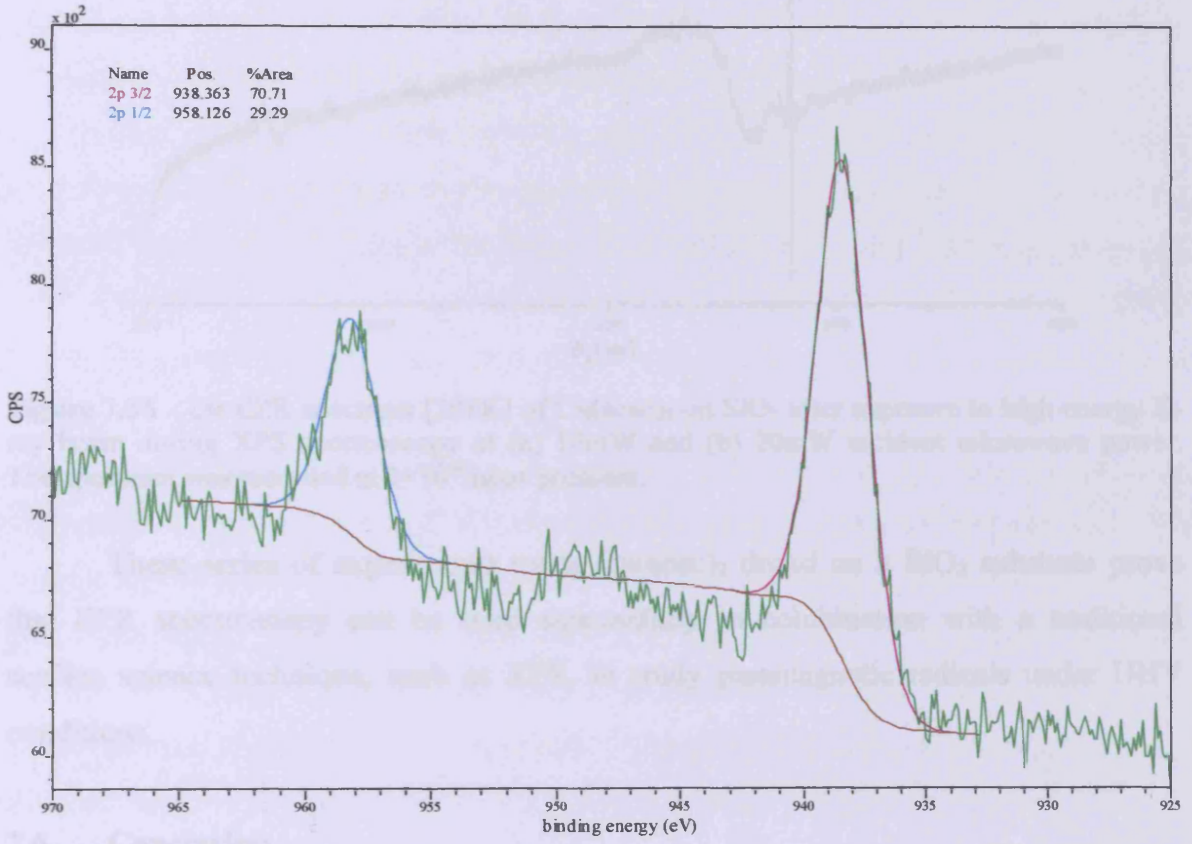

Figure 7.33 XPS spectrum of the $2p_{3/2}$ and $2p_{1/2}$ photoemission lines from $Cu(acac)_2$ dosed on SiO_2.

Following the XPS investigation, a final EPR spectrum of the sample was recorded, shown in Figure 7.34, in order to ascertain if the XPS treatment had led to auto-reduction of the paramagnetic Cu(II) to diamagnetic Cu(I). As seen in the figure, the intensity of the EPR signal arising from the $Cu(acac)_2$ complex was greatly reduced after the XPS measurement compared to the original spectrum recorded prior to the XPS study. Care was taken to ensure that the position of the crystal inside the cavity (height and angle, etc) was identical in both measurements. From this result, it was concluded that there had been some level of reduction of the copper ligand during the XPS investigation. This led to a lower number of paramagnetic spins remaining on the surface of the SiO_2 substrate, and a subsequent decrease in the intensity of the EPR spectrum.

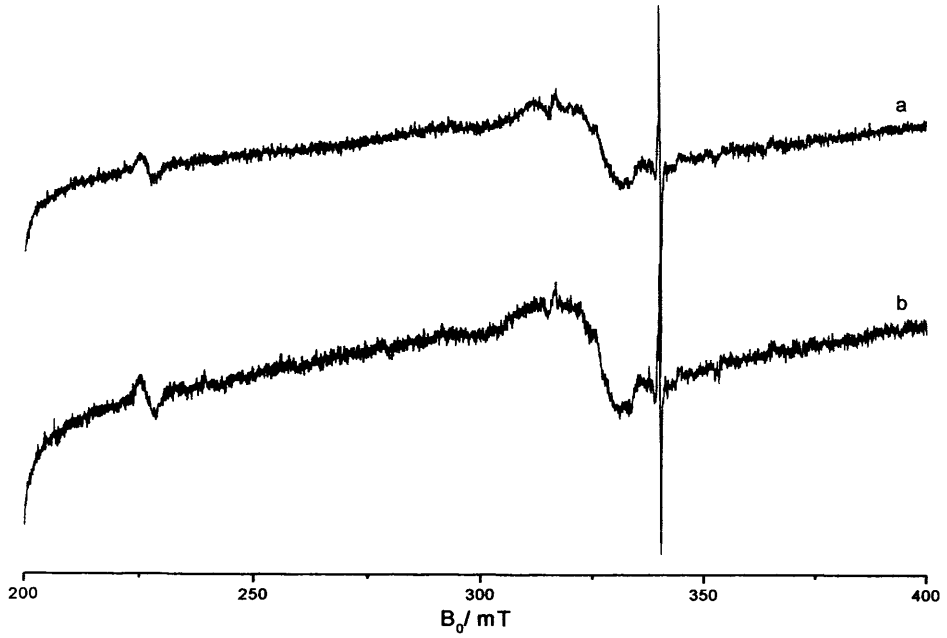

Figure 7.34 *cw*-EPR spectrum [298K] of $Cu(acac)_2$ on SiO_2 after exposure to high energy X-ray beam during XPS spectroscopy at (a) 10mW and (b) 20mW incident microwave power. The spectrum was recorded at 1×10^{-6}mbar pressure.

These series of experiments using $Cu(acac)_2$ dosed on a SiO_2 substrate prove that EPR spectroscopy can be used successfully in combination with a traditional surface science technique, such as XPS, to study paramagnetic radicals under UHV conditions.

7.5 Conclusion

The content of the current chapter details the work performed on the Omicron Multiprobe® Surface Science Ultra-High Vacuum system over a 24 month period. As has been discussed, the physical and technical requirements of this system are particularly demanding, and therefore much time was spent on optimising the system to achieve ultimate sensitivity. The detection limit of the system was determined from oxygen and DPPH sensitivity studies to be 5.4×10^{14} spins. This limit was shown to be lower than monolayer coverage on a $TiO_2(110)$ surface, thereby confirming that the study of surface defects on the surfaces of single crystal metal oxides is a viable investigation.

Much time was spent during the optimising process on developing a sample holder for the single crystals which would allow accurate positioning of the sample inside the cavity whilst simultaneously achieving maximum Q factors. The early designs tested allowed the entire single crystal to be critically coupled inside the

resonant cavity, but provided inefficient cooling to the samples. Later designs provided improved cooling to the sample due to improved thermal conductance of the sample holder, but were found to have a negative effect on the tuning characteristics of the cavity, such that only a small portion of the sample could be located inside the cavity during a measurement. The final design of the holder incorporated a narrow piece of sapphire rod coupled to a copper block, which provided good thermal conductance to the sample and had excellent tuning characteristics.

The concept of combining EPR with the more traditional surface science technique of XPS was proven during the investigation of $Cu(acac)_2$ dosed on the surface of multi-faceted SiO_2. Due to the broad nature of the Cu^{2+} EPR spectrum, spanning over ~200mT, the number of spins used on this sample was 3 orders of magnitude higher than the lower detection limit of the system. The unpaired electron in the d orbital of the copper ligand resulted in an axial EPR signal; the perpendicular component could be clearly resolved, although the parallel component was not visible in the spectra. The observation of an amorphous signal, arising from all orientations of the copper ligand with respect to the magnetic field, emphasised the importance of a controlled dosing procedure onto the substrate. The presence of the copper ligand on the surface of the SiO_2 substrate was confirmed by the identification of Cu 2p photoemission lines in the XPS spectrum. Photoemission lines originating from the SiO_2 substrate were also identified in the XPS spectrum.

The investigation of the $TiO_2(110)$ single crystal metal oxide proved to be experimentally challenging. However, a weak signal in the EPR spectra at $g = 1.97$ was provisionally assigned to a reduced titanium centre, and this assignment was supported by the photoemission lines in the XPS spectra. In order to confirm this assignment, further investigation using the final design of sample holder, and adsorption of oxygen would need to be performed.

The combination of these two techniques can be used in the future to characterise single crystal substrates and surface adsorbed radicals. In particular, XPS can be used to determine surface composition and to identify any surface impurities or contaminants. As shown in section 7.6.1, one of the main advantages of XPS spectroscopy is the ability to determine the oxidation state of the sample. During investigations where surface treatments of the substrate lead to the production of paramagnetic ions, XPS can be used to confirm the presence of these radicals even if they cannot be resolved by EPR spectroscopy. Although a quantitative approach was

not adopted during the course of this investigation, both XPS and EPR spectroscopy can be used quantitatively to determine the number of paramagnetic species in the sample. Using grazing angle techniques, it would also be possible to determine the depth of the species giving rise to the XPS photoemission lines. This approach would be particularly useful to confirm the presence of sub-surface electrons in samples of reduced TiO_2 as proposed for the polycrystalline sample in Chapter 5.

One of the biggest obstacles encountered during the investigations detailed in this chapter was the inefficient cooling of the single crystal samples, which prevented the identification of paramagnetic centres in the EPR spectra. In order for the UHV-EPR spectrometer to be of greatest use in the future, it would be necessary to resolve this issue of sample cooling. In connection with this, it would also be beneficial if a more accurate measure of sample temperature could be provided. This would require a thermocouple attachment to the single crystal itself, which is a technique already adopted by several groups.[10,12]

As mentioned previously, the cylindrical cavity was chosen for this investigation due to the increased sensitivity over the standard rectangular cavity. However, the electric and magnetic field profiles in the cylindrical cavity require incredibly accurate positioning of the sample inside the cavity to achieve optimum conditions and maximum sensitivity. On a system where the geometric dimensions are fixed, and the margin for error in these dimensions is minimal, this accurate positioning proved difficult to achieve. Therefore, it may be interesting in the future to incorporate a standard rectangular cavity which is less sensitive to sample positioning onto the UHV-EPR spectrometer. This would help to explore if the problems of accurate positioning of the sample inside the cylindrical cavity are actually outweighed by the increased sensitivity of the cavity.

In order to circumvent the problems of paramagnetic impurities in the single crystals used throughout this investigation, future work on the system will involve the formation and study of thin-layers of metal oxides on suitable substrates. It will be important to ensure that any substrate chosen is itself free of any paramagnetic species, and that the lattice constants of the substrate closely match those of the thin film.

Although it is recognised that EPR spectroscopy could not eliminate other classical surface science methods, it is hoped that it will be an additional, complimentary tool for the study of particular aspects of adsorption which are currently difficult to achieve with other methods.

7.6 References

[1] H.W. Spiess, *Ber. Bunsegnes. Phys. Chem.*, **1997**, *101*, 153.

[2] S. Bagdonat, W Göpel, R. Haul, *Z. Phys. Chem.*, **1973**, *87*, 11.

[3] D. Kaplan, D. Lepine, Y. Petroff and P. Thirry, *Phys. Rev. Lett.*, **1975**, *35*, 1376.

[4] D. Haneman, *Phys. Rev.*, **1968**, *170*, 705.

[5] B.P. Lemke, D. Haneman, *Phys. Rev. Lett.*, **1975**, *35*, 1379.

[6] Y. Li, M. Farle, K. Baberschke, *Phys. Rev. B*, **1990**, *41*, 9596.

[7] M. Farle, A. Berghaus, Y. Li, K. Baberschke, *Phys. Rev. B*, **1990**, *42*, 4873.

[8] M. Nilges, M. Shiotani, C.T. Yu, G. Barkley, Y. Jera, J.H. Freed, *J. Chem. Phys.*, **1980**, *73*, 588.

[9] M. Farle, M. Zomack, K. Baberschke, *Surf. Sci.*, **1985**, *160*, 205.

[10] M. Zomack, K. Baberschke, *Surf. Sci.*, **1986**, *178*, 618.

[11] J. Korringa, *Physica*, **1950**, *16*, 601.

[12] U.J. Katter, H. Schlienz, M. Beckendorf, H.-J. Freund, *Ber. Bunsenges. Phys. Chem.*, **1993**, *97*, 340.

[13] M. Zomack, K. Baberschke, *Phys. Rev. B*, **1987**, *36*, 5756.

[14] M.E. Bartram, B.E. Koel, *Surf. Sci.*, **1989**, *213*, 137.

[15] C. Kittel, E. Abrahams, *Phys. Rev. B*, **1953**, *90*, 238.

[16] U.J. Katter, T. Risse, H. Schlienz, M. Beckendorf, T. Kluner, H. Hamann, H-J Freund, *J. Mag. Res.*, **1997**, *126*, 242.

[17] H. Schlienz, M. Beckendorf, U.J. Katter, T. Risse, H-J Freund, *Phys. Rev. Lett.*, **1995**, *74*, 761.

[18] P.G. Gray, A.D. Yoffe, *Chem. Rev.*, **1955**, *55*, 1069.

[19] D.L. Freeman, J.D. Doll, *J. Chem. Phys.*, **1983**, *78*, 6002.

[20] T. Risse, T. Hill, M. Beckendorf, U.J. Katter, H. Schlienz, H. Hamann, H.-J. Freund, *Langmuir*, **1996**, *12*, 5512.

[21] T. Risse, T. Hill, J. Schmidt, G. Abend, H. Hamann, H-J Freund, *J. Chem. Phys.*, **1998**, *108*, 8615.

[22] T. Risse, T. Hill, J. Schmidt, G. Abend, H. Hamann, H-J Freund, *J. Phys. Chem. B*, **1998**, *102*, 2668.

[23] M. Sterrer, E. Fischbach, T. Risse, H-J Freund, *Phys. Rev. Lett.*, **2005**, *94*, 186101.

[24] M. Yulikov, M. Sterrer, M. Heyde, H-P Rust, T. Risse, H-J Freund, G. Pacchioni, A. Scagnelli, *Phys. Rev. Lett.*, **2006**, *96*, 146804.

[25] M. Sterrer, M. Yulikov, E. Fischbach, M. Heyde, H-P Rust, G. Paccioni, T. Risse, H-J Freund, *Angew. Chem. Int. Ed.*, **2006**, *45*, 2630.

[26] M. Sterrer, E. Fischbach, M. Heyde, N. Nilius, H-P Rust, T. Risse, H-J Freund, *J. Phys. Chem. B*, **2006**, *110*, 8665.

[27] U. Diebold, *S.Sci. Rep.*, **2003**, *48*, 53.

[28] D.R. Linde, *CRC Handbook of Chemistry and Physics 84th Edition*, **2003**, *CRC Press.*

[29] www.goodfellows.com.

[30] J.M Herrmann, J. Disdier, P.Pichat, *Chem. Phys. Lett.*, **1984**, *108*, 618.

[31] M. Radeka, M. Wierzbicka, S. Komornicki, M. Rekas, *Physica B*, **2004**, *348*, 160.

[32] D. Dvoranová, V. Brezová, M. Mazúr, M.A. Malati, *App. Catal. B*, **2002**, *37*, 91.

[33] K. Köhler, C.W. Schläpfer, A. von Zelewsky, J. Nickl, J. Engweiler, A. Baiker, *J. Catal.*, **1993**, *143*, 201.

[34] W. Göpel, G. Rocker, R. Feierabend, *Phys. Rev. B*, **1983**, *28*, 3427.

[35] G. Hopfengärtner, D. Bormann, I. Rademacher, G. Wedler, E. Hums, G.W. Spitznagel, *J. Elect. Spec. Rel. Phen.*, **1993**, *63*, 91.

[36] J.M. Pan, B.L. Maschhoff, U. Diebold, T.E. Madey, *J. Vac. Sci. Technol. A*, **1992**, *10*, 2470.

[37] M.A. Henderson, *Surf. Sci.*, **1996**, *355*, 151.

[38] U. Diebold, J. Lehman, T. Mahmoud, M Kuhn. G Leonardelli, W. Hebenstreit, M. Schmid, P. Varga, *Surf. Sci.*, **1998**, *411*, 137.

[39] M. Li, W. Hebenstreit, L. Gross, U. Diebold, M. A. Henderson, D. R. Jennison, P. A. Schultz, M. P. Sears, *Surf. Sci.*, **1999**, *437*, 173.

[40] M. Li, W. Hebenstreit, U. Diebold, *Phys. Rev. B*, **2000**, *61*, 4926.

[41] J.F. Mauder, W.F. Stickle, P.E. Sobol, K.D. Bomben, *Handbook of X-Ray Photoelectron Spectroscopy*, **1992**, *Perkin-Elmer Corp.*, USA.

[42] T.L. Barr, *J. Vac. Sci. Technol. A*, **1991**, *9*, 1793.

Chapter 8
Conclusions

Throughout this thesis, EPR spectroscopy has been used to identify and characterize a number of different radicals over the surface of samples of polycrystalline TiO_2. The sensitivity of the technique is much greater than many other spectroscopic methods, and the variable temperature capabilities allow the detection of thermally unstable radicals which may not be detected by other spectroscopic techniques at room temperature.

The results discussed in Chapter 5 have shown that oxygen centred radicals have different rates of generation and subsequent stabilities at different sites on the surface of the metal oxide. For example, it has been shown that the superoxide anion is preferentially formed at vacancy sites on the TiO_2 surface giving rise to an EPR signal with a low value of g_{zz}. Additionally, at higher reduction temperatures more stabilisation sites become available to the anion, as evidenced by the heterogeneity of signals in the g_{zz} component of the orthorhombic EPR signal. The speciation of radicals on the surface was also manifested in the A_{xx} component of the $^{17}O_2^-$ signal; three different hyperfine coupling parameters were resolved, corresponding to the well-defined sites (I–III) identified in the $^{16}O_2^-$ spectrum. This result highlights how the sensitivity of the EPR technique is able to identify structural differences on the surface of a polycrystalline sample through the specificity of the g and A tensors of the spin Hamiltonian.

It has also been demonstrated that the O_2^- anion stabilised at the oxygen vacancy site exhibits different thermal, chemical and photo-reactivities compared to anions bound at non-vacancy sites. For example, O_2^- anions stabilised at vacancy sites are only stable on the surface to temperatures ~333K, whereas those at non-vacancy bound sites are stable at temperatures >353K. Vacancy bound superoxide anions have been shown to be labile under the influence of low temperature UV irradiation, and furthermore, they show preferential chemical reactivity with adsorbed acetone when the oxygen and organic are added sequentially to the reduced surface. Evidence was provided which indicated the migration of superoxide radicals over the surface of polycrystalline TiO_2. Adsorption of oxygen to the thermally reduced sample at low temperatures, followed by sample annealing, led to a decrease in the *relative* contribution to the EPR signal from the vacancy bound sites, despite the overall signal intensity remaining constant during the annealing process.

Under the influence of UV irradiation charge carriers are generated, which subsequently undergo reaction with adsorbates to form transient intermediates. It has been demonstrated that when oxygen is co-adsorbed with an excess of a ketone substrate over TiO_2 followed by low temperature UV irradiation, a transient peroxy $ROO^{\bullet}$ radical is formed, which is unstable at temperatures >200K. The peroxy radical is formed *via* a charge transfer event between the photo-generated hole and the adsorbed organic. The peroxy radical has been identified on the surface using a series of organics (namely acetone, butanone, heptanone, cyclopentanone and cyclohexanone), which all exhibited the same decrease in signal intensity of the EPR signal on gentle annealing. This reaction is particularly relevant to the study of the complete photooxidation of volatile organic compounds into carbon dioxide and water. Through the use of ^{17}O-labelled oxygen, the hyperfine coupling constant was used to calculate the spin density on the terminal oxygen of the peroxy radical. Only a small amount of delocalization of the spin occurs onto the –R group of the peroxy. However, it was demonstrated that as the electron withdrawing power of the -R group increased, the positive charge on the inner oxygen increased leading to an increase in the spin density on the terminal oxygen.

The reaction of acetone with the superoxide anion in the dark was also studied. The EPR signal due to the superoxide anion irreversibly disappeared on exposure to the acetone and a new EPR signal with the g_1 values of 2.032 and 2.035 was identified. The radical responsible for this signal was unstable at temperatures >250K. From the information provided by the g values and hyperfine coupling parameters, the radical responsible for the new signal was assigned to an $[acetone\text{-}O_2^-]_{(a)}$ surface complex formed by nucleophilic attack of the superoxide on the electrophilic carbon atom of the carbonyl group of the acetone. It has been shown that the different stabilisation sites for the superoxide radical on the surface of the TiO_2 exhibit different and selective reactivities with the adsorbed acetone, which must be investigated further in future studies.

A reaction was also seen to occur between the adsorbed acetone molecule and the reduced surface. Thermal annealing of TiO_2 under vacuum results in the removal of lattice oxygen from the surface (and bulk) of the metal oxide, generating Ti^{3+} cations. Electron transfer from the Ti^{3+} cation into the antibonding orbital of the carbonyl group of the acetone molecule resulted in the formation of an unstable radical anion, $\{CH_3COCH_3^{\bullet-}\}^*$. This radical underwent fast dissociation to $CH_3^{\bullet}$ and $CH_3CO^{\bullet}$

radicals, which were not detected in the EPR spectrum. Subsequent addition of molecular oxygen at low temperature, followed by gentle annealing, identified two new EPR signals. The two signals exhibited different thermal stabilities indicating that they originated from two independent radicals. The use of ^{17}O-labelled O_2 identified these radicals as the acyl and peroxyacyl radicals, $CH_3OO^{\bullet}$ and $CH_3COOO^{\bullet}$, respectively.

It was previously shown on the polycrystalline samples of P25 TiO_2 that EPR can be used to identify structural differences in the stabilisation sites for radicals on the surface, through an observed heterogeneity in the g_{zz} component of the superoxide (O_2^-) signal. However, it is impossible to assign these stabilisation sites to specific locations on the surface on the powdered samples; for this it is necessary to perform detailed investigations of the well-defined single crystal surface. An EPR spectrometer was therefore incorporated as part of a multi-chamber Omicron Multiprobe® Surface Science Ultra-High Vacuum (UHV) system, which enabled the study of single crystals of metal oxides. Much of the work performed on this system during the course of this investigation was devoted to optimising the operating conditions, including the development of a suitable sample holder for use in the EPR cavity and improving the sample cooling system to increase ultimate sensitivity of the system. Several calibration experiments were performed which determined the minimum detection limit of the system to be 2.5×10^{14} spins, which is lower than monolayer coverage on the $TiO_2(110)$ surface.

Using a sample of $Cu(acac)_2$ dosed onto a SiO_2 substrate it was also shown that XPS and EPR can be used in combination as surface sensitive techniques to give detailed information of the physical and chemical characteristics of a sample. The XPS spectrum clearly identified the Cu 2p photoemission lines indicating that the $Cu(acac)_2$ had been successfully dosed onto the surface. The d^9 Cu^{2+} gave rise to an axial EPR spectrum; the perpendicular component could be clearly resolved, although the parallel component was not visible in the spectra.

The investigation of single crystal metal oxides was hindered by the presence of large paramagnetic impurities in the crystals, giving rise to sharp, intense EPR signals throughout a large magnetic field. Further, the difficulties encountered in providing sufficient cooling to the samples delayed the process of recording a high quality, low temperature measurement. However, a weak signal which exhibited the correct temperature dependency for a paramagnetic reduced titanium metal centre was assigned

to Ti^{3+} cations and this assignment was supported by the presence of Ti^{3+} photoemission lines in the XPS spectrum.

The work presented in this thesis has shown for the first time, how *cw*-EPR spectroscopy can be used to identify specific stabilisation sites for oxygen centred radicals over *polycrystalline* samples of metal oxide. In order to make accurate assignments for the location of radicals on the surface, attention was focussed towards single crystal samples with a well-defined surface morphology. UHV-EPR investigations were performed on $TiO_2(110)$ in order to combine the wealth of knowledge from the polycrystalline samples acquired *via* EPR spectroscopy to the detailed information on single crystals available from more traditional surface science techniques. Further work in this area would require theoretical calculations to be performed to support the experimental results.

In the study of adsorbed organics over thermally reduced TiO_2, the importance of performing the experiments at low temperature was highlighted. In particular, all of the radicals observed were thermally unstable and could not be detected in the EPR spectrum at temperatures above 250K. The thermal decay of these radicals explains why they have not been widely studied by other spectroscopic techniques, thereby proving the importance and relevance of EPR spectroscopy in these studies. Moreover, the results indicate that future investigations should be performed at low temperatures for a more complete understanding of reaction mechanisms to be obtained.

References

[1] E. Carter, A.F. Carley, D.M. Murphy, *ChemPhysChem*, **2007**, *8*, 113.
[2] E. Carter, A.F. Carley, D.M. Murphy, *J. Phys. Chem. C*, **2007**, submitted.

Appendix 1
UHV Theory and System Specifications

In the following sections the basic theory and requirements of Ultra-High Vacuum systems are discussed. Reference will be made to gas kinetics, operating procedures to obtain high vacuum conditions, and the surface analytical techniques which form the Omicron Multiprobe® Surface Science Ultra-High Vacuum (UHV) system.

A1 Necessity of UHV

An Ultra-High Vacuum environment is required for surface science investigations to ensure that atomically clean surfaces can be prepared and so that these surfaces remain free of contaminants for the duration of the experiment. Additionally, many of the techniques used in surface science analysis rely on the production and detection of ionized particles which must be unaffected by the presence of gas phase molecules. These two factors can be further understood on consideration of the properties described by the ideal gas law and gas kinetics.

A particle in an ideal gas phase will travel a distance between collisions, referred to as the mean free path, determined by:

$$\lambda = \frac{kT}{1.414\,P\,\sigma} \qquad \text{(A.1)}$$

where λ = mean free path (m), k = Boltzmann constant (1.38×10^{-23} JK^{-1}), T = temperature (T), P = pressure (Nm^{-1}), σ = collisional cross section (m^2). At atmospheric pressure the mean free path of a molecule is approximately 7×10^{-8}m, whereas in conditions of ultra-high vacuum (10^{-10} Torr) the mean free path increases to 5×10^{5}m.

The length of time that a surface remains free of contaminants can be calculated by considering the number of particles hitting the surface and the probability that these particles will stick to the surface. The number of particles hitting the surface per unit area per unit time is known as the incident flux, and is calculated from:

$$F = \tfrac{1}{4}\, n\, c \qquad \text{(A.2)}$$

where F = incident flux ($molecules m^{-2}s^{-1}$), n = molecular gas density (molecules m^{-3}), c = average molecular speed (ms^{-1}).

The molecular gas density can be calculated from the ideal gas equation:

$$n = \frac{N}{V} = \frac{P}{kT} \tag{A.3}$$

and the average molecular speed is derived from the Maxwell-Boltzmann distribution of gas velocities:

$$c = \sqrt{\frac{8kT}{m\pi}} \tag{A.4}$$

On combination of the ideal gas law and the Maxwell-Boltzmann distribution given in Equations A.3 and A.4, the incident flux can therefore be described by:

$$F = \frac{P}{\sqrt{2\pi mkT}} \tag{A.5}$$

From Equation A.5 it can be seen that the incident flux is directly proportional to the gas pressure, therefore a reduction in gas pressure by obtaining vacuum conditions leads to a reduction in the incident flux and consequently a longer time period before surface contamination becomes a concern. The incident flux must then be combined with the sticking coefficient of the gas in order to determine how much coverage will form in a certain time period. The sticking coefficient is a probability of the likelihood that an incident molecule will adsorb to the surface as opposed to undergoing an elastic collision. The sticking coefficient is a function of several parameters including the nature of the gas, the nature of the surface, the temperature inside the chamber and previous surface coverage (i.e. the sticking coefficient can vary as the surface changes from clean to contaminated).

The surface coverage can be defined in several ways, but two definitions are used more frequently than others. The first defines surface coverage as a fraction of the maximum obtainable coverage i.e.:

$$\theta = \frac{actual\ \text{cov}erage}{saturation\ \text{cov}erage} \tag{A.6}$$

and therefore θ lies in the range between 0 (no coverage) and 1 (maximum coverage). Alternatively, surface coverage is defined as a ratio of the number of adsorbed species on the surface to the number of available adsorption sites on the surface i.e.:

$$\theta = \frac{number\ of\ adsorbed\ species\ per\ unit\ area}{number\ of\ surface\ substrate\ atoms\ per\ unit\ area} \quad (A.7)$$

A monolayer is described as a single layer of adsorbed atoms on the surface of the solid, and the monolayer time is the time taken for the monolayer to form. This can be calculated from:

$$t = \frac{3.2 \times 10^{-6}}{P} \quad (A.8)$$

where a unit sticking coefficient (i.e. every atom that strikes the surface is adsorbed) has been assumed. If the time required to perform a surface science experiment is one hour then the pressure required for this is $<10^{-9}$mbar, which is in the ultra-high vacuum regime.

A2 Achieving UHV

A2.1 Pumping Systems

The chambers on the Omicron Multiprobe® Surface Science System are pumped by a series of rotary, turbo, ion and titanium sublimation pumps. Each pump is used for a specific purpose, and the different pumps operate most efficiently in different pressure regimes.

- Rotary pumps physically remove the gas from the system and are able to create a vacuum of 10^{-2} mbar from atmospheric pressures. Rotary pumps are most often used as backing pumps for turbo molecular pumps.
- Turbo pumps also physically remove gas from the system and are able to obtain base pressures of 10^{-9} mbar. Most modern turbo pumps are able to pump down from atmospheric pressures. Gas molecules in the chamber collide with the blades of the turbo pump where they are directed towards the backing pump to be removed.
- Ion pumps trap gases inside the system. They consist of a parallel array of stainless steel tubes, two titanium plates with a high voltage across them placed a short distance from the end of the tubes, and a strong magnetic field parallel to the tubes. Electrons are released from the negative plate and are constrained on helical trajectories through the stainless steel tubes, where ionization occurs on impact with gas molecules. The potential energy of the ion is then converted

into kinetic energy, and the ion is accelerated towards the titanium plate where sublimation occurs. Burial of the original atom or molecule in the thin film of titanium follows, resulting in an effective lowering of the pressure in the chamber.

- Finally, titanium sublimation pumps (TSPs) are used to reach base pressures of $\sim 10^{-11}$ mbar. The pump consists of three titanium/molybdenum alloy filaments through which a high current is passed. During this process the filaments glow red hot and titanium is sublimated from the filament. The titanium coats the walls of the chamber and reacts with any active gas molecules in the chamber. These reacted molecules can no longer contribute to the pressure of the UHV chamber and so the pressure inside the chamber is reduced. TSPs do not remove gas molecules from the chamber and so the TSP must remain open when the system is baked so that the trapped molecules are released into the chamber and removed from the system by the turbo and rotary pumps.

The A, C, P and STM chambers are all pumped independently using a combination of rotary, turbo, ion and titanium sublimation pumps to achieve base pressures of 2×10^{-10} Torr. The quartz dewar in which the EPR samples are located is connected to a rotary and turbo pump to achieve a base pressure of 10^{-7} Torr when isolated from the main A chamber.

A2.2 Bake-out Procedure

The first step in achieving UHV conditions involves heating the chamber to promote desorption of gas molecules from the chamber walls. During this process the Omicron Multiprobe® Surface Science System is enclosed in bake-out covers which are fitted with heaters; the system is left at a temperature of 388K for a period of 60 hours. During this time the rotary and turbo pumps are switched on and are open to the chambers in order to remove the desorbed gases from the system. The ion pumps and titanium sublimation pumps are switched off but are left open so that any trapped gas atoms or molecules may be released into the chamber and subsequently removed.

Once the bake-out procedure is complete and the covers have been removed from the system it is necessary to undergo a degassing procedure. The ion gauges, X-ray filaments and mass spectrometer filaments all need to be degassed, which involves slowly increasing the current flow through the filaments to promote desorption of gases.

This degassing procedure is performed while the chambers are still warm after bake-out to prevent any desorbed gasses from sticking to cold chamber walls.

A2.3 UHV Chambers

The central (or C) chamber is equipped with several metal evaporators and is set up for laser Raman spectroscopy. Base pressures of 10^{-10}mbar can be achieved using a pumping system that consists of rotary, turbo, ion and titanium sublimation pumps. Samples are cleaned and prepared for study by the surface science techniques listed above in the preparation (or P) chamber. The chamber is equipped with metal evaporators and an ion sputtering gun. A gas line is connected to the chamber via a leak valve that allows controlled flow of gases into the chamber; the composition of these gases can be analysed using mass spectrometry. Samples can be annealed in the P chamber through either resistive heating of the sample plates, direct heating of the sample or by electron beam heating.

Samples can be placed inside the P chamber through the fast-entry lock system, which allows samples to be put inside the system without having to bring the whole chamber up to atmospheric pressures. Directly beneath the P chamber is an electrochemical cell, where in-situ surface science studies can be performed on reactions as they are in progress. Base pressures of 10^{-10} mbar can be achieved using a pumping system that consists of rotary, turbo, ion and titanium sublimation pumps.

Adjoining the P chamber is another chamber where Scanning Tunnelling Microscopy (STM) and Atomic Force Microscopy (AFM) can be performed. The STM chamber can be isolated from the P chamber and therefore has its own pumping system. The chamber is initially brought down to a pressure of ~10^{-10} mbar by pumping on the rotary and turbo pumps through the P chamber. When the STM chamber is isolated from the P chamber it is pumped by ion and titanium sublimation pumps which help to minimise vibrations in the chamber, and achieve base pressures of 10^{-12} mbar. There is a carousel inside the STM chamber that can hold up to a maximum of 12 samples.

A3 Experimental techniques

A3.1 X-Ray Photoelectron Spectroscopy (XPS)

XPS is a surface sensitive technique which can be used to elucidate atomic compositions and to gain information on the nature of the bonding in the studied material. The use of XPS in surface science analysis has increased dramatically since its development in the mid-1960's by Siegbahn *et al.*[1] The technique involves

irradiating a surface with monochromatic X-rays and analyzing the energy of the electrons emitted from the surface. The data provided from XPS spectra allows identification of chemical composition in both a qualitative and quantitative manner, and additionally it can provide information on the chemical nature and environment of the elements present.

A3.1.1 Photoemission

The principle of the technique lies in the photoelectric effect, as described by Einstein in 1905.[2] Incident radiation interacts with atoms in the surface region and imparts energy to the electrons within the atom. If the electrons have sufficient energy, they are able to escape the surface of the material as a photoelectron. The electrons emitted from the surface can originate from the valence band of the atom or from the core levels. Each core atomic orbital has a specific binding energy associated with it; therefore each element gives rise to a characteristic set of photoemission peaks. The identification of these peaks can therefore be used to identify the presence of elements in the sample studied, which explains the origin of the alternative acronym Electron Spectroscopy for Chemical Analysis (ESCA). The incident radiation used during an XPS experiment is typically Mg Kα (1253.6eV) or Al Kα (1486.6eV).

Electrons originating from the outer valence shells can be studied to provide information on the nature of the bonding characteristics of the materials under investigation. Although valence shell electrons will be photoemitted during an XPS investigation, they are best studied using the similar technique of Ultra-Violet Photoelectron spectroscopy, which uses He I (21.2eV) or He II (40.8eV) radiation. The lower energy radiation means that core electrons will not be excited. The inherent line-width of this radiation is much narrower than X-ray radiation, which leads to enhanced resolution. The principle of photoelectron spectroscopy (XPS and UPS) is shown diagrammatically in Figure A.1.

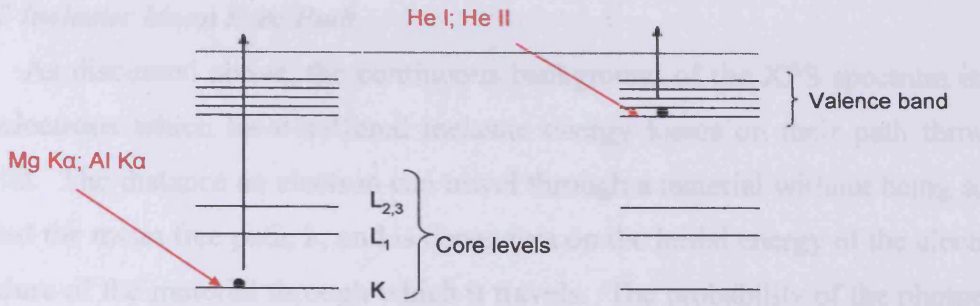

Figure A.1 Schematic illustration of the photoexcitation events during photoelectron spectroscopy.

The binding energy is the energy difference between the ionized and neutral atom (see Equation A.9), and is unique to each element. This allows XPS to identify elements in the surface region of the analyzed material. Further, the relative concentration of the elements can also be determined from the intensity of the photoemission lines.

$$E_K = h\nu - E_B - \Phi_S \qquad (A.9)$$

The process of photoemission of core level electrons, and the resulting kinetic energies of these electrons giving rise to peaks in the XPS spectrum, is shown in Figure A.2.

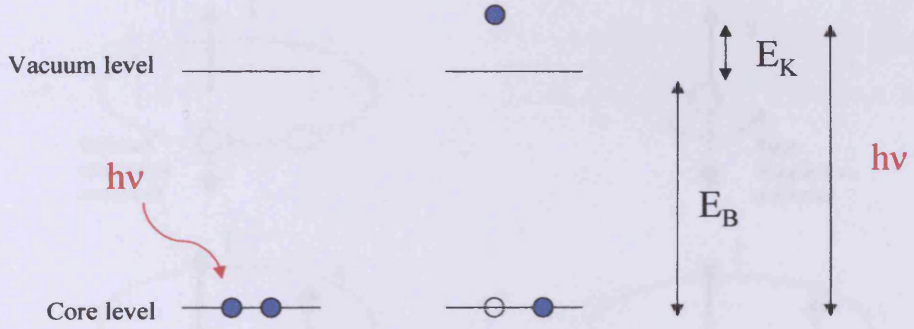

Figure A.2 Photoemission of core level electrons, studied in XPS.

An XPS spectrum is displayed as number of electrons, usually expressed in counts per second, *versus* electron binding energy. The discrete lines, known as photoemission lines, are due to the excitation of electrons from core energy levels which have suffered no energy loss on their path through the material to the surface. These peaks are superimposed on a continuous background which arises from electrons that undergo inelastic energy loss; due to this decrease in kinetic energy of the electron they contribute to the background on the high binding energy side of the peak.

A3.1.2 Inelastic Mean Free Path

As discussed above, the continuous background of the XPS spectrum is due to photoelectrons which have suffered inelastic energy losses on their path through the material. The distance an electron can travel through a material without being scattered is called the mean free path, λ, and is dependent on the initial energy of the electron and the nature of the material through which it travels. The probability of the photoelectron travelling through the material without suffering inelastic losses decreases with depth and can be calculated from:

$$P(d) = \exp(-d/\lambda) \qquad (A.10)$$

The variation of inelastic mean free path with the initial energy of the electron can be described by the "universal curve" which is a qualitative tool for predicting the surface sensitivity of an XPS experiment.

A3.1.3 Spin-orbit coupling

An electron in any orbital with orbital angular momentum will experience coupling between the magnetic fields of the electron spin (s) and the angular momentum (l), shown in Figure A.3.

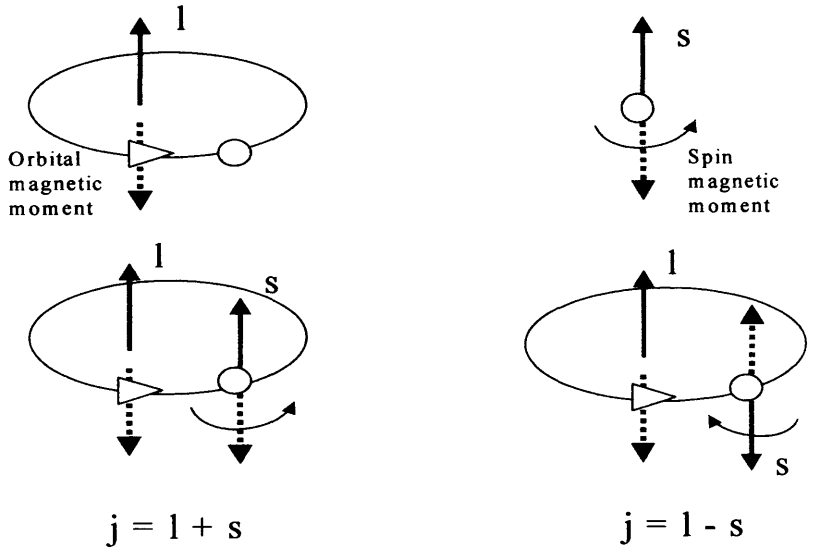

Figure A.3 Principle of spin-orbit coupling.

Spin-orbit coupling is usually treated using either the Russell-Saunders coupling approximation or the j-j coupling approximation. The total angular momentum (j) can be calculated as follows:

$$j = |l \pm s| \qquad (A.11)$$

Photoemission arising from s orbitals, where l = 0, results in singlet peaks because the total angular momentum j can only take on the value j = ½. For p orbitals, where l = 0 or 1, the total angular momentum is calculated from:

$$j = 0 + ½ = ½ \qquad (l = 0, s = 1/2)$$

$$j = 1 + ½ = 3/2 \qquad (l = 1, s = ½)$$

The degeneracy (g) of the levels can be calculated from:

$$g = 2j + 1 \qquad \text{(A.12)}$$

This leads to the set of energy levels shown in Table A.1

Table A.1 Degeneracy of subshells.

Subshell	J values	Degeneracy
S	½	-
P	½, 3/2	1,2
D	3/2, 5/2	2,3
F	5/2, 7/2	3,4

The energy level with the lower j value has the higher binding energy in the doublet, for example Ti $2p_{1/2}$ (464.5eV) and Ti $2p_{3/2}$ (458.7eV). The magnitude of the spin orbit splitting increases with nuclear charge.

A3.1.4 Chemical Shift

The position of photoemission lines is dependent not only on the core level from which the photoelectron originates, but also on the oxidation state of the ion and the physical and chemical environment. Atoms of high oxidation state exhibit high binding energy, and therefore lower kinetic energy, due to the additional unshielded coulombic attraction from the nucleus. This results in peaks at higher binding energy in the spectrum. This is evidenced in the case of titanium, which in the metallic state Ti^0 has a $2p_{3/2}$ peak energy of 453.7eV and in TiO_2 the Ti^{4+} $2p_{3/2}$ peak is seen at 458.7eV.[3]

Additionally, in the case of semiconducting materials such as TiO_2, slight charging of the material during the course of the XPS measurement can lead to changes in peak energy. The amount of chemical shift due to charging is the same for each

photoemission peak and is usually monitored through changes in peak position of the C 1s peak (284.5eV).

Although chemical shifts in XPS are readily observable and interpretable, the resolution of chemical shifts is itself limited by the width of the photoemission peaks. These are themselves limited by the lifetime of the final state of the electron, by the linewidth of the incident radiation and the resolving power of the electron detector.

A3.1.5 Instrumentation

The XPS spectrometer used in this investigation incorporates a DAR 400 X-ray twin anode source and power supply and an EA125 Energy Analyser. The X-ray source is shown diagrammatically in Figure A.4. Electrons originating from the heated filament are extracted and follow a trajectory to either the Mg Kα or Al Kα anode, which are held at a high positive potential. The anode is cooled by a continuous flow of water to prevent evaporation of the magnesium or aluminium coatings. The X-rays generated at the anode pass through the thin aluminium foil window to the sample.

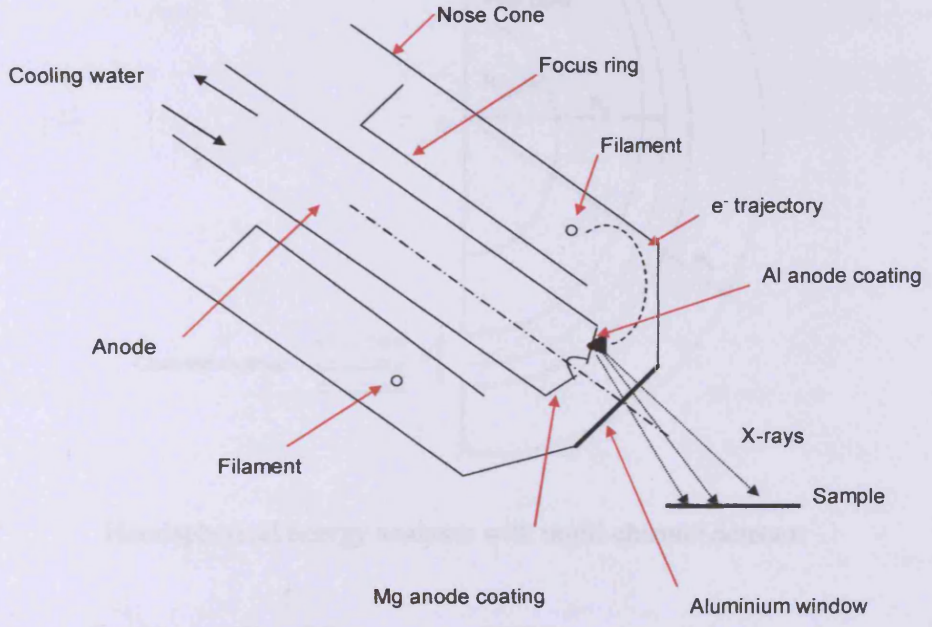

Figure A.4 Schematic of the XPS anode under operating conditions. Taken from Omicron manual.

The photoelectrons pass through a hemispherical energy analyser before arriving at the detector. The energy analyser consists of two concentric hemispheres with a potential difference applied between them. The path of the electron is altered as a result

of the electric field arising from this potential difference, so that only electrons of a certain energy, known as the pass energy, are collected at the detector. Electrons with less kinetic energy than the pass energy are attracted to the inner plate (held at positive potential), whereas those with kinetic energy greater than the pass energy hit the outer plate (held at negative potential) and are lost. By adjusting the potential difference between the two plates, a spectrum can be recorded of photoelectrons with different pass energies.

The intensity observed in the analyser is amplified by the positioning of an array of seven channeltrons (detectors) at different positions along the exit slit. The electrons detected at the channeltrons offset from the centre of the slit are offset in energy compared to the "true" energy by an amount which is proportional to the position of the channeltron. Before the intensity from each channeltron is summed together to give an overall intensity, the software calibrates for the energy offset.

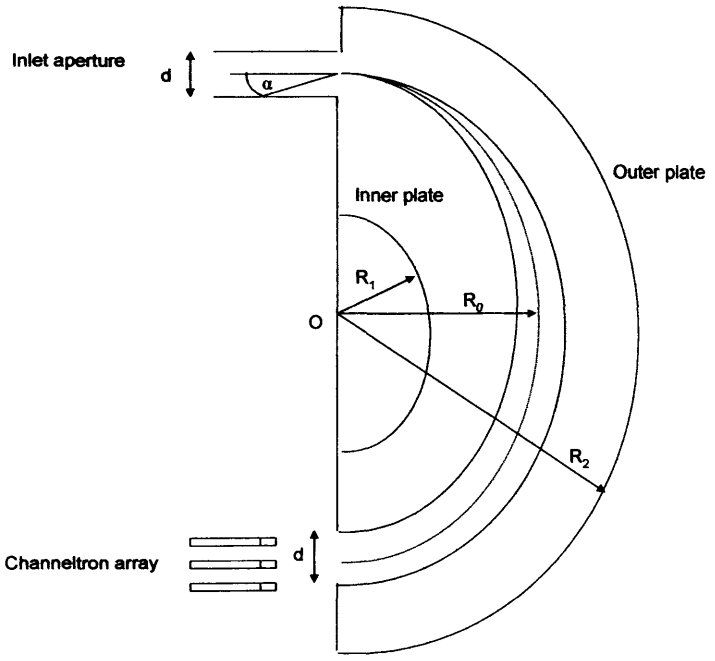

Fig A.5 Hemispherical energy analyser with multi-channel detector

A3.2 Scanning Tunnelling Microscopy (STM)

The variable temperature scanning probe microscopy (VT SPM) system allows atomic resolution images to be obtained of surfaces. The technique involves bringing a fine tip towards the surface of the sample and applying a voltage between the sample and the tip. When the separation distance between the sample and the tip is of the order of angstroms a tunnelling current can exist between them. The magnitude of the

tunnelling current is sensitive to the separation distance and hence any changes in the topography of the sample will be measured by a change in the magnitude of the tunnelling current. Most STM experiments are performed in a constant current mode, where the magnitude of the tunnelling current is kept constant and the separation distance between the tip and the sample is adjusted as the tip is rastered across the surface. STM images can only be resolved from conducting samples.

A3.3 Atomic Force Microscopy (AFM)

AFM is another technique which provides atomically resolved images of the sample surface. On the Omicron Multiprobe® System, AFM images are recorded using the VT SPM system mentioned above. Its advantage over STM is that it does not require the sample to be conducting, and can therefore be used to study those samples where STM is not possible. AFM utilises an atomically sharp tip which is rastered across the surface of the sample in the same way as the tip used in STM. The tip is on the end of a cantilever which bends in response to the repulsive force between the tip and the sample. The extent of bending of the cantilever as it is moved across the surface of the sample leads to a topographical image of the sample. Most AFM experiments are performed in constant force mode, where the repulsive force between the sample and the tip is kept constant and the cantilever is moved up and down to accommodate this pre-determined force.

A3.4 Low Energy Electron Diffraction (LEED)

The Omicron Multiprobe® Surface Science System is fitted with an Omicron SpectraLEED rear-view optics unit. LEED is the principle technique for determining the structure of surfaces and may provide both qualitative and quantitative information on the sample. In the process of a LEED experiment, a beam of electrons of uniform energy, usually in the 20–200eV range, is incident on the sample in a direction normal to the surface. Elastically scattered electrons produced during this irradiation are incident on a fluorescent screen that displays the spot pattern. Any non-elastically scattered electrons are removed from the beam by a series of retarding grids placed directly in the path of the fluorescent screen. By utilising the de-Broglie relation set out in the theory of wave-particle duality and the Bragg condition of constructive interference, analysis of the size and distribution (including symmetry) of the spots can

yield information on the identity of the substrate unit cell and additionally on the unit cell of any adsorbates.

A3.5 Ion Scattering Spectroscopy (ISS)

ISS is performed using an EAC2000-64 unit with EA125 analyser. ISS, otherwise known as Low Energy Ion Scattering (LEIS), can be used to determine the composition of the surfaces of samples. A beam of ions is incident on the sample where collisions between the ions and the atoms on the surface of the sample will result in backscattering of the incident ions. Analysis of the energy spectrum of these backscattered electrons can provide information on the mass of the atoms on the surface and can therefore aid in the identification of the surface composition. The incident ions are He^+ in the energy range from 0.5 to 5keV. The low electron affinity of Helium ions (0 $kJmol^{-1}$)[4] results in a high probability of electron transfer from the atoms on the surface to the ion beam resulting in neutralisation. After two or more collisions of the incident ion with the surface, electron transfer is likely to have occurred. Therefore, if the detector is set to only detect ions of the same nature as the incident ion beam i.e. He^+ then only ions which have undergone only one collision will be detected. Those ions that have undergone multiple collisions with the surface will contribute to the background of the spectrum. If grazing angle studies are performed on the sample then information on the inter-atomic spacing of the surface atoms can also be obtained.

A3.6 Ultraviolet Photoelectron Spectroscopy (UPS)

UPS measurements are performed using an Omicron VUV Source HIS13 unit. UPS spectroscopy is used to study the electronic structure of samples and enables the complete band structure of a sample to be mapped out in k-space. It works largely on the same principle as XPS which is discussed in detail above. The source of radiation used in UPS is He I radiation of energy 21.2eV which is only capable of ionising electrons from the valence levels.

References

[1] C. Nordling, K. Siegbahn, *Revue Roumaine de Physique*, **1966**, *11*, 797.

[2] A. Einstein, *Annalen der Physik*, **1905**, *17*, 132.

[3] A. Fahlman, C. Nordling, G. Johansson, K. Hamrin, *J. Phys. Chem. Solids,* **1969**, *30*, 1835.

[4] www.webelements.com